Dimensionnements et comparaisons de convertisseurs électromécaniques à bas coût et à grande disponibilité pour véhicules électriques

Chao Liu

NNT : 2016SACLC049

THESE DE DOCTORAT
DE
L'UNIVERSITE PARIS-SACLAY
PREPAREE A
"CENTRALESUPELEC"

ECOLE DOCTORALE N° 575
Physique et ingénierie : Electrons, Photons, Sciences du vivant

Spécialité de doctorat : Génie électrique

Par

Mme Chao Liu

Dimensionnements et comparaisons de convertisseurs électromécaniques à bas coût et à grande disponibilité pour véhicules électriques

Thèse présentée et soutenue à Gif-sur-Yvette, 06/07/2016 :

Composition du Jury :

M. Takorabet Noureddine, Professeur, Université de Lorraine, Président du jury
M. Roger Daniel, Professeur, Université Artois, Rapporteur
M. Amara Yacine, Maître de Conférences HdR, Université du Havre, Rapporteur
M. Marchand Claude, Professeur, Université Paris-Sud, Examinateur
M. Dessante Philippe, Professeur, CentraleSupélec, Directeur de thèse
M. Krebs Guillaume, Maître de Conférences, Université Paris-Sud, Co-encadrant de thèse

Université Paris-Saclay
Espace Technologique / Immeuble Discovery
Route de l'Orme aux Merisiers RD 128 / 91190 Saint-Aubin, France

université PARIS-SACLAY | ÉCOLE DOCTORALE Physique et ingénierie : électrons, photons, sciences du vivant (EOBE)

Titre : Dimensionnements et comparaisons de convertisseurs électromécaniques à bas coût et à grande disponibilité pour véhicules électriques (en français)

Mots clés : machine asynchrone, machine synchrone à réluctance variable, modèle analytique, dimensionnement sur cycle et comparaison

Résumé : Aujourd'hui, l'électrification des véhicules constitue une des solutions mises en œuvre par les constructeurs automobiles dans la lutte contre les émissions de gaz polluants et pour la réduction des consommations. Comme le prix des aimants terres rares a fortement augmenté ces dernières années, les moteurs électriques sans aimants permanents sont attractifs, comme les moteurs asynchrones, synchrones à rotor bobiné, à réluctance variable (double saillance ou synchrone). Dans cette thèse, les machines asynchrones et synchrones à réluctance variable sont étudiées et comparées pour des véhicules électriques. Ces deux machines ont un coût faible et possèdent des structures de puissance et de contrôles similaires.

Des modèles analytiques non linéaires de machines asynchrones et synchrones à réluctance variable sont établis et validés. En outre, leurs modèles économiques et mécaniques sont également mis en œuvre. Sur la base des modèles analytiques établis, la géométrie et les paramètres de commande des machines étudiées sont dimensionnés afin de réduire les pertes énergétiques durant des cycles de conduite. Une optimisation bi-objective est proposée afin de minimiser en même temps les pertes énergétiques et le coût du moteur. Enfin, les machines optimisées sont comparées, à l'aide de Fronts de Pareto, pour évaluer leurs performances électriques, énergétiques et économiques.

Title : Designs and comparisons of different electrical converters without magnets for the application of electrical vehicles

Keywords : induction machine, synchronous reluctant machine, analytical model, design over the driving cycle and comparison

Abstract : Today, the concerns of the energy crisis and the reduction of gas emissions stimulate the research in several electric vehicle domains. As the cost of rare earth magnetic materials has increased significantly in recent years, electrical motors without permanent magnets draw more attention, such as induction motors, wound-synchronous motors, switched reluctance motors, and synchronous reluctant motors. In this thesis, induction and synchronous reluctant machines are chosen to be studied for the electric vehicle traction application since they are low costly and fed up with similar power electronics and control strategies.

Nonlinear analytical models of induction and synchronous reluctant machines are established and validated. Besides, economical and mechanical models are developed as well. Based on established analytical models, the geometry and the control parameters of these studied machines are calculated to define the total energy losses during the driving cycle. A bi-objective optimization is carried out to minimize total energy losses and motor costs. At last, the optimized machines are compared from their electric, energetic and economic performances, with the help of the Pareto Fronts obtained.

Université Paris-Saclay
Espace Technologique / Immeuble Discovery
Route de l'Orme aux Merisiers RD 128 / 91190 Saint-Aubin, France

Université Paris-Saclay
Espace Technologique / Immeuble Discovery
Route de l'Orme aux Merisiers RD 128 / 91190 Saint-Aubin, France

Qui se sait profond tend vers la clarté; qui veut le paraître vers l'obscurité ; car la foule tient pour profond tout ce dont elle ne peut voir le fond.

- *Friedrich Nietzsche*

Remerciements

Les travaux présentés dans ce mémoire ont été effectués au sein du Laboratoire Génie électrique et électronique de Paris (GeePs LGEP UMR-8507).

Mes premiers remerciements vont à Monsieur N. Takorabet, Professeur à l'Université de Lorraine pour l'honneur qu'il m'a fait en acceptant de présider mon Jury.

J'adresse également mes remerciements à Monsieur D. Roger, Professeur à l'Université Artois, et à Monsieur Y. Amara, Maître de conférences à l'Université du Havre, pour l'intérêt qu'ils ont porté à ce travail en acceptant d'être les rapporteurs de ma thèse et pour leur participation à mon jury.

Je remercie très sincèrement Monsieur C. Marchand, directeur du GeePs, pour m'avoir accueilli dans son laboratoire. Ses précieux conseils et son expérience m'ont permis de finaliser ce travail de recherche.

Je tiens à remercier Monsieur J.-C. Vannier, directeur du departement d'Electrotechnique et de Systemes d'Energie de CentraleSupelec, pour m'avoir accueilli au sein de son departement et pour ses aides dans ma recherche doctorale.

Je souhaite à remercier également Monsieur F. Bouillaut, ancient directeur du GeePs, pour ses conseils et ses aides.

Je tiens à exprimer toute ma gratitude à mon directeur de thèse, Monsieur P. Dessante, Professeur à CentraleSupélec, pour ses conseils pertinents et ses patiences qui m'ont permis à progresser tout au long de cette thèse.

Je remercie chaleureusement Monsieur G. Krebs, Maître de conférences à l'Université Paris-Sud, pour avoir co-encadré cette thèse. Je tiens à le remercier pour sa disponibilité et pour ses conseils.

Je tiens à remercier Monsieur A. Arzandé, Professeur à CentraleSupélec, pour l'aide aportée et ses conseils avisés.

Je tiens à remercier Monsieur O. Hubert, et Monsieur L. Sandandrea, pour leurs aides sur le plan informatique.

Je remercie mes collègues chioises du GeePs, pour leurs encouragements lors de la rédaction de thèse et pour l'aide aportée à la soutenance.

Je tiens également à remercier l'ensemble des chercheurs et enseignants du GeePs et CentraleSupélec qui ont su créer une ambiance de travail agréable.

Enfin et surtout, j'adresse mes plus vifs remerciements à mes parents, ma famille et mes amis pour leurs encouragements et leur soutient durant ma vie universitaire.

Contents

List of Figures

List of Tables

Chapter 1 Introduction

Chapter 1 Introduction

1.1 Introduction

The study of Electric Vehicles (EVs) are one of the most popular engineering topics in the 21st century. This thesis takes electric vehicles as the basic context, and focuses on the study of their power train system. The research of the EV power train includes topics such as Power Electronics (PEs), Electric Machines (EMs), thermal managements, and traction drive system designs. Although improving the battery performances, and developing the fast-charging technology are the key research challenges, other research such as developing suitable power electronics and electric machines is indispensable as well. With the market achievable batteries and power converters, we dedicate on designing and comparing low cost electric machines: Induction Machines (IMs) and Synchronous Reluctant Machines (SynRMs), for EV traction applications. The two machines are chosen since they work with similar power converters and controllers, and they are assumed to be comparable following electromechanical performances and manufacturing cost.

In this chapter, some general introductions concerning the research context such as the environment, the energy crisis raised by fossil fuels, the state of art of vehicle industry, and the EV power train will be presented. At last, the objectives and outline of the thesis will be stated.

1.2 Environment, Energy and Mineral Resource crisis

In this section, we introduce the state of the environmental, energetic and mineral crisis mainly concerning fuel fossils, and the market state of some metallic mineral resources.

1.2.1 State of the environmental problems

- ***Environmental crisis raised by fossil fuels***

The industrial revolution, which broke out in the late 18th century, has made a major turning in history, from many aspects such as the daily life, the division of the nation power, and the environment. From that, several factors have brought the amazing transformation to the human society: from iron to steel, from the carriage to the car, and from the newspaper to the Internet. Meanwhile, people have perceived the monetary cost of the environmental damage in the industrialization process. The water pollution, the land desertification, and the greenhouse effect worsened our living conditions. Some extreme climates appear more and more frequently, such as the global warming, El Niño phenomenon, droughts and floods. From [NANA11], the average temperature of the Earth's surface increased by about 0.8 °C over the past 100 years, with about 0.6 °C of this warming occurring over just the past three decades.

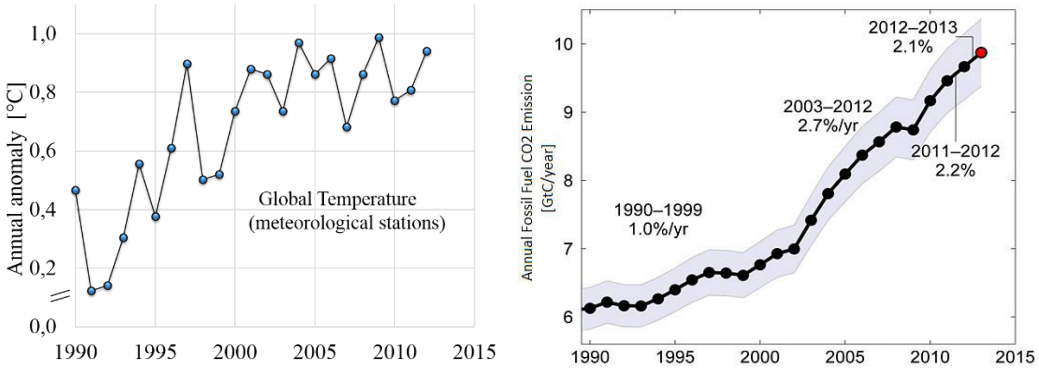

Figure 1.2.1 The annual evolution of global mean surface temperature (a) and of the fossil-fuel related CO_2 emissions (b) ([HRSL10])

Figure 1.2.1 shows that the global mean surface temperature increases significantly from the 1990s, which coincides with the explosive growth of the fossil-fuel CO_2 emission. Carbon dioxide ([WORL07]) is considered as one of the main gases that contributes to global warming. From Figure 1.2.2, it is noted that the carbon dioxide emission mainly comes from the fossil fuel combustion, in which the fossil fuel electricity production and the transportation are mainly involved. The transportation sector is the second largest source as it uses mainly petroleum based fuels (gasoline, diesel and kerosene). The CO_2 emission raised by the transport have increased quickly since the 1990s ([EPA14]). The road transportation accounts for more than 70% in the carbon dioxide emission of the whole transportation sector. It includes automobiles, light-duty trucks and freights.

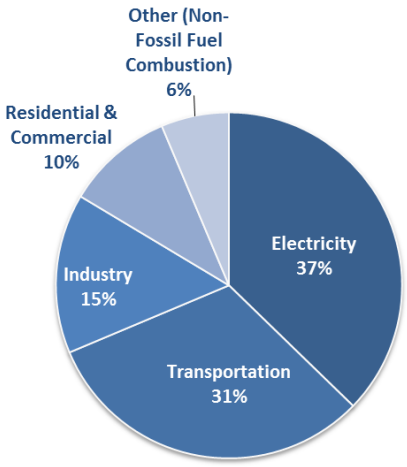

Figure 1.2.2 Sources of carbon dioxide emissions with their average proportion ([EPA14])

The use of fossil fuels raises serious environmental concerns, not only on the greenhouse effect that it brings, but also on the fatal damage to human health. The emission of other air pollutants by fossil fuel combustion, is proved to be responsible for many respiratory infection and lung cancer cases. The air pollution kills around 7 million lives annually.

- ***Environmental Initiatives***

Considering the pressure of the environmental organizations and their nations' long-term development, the government in many countries seeks for alternatives of fossil fuels. In European and Asian countries, some fossil fuel power stations are urged to be closed. More nuclear power stations are constructed instead, although the nuclear power itself has some potential threat on the ecological system. Private cars and petroleum fuels are imposed with high additional taxes. Metropolitans are encouraged to take more public transportation rather than private cars. These initiatives are effective to reduce the amount of the fuel consumption, but they could not avoid the utilization of the petroleum fuels. The electric and hybrid vehicles are considered as best alternatives of the conventional road vehicles. They are usually powered by the electrochemical battery, the fuel cell or mixed energy. The research of the electric and hybrid vehicles is one of the research topics that are mostly associated with human interests.

1.2.2 State of the energy problems

Among the diverse primary sources, the petroleum holds 35 percent, the coal holds 25 percent, and the natural gas holds 25 percent in 2013 ([RAGL14]). Fossil fuels still account for the main part nowadays. It takes typically millions of years to transform the organisms to fossil fuels. Thus, fossil fuels are considered as non-renewable resources. From Figure 1.2.3, it is not surprising that the annual average price of oil increased 5 times from 2000 to 2014. In 2015, the oil price slumped because of some political factors and the technology development in exploiting the shale oil ([ORGA13]).

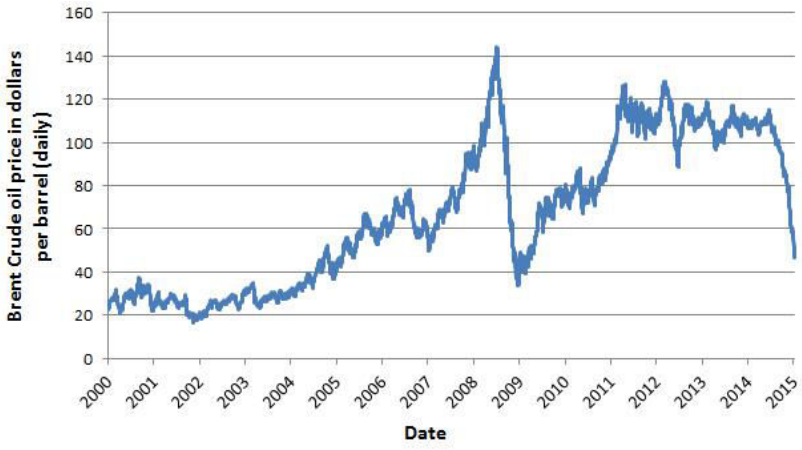

Figure 1.2.3 Annual trend of the price for purchases of oil ([FONG15])

Although the technology advancement makes it cost less and less in exploiting the unconventional oil such as the shale and the offshore oil, their cost is still not comparable with the conventional oil cost. Besides, scientists have warned the hidden trouble that may be raised by the exploitation of these unconventional oil, such as the earthquake and the landslide ([THKR99]). Anyway, the conventional and unconventional oil are exhaustible resources. The oil price keeps climbing in the long run if the market requirement does not alter.

Other primary sources such as the wind, the solar energy, and the hydro are renewable and green resources since they are harmless to the environment and available worldwide. The deployment of the renewable energy is encouraged in many countries, and that improves the energy

efficiency significantly. From a report in 2014 ([REN14]), renewable energy contributed 19 percent to humans global energy consumption and 22 percent to the production of electricity. Renewable energy are considered as future energy. However, they are still not comparable with conventional energy resources from the energy efficiency and the unit cost.

1.2.3 State of mineral resources

All mineral resources, including the most used mines in the energy conversion field (copper, aluminum, iron, rare earth magnets and so on) are non-renewable. Their price depends on the market's requirement and the explored reserves.

- ***Copper***

The ductility, and the excellent conductivity of heat and electricity make copper a key element in electrical wiring, plumbing, communications and marine applications. From 2002 to 2012, the copper price has raised from 2000$/tonne to 9000$/tonne (see Figure 1.2.4). Due to the newly discovered applications and the growing requirement in developing countries, the copper's long-term value is considered increasing.

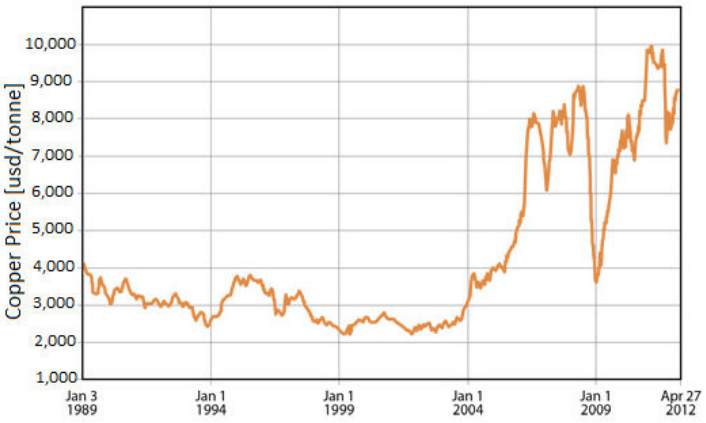

Figure 1.2.4 Copper price trend from 1989 to 2012 ([INVE13])

- ***Aluminum***

Compared with other metals, aluminum is light and has good conductivity. Besides, it is a kind of paramagnetic material. Aluminum and its alloys are important materials for the aerospace and civil industries. More than two hundred kinds of minerals contain aluminum, it is one of the most abundant metals in the world. The unit price of aluminum raises about two times in the last past twenty years, as shown in Figure 1.2.5.

Figure 1.2.5 Aluminum price trend from 1993 to 2013 ([INVE14])

- ***Steel***

Iron is a kind of ferromagnetic materials. It is significantly hardened and strengthened when alloyed with a portion of carbon or other elements, which makes steels. Due to the high tensile strength and magnetic properties, steels are largely used in energy conversion devices and civil applications. The abundant storage of iron and advance production methods cut down the steel price. From Figure 1.2.6, one could see that the steel price is much lower than aluminum and copper.

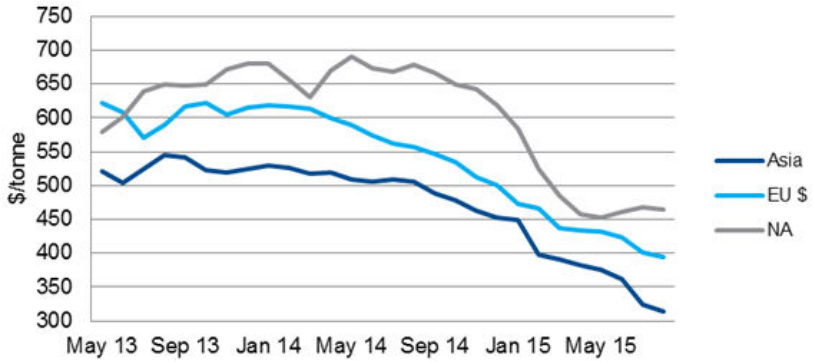

Figure 1.2.6 Regional steel price trend ([[TSIH15]])

- ***Permanent magnets***

Permanent magnets are a family of ferromagnetic materials which generates external magnetic fields of considerable strength permanently. They are used widely in industry, like in energy conversion devices, hard drives and so on. Considering magnetic properties and the cost, there are mainly four classes of materials which are used to produce permanent magnets for industry application ([FURL01]): Neodymium Iron Boron (NdFeB), Samarium Cobalt (SmCo), Ceramic (Ferrite) and Alnico. From the comparisons in Table 1.2.1, the NdFeB materials present great advantages in coercive field strength and adhesive force density, but not in the price. Among them, ferrite magnets are the most attractive one from the view of unit cost. However, ferrite magnets are much weaker than NdFeB materials in unit adhesive force ([CANO07]), they are about 2~3 times cheaper than NdFeBs under the same adhesive force. Compared to other

common materials, permanent magnet materials are much higher in terms of the unit price. Besides, the processing cost of permanent magnets are much higher due to their mechanical rigidity. Since permanent magnet materials such as NdFeB and SmCo contain rare-earth elements, their prices are expected to keep rising. Smart companies are seeking alternatives to permanent magnets, such as the research of nanocomposite magnet materials ([SMKB13]), and the use of electric motors without permanent magnets.

Material	Class	B_r (T)	H_{ci} (kA/m)	BH_{max} (kJ/mm^3)	T_{max} (°C)	Price 2014 ($/kg)
NdFeB	39H	1.28	2100	400	150	90
NdFeB	B10N	0.68	1030	100	150	60
SmCo	26	1.05	1000	260	300	40
Ferrite	8	0.39	320	35	300	5
Alnico	5	1.25	64	55	540	20

Table 1.2.1 Common magnet material comparisons ([ALLI15])

In this section, we have discussed the ecological concerns raised by the deployment of fossil fuels. The wide application of fuels in electricity production and transportation fields brings severe pollutions and climate crisis. Apart from the ecological harms, the depletion of fossil fuels makes their cost keep rising. Diverse initiatives are promoted in order to abate the reliance of fuels. Researchers are devoted to developing alternative solutions to the fossil fuels, such as generating electricity from green energy, and developing electric power transportations. At last, we have introduced several common industrial materials. The market price depends on the market's requirement and the explored reserves. Since metal ores and rare-earth materials are non-renewable, the price of these materials keeps rising in the long run. Among them, the permanent magnet materials are the most costly since they contain rare-earth elements.

1.3 Evolution of automobiles

Automobiles, as an important part of the current transport system, play an important role in humans' daily life. The vehicle industry covers the design, manufacturing, and selling of automobiles. It is one of the most important sectors in any nation's economy. The earliest automobiles in history could be tracked back in the 18th century.

1.3.1 Early history of the automobile

The first automobile was invented in 1768 by Nicolas-Joseph Cugnot, and it was powered by steam ([ECKE01]). Then François Issac de Rivaz designed the first car powered by an internal combustion engine in 1807, which was fueled by hydrogen. Anyos Jedlik invented the first electric car in 1828, which was a small one powered by a primary cell and an electric motor designed by himself. An Austrian Siegfried Marcus invented the first liquid-fuelled Internal Combustion Engine (ICE) in 1870. Following that, the first gasoline powered automobile was invented by Karl Benz in 1885. The first diesel engine for the use of automotive propulsion was designed and made by a German Rudolf Diesel in 1897. Before the breakout of the ICE technology and the refining of petroleum, ICE cars and electric cars competed in the market share. However, the gasoline car has taken a dominant share since the 1930s. By the end of 1930s, most of the mechanical technologies applied in modern automobiles have come out, such as hand brakes, multi-speed transmissions, and steerings.

1.3.2 State of the automobile industry

After the World War II, the automobile industry, especially gasoline and diesel cars emerged. The improvement of safety devices and automatic transmission technology popularized automobiles in the daily life ([SETR03]).

After eighty years of development, the ICE automobile industry has entered the maturation period. The oil depletion and the ecological concerns stimulate the research in electric and hybrid cars. From the late 1990s, countries like Japan and U.S.A. have rolled out some different electric and hybrid car models. Hybrid vehicles, as the transition product from chemical to purely electrical energy sources, they use the power from the ICE system and the electric motor alternatively ([MIMG11]). The initial cost of hybrid cars is much higher than that of conventional cars. The lack of plug-in technology in hybrid cars make them less attractive than electric and ICE cars. As the development of electric vehicles, the hybrid vehicle market share will cut down year by year according to experts' prediction.

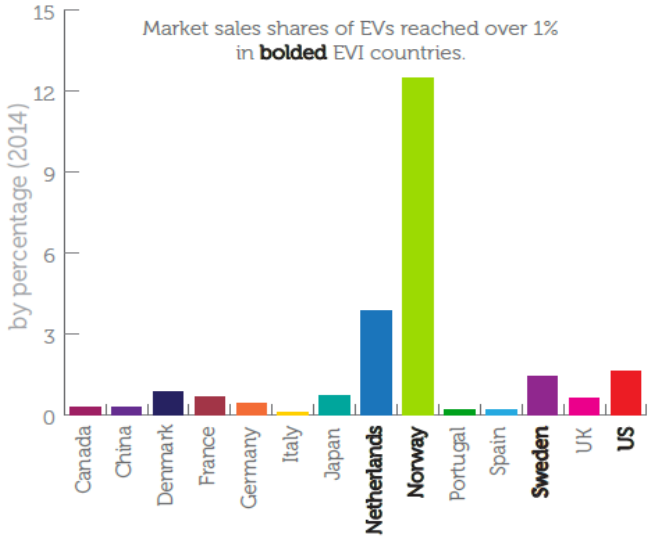

Figure 1.3.1 Electric vehicle market share in different countries in 2014 ([INTE15])

Electric Vehicles (EVs), is no doubt the focus for automobile manufacturers. The increasing market share inspires the development of EV industry ([ZACH14]). For example, Nissan Leaf, as the world's all-time best-selling electric car model, the sales were more than 200 thousand units by the end of 2015. Tesla Model S, as the first all-electric sport car model, the sales passed 100 thousand units by the end of 2015, three years after its first introduction. In Figure 1.3.1, the EV market share over different nations in 2014 has been presented ([INTE15]). Norway is the first country where EVs take up more than 10% market share. In countries like Netherland, Sweden and U.S.A, EV sales pass over 1% market share. Automobile experts predict that the EV sales increase 4 times from 2015 to 2020, which indicates that annual EV sales will reach over 6 million units by the end of 2020.

In this section, we take a quick review of the history and the state of the automobiles. Since electric vehicles show the promising future, we take the propulsion system of EVs, especially the electric motors as the research focus in this thesis. Electric vehicles will be introduced in the next section.

1.4 Electric Vehicles

Electric vehicles, which are mainly powered by electric energy, are considered as the best alternatives to the conventional vehicles. The first electric automobile appeared at the late 19th century, earlier than the automobiles using petrol internal combustion engines ([GUAR12]). However, the development of electric vehicles has stagnated until the end of the 20th century, since their performances were largely limited by the power sources.

1.4.1 Electric vehicle type

The EV family includes mainly three kinds of vehicles which are distinguished by the energy sources ([EHGE10]):

- ***Battery electric vehicles***

The battery electric vehicles (BEVs), are all-electric vehicles powered only by batteries. The battery power volume and maximum voltage influence directly the vehicle endurance time and speed range. As the advance of the battery technology, BEVs will become more and more attractive.

- ***Plug-in hybrid electric vehicles***

Similarly to hybrid vehicles, a plug-in hybrid electric vehicle (PHEV) is powered by batteries and fuel (gasoline or diesel) alternatively. The applied batteries are rechargeable by external sources such as an electric grid or some energy storage devices. The electric energy is transmitted via EMs, while the chemical energy is transmitted via ICEs. When a PHEV work under all-electric mode, the unit distance cost is lower than a conventional car. The ICE makes a PHEV comparable with a conventional car from the point of view of the driving range.

- ***Fuel cell electric vehicles***

Fuel cell electric vehicles (FCEVs) refer to the electric vehicles which use fuel cells as the energy sources. Fuel cells produce electricity through a chemical reaction of charged hydrogen ions with oxygen. Different with conventional batteries, fuel cells are always fueled to keep the chemical reaction. The higher initial cost of fuel cells and safety concerns limit the market share of FCEVs. The first civil FCEV model was released in the year of 2014, by the manufacturer Honda.

Until now, BEVs and PHEVs account for the majority in the whole market share. As shown in Figure 1.4.1, the BEV sales increase more than 30 times from 2010 to 2014 while the PHEV sales went up since the year of 2012. However, as the PHEVs are still transition models from conventional cars to all-electric cars, the market share of PHEVs is considered to cut down in the long run. In the future, BEVs are no doubt the principle EV classes when the battery and charging technologies are advanced enough. Thus, we focus on the study of the power train system of battery electric vehicles in this thesis.

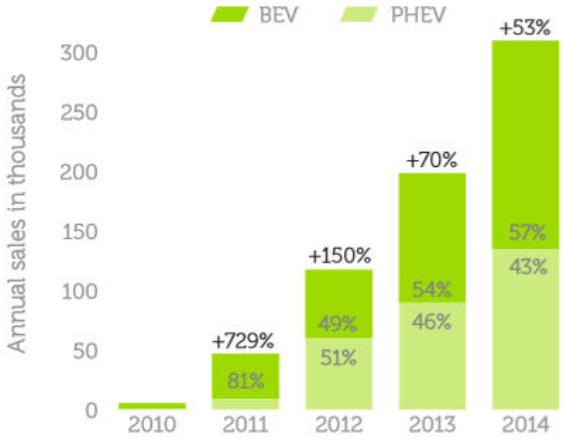

Figure 1.4.1 The evolution of global electric vehicle sales from 2010 to 2014 ([INTE15])

1.4.2 Power train system

The power train system (see Figure 1.4.2) of BEVs includes mainly the battery, the power converter and the electric machine ([PIST10]). The batteries are recharged via the adapted charger at a home garage or at some recharging points. A suitable power converter converts the d.c. voltage into the a.c. voltage with a micro-controller, to power the electric machine. The powered EM converts the electricity into the mechanical power, and transmits it to the differential devices.

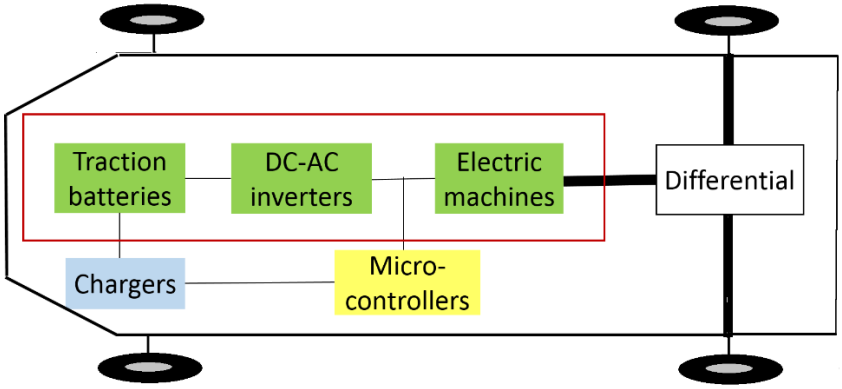

Figure 1.4.2 The power train system of a BEV

- ***Battery***

Battery is one of the key components which determine EV performances ([BCMW11]). The applied batteries should be able to adapt the fast-recharging technology. Besides, they are required to have high power density and low cost. Lead-acid, nickel-zinc, lithium-ion and lithium-polymer batteries are the four most frequently used types for the EV applications. From Table 1.4.1, the lithium-ion and lithium-polymer batteries are dominant in energy volume and mass densities. However, lead-acid ones were more used in the earlier EV models. More and more manufacturers adopt lithium-ion and lithium-polymer batteries due to their yearly decreasing cost ([LHLH13]). As shown in Figure 1.4.3, the battery unit cost decreased 60% from 2011 to 2013, while the energy density increased a half. Following this trend, the battery unit cost will fall to 50$/kWh, and the energy density will increase to 400Wh/L by the year of 2022.

Battery type	Energy/weight *Watthours/kg*	Energy/volume *Watthours/L*	Power/weight *Watt/kg*	Energy/usd *Watthours/$*
Lead-acid	30-40	60-75	180	4-10
Nickel-zinc	60-70	170	900	2-3
Lithium-ion	160	270	1800	3
Lithium-polymer	130-200	300	2800	3-5

Table 1.4.1 Battery type comparisons from their energetic and economic performances ([PIST10])

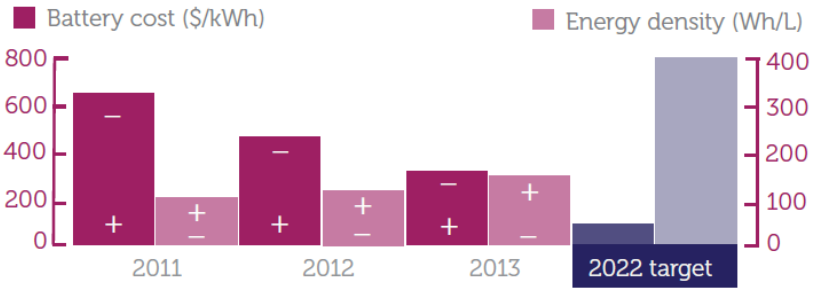

Figure 1.4.3 The estimation of EV battery progresses in the cost and the energy density ([INTE15])

- ***Power converter and micro controller***

The power converter converts d.c. voltage to quasi-sinusoidal voltage, in order to power an a.c. electric machine. A power converter for a low-power or medium-power three-phase a.c. EM, usually consists of six IGBTs and six inversely polarized diodes, as shown in Figure 1.4.4. The power converter is controlled by a micro controller using PWM techniques, which allows that the power train works within a wide speed range ([BOSE02]). Recently, the power converter is required to be bidirectional: when the EM works at motor mode, the converter converts d.c. voltage to a.c. one to power the motor; when it works at brake mode, the converter converts a.c. power to d.c. power to recharge the battery. This strategy expands the driving range, but increases the control complexity. In EV applications, power converters are required to be stable, high temperature durable and low cost ([EHGG03]).

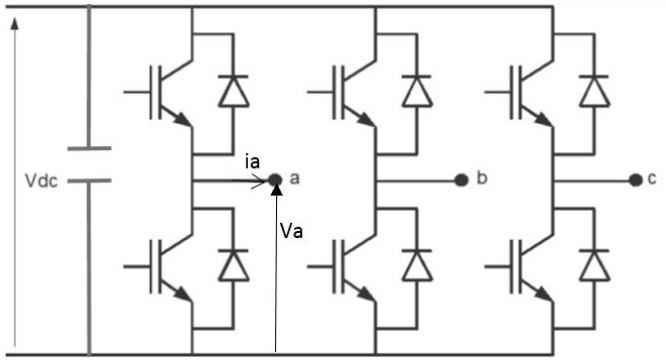

Figure 1.4.4 Equivalent scheme of a three-phase IGBT power converter

- ***Electric machine***

The electric machine is one of the key components which influence the EV performances. The work range of EMs are largely influenced by the battery and the power converter. The amplitude of the phase voltage V_a is limited by the battery voltage V_{dc}: $V_a < \sqrt{2/3}V_{dc}$ (see Figure 1.4.4). And the maximum phase current i_a is limited by the electrical volume of the power converter.

In this section, different types of electric vehicles have been presented. Battery electric vehicles and plug-in hybrid vehicles are the two main EVs in the market. Since the battery electric vehicles are the trend of the EV market, we take the BEV as the research context. The power train of the BEV is then presented. Batteries, power converters, and electric machines are the key components in the power train system. The discussions of different classes of EMs for EV applications will be detailed in Section 1.5.

1.5 Electric machines applied in EV applications

As one of the key components in the power train system, electric machines are largely studied and compared for EV traction applications. We start from a general review of different kinds of electric machines.

1.5.1 Review of electric machines

Generally, electric machines are composed of d.c. and a.c. machines ([BEKI98] [KRIS01]). D.c. machines are powered by direct sources while a.c. machines are powered by alternative sources. In an a.c. EM, we suppose that the poly-phase a.c. winding is installed in the stator. A.c. machines are divided into synchronous and induction machines according to the generation of rotor magnetic field. In synchronous machines, the rotor magnetic field is generated by permanent magnets (permanent magnet synchronous machines (PMSMs)), or by a direct current excited winding (Wound-rotor synchronous machines). Reluctant machines are considered as synchronous machines, and they include synchronous reluctant machines and switched reluctant machines (SRMs). Although there is no rotor magnetic field, the rotor in reluctant machines rotates at a synchronous speed with proper controls. The general classification of common electric machines is presented in Figure 1.5.1. Other types such as axial flux machines and flux-switching machines are not discussed here.

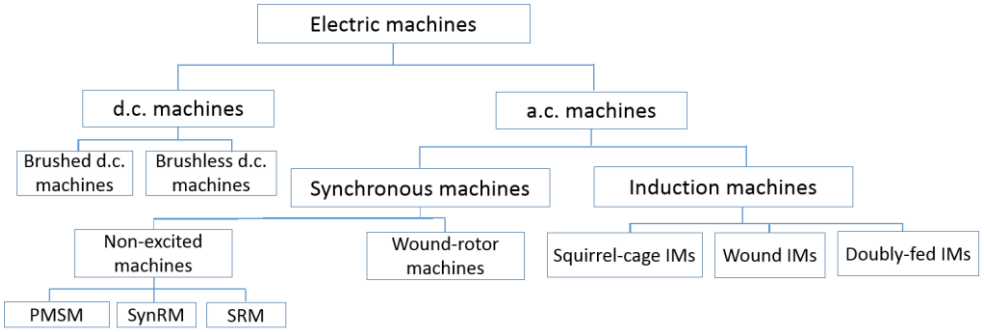

Figure 1.5.1 General classification of electric machines

- ***D.c. machines***

D.c. machines include brushed and brushless machines (see Figure 1.5.2). In brushed d.c. ones, the windings are fed by d.c. sources via a pair of fixed brushes, and the stator is composed of a pair of magnets. The rotor rotation makes windings fed by direct currents or voltages alternatively, that creates a static magnetic field which aligns perpendicular to the permanent magnetic field. Brushed d.c. machines are the earliest commercial electric machines, because they do not require power converters. Because of the constraint on the use life of brushes, brushed machines are now replaced by brushless d.c. machines in most applications. Brushless machines are fed by d.c. sources via power converters. The power converters convert direct currents or voltages to alternative ones, bidirectional waves rather than sinusoidal waves. Usually the rotor part is with permanent magnets, similar to permanent magnet synchronous machines.

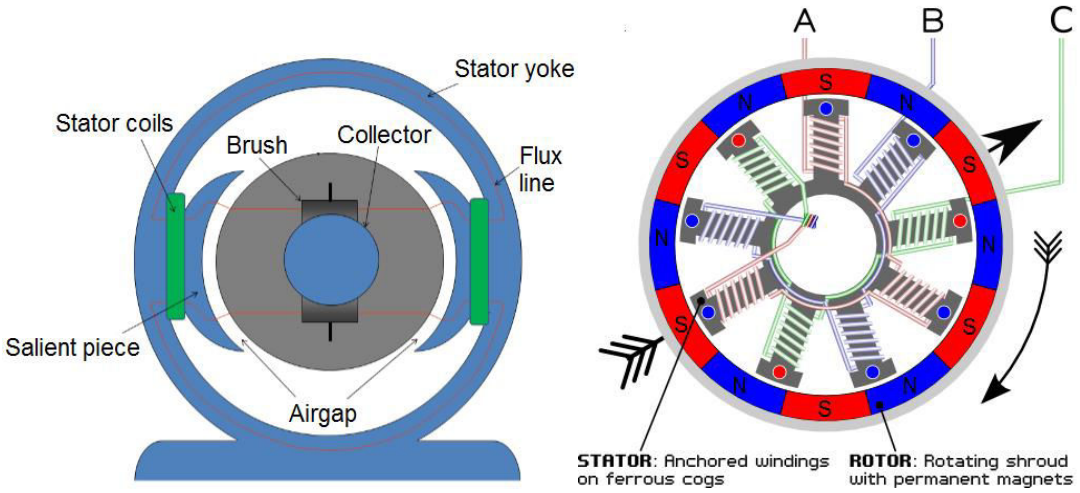

(a) (b)

Figure 1.5.2 Configurations of brushed d.c. machines (a) and of brushless d.c. machines (b) ([BEKI98])

D.c. machines present the advantages like high starting torque and simple inverter controls. They are usually found in low power applications like some civil appliances.

- ***Induction machines***

Induction machines refer to a.c. EMs rotating at an asynchronous speed, which generates a speed ratio to the synchronous pulsation ([BONA10]). The source winding produces a traveling field in the machine air-gap. This traveling field will induce voltages in conductors on the rotor. Then a.c currents occur in the rotor with closed circuit loop. The rotor should contain inductive material and closed circuit loop. There are mainly two kinds of rotors: wound rotor and squirrel cage (see Figure 1.5.3). Most squirrel cage rotors are with aluminum bars and rings, and wound rotors are with coils made of copper. In the wound rotor, a part of coil ends are grafted on to each other while the others are connected to the slip for the purpose of control. The stator and winding configurations are similar to PMSMs and SynRMs. The three-phase squirrel induction machines take up more than 30% market share in the European Union. When the wound rotor is fed by a three phase excitation, this kind of induction machine is called doubly fed induction machine. Doubly fed induction machines are largely used as wind turbine generators due to the easy adjustment of the rotor excitation frequency following the wind speed.

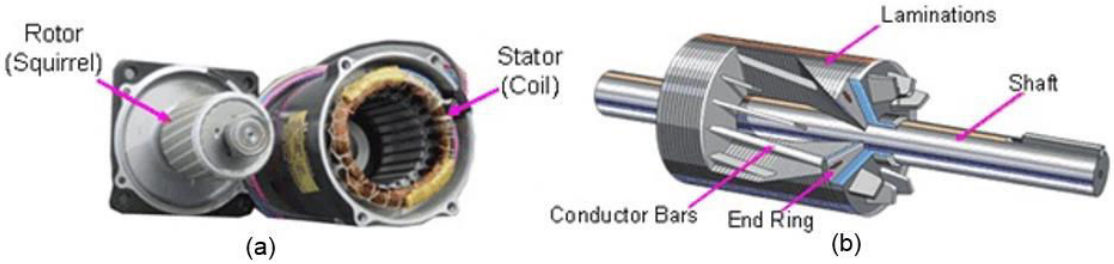

Figure 1.5.3 Configurations of IMs (a) rotor and stator (b) squirrel cage rotor ([POLI11])

Induction machines are largely used in industrial applications due to their moderate cost. Besides, they are highly efficient at high rotation speeds. The inverter-fed IMs work at variable speeds with proper control strategies.

- ***Synchronous machines***

Synchronous machines are the biggest electric machine families, which are widely used in diverse industrial applications, from low power to super high power cases. The stator structure of different synchronous machines is similar to IM stators, and it is composed of multi-phase windings fed by a.c. sources to generate an alternative traveling magnetic field. With different rotor structures, synchronous machines are mainly divided into dc-excited and non-excited machines. Non-excited synchronous machines include PMSMs, SRMs, SynRMs and so on. Now we will take a general survey on rotor excited synchronous machines, PMSMs, SRMs, and SynRMs.

1. Wound-rotor synchronous machines

In wound-rotor machines, rotor parts are composed of wound coils excited by direct currents and steel. As shown in

Figure 1.5.4, there are two kinds of rotor structures: round rotor and salient pole rotor. Since there is an additional degree of freedom (rotor current), the optimal field weakening and optimal power factor are achievable. Wound-rotor synchronous machines with round rotor are often used as high-speed turbines, while machines with salient pole rotor are used with low-speed hydro turbines. They are usually applied in high power applications.

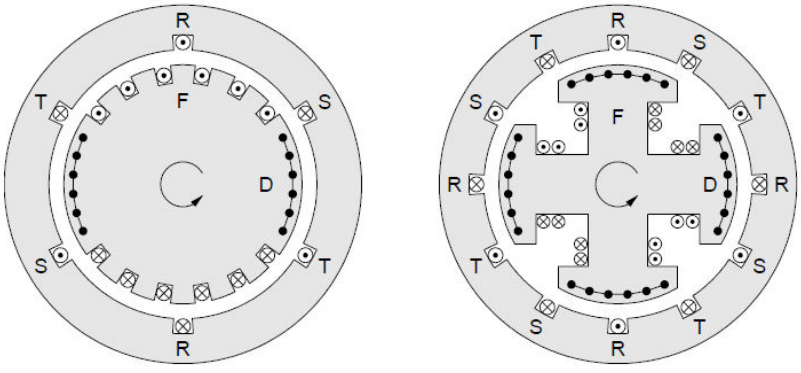

Figure 1.5.4 Configuration of wound-rotor synchronous machines (a) with round rotor (b) with salient pole rotor ([BEKI98])

Wound-rotor synchronous machines are with medium energy efficiency, power density and high cost due to the large adoption of copper. They are mechanically robust and could be controlled by modern control strategies.

2. Permanent magnet synchronous machines

The rotors of permanent magnet synchronous machines are with permanent magnets while the stators are with multi-phase ([BIBC00]). The stator and winding configuration of PMSMs are similar to SynRMs and IMs. The amount and position of magnets influence the PMSM performances. In Figure 1.5.5, several popular rotor structures are introduced: surface permanent magnet (SPM) rotor, surface inset permanent magnet (SIPM) rotor, interior permanent magnet (IPM) rotor and IPM rotor with circumferential orientation. Different rotor structures present different magnetic and mechanical characteristics. IPM and SIPM synchronous machines are mechanically robust since their rotors are free of ribs. IPM synchronous machines with circumferential orientation are considered as a kind of reluctant machines since the torque due to permanent magnets and due to the variation of the reluctance are generated at the same time. This kind of structure has a higher power density than other PMSMs ([BIBO02]).

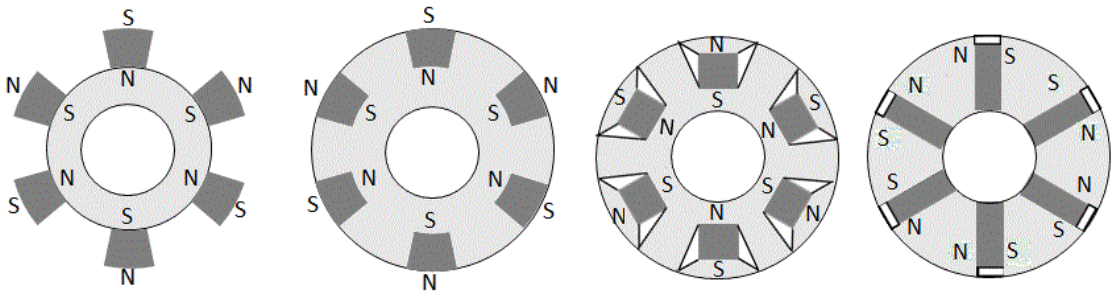

(a) (b) (c) (d)

Figure 1.5.5 Rotor configurations of the surface PMSM (a), of the surface inset PMSM (b), of the interior PMSMs (c) and of the interior PMSM with circumferential orientation

The energy efficiency of PMSMs are higher than wound-rotor synchronous machines since there are no copper losses at the rotor part (magnet losses are usually much weaker than copper losses). The torque density, power factor are almost the highest among all the electric machines. They are the best electric machines from many points of view, except the economic one. The cost of PMSMs is much higher than reluctant or induction machines as a result of the permanent magnet adoption.

3. Switched reluctant machines

Switched reluctant machines are kind of reluctant machines which converts the power through the variation of magnetic reluctance at different rotor positions. There is no magnets or d.c. excited coils at the rotor parts. The stators and rotors are both with salient structures, and are only made of steel laminations ([ARAM12]). The rotor pole number is different with stator pole number in a SRM. Multi-phase concentrated windings are installed at stator parts. As shown in Figure 1.5.6, the structure of 4 phase, 8 stator pole and 6 rotor pole (8/6) and the structure of 3 phase, 12 stator pole and 8 rotor pole (12/8) are some typical structures of SRMs. The a.c. sources switch according to rotor positions to create a magnetomotive force which attempts to

align each rotor pole to its closest stator pole. The source waves are square or triangle rather than sinusoidal ([YDGD09]).

Compared with other a.c. machines, SRMs are mechanically robust (no slot opening in stators and rotors), reliable (each phase is electrically and magnetically independent), and low cost (no permanent magnets or coils at rotors). However, the torque ripple is more important than other machines. Since the operation of SRMs highly depends on the control strategy, reliable and complex controllers are required for SRMs, which increases the set cost of SRMs. SRMs have been used in special applications requiring reliable EMs such as aerospace fields.

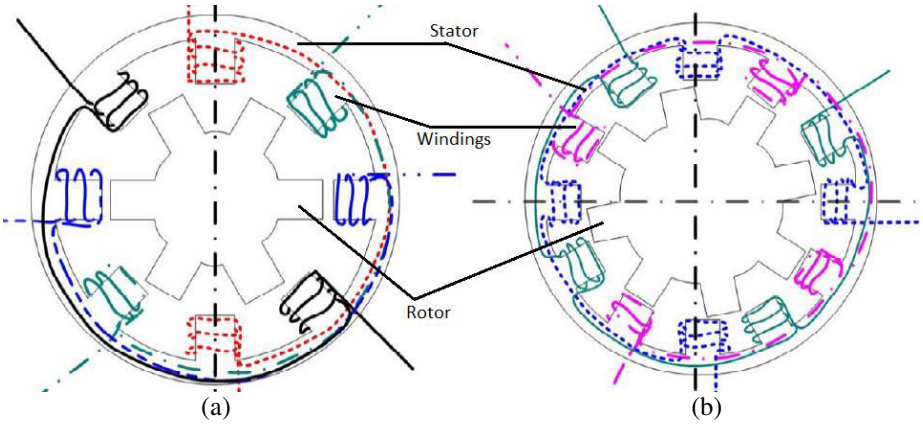

Figure 1.5.6 Configurations of SRMs (a) with 4 phases 8/6 (b) and with 3 phases 12/8 ([ARAM12])

4. Synchronous reluctant machines

Synchronous reluctant machines generate reluctant torque due to the salient structure of rotors ([MHCS91]). The stator and winding structure are similar to PMSMs. The stator windings are fed with sinusoidal sources, and the rotor special structures introduce internal flux barriers. Some common rotor structures of SynRMs are presented in Figure 1.5.7, which include salient structure, Transversally Laminated (TL) structure and Axially Laminated (AL) structure ([BOFN92][SOMI94]). Salient rotors were earliest SynRM structures, they are not much applied because of the high torque ripple. The flux barriers are punched to obtain favorable flux paths in TL rotors, where the laminations are standard flat. The AL rotors are made of steel laminations interleaved with non-magnetic materials. SynRMs with AL rotors have the highest saliency ratio among different rotor structures. The TL rotor type attracts much more interest, since it is probably the only SynRM structure with moderate costs. The speed controllers of SynRMs are similar to induction machines.

TLSynRMs are considered as low cost EMs ([HAAT03]). However, they are usually with low power factor, and relatively high torque ripple ([LIPO91] [BOLD96]). Since TLSynRMs have been studied and developed recently, they have not been much used in industrial applications. TLSynRMs are considered as best alternatives of IMs since they have similar power inverters, similar windings, and comparable electrical and ecological performances.

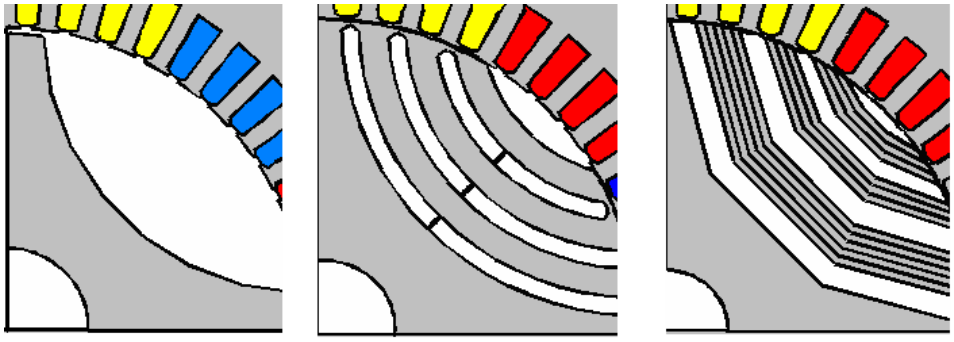

(a) (b) (c)

Figure 1.5.7 Rotor configurations of SynRMs (a) salient pole structure (b) transversally laminated anisotropic structure and (c) axially laminated anisotropic structure ([HAAT03])

1.5.2 Electric Machines applied in EV applications

There are various types of electric motors that could be applied in EV traction systems, such as permanent magnet motors, switched reluctance motors, and induction machines ([NAKA06] [CHCL08]). Several criteria are used to evaluate these EMs for EV traction applications ([EHGG03] [XUCC08]):

- Energy efficiency over the whole speed and power range;
  High energy efficiency is required over the whole speed range, which helps to reduce the battery volume.
- Cost;
  Low cost EMs could reduce the initial EV cost.
- Power density;
  High power density EMs make the power train more compact.
- Overload capability;
  Good overload capability of EMs are required to tackle some emerging cases.
- Control complexity;
  EMs with complex control strategies increase the cost of micro-controllers, and decrease the reliability of EMs.
- Power factor;
  High power factor EMs could reduce the electrical sizes of batteries and power inverters.
- Mechanical robustness.
  EM structure are required to be robust over the whole speed range, especially in high speed range.

However, there are not yet common industrial standards for electric machines in EV applications.

- ***D.C. motors***

Compared with a.c. motors, the implementation of d.c. motors is simpler. Besides, they can be overdriven in a short time. They are often used in traction applications such as electric locomotives and trams. Unfortunately, because of limitations on the speed range and on the torque density, d.c. motors are rarely applied for the EV traction applications.

- ***Induction machines***

Several sport car series take induction motors for their high performances in high rotation speed and moderate cost, such as Tesla Roadster and BMW Mini-E. All these motors are squirrel cage IMs. The IM can work within a wide speed range with proper control strategies such as direct torque control ([BIJA14]).

- ***Permanent magnet synchronous machines***

Most vehicle manufacturers take PMSMs in their hybrid and electric vehicles, such as Ford Focus, Honda Fit, Nissan Leaf and Toyota Prius, because of their high energy efficiency, high power density and good overload capability ([CHSO03] [ZHLI08]). As the cost of EVs is still not comparable to ICE vehicles, decreasing the cost of components in the power train is required. PMSMs are not preferred from this point of view.

- ***Wound-rotor synchronous machines***

Wound-rotor synchronous machines with salient pole rotors are highly performant at low speed range ([FDVM07]). They could generate high torque at very low rotation speed without excessive overload of sources. Thus wound-rotor synchronous machines are applied in some special traction applications. In EV applications, they could be designed as auxiliary traction motors. They are adopted by Renault, in the ZOE model.

- ***Switched reluctant machines***

Mature variable speed control techniques for switched reluctant machines have not been developed yet. Although there are many discussions on the use of SRMs for traction and automotive applications ([FAMO05] [SMĆS10]), few industrial applications have been realized.

- ***Synchronous reluctant machines***

Synchronous reluctant machines could be controlled with common control strategies. The power inverter of SynRMs is almost the same as IMs. TLSynRMs are considered as the best alternative of IMs since both of them are low cost EMs ([LIPO91] [FBDF13]).

The key characteristics of different EMs for EV applications are resumed in Table 1.5.1. From the above comparisons, PMSMs are the most appropriate EMs for EV traction applications except for the cost. Since low cost EMs are our research focus, PMSMs will not be studied in this thesis. Instead, IMs, SynRMs and SRMs are the most interesting ones in our research. Because the power inverter and control strategies of SRMs are more sophisticated than the other two, SRMs will not be discussed here neither.

Machine type	Energy efficiency	Cost	Power factor	Control complexity	Power density
D.c. machines	Medium	Medium	Medium	Low	Low
PMSMs	High	High	High	Medium	High
Wound-rotor SMs	Medium	Medium	Variable	Medium	High
IMs	Medium	Low	Medium	Medium	Medium
SynRMs	Medium	Low	Low	Medium	Medium
SRMs	Medium	Low	Low	High	Medium

Table 1.5.1 Key characteristics of different EMs for EV applications

In this section, a general review of different kinds of electric machines have been made firstly, which includes d.c. machines, induction machines and synchronous machines. The requirements on the electric machine performance for EV applications were described, and different machines are compared from some key characteristics. We concluded that IMs and SynRMs are two interesting candidates of best low cost electric machines for EV applications. Induction machines and synchronous reluctant machines will be introduced in detail in the next two sections.

1.6 Induction Machines

In recent years, induction motors have been converted in variable speed traction applications. We focus on the discussions of squirrel cage IMs in this thesis.

1.6.1 Configurations

As introduced in Section 1.5, the stator of squirrel cage IMs are similar to most a.c. EMs, and the rotor structure resembles a squirrel cage. The stator consists of a.c. windings and iron cores. There are several types of a.c. winding types, which have been studied in many literatures ([BBPG06] [BONA10]). Except in some particular cases, distributed windings are applied in most a.c. EMs rather than concentrated windings, since less harmonics are induced. Distributed windings include single-layer windings and fractional multilayer windings. Fractional multilayer windings help reduce harmonics. However, the single-layer winding is chosen to apply in our electric machines to simplify the optimization steps.

The conducting bars are embedded in slots in the rotor iron and connected at each end by conducting end rings. The applied conductive materials are usually copper or aluminum. The cost of copper is four times more than aluminum from Section 1.2. Obviously, cages made of aluminum are preferred in our case. From [BONA10], different rotor slot shapes imply different utilities. For instance, closed rotor slots (Figure 1.6.1 (a)) are used to reduce torque pulsation at

the expense of large leakage inductance, which results in high starting current. Semi-closed trapezoidal slots (Figure 1.6.1 (b)) are often applied in variable speed and torque applications, this kind of rotor slot geometry will be applied in our case. Closed and semi-closed double cage slots (see Figure 1.6.1 (c, d)) are applied in cases requiring high starting torque and low starting current, but the double cage structures reduce the pullout torque at the same time.

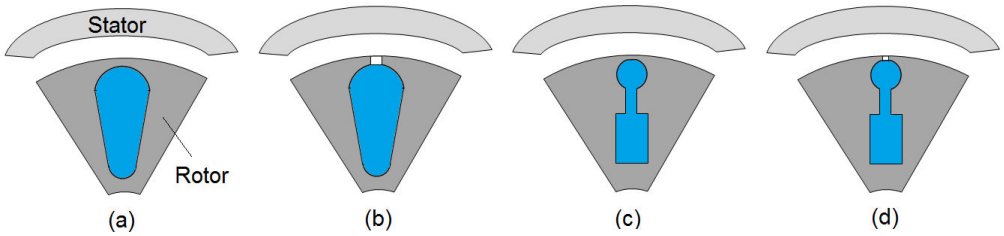

Figure 1.6.1 Rotor slot shape of squirrel IMs: semi-closed trapezoidal slots (a) closed slots (b) closed double cage slots (c) semi-closed double cage slots

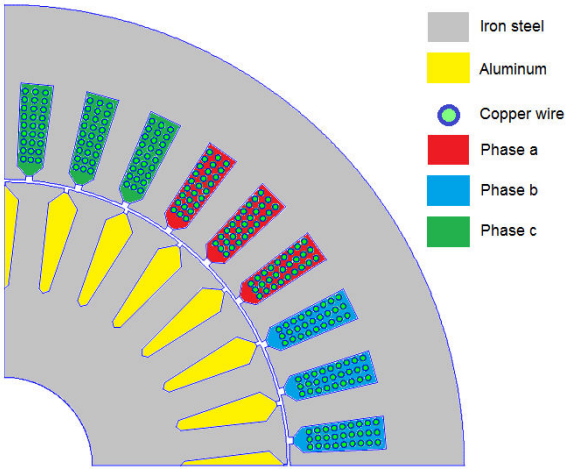

Figure 1.6.2 Studied induction machine geometry and applied materials

An example of studied induction machine geometry is illustrated in Figure 1.6.2, and the winding scheme is described in Figure 1.6.3.

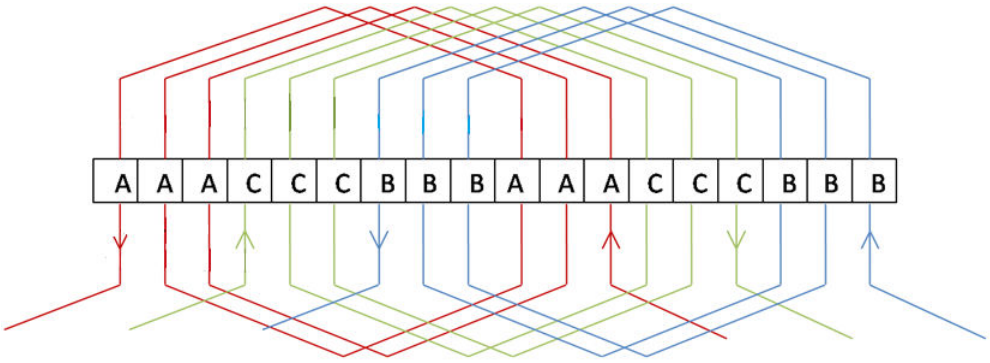

Figure 1.6.3 An instance of stator winding scheme: single layer winding

1.6.2 Speed control strategies

The control strategy for induction machines is the most developed control techniques, and some of them have been used for other kinds of EMs such as PMSMs or SynRMs for variable

speed applications. When IMs work over a variable speed range, there are several frequency control strategies ([BONA10]):

- ***Scalar control***

Scalar control strategy goals to keep the phase flux linkage constant, thus the ratio between the phase voltage V_s and the frequency f should also be a constant in the variable speed range. The real rotation speed concerns two factors: the frequency f and the slip ratio s. Since the slip ratio usually is not constant over the torque range, the simple open-loop system cannot control the speed precisely. The slip compensation function can be added into the control system. An example of the phase voltage versus frequency profile under scalar control is presented in Figure 1.6.4, where f_c is the cut-off frequency, and the f_{rated} is the rated frequency. At 0-f_c range, the ratio V_s/f is not linear, since the voltage drop across the stator phase resistance should be compensated. At f_c-f_{rated} range, the ratio keeps as constant. When the frequency is higher than the rated value, the phase voltage is limited due to the core magnetic saturation. Therefore, the phase flux linkage cuts down as the increase of the frequency, and the region is called "field weakening region".

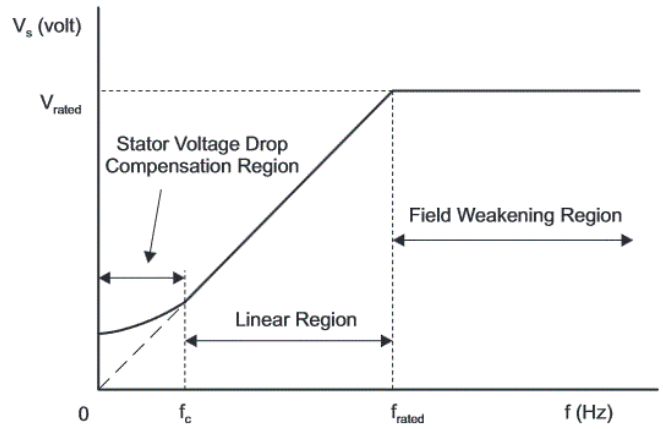

Figure 1.6.4 Phase voltage vs the feeding frequency under scalar control ([AKGA13])

Scalar control is the oldest control strategy, it is simple but with high response time. Since this strategy neglects the variation of rotor resistance due to skin effect and the core saturation, the constant power range of IMs may degrade. Scalar control strategy is now only used for some light load applications.

- ***Vector control***

Vector control is a kind of modern control strategy ([TEXA98] [POPE00]), and it uses mathematical transformation to decouple the torque and the electrical parameters (phase voltage or current). Among different vector control strategies, field oriented control (FOC) strategy is the most popular one to apply in variable speed applications. FOC is based on Park transformation (see Section 2.3) in order to transform a three phase time varying system into d-q coordinates time invariant system. The d-axis coincides with the rotor flux direction, and the stator and rotor flux linkage along direct and quadrature axis could be expressed as:

$$\begin{aligned} \Psi_{sd} &= L_s i_{sd} + L_m i_{rd} \\ \Psi_{sq} &= L_s i_{sq} + L_m i_{rq} \\ \Psi_{rd} &= L_r i_{rd} + L_m i_{sd} \\ \Psi_{rq} &= L_r i_{rq} + L_m i_{sq} = 0 \end{aligned} \quad 1.6.1$$

Where:

- Ψ_{sd}: the stator flux linkage along the *d*-axis;
- Ψ_{sq}: the stator flux linkage along the *q*-axis;
- Ψ_{rd}: the rotor flux linkage along the *d*-axis;
- Ψ_{rq}: the rotor flux linkage along the *q*-axis;
- L_s: the total stator phase inductance;
- L_r: the total rotor phase inductance;
- L_m: the equivalent magnetizing inductance;
- i_{sd}: the stator phase current along the *d*-axis;
- i_{sq}: the stator phase current along the *q*-axis;
- i_{rd}: the rotor phase current along the *d*-axis;
- i_{rq}: the rotor phase current along the *q*-axis.

The rotor current along the direct axis i_{rd} is null as the Ψ_{rq} is cancelled, and the rotor current along the *q*-axis is linked with the stator current:

$$i_{rq} = -\frac{L_m i_{sq}}{L_r} \quad 1.6.2$$

With the short-circuited rotor cage structure, the slip ratio in FOC model is determined by the ratio between the rotor phase current and the flux linkage:

$$s = -\frac{R_r i_{rq}}{\Psi_{rd}} \quad 1.6.3$$

Where R_r is the rotor phase resistance. Combining equation 1.6.1-1.6.3, the electromagnetic torque is then expressed by the following equation:

$$\begin{aligned} T_{em} &= \frac{3}{2} p(\bar{\Psi}_s \times \bar{\imath}_s) = \frac{3}{2} p\left(\Psi_{sd} i_{sq} - \Psi_{sq} i_{sd}\right) \\ &= \frac{3}{2} p \frac{L_m}{L_r} (L_m i_{sd}) i_{sq} \end{aligned} \quad 1.6.4$$

From equation 1.6.1-1.6.4, the electrical and magnetic parameters could be controlled by stator currents along *d*-axis and *q*-axis. The basic scheme of FOC strategy is described in Figure 1.6.5.

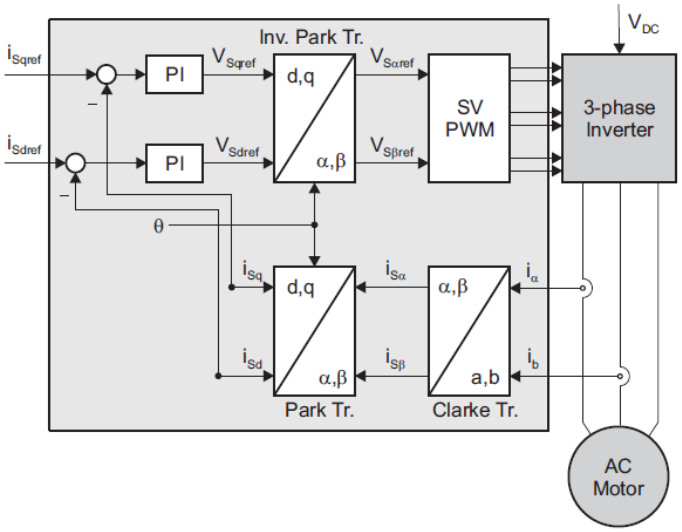

Figure 1.6.5 The basic scheme of FOC strategy ([TEXA98])

The core of the FOC strategy is to find the rotor flux position. In synchronous machines, the flux position could be directly measured by position sensor or integration of rotor speed since the rotor speed is synchronous. However, these methods are not suitable for the IM control. Particular methods are applied for IM cases, they could be categorized into two types: indirect and direct schemes. In the indirect FOC scheme, the slip ratio should be estimated via the measured or estimated rotor speed, in order to deduce the synchronous speed. While in the direct FOC scheme, the synchronous speed is estimated based on the flux angle from flux sensor or flux estimator. The adoption of sensorless FOC drive is a popular way to decrease the EM set cost, and the rotation speed is deduced from the measured phase currents and voltages via some mathematical ways. The detail discussion of FOC strategy applied in IMs are referred in many literatures ([ONG98] [BOSE02]).

The configuration of studied IMs was discussed. Then scalar and vector control strategies were presented.

1.7 Synchronous Reluctant Machines

As stated in Section 1.5, transversally laminated synchronous reluctant machines are studied in this thesis.

1.7.1 Characteristics

TLSynRMs are low costly, but they present relatively low power factor and high torque pulsation. Besides, they are not highly robust at high speed rotation speeds because of the important centrifugal forces imposing on the thin bridges ([BOLD96]). Power factor, torque pulsation and mechanical robustness are some of most important criteria in designing a SynRM. Similar to other synchronous machines, the electromagnetic torque and the maximum power factor of a SynRM (without magnet assisted) could be computed from some electromagnetic parameters, with phase resistance neglected ([HAAT03] [NIAZ05]).

$$T_{em} = \frac{3}{2}p(L_d - L_q)i_{sd}i_{sq} = \frac{3}{4}p(L_d - L_q){i_s}^2 sin(2\alpha) \qquad 1.7.1$$

$$PF_{max} = \frac{k_{sr}-1}{k_{sr}+1} \quad \text{with} \quad k_{sr} = \frac{L_d}{L_q}$$

Where:

- p: the pole pair number;
- L_d: the magnetizing inductance along the *d*-axis;
- L_d: the magnetizing inductance along the *q*-axis;
- i_{sd}: the stator phase current along the *d*-axis;
- i_{sq}: the stator phase current along the *q*-axis;
- i_s: the stator phase current amplitude;
- α : the vector current angle with *d*-axis;
- L_d: the magnetizing inductance along *d*-axis;
- L_q: the magnetizing inductance along *q*-axis;
- k_{sr}: the saliency ratio.

In Figure 1.7.1, the electromagnetic torques under different current angles, phase current amplitudes, and the value of magnetizing inductance difference are computed linearly. One could see that the torque reaches its maximum value when the current angle is equal to 45°, and it is null when the current angle is equal to 0° or 90°. Besides, the torque value is proportional to the square of phase current amplitude and to the magnetizing inductance difference. The maximum power factor increases with the motor saliency ratio, as shown in Figure 1.7.2. However, since the saliency ratio of most TLSynRMs is below 10, the maximum power factor is usually below 0.8 ([HAAT03]). To achieve important torque density and power factor, the SynRM should be defined with high magnetizing inductance along d-axis, and high saliency ratio.

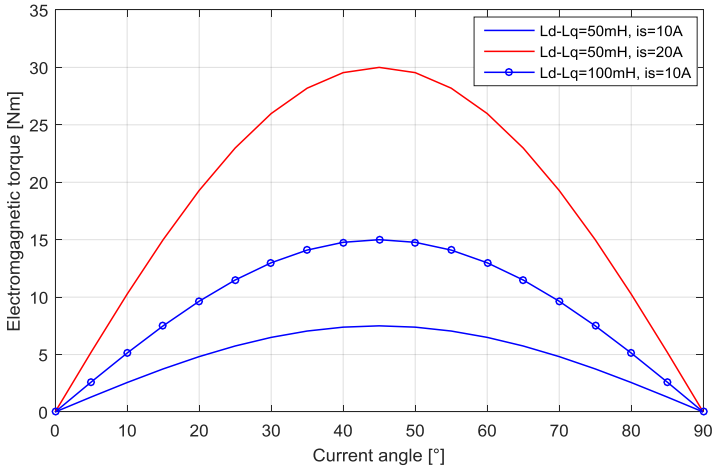

Figure 1.7.1 Example of the variation of SynRM torque with current angle, phase current amplitude and inductance

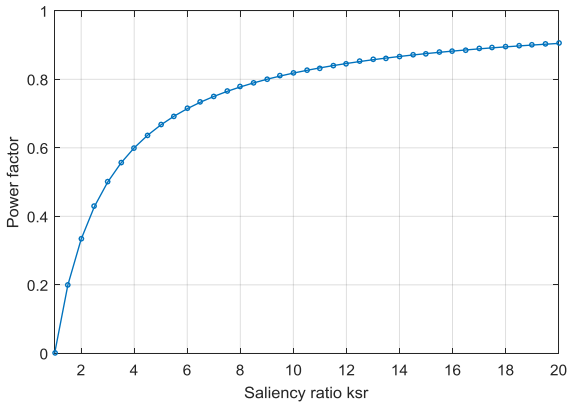

Figure 1.7.2 The variation of the maximum power factor with saliency ratio

From [BOLD96], the estimation of the magnetizing inductance along *d*-axis is similar to the magnetizing inductance of IMs, which is expressed in equation 1.7.2.

$$L_d \cong L_m = \frac{3\mu_0}{\pi}\frac{D_g L}{g_{eff}}\left(\frac{k_{w1}n_s}{p}\right)^2 \qquad 1.7.2$$

Where:

- k_s: the fundamental winding coefficient;
- n_s: the winding turn number per phase;
- τ_p: the pole pitch;
- L: the motor length;
- g_{eff}: the effective air-gap width;
- D_g: the outer diameter of the rotor;
- p: the pole pair number.

The analytical computation of the *q*-axis magnetizing inductance is difficult due to the determination of the nonlinear permeability of the q-axis iron. In neglect of the iron saturation, the *q*-axis magnetizing inductance may be expressed by:

$$L_q \cong \frac{3\mu_0}{\pi}\frac{D_g L}{g_{eff} + \sum e_b}\left(\frac{k_{w1}n_s}{p}\right)^2 \qquad 1.7.3$$

Where e_b is the width of each barrier in one pole.

And the intrinsic saliency ratio of a given SynRM may be defined by a simple analytical equation, proposed in [SOSM93]:

$$k_{sr\_in} \cong \frac{aD_g}{g_{eff}} \qquad 1.7.4$$

Where a is the ratio of the barrier thickness to the sum of the barrier and lamination thickness.

This intrinsic value is the maximum theoretically achievable value of the saliency ratio. From equation 1.7.1-1.7.4, the design of a SynRM concerning the power factor and the saliency ratio should be careful in dimensioning the rotor barrier width, the rotor radius, and the stator winding.

In a SynRM, the variation of magnetic resistance between flux barriers and teeth produces important ripple. The torque pulsation of a given SynRM is difficult to be defined analytically. Despite the inherent limitation of SynRMs, the stator winding type would influence also the torque ripple (cogging torque [GUCX09]). From [LIUW07] [BONA10], the use of a fractional multi-layer winding or a stator-rotor skew could reduce the torque ripple. In several articles [SHMT04] [WZOK15], modeling and experimental results have proved that the asymmetric arrangement of rotor barriers would reduce the torque ripple significantly while keeping the average torque at the same level with the case with symmetric rotor barriers.

1.7.2 Configurations

The a.c. winding in the stator is supplied to generate quasi-sinusoidal space varying magnetic field. The stator winding structure and slot geometry of studied SynRMs are supposed to be the same as IMs (see Section 1.6).

The rotor geometry, especially the barrier geometry influences the motor magnetizing inductance, torque ripple and so on. In Figure 1.7.3, two modern transversally laminated rotors are presented. The rectangular barriers are usually applied in permanent magnet assisted SynRMs. And the rotor with round barriers helps decrease the rotor leakage inductance, this structure is often found in pure SynRMs.

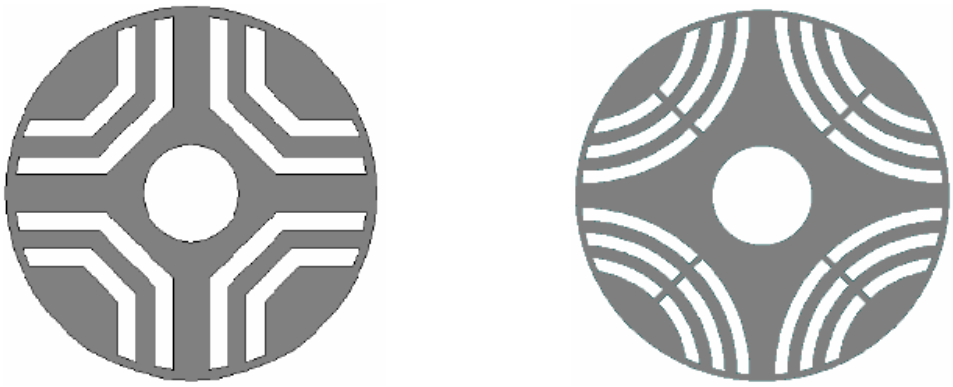

(a) (b)

Figure 1.7.3 Transversally laminated rotor: rectangular barriers (a) round barriers (b) ([NIAZ05])

The author in [NIAZ05] has proposed a rotor geometry with non equi-wide barriers arranged. As shown in Figure 1.7.4, the barrier width along *d*-axis is larger than that along *q*-axis. Thus, SynRMs with this structure are with higher saliency ratio.

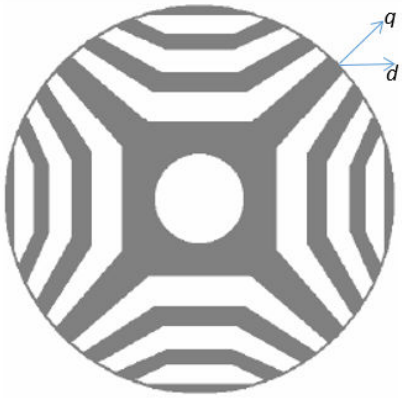

Figure 1.7.4 TLSynRM rotor with non equi-wide barriers arranged ([NIAZ05])

The authors in [SHMT04] [WZOK15] have proposed and validated a rotor structure arranging barriers with different spans in adjacent poles, which helps reduce the torque ripple significantly without degrading the average torque (see Figure 1.7.5 (a)). In [KOLE10], a rotor structure without radial bridges was presented, as shown in Figure 1.7.5 (b). In order to decrease the stresses imposed on the tangential bridges, the barriers were filled with particular materials. Besides, some extra supporting filler areas were added on the barriers (areas marked with "*x*") to increase the rotor robustness.

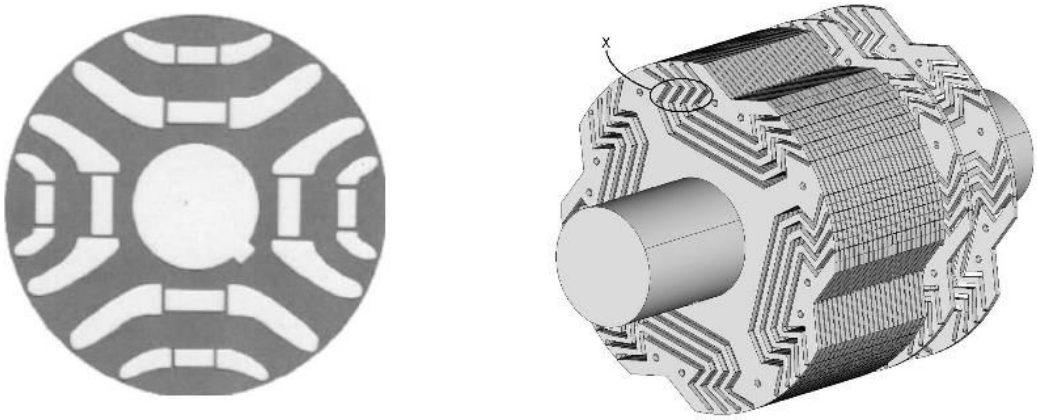

(a) (b)

Figure 1.7.5 Rotor geometries to decrease the torque pulsation and to decrease stresses imposed on bridges: the rotor with asymmetric barriers ([WZOK15]) (a) the rotor with dovetail shaped poles without supporting bridges ([KOLE10]) (b)

Considering the design complexity, simple rotor structures are preferred. The rotor with round barriers (see Figure 1.7.3 (b)) will be adopted in our case.

In this section, the characteristics of SynRMs including the torque, the power factor, and the torque pulsation were discussed. Then different rotor configurations of TLSynRMs were reviewed.

1.7.3 Control strategy

Vector control of a SynRM is simpler than FOC strategy for an IM since there is no flux orientation. From their purposes, the control strategies could be classified as:

- Constant *d*-axis current control
- Fast torque response control
- Maximum torque per ampere control
- Maximum power factor control

The further discussions of vector control of SynRMs were referred to [BOLD96] [BOSE02].

1.8 Review of comparisons between IMs and SynRMs

Before this thesis, many comparisons between induction machines and synchronous reluctant machines have been conducted. A general review of these comparisons will be made in this section.

1.8.1 Analytical comparisons

The earliest comparisons have been made by Prof. Lipo in [LIPO91]. Lipo realized the comparisons in an analytical way. Assuming that:

- IM is driven with FOC strategy (see Section 1.6);
- the stator and winding of the SynRM and the IM are the same;
- the air-gap width of two machines is identical;
- the saliency ratio of the SynRM presents a mean value (around six).

The expressions of the electromagnetic torque generated by an IM and a SynRM are stated in equation 1.6.4 and 1.7.1. When two motors are fed up with the same currents, the ratio of the torques generated by the SynRM and the IM may be evaluated by equation 1.8.1.

$$\frac{T_{SynRM}}{T_{IM}} = \frac{\frac{L_d}{L_m}(1-\frac{1}{k_{sr}})i_{sd\_SynRM}i_{sq\_SynRM}}{\frac{L_m}{L_r}i_{sd\_IM}i_{sq\_IM}} \approx \frac{0.94\left(1-\frac{1}{6}\right)}{0.95} = 0.82 \qquad 1.8.1$$

This equation indicates that the SynRM produces less torque than the IM under the same current supplies. However, the copper losses of the SynRM are about a half than the IM, since the rotor copper losses of the IM are important as well.

Now providing that the two machines consume the same quantity of copper and iron losses, the stator current amplitude of the SynRM is $\sqrt{2}$ times than the IM current amplitude:

$$\hat{\imath}_{s\_SynRM} = \sqrt{2}\hat{\imath}_{s\_IM} \qquad 1.8.2$$

Since only stator iron losses are counted in both two machines, the magnetic flux passing through the *d*-axis and the *d*-axis phase current of two motors are the same:

$$i_{sd\_SynRM} = i_{sd\_IM} \qquad 1.8.3$$

The *q*-axis current of the SynRM becomes $\sqrt{3}$ times than that of the IM in keeping $\sqrt{2}$ times phase current:

$$i_{sq\_SynRM} = \sqrt{3} i_{sq\_IM} \quad 1.8.4$$

Combining the above equations, the torque ratio is estimated as:

$$\frac{T_{SynRM}}{T_{IM}} \approx 0.82 \cdot \sqrt{3} = 1.42 \quad 1.8.5$$

It is proved that the SynRM is capable to produce higher torque while consuming the same losses as the IM, with some important hypotheses taken. Similar analytical comparisons have been made in [RAMI07] as well.

1.8.2 Experimental comparisons

Authors in [BCPV05] have compared a squirrel cage IM and a TLSynRM experimentally. In the designed experiment, the parameters of EMs were measured under steady state (constant speed and constant torque, see Table 1.8.1). One could see that at the given speed (around 1200 rpm), the torque and the energy efficiency of the SynRM were higher than the IM under the same winding temperature. When the two motors provided the same torque, the winding temperature of the SynRM was lower than the IM. The experimental data suggests that the performances of the SynRM are better than IM at medium rotation speed, except for the power factor.

	I.M. (1)	TLSyRM (eq. torque) (2)	TLSyRM (eq. temp.) (3)
T [Nm]	27.1	27.1	31.7
n_0 [rpm]	1202	1100	1100
N [rpm]	1101	1100	1100
Average windings overtemperature [°C]	104	80	108
V_{rms} [[V]	323	305	317
I_{rms} [A]	8.63	9.56	10.8
P_{in} [W]	4050	3750	4480
P_{out} [W]	3125	3122	3652
Efficiency	0.772	0.832	0.815
Fundamental power factor	0.839	0.743	0.756
P_{jstat} [W]	442	508	705
P_{jrot} [W]	295	0	0
P_{loss} [W]	925	628	828
P_{in}-P_{out}-P_{js}-P_{jr}	189	120	123

(a)

	I.M. (1)	TLSyRM (eq. torque) (2)	TLSyRM (eq. temp.) (3)
T [Nm]	15.2	15.1	16.6
n_0 [rpm]	1300	1200	1200
N [rpm]	1190	1200	1200
Average windings overtemperature [°C]	102	85	103
V_{rms} [[V]	350	336	346
I_{rms} [A]	5.32	5.45	5.92
P_{in} [W]	2673	2390	2690
P_{out} [W]	1894	1897	2086
Efficiency	0.709	0.794	0.775
Fundamental power factor	0.830	0.754	0.757
P_{jstat} [W]	394	392	489
P_{jrot} [W]	184	0	0
P_{loss} [W]	779	493	604
P_{in}-P_{out}-P_{js}-P_{jr}	201	101	115

(b)

Table 1.8.1 Experimental comparisons between an IM and a TLSynRM at constant speeds and torques ([BCPV05])

Similarly, authors in [GMWK00] have conducted the comparisons at high power (110kW). However, the SynRM seems to be less performant than IMs at high speed region, mainly due to its limited constant flux weakening region. Besides, the two motors were driven with different converters in their experiments which might affect the results.

In [HAAT03], a TLSynRM rotor structure was designed and manufactured based on a standard 30kW four-pole IM, when two motors were supplied by a standard sensorless Direct Torque

Controlled (DTC) drive. At no-load cold machine tests, SynRMs had around 20% more losses than IMs since the iron losses in SynRMs are more important. At load tests, both two machines were coupled with a d.c. machine. The designed SynRM gave a similar energy efficiency and power factor with the standard IM at rated power. There is no significant difference between the total losses of the SynRM and the IM due to the absence of rotor copper losses in the SynRM. This work proved that it is feasible that the two kind of EMs work with the same converter supply and have a comparable electrical performances.

The author in [ORTE13] have compared the two machines within various speed range. With two industrial standard IM and SynRM, the two motors were driven with advanced vector control strategies. The control parameters were optimized with the help of finite element analysis and different evolution algorithm, associated with the same rated converter. It is claimed that the total apparent power consumed by the SynRM under full load is higher than that of the IM. However, the consumption average of the SynRM is lower if intermittent loads are applied. On the other hand, the results suggest that the IM has better overload capacity than the SynRM. Since the two motors have the same stator which was originally designed for an IM, it is not surprising that the IM is better performant than the SynRM.

From analytical and experimental comparisons in the mentioned comparisons, the SynRM is supposed to be more efficient than the IM at low and medium speed ranges, but it has lower power factor. However, these previous comparisons are relatively coarse since the speed and torque ranges have not been considered. And the two kind machines have not been designed under the same specification.

1.9 Objective and Outline of the thesis

The overuse of fossil fuels brings humans results such as rising global temperature, air and water pollution, and the drain of fossil mines. That stimulates researchers to develop other green sources to replace the fossil fuels. The road transportation sector takes up an important portion in the fossil fuel consumption. In this context, the electric vehicle has become a research focus since the 1990s. The electric vehicle, especially the battery electric vehicle, has raised much market interest, and its market share is increasing year by year. However, the electric car share is still minor before the conventional ICE vehicle, because of the limit in the charging technology, in the driving range, and the lack of cost competitiveness. The power train system is the most important part of an EV, including the battery, the power inverter, and the electric motor. The study of the electric motor for the EV traction application is the research interest in this thesis. Different kinds of electric machines have been reviewed and compared, from different criteria for traction applications. The cost is an important factor during the selection of the electric motor in our research. Thus, permanent magnet synchronous machines and d.c. machines will not be studied in this thesis. Besides, the control complexity of switched reluctant machines makes it more difficult to carry out the comparisons with other a.c. machines. Switched reluctant machines are excluded in our research field as well. Induction ma and synchronous reluctant machines are the two types of electric machines which we will study, design and compare for the EV traction application.

Then, we have conducted reviews of induction machines and synchronous reluctant machines separately. The cost advantage of squirrel cage IMs and transversally laminated SynRMs makes them the candidate electric machines in this thesis. Then the characteristics and control strategies for these two electric machines have been discussed. Pure SynRMs present a relatively lower power factor, and the torque pulsation of SynRMs is higher than other a.c. machines (except switched reluctant machines). Both IMs and SynRMs are usually driven with vector control strategies, and the IM field oriented control is bit more complex since one should seek for the rotor flux position all the time. However, the control complexity of two machines are similar since the control of SynRMs should take care of the power factor and the torque ripple at the same time. Considering the design complexity, the chosen motor geometry of the two machines is quite simple, details such as the cage rings, the rotor inclination, and the insulation materials of squirrel cage IMs are not considered in the design step. With the same principle on the rotor geometry of SynRMs, the asymmetric barrier and the non equi-wide barrier are not considered as well, the structure with classical roundly arranged barriers is selected. Both two machines have the same kind of winding type and stator slot geometry. The geometry of the two studied machines and the winding type have been defined in the previous sections.

Since the comparisons between induction machines and synchronous reluctant machines have been made in many literatures, a review of these comparisons has been carried out. Analytical comparisons have suggested that the energy efficiency of SynRMs is higher than IMs. Some experimental data have validated it at a medium rotation speed. The SynRM seems to have obvious advantage in thermal performances under the same torque production as the IM. From analytical and experimental results, the power factor of the SynRM is lower than the IM. However, the SynRM stator has not been designed, and the speed and torque range has not been discussed in the literatures. It is claimed that there is no significant difference in the energy

efficiency and power factor. Besides, when the SynRM has the same stator which was originally designed for the IM, it is found that the IM has better overload capacity. From the above comparisons, we have found that the comparisons were carried out when the two machines were not designed or not separately designed for the same variable speed traction application.

As a consequence, the objective of the thesis includes the following terms:

- A bibliographical work of candidate machines: squirrel cage induction machines, and transversally laminated synchronous reluctant machines;
- Establishment of analytical or semi-analytical models of studied machines, which describe the electromagnetic behaviors of electric machines, estimate the power train system cost, and evaluate the mechanical robustness of synchronous reluctant machines. The models should be fast and precise enough, in order to be integrated in the design procedure.
- Electric machine optimization based on the developed analytical models. The two optimizations are carried out with the same optimization scheme under the same specifications. Mono-objective and bi-objective optimizations are performed respectively.
- Comparisons of the two optimized machines under mono-objective optimization, and comparisons of the Pareto Front under bi-objective one.

In the following, the plan of this thesis memory consists of:

Chapter 1:

In the Introduction, we have discussed the research context and stated the research objectives. Besides, the bibliography of electric machines for the EV traction application, especially the study of induction machines and synchronous reluctant machines has been carried out.

Chapter 2:

In this chapter, the multi-physical model of the traction system is presented, which includes electromagnetic, energetic, economic and mechanical modellings. All the models of induction and synchronous reluctant machines are analytical in order to reduce optimization time. The principles of all described models are presented: electromagnetic models evaluate the electric and magnetic behaviors of electric machines with the awareness of motor geometry and control states; energetic models estimate the system loss with a given control state; economic models estimate the power train system cost with defined motor geometry, and with rated battery and power inverter; the mechanical model evaluates the robustness of rotor bridges of synchronous reluctant machines. Besides, the coupling relations between these models are described as well.

Chapter 3:

The electromagnetic models and the mechanical model are validated with finite element analysis in this chapter. For the induction motor, the analytical model is validated with different rotor bar shapes. And it is validated with harmonic, transient finite element analysis. Besides, it

is validated with a method combining the analytical model and the static finite element analysis as well. The analytical model of the synchronous reluctant machine is validated with static finite element method, and on different rotor geometries. The mechanical model is validated with finite element analysis for linear elasticity. The analytical errors of these models are resumed and analyzed.

Chapter 4:

This chapter describes the optimization methodology, including the chosen optimization algorithm, the optimization objectives, the optimization variables and the constraints. Driving cycles containing the electric drive information, is represented with several selected working points with some numerical method, for the purpose to save computation time. Since the motor geometry and control parameters are both optimization variables, the optimization scheme describes the arrangement of the two optimizations. The mono-objective and bi-objective optimizations for induction and synchronous reluctant machines are carried out separately. Then the two optimized machines in the mono-objective optimization are compared following their electric, energetic and economic performances. The Pareto Fronts in the bi-objective optimization are compared as well. The comparison data are analyzed and concluded at last.

1.10 References

[ALLI15] Alliance LLC, "Magnet Commodity Prices," *Industrial Permanent Magnets: http://www.allianceorg.com/magnetandmaterialcosts.html*, Jun-2015.

[AKGA13] B. Akin and N. Gara, "Scalar (V/f) Control of 3-Phase Induction Motors." Texas Instruments Incorporated, Jul-2013.

[ARAM12] A. Arifin, I. Al-Bahadly, and S. C. Mukhopadhyay, "State of the Art of Switched Reluctance Generator," *Energy and Power Engineering*, vol. 04, no. 06, pp. 447–458, 2012.

[BBPG06] N. Bianchi, S. Bolognani, M. D. Pre, and G. Grezzani, "Design considerations for fractional-slot winding configurations of synchronous machines," *IEEE Transactions on Industry Applications*, vol. 42, no. 4, pp. 997–1006, Jul. 2006.

[BCMW11] A. G. Boulanger, A. C. Chu, S. Maxx, and D. L. Waltz, "Vehicle Electrification: Status and Issues," *Proceedings of the IEEE*, vol. 99, no. 6, pp. 1116–1138, Jun. 2011.

[BCPV05] A. Boglietti, A. Cavagnino, M. Pastorelli, and A. Vagati, "Experimental comparison of induction and synchronous reluctance motors performance," in *Industry Applications Conference, 2005. Fourtieth IAS Annual Meeting. Conference Record of the 2005*, 2005, vol. 1, pp. 474–479 Vol. 1.

[BEKI98] H. W. Beaty and J. L. Kirtley, *Electric motor handbook*, New York: McGraw-Hill, 1998.

[BIBC00] N. Bianchi, S. Bolognani, and B. J. Chalmers, "Salient-rotor PM synchronous motors for an extended flux-weakening operation range," *IEEE Transactions on Industry Applications*, vol. 36, no. 4, pp. 1118–1125, Jul. 2000.

[BIBO02] N. Bianchi and S. Bolognani, "Interior PM synchronous motor for high performance applications," in *Power Conversion Conference, 2002. PCC-Osaka 2002. Proceedings of the*, 2002, vol. 1, pp. 148–153 vol.1.

[BIJA14] Z. Bitar and S. A. Jabi, "Studying the Performances of Induction Motor Used in Electric Car," *Energy Procedia*, vol. 50, pp. 342–351, 2014.

[BOFN92] I. Boldea, Z. X. Fu, and S. A. Nasar, "Performance evaluation of axially-laminated anisotropic (ALA) rotor reluctance synchronous motors," in *Industry Applications Society Annual Meeting, 1992., Conference Record of the 1992 IEEE*, 1992, pp. 212–218 vol.1.

[BOLD96] I. Boldea, *Reluctance synchronous machines and drives*, Oxford: Clarendon Press, 1996.

[BONA10] I. Boldea and S. A. Nasar, *The induction machines design handbook*, 2nd ed. Boca Raton, FL: CRC Press/Taylor & Francis, 2010.

[BOSE02] B. K. Bose, *Modern power electronics and AC drives*. Upper Saddle River, NJ: Prentice Hall, 2002.

[CANO07] C. B. Carter and M. G. Norton, *Ceramic materials: science and engineering*. New York, NY: Springer, 2007.

[CHCL08] K. T. Chau, C. C. Chan, and C. Liu, "Overview of Permanent-Magnet Brushless Drives for Electric and Hybrid Electric Vehicles," *IEEE Transactions on Industrial Electronics*, vol. 55, no. 6, pp. 2246–2257, Jun. 2008.

[CHSO03] Y. K. Chin and J. Soulard, "A permanent magnet synchronous motor for traction applications of electric vehicles," in *Electric Machines and Drives Conference, 2003. IEMDC'03. IEEE International*, 2003, vol. 2, pp. 1035–1041 vol.2.

[ECKE01] E. Eckermann, *World history of the automobile*. Warrendale, Pa.: Society of Automotive Engineers, 2001.

[EHGE10] M. Ehsani, Y. Gao, and A. Emadi, *Modern electric, hybrid electric, and fuel cell vehicles: fundamentals, theory, and design*, 2. ed. Boca Raton, Fla.: CRC Press, 2010.

[EHGG03] M. Ehsani, Y. Gao, and S. Gay, "Characterization of electric motor drives for traction applications," in *Industrial Electronics Society, 2003. IECON '03. The 29th Annual Conference of the IEEE*, 2003, vol. 1, pp. 891–896 vol.1.

[EPA14] EPA, "Draft U.S. Greenhouse Gas Inventory Report: 1990-2014," United States Environmental Protection Agency, Dec-2014.

[FAMO05] J. Faiz and K. Moayed-Zadeh, "Design of switched reluctance machine for starter/generator of hybrid electric vehicle," *Electric Power Systems Research*, vol. 75, no. 2–3, pp. 153–160, Aug. 2005.

[FBDF13] M. Ferrari, N. Bianchi, A. Doria, and E. Fornasiero, "Design of synchronous reluctance motor for hybrid electric vehicles," in *Electric Machines Drives Conference (IEMDC), 2013 IEEE International*, 2013, pp. 1058–1065.

[FDVM07] D. Fodorean, A. Djerdir, I. A. Viorel, and A. Miraoui, "A Double Excited Synchronous Machine for Direct Drive Application 2014-Design and Prototype Tests," *IEEE Transactions on Energy Conversion*, vol. 22, no. 3, pp. 656–665, Sep. 2007.

[FONG15] J. Fong, "Spot price of Brent Crude from 2000 to 2015," http://www.vox.com/2014/12/16/7401705/oil-prices-falling, Jan-2015.

[FURL01] E. P. Furlani, *Permanent magnet and electromechanical devices: materials, analysis, and applications*, San Diego, Calif.: Acad. Press, 2001.

[GMWK00] J. J. Germishuizen, F. S. V. der Merwe, K. V. der Westhuizen, and M. J. Kamper, "Performance comparison of reluctance synchronous and induction traction drives for electrical multiple units," in *Industry Applications Conference, 2000. Conference Record of the 2000 IEEE*, 2000, vol. 1, pp. 316–323 vol.1.

[GUAR12] M. Guarnieri, "Looking back to electric cars," 2012, pp. 1–6.

[GUCX09] Z. Guo, L. Chang, and Y. Xue, "Cogging torque of permanent magnet electric machiens: An overview," in *Electrical and Computer Engineering, 2009. CCECE '09. Canadian Conference on*, 2009, pp. 1172–1177.

[HAAT03] J. Haataja, "A comparative performance study of four-pole induction motors and synchronous reluctance motors in variable speed drives," Thesis (Lappeenranta University of Technology), Jun-2003.

[HRSL10] J. Hansen, R. Ruedy, M. Sato, and K. Lo, "Global surface temperature change," *Reviews of Geophysics*, vol. 48, no. 4, Dec. 2010.

[INTE15] International Energy Agency, "Global EV Outlook 2015," International Energy Agency: http://www.iea.org, Dec-2015.

[INVE13] InvestmentMine, "Historical Copper Prices and Price Chart," http://www.infomine.com/investment/metal-prices/copper/all/, Dec-2013.

[INVE14] InvestmentMine, "Historical Aluminum Prices and Price Chart," http://www.infomine.com/investment/metal-prices/aluminum/all/, Sep-2014.

[KOLE10] J. Kolehmainen, "Synchronous Reluctance Motor With Form Blocked Rotor," *IEEE Transactions on Energy Conversion*, vol. 25, no. 2, pp. 450–456, Jun. 2010.

[KRIS01] R. Krishnan, *Electric motor drives: modeling, analysis, and control*, Upper Saddle River, NJ: Prentice Hall, 2001.

[LHLH13] L. Lu, X. Han, J. Li, J. Hua, and M. Ouyang, "A review on the key issues for lithium-ion battery management in electric vehicles," *Journal of Power Sources*, vol. 226, pp. 272–288, Mar. 2013.

[LIPO91] T. A. Lipo, "Synchronous reluctance machines-a viable alternative for AC drives?" *Electric Machines & Power Systems*, vol. 19, no. 6, pp. 659–671, Nov. 1991.

[LIUW07] T. A. Lipo, University of Wisconsin--Madison, and Wisconsin Power Electronics Research Center, *Introduction to AC machine design*, Madison, WI: Wisconsin Power Electronics Research Center, University of Wisconsin, 2007.

[MHCS91] T. J. E. Miller, A. Hutton, C. Cossar, and D. A. Staton, "Design of a synchronous reluctance motor drive," *IEEE Transactions on Industry Applications*, vol. 27, no. 4, pp. 741–749, Jul. 1991.

[MIMG11] C. Mi, M. A. Masrur, and D. W. Gao, *Hybrid electric vehicles: principles and applications with practical perspectives*, Chichester: Wiley, 2011.

[NAKA06] G. Nanda and N. C. Kar, "A Survey and Comparison of Characteristics of Motor Drives Used in Electric Vehicles," in *Electrical and Computer Engineering, 2006. CCECE '06. Canadian Conference on*, 2006, pp. 811–814.

[NANA11] National Research Council (U.S.) and National Academies Press (U.S.), Eds., *America's Climate Choices*, Washington, D.C: National Academies Press, 2011.

[NIAZ05] P. Niazi, "Permanent magnet assisted synchronous reluctance motor design and performance improvement," Thesis (Texas A&M University), Dec-2005.

[ONG98] C.-M. Ong, *Dynamic simulation of electric machinery: using MATLAB/SIMULINK*, Upper Saddle River, NJ: Prentice Hall PTR, 1998.

[ORGA13] Organisation for Economic Co-operation and Development, *World energy outlook 2013*. Paris: International Energy Agency, 2013.

[ORTE13] A. Ortega, "Design and Comparison of Induction Motor and Synchronous Reluctance Motor for Variable Speed Applications: Design Aided by Di_erential Evolution and Finite Element Analysis," Thesis (The Ohio State University), Oct-2013.

[PIST10] G. Pistoia, *Electric and hybrid vehicles: power sources, models, sustainability, infrastructure and the market*, Amsterdam: Elsevier, 2010.

[POLI11] Politeknik Merlimau, "Electrical Technology," etpmm, 2011.

[POPE00] M. Popescu, *Induction motor modelling for vector control purposes*, Espoo: Helsinki University of Technology, 2000.

[RAGL14] M. Ratner and C. Glover, "U.S. Energy: Overview and Key Statistics," Congressional Research Services, 27-Jun-2014.

[RAMI07] T. Raminosoa, "Optimisation des performances des machines synchro-reluctantes par reseaux de permeances," Thesis (INP de Lorraine), Jan-2007.

[REN14] REN21, "Renewable Energy Policy Network for the 21st Century," 2014.

[SETR03] L. J. K. Setright, *Drive on!: a social history of the motor car*, London: Granta, 2003.

[SHMT04] M. Sanada, K. Hiramoto, S. Morimoto, and Y. Takeda, "Torque Ripple Improvement for Synchronous Reluctance Motor Using an Asymmetric Flux Barrier Arrangement," *IEEE Transactions on Industry Applications*, vol. 40, no. 4, pp. 1076–1082, Jul. 2004.

[SMĆS10] S. Smaka, Š. Mašić, M. Ćosović, and I. Salihbegović, "Switched reluctance machines for hybrid electric vehicles," in *Electrical Machines (ICEM), 2010 XIX International Conference on*, 2010, pp. 1–6.

[SMKB13] R. Skomski, P. Manchanda, P. Kumar, B. Balamurugan, A. Kashyap, and D. J. Sellmyer, "Predicting the Future of Permanent-Magnet Materials," *IEEE Transactions on Magnetics*, vol. 49, no. 7, pp. 3215–3220, Jul. 2013.

[SOMI94] W. L. Soong and T. J. E. Miller, "Field-weakening performance of brushless synchronous AC motor drives," *IEEE Proceedings - Electric Power Applications*, vol. 141, no. 6, pp. 331–340, Nov. 1994.

[SOSM93] W. L. Soong, D. A. Staton, and T. J. E. Miller, "Validation of lumped-circuit and finite-element modelling of axially-laminated brushless motors," in *Electrical Machines and Drives, 1993. Sixth International Conference on (Conf. Publ. No. 376)*, 1993, pp. 85–90.

[TEXA98] Texas Instruments Europe, "Field Orientated Control for 3-Phase AC-Motors," Texas Instruments Incorporated, Feb-1998.

[THKR99] A. Tuvikene, S. Huuskonen, K. Koponen, O. Ritola, U. Mauer, and P. Lindstrom-Seppa, "Oil Shale Processing as a Source of Aquatic Pollution: Monitoring of the

Biologic Effects in Caged and Feral Freshwater Fish," *Environmental Health Perspectives*, vol. 107, no. 9, p. 745, Sep. 1999.

[TSIH15] TSIHRC Monthly Average, "Iron ore & steel price analysis and forecast for Q4 2015," http://www.fastmarkets.com/base-metals/iron-ore-steel-price-analysis-forecast-q4-2015, Oct-2015.

[WORL07] World Bank, "Global environment division greenhouse gas assessment handbook – a practical guidance document for the assessment of project-level greenhouse gas emissions," 10-Nov-2007.

[WZOK15] K. Wang, Z. Q. Zhu, G. Ombach, M. Koch, S. Zhang, and J. Xu, "Torque ripple reduction of synchronous reluctance machines: using asymmetric flux-barrier," *COMPEL - The international journal for computation and mathematics in electrical and electronic engineering*, vol. 34, no. 1, pp. 18–31, Jan. 2015.

[XUCC08] X. D. Xue, K. W. E. Cheng, and N. C. Cheung, "Selection of electric motor drives for electric vehicles," in *Power Engineering Conference, 2008. AUPEC '08. Australasian Universities*, 2008, pp. 1–6.

[YDGD09] Z. Yueying, W. Dafang, Z. Guifan, Y. Dongyu, and W. Yu, "Research progress of switched reluctance motor drive system," in *Mechatronics and Automation, 2009. ICMA 2009. International Conference on*, 2009, pp. 784–789.

[ZACH14] Zach, "Electric cars hitting the market in 2015," EV Obsession: http://evobsession.com/new-electric-cars-market-2015-list/, 30-Dec-2014.

[ZHLI08] Q. Zhang and X. Liu, "Permanent magnetic synchronous motor and drives applied on a mid-size hybrid electric car," in *Vehicle Power and Propulsion Conference, 2008. VPPC '08. IEEE*, 2008, pp. 1–5.

Chapter 2 Multi-physical modelling of IM and SynRM

Chapter 2 Multi-physical modelling of IM and SynRM

2.1 Introduction

As mentioned in Chapter 1, the most important performances of electric machines in variable speed drives are the motor efficiency and the power factor over the driving cycle, the motor cost and the mechanical robustness. First of all, a precise electromagnetic model is required to estimate the electromagnetic and electric behaviours of electric machines. Besides, a complete energy loss model should be constructed to evaluate the mean energy efficiency of the traction system. An economic model to estimate the cost of the traction system is introduced as well. Besides, as stated in Chapter 1, a great concern for the synchronous reluctant machine relies on the mechanical robustness of the rotor in high rotation speed. A mechanical model to evaluate the reliability of the rotor geometry should be complemented as well. The general structure of the electric vehicle traction system is defined in Figure 2.1.1. In the electric power train, the mechanical torque is provided by an inverter-fed electrical machine, which is powered by a d.c. battery.

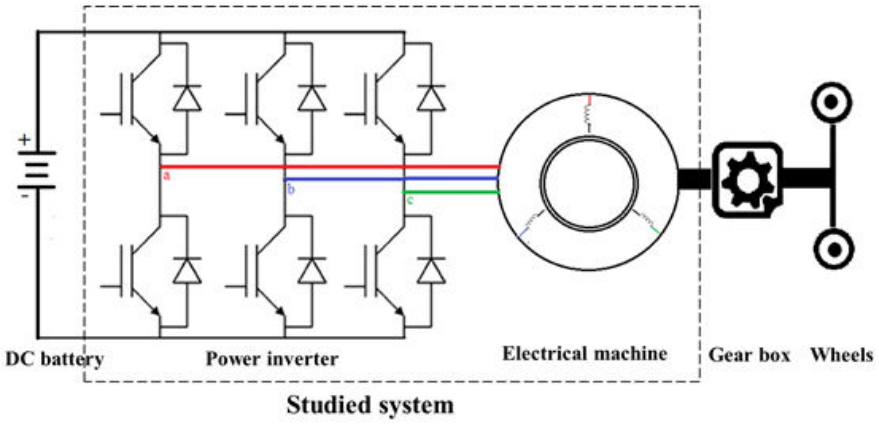

Figure 2.1.1 Equivalent scheme of power train for EV application

- ***Electromagnetic model***

The electromagnetic model is required to evaluate electromagnetic and electric behaviours (torque, phase voltage and current, power factor, induction distribution, slot current density etc.) of EMs under steady state, with the awareness of machine geometries and electrical controls. In this chapter, the electromagnetic models of an induction machine and a synchronous reluctant machine will be introduced. The description of electromagnetic models for two different kinds of EMs is settled in the same chapter, because there are many similarities between them.

- ***Loss model***

Since vehicle driving cycles contain multiple working points, the consideration of the motor losses only at one single working point is not enough. In the loss model, the losses occurring in the whole traction system will be described, which include losses in the power converter, in the conducting cables, and in the electric machine. The traction system energy efficiency over the driving cycle will be defined.

- ***Cost model***

The cost of the electromechanical converter is estimated, including the costs of the d.c. battery, the power converter and the EMs. The d.c. battery and the power converter costs are considered as commercial costs and identified by their power range, while a relatively coarse model to estimate manufacturing costs of EMs from their geometries is introduced in this chapter.

- ***Mechanical model***

As induction machines are widely used in industry over twenty years, their mechanical properties have been well studied. In several literatures ([PNMS09] [BONA10]), IM design considering mechanical robustness has been introduced already. Mechanical models of synchronous reluctant machines, especially analytical models, have not been discussed much in literatures. An analytical model to estimate the robustness of rotor for SynRMs will be introduced.

All the models above will be applied for traction system designs, they are required to be fast, robust and accurate to evaluate electromagnetic, electric, energetic and economic performances of the EV traction system.

2.2 Review of modelling techniques for EMs

The electromagnetic model is one of the most important and complicated ones in the multi-physical modelling system. We will start from a brief review of modelling techniques for EMs, especially for induction machines and synchronous reluctant machines.

Electric machines are mainly modeled by three common approaches: analytical models or semi-analytical models, finite element analysis (FEA), and magnetic equivalent circuit (MEC).

- ***Analytical models or semi-analytical models***

Analytical models are no doubt the fastest models, which are applied mostly for the presizing of electromagnetic systems, and for control system designs. Analytical models are developed directly from Maxwell's equations and empirical formulas. When analytical equations are solved numerically, it is called semi-analytical model. In this document, pure analytical models and semi-analytical models are both named as analytical models.

Analytical or semi-analytical models could be quite different for different kinds of EMs. For example, lumped parameter circuit is utilized in induction motor and a.c. transformer analysis ([ALGE65]), but not often in synchronous machine analysis. The analytical formulas of permanent magnets can be implemented into analytical models of permanent magnet machines ([JANN10]). Generally, analytical models are not suitable for detail analysis of electromagnetic

behaviours. FEA and MEC are often coupled with analytical models ([PCFB03] [BENH96] [TBDB14]) owing to their flexibility.

- ***Finite Element Analysis***

Finite element analysis (FEA) has been applied in EM analysis since the early 1970s ([SALO95]). It is considered as the most accurate tool today to model electromagnetic, thermal and mechanical performances of electric machines, and other electromagnetic devices as well. Due to the virtue of FEA, flux leakages and harmonic effects are taken into account automatically. Skin effects, harmonic losses (caused mainly by steel saturation), and other specific issues can be included in harmonic FEA or in time-domain FEA ([BENH96] [MCCL99]). Besides, a 3D FEA tool can be utilized for the design of end-windings, insulation materials and other motor details ([SBLO10] [ZHPH13]). However, the computation time and the inconvenience for the design implementation make FEA an arguable choice for motor design applications. In some professional FEA softwares, modelling and design work combine FEA with analytical model to economize time properly.

- ***Magnetic Equivalent Circuit***

Magnetic equivalent circuit model, also known as semi-numerical model ([OSTO89]), was firstly used in electrical machine design in the late 1980s, and then was further developed in recent years ([RARI97] [SKCB07]). It is a compromise approach between FEA and analytical model. Compared with analytical models and FEA, it has a moderate computation time and moderate precision. It could be extended into a 3D model as well. The accuracy of MEC depends on mesh size and model complexity. Harmonic or skin effects could not be included automatically in MEC model, if there are no extra harmonic models developed ([OSTO89] [PERH02]). Besides, although different formulas have been presented in several literatures, the complete loss calculation is not yet developed in detail under the context of MEC models.

These three approaches are resumed in a general case in the following Table 2.2.1.

Criteria	Analytical models	FEA	MEC
Accuracy	-	+	0
Computation time	++	-	0
3D capability	-	++	+
Simplicity of implementation	++	-	0
Parameterization	+	0	0

Table 2.2.1 Criteria of different modelling methods for motor design

The electromagnetic modelling of IM and SynRM will be discussed respectively in the following subsections.

2.2.1 Induction machine

The magnetic field induced by stator winding, induces voltages and produce currents in the rotor conductors (cage). To simplify the analysis, the induction machines could be treated as an a.c. transformer. Thus the lumped parameter circuit is suitable for IM modelling ([ALGE65]).

In traditional analytical models, empirical formulas are applied to compute the equivalent parameters, and the core saturation is considered with a general saturation coefficient ([LIPO04]). Authors in [AMKR10] realized a 3D MEC modelling for cage induction motor, which is compared with experimental results. It showed that MEC modelling has no obvious advantage in accuracy compared with analytical and FEA modellings. Among different FEA techniques, harmonic and time-domain FEA methods are taken to model rotor penetration phenomenon ([MEEK10]), which are more time consuming compared with static FEA. Authors in [PCFB03] proposed a method which combines time-domain FEA and lumped parameter circuit to compute equivalent parameters. This method is more precise and more robust than pure analytical models, but still not interesting in calculation efforts. In this chapter, an analytical model based on lumped parameter circuit will be introduced. This model is validated by FEA tool, and it improves the robustness and the precision in considering rotor skin effect and iron saturation. The computation time is compatible with a design procedure.

2.2.2 Synchronous reluctant machine

Analytical models of SynRMs without consideration of iron saturation have been studied in many literatures, such as in [XXLN90] [LEVI95]. They are usually applied in vector control, and *d-q* quantities are coupled. However, these models seem to be not precise enough for motor design according to the validation results. Authors in [LURR02] presented an analytical model with saturation considered. This model is not ideal as the iron saturations are evaluated with only two saturation coefficients, and it is mostly applied on the control of SynRM. In [BBBD09], an analytical model taking the rotor position and harmonics into consideration was proposed. This model gives the estimation of torque ripple, without iron saturation. In [TBDB14], an analytical model without saturation, based on MEC techniques has been described. This model shows a very good precision compared with FEA when iron saturation is neglected. Authors in [PDVJ14] have proposed an analytical model for permanent magnet assisted SynRMs. In this model, the stator and rotor core saturation, especially the saturation in the tangential and radial bridges are considered with the equations derived directly from Maxwell's equations. It has been validated by FEA tool and experiments, which showed good accuracy with different feedings. As the methodology to consider the saturation in this model is similar to the one in the analytical model of IMs, we have chosen to develop this kind of model for the SynRM without magnet, and to validate this model by FEA analysis as well.

In this section, a general review of modelling techniques for EMs has been made. Three common techniques (analytical models, FEA and MEC) have been discussed from different criteria of design application. Then reviews of modelling methods for IMs and SynRMs have been made respectively. In this thesis, two analytical models for IMs and SynRMs will be developed and validated by FEA.

2.3 Bases of electromagnetic models

Before introducing electromagnetic models, some basic theories and principles which are applied in the models will be presented in this section.

2.3.1 Maxwell's Equations

Maxwell's equations are assumed to form the foundation of electromagnetic phenomena ([HABU12]). Maxwell's four equations applied in a time-varying electromagnetic field can be expressed by the following formulas in a differential way:

$$\begin{aligned} &\text{Gauss's law:} && \nabla \cdot \vec{D} = \rho_v \\ &\text{Gauss's law for magnetism:} && \nabla \cdot \vec{B} = 0 \\ &\text{Faraday's law:} && \vec{\nabla} \times \vec{E} = -\frac{\partial \vec{B}}{\partial t} \\ &\text{Ampere's law:} && \vec{\nabla} \times \vec{H} = \vec{J} + \frac{\partial \vec{D}}{\partial t} \end{aligned} \qquad 2.3.1$$

Where $\vec{D}$, $\vec{B}$, $\vec{E}$ and $\vec{H}$ represent the electric flux density, the magnetic flux density, the electric field intensity, and the magnetic field intensity respectively, ρ_v and $\vec{J}$ represent the charge density and the current density at the position considered, and ∇ represents the Nabla operator.

Two expressions assure the relations $\vec{D}$ to $\vec{E}$ and $\vec{B}$ to $\vec{H}$ in an isotropic medium with permittivity ε and permeability μ:

$$\begin{aligned} \vec{D} &= \varepsilon \vec{E} \\ \vec{B} &= \mu(H)\vec{H} \end{aligned} \qquad 2.3.2$$

Maxwell's four equations in 2.3.1 could be expressed in an integral way with Stoke's theorem applied:

$$\begin{aligned} \oiint_{\partial\Omega} \vec{E} \cdot d\vec{S} &= \frac{1}{\varepsilon} \iiint_{\Omega} \rho_v \cdot dV \\ \oiint_{\partial\Omega} \vec{B} \cdot d\vec{S} &= 0 \\ \oint_{\partial\Sigma} \vec{E} \cdot d\vec{l} &= -\frac{d}{dt} \iint_{\Sigma} \vec{B} \cdot d\vec{S} \\ \oint_{\partial\Sigma} \vec{H} \cdot d\vec{l} &= \iint_{\Sigma} \vec{J} \cdot d\vec{S} + \frac{d}{dt} \iint_{\Sigma} \vec{D} \cdot d\vec{S} \end{aligned} \qquad 2.3.3$$

Here we define the magnetic flux Φ, the electromotive force (e.m.f.) V and the current I as:

$$\begin{aligned} \Phi &= \iint_{\Sigma} \vec{B} \cdot d\vec{S} \\ V &= \oint_{\partial\Sigma} \vec{E} \cdot d\vec{l} \end{aligned} \qquad 2.3.4$$

$$I = \iint_{\Sigma} \vec{J} \cdot d\vec{S}$$

The Faraday's law could be explained as:

$$V = -\frac{d\Phi}{dt} \qquad 2.3.5$$

When the electric flux density $\vec{D}$ is assumed to be zero in static cases or in dynamic cases without dielectric medium considered, the Ampere's law could be simplified as:

$$\oint_{\partial\Sigma} \vec{H} \cdot d\vec{l} = I \qquad 2.3.6$$

The simplified Faraday's and Ampere's laws will be applied in the analytical models.

2.3.2 Application of Maxwell's Equations

In order to explain the modelling methodology of EMs more explicitly, we decide to apply the Maxwell's theories in a simple case. A two-stage transformer is cut out, the primary and secondary windings are then separated by two air-gaps. The primary winding has N_1 turns and is fed by a current i_1, and the secondary winding is taken off as shown in Figure 2.3.1.

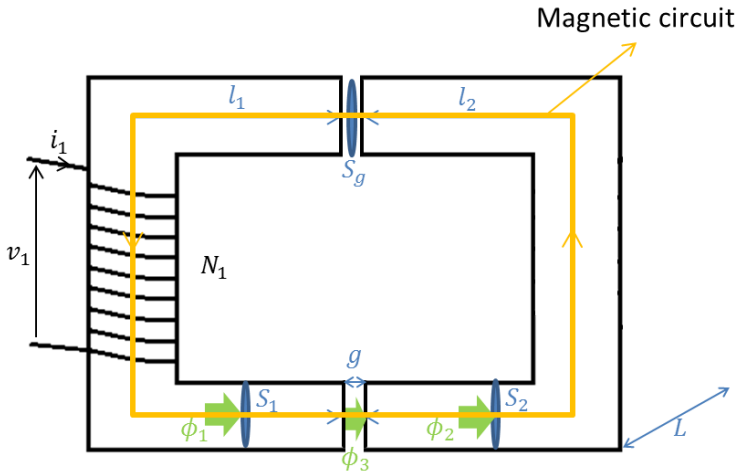

Figure 2.3.1 Example of application of Maxwell's equations

To apply Ampere's law, a magnetic circuit is chosen (the orange line in Figure 2.3.1):

$$N_1 i_1 = \int_0^{l_1} H_1(x)dx + \int_0^{g} H_g(x)dx + \int_0^{l_2} H_2(x)dx + \int_g^{2g} H_g(x)dx \qquad 2.3.7$$

Where H_1, H_2, H_g are the field intensities at the primary core, the secondary core and the air-gap, and l_1, l_2, g are the average lengths of magnetic line in the primary core, the secondary core, and the air-gap. The induction in the upper half part is anti-symmetric to that in the lower part due to the symmetric structure of the transformer. In each cross-section of the described magnetic circuit, the field density distribution is assumed to be uniform.

In this case, all the leakage fluxes in the air-gaps and cores are neglected. With Gauss's law, the following relations could be deduced:

$$B_1(x)S_1 = B_2(x)S_2 = B_g(x)S_g \qquad 2.3.8$$

Where B_1, B_2, B_g are the inductions at the primary core, the secondary core and the air-gap, and S_1, S_2, S_g are the cross-section area of the primary core, the secondary core, and the air-gap. Considering the medium electromagnetic properties, the following relations are deduced:

$$\text{In the air-gap:} \quad B_g = \mu_0 H_g$$
$$\text{In the cores:} \quad B_1 = BH(H_1) \quad B_2 = BH(H_2) \qquad 2.3.9$$

Where μ_0 is the permeability of free space: $\mu_0 = 4\pi \times 10^{-7} H/m$, and *BH* represents the non-linear magnetic property of the material in the core.

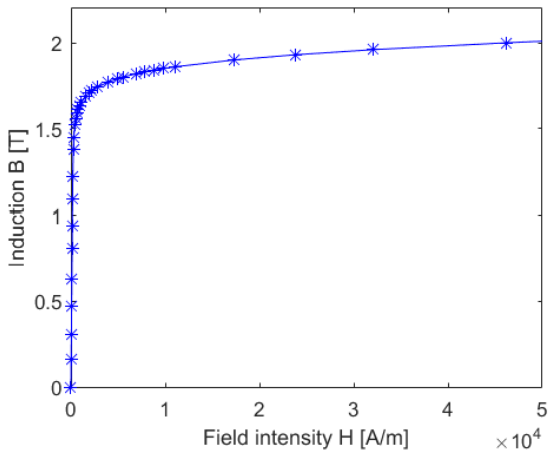

Figure 2.3.2 Magnetic property of steel M330-35

For example, the simplified magnetic property of steel M330-35 is shown in Figure 2.3.2, the material hysteresis and the temperature influence are neglected. Combining equations 2.3.7-2.3.9, the inductions in the air-gap and the cores will be solved numerically. The nonlinear function appearing in equation 2.3.9 makes it difficult to find analytical solutions. The Newton-Raphson or Secant methods can be applied to solve it (see [ALIS98]). To accelerate the solving time, the initial values are set as the solution of the linear model (when *BH* relation is linear). The derivation of the function is called for Newton-Raphson method, while not required for Secant method. With the deduced inductions, the flux and the e.m.f. could be found.

2.3.3 *Dq* axis representation

Park transformation, or *dq* transformation ([SARM79] [VANN07]) is a transformation of reference frames, from three-phase *abc* axis reference to *dq0* axis reference. It was firstly proposed by Robert H. Park in 1929 ([PARK29]). Park transformation is largely used in analysis of a.c. EMs in order to eliminate the effect of time varying inductances and to simplify the calculations.

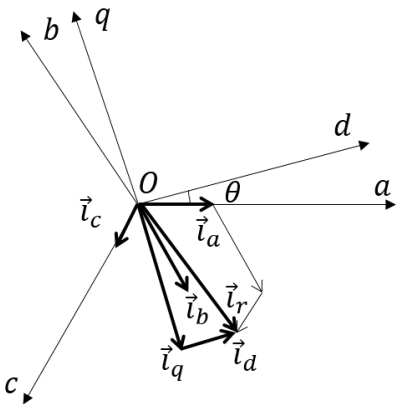

Figure 2.3.3 The vector sum of the three-phase winding electromagnetic forces under *abc* and *dq* references

The magnetomotive force (m.m.f.) generated by one phase winding $\bar{F}_a$ could be expressed as:

$$\vec{F}_a = n_a i_a \vec{a} \tag{2.3.10}$$

Where n_a is the turn number in phase a, i_a is the phase current, and $\vec{a}$ is the unit vector following the m.m.f. direction (see Figure 2.3.3). To simplify the expressions, the current vector $\bar{\imath}_a$ is defined as the production of the current i_a and the direction vector $\vec{a}$. The sum of each phase winding electromagnetic forces could be represented by the vector sum of the three-phase currents $\vec{\imath}$:

$$\vec{F} = n_a \vec{\imath} \qquad \text{With } \vec{\imath} = i_a \vec{a} + i_b \vec{b} + i_c \vec{c} \tag{2.3.11}$$

When Park transformation is applied in three-phase currents i_a, i_b and i_c, the new currents i_d, i_q and i_0 in *dq* reference could be expressed as:

$$\begin{bmatrix} i_d \\ i_q \\ i_0 \end{bmatrix} = P \begin{bmatrix} i_a \\ i_b \\ i_c \end{bmatrix} \quad \text{with } P = \frac{2}{3} \begin{bmatrix} \cos\theta & \cos\left(\theta - \frac{2\pi}{3}\right) & \cos\left(\theta + \frac{2\pi}{3}\right) \\ \sin\theta & \sin\left(\theta - \frac{2\pi}{3}\right) & \sin\left(\theta + \frac{2\pi}{3}\right) \\ \frac{1}{2} & \frac{1}{2} & \frac{1}{2} \end{bmatrix} \tag{2.3.12}$$

Where *P* is an invertible matrix, and θ represents the shift angle between axis *a* and axis *d*. $\vec{\imath}$ could be represented by i_d and i_q, as shown in Figure 2.3.3.

Similarly, the transformation could be applied in any three-phase quantity such as the phase voltage and the flux linkage. To analyze a three-phase winding in the EM, several hypothese are taken:

- The three-phase system is balanced under steady state;
- Magnetomotive forces generated by the winding have a sinusoidal distribution;
- Core saturation is neglected.

In *abc* reference frame, the electrical equations of the system are defined as:

$$v_{abc} = Ri_{abc} + \frac{d}{dt}\Psi_{abc} \tag{2.3.13}$$

Where R is the electrical resistance of one phase, v_{abc} are phase voltages, i_{abc} are phase currents, and Ψ_{abc} are flux linkages passing though one phase winding. Under dq reference, 2.3.13 is transformed into the following expression:

$$\begin{aligned} v_{dq0} &= Ri_{dq0} + \frac{d}{dt}\Psi_{dq0} + A\frac{dA^{-1}}{dt}\Psi_{dq0} \\ v_d &= Ri_d + \frac{d\Psi_d}{dt} - \Psi_q\omega \\ v_q &= Ri_q + \frac{d\Psi_q}{dt} + \Psi_d\omega \\ v_0 &= Ri_0 + \frac{d\Psi_0}{dt} \end{aligned} \tag{2.3.14}$$

Where ω is the rotation velocity of the d-axis. This expression can be applied to simplify transient calculation with transformation relations respected.

As the electromagnetic torque is the derivation of magnetic coenergy ([VANN07]), the torque could be deduced as equation 2.3.15, with the assumption of constant feeding currents.

$$T = \frac{1}{2}\frac{3\vec{\imath}}{2}\frac{d\vec{\Psi}}{d\theta} \tag{2.3.15}$$

In dq reference, torque expressions could be found by equation 2.3.16.

$$T = \frac{3(i_d\vec{d} + i_q\vec{q})}{4}\left(\frac{d\Psi_d}{d\theta}\vec{d} + \frac{d\Psi_q}{d\theta}\vec{q} + \Psi_d\frac{d\vec{d}}{d\theta} + \Psi_q\frac{d\vec{q}}{d\theta}\right) \tag{2.3.16}$$

Ψ_d and Ψ_q represent the flux linkages along d and q axis. The term Ψ_0 is neglected as it represents the flux that does not pass through the air-gap, and its derivation with angular position is assumed to be null. Flux linkage Ψ_d and Ψ_q can be also expressed by the product of the phase inductance by the current:

$$\begin{aligned} \Psi_d &= L_d i_d = L_d\vec{\imath}\cdot\vec{d} \\ \Psi_q &= L_q i_q = L_q\vec{\imath}\cdot\vec{q} \end{aligned} \tag{2.3.17}$$

Since the phase current is constant and the inductances are independent with the position, the derivations of the flux linkage Ψ_d and Ψ_q with the position are deduced as:

$$\frac{d\Psi_d}{d\theta} = L_d\vec{\imath}\cdot\frac{d\vec{d}}{d\theta} = L_d\vec{\imath}\cdot\vec{q} = L_d i_q \tag{2.3.18}$$

$$\frac{d\Psi_q}{d\theta} = L_q\vec{\imath}\cdot\frac{d\vec{q}}{d\theta} = -L_q\vec{\imath}\cdot\vec{d} = -L_q i_{qd}$$

With equation 2.3.16-2.3.18, the electromagnetic torque could be expressed by the following equation 2.3.19.

$$T = \frac{3}{2}p\left(\Psi_d i_q - \Psi_q i_d\right) \qquad 2.3.19$$

The electromagnetic torque calculated from equation 2.3.19 does not concern the cogging torque generated by flux harmonics, it is considered as the average torque rather than the instantaneous one.

In this section, four Maxwell's equations have been introduced and developed into the form that will be applied in the analytical modelling. Park transformation has been introduced and applied in the electrical equations. The expressions of phase voltages and electromagnetic torque under *dq0* reference have been presented as well. These principles and formulas will be applied in the electromagnetic models.

2.4 Electromagnetic model of Induction Machines

The electromagnetic model of IMs will be introduced in this section. This model is based on a lumped parameter circuit, and takes rotor skin effect and iron saturation into consideration.

2.4.1 Lumped parameter circuit and vector presentation

- ***Magnetomotive force distribution of a.c. windings***

For a squirrel cage IM, the fed winding produces a traveling field in the EM air-gap, which is regarded as the primary. In most rotary IMs, the secondary is the rotor. From [LIPO04], the fundamental m.m.f. generated by the stator winding at the angular position θ is expressed by equation 2.4.1.

$$F_s(\theta) = \frac{m}{\pi}\frac{n_s k_{w1}\hat{\imath}_s}{p}\cos(p\theta) \qquad 2.4.1$$

Where:
- $\hat{\imath}_s$: the amplitude of the phase current;
- n_s: the winding turn number per phase;
- m: the winding phase number;
- p: the pole pair number;
- k_{w1}: the fundamental winding coefficient. The winding coefficient is determined by winding type and slot opening. The fundamental winding coefficient for an unskewed single-layer distributed winding is described by equation 2.4.2:

$$k_{w1} = \frac{sin\left(\frac{\pi}{2m}\right) sin\left(\frac{q\tau_s}{2}\right) sin\left(\frac{b_{os}}{D_{ag}}\right)}{qsin\left(\frac{\tau_s}{2}\right)\frac{b_{os}}{D_{ag}}} \qquad 2.4.2$$

Where:
- q: the slot number per pole per phase;
- τ_s: the coil span pitch;
- b_{os}: the slot opening width;
- D_{ag}: the mean diameter of air-gap.

In Figure 2.4.1, a three-phase full pitch winding with single layer is presented.

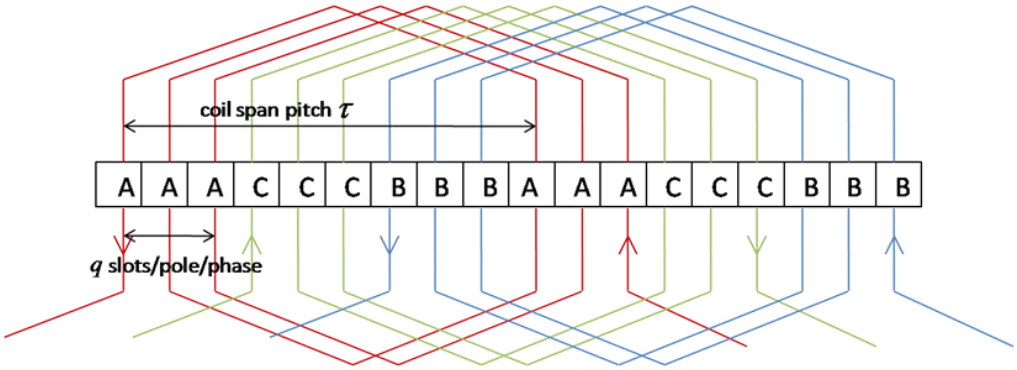

Figure 2.4.1 Three-phase full pitch winding distribution in a pair of poles

This traveling field will induce voltages in cage conductors, treated as the secondary. Under steady state, supposing that the rotor rotates at the angular speed Ω_r, the flux in the air-gap rotates at the relative angular speed $\frac{\omega_s}{p} - \Omega_r$ with respect to the rotor reference (the fed current pulsation ω_s). The a.c. currents occur in the cage bars and rings, as the squirrel cage structure assures the closed loop of currents, with the frequency $\omega_s - p\Omega_r = s\omega_s$ (slip ratio: s). From [ALGE65] [BONA10], the rotor cage could be regarded as a multi-phase winding. The rotor phase number m_r and the winding turn number per phase n_{rr} are assumed as (the current loop in one phase is described in Figure 2.4.2):

$$m_r = \frac{n_r}{p} \ , \ \ n_{rr} = \frac{1}{2} \qquad 2.4.3$$

Where n_r is the rotor bar number.

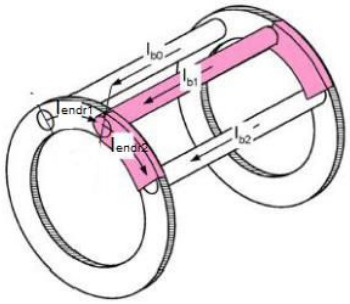

Figure 2.4.2 Bar and ring current distributions in the rotor ([BONA10])

Similarly, the fundamental of the m.m.f. generated by the rotor winding is (when the rotor slots are not skewed):

$$F_r(\theta) = -\frac{m_r}{\pi}\frac{n_{rr}k_{w1}^r\hat{\imath}_r}{p}\cos(p\theta-\beta) \quad 2.4.4$$

Where k_{w1}^r is the fundamental winding coefficient for rotor, $\hat{\imath}_r$ is the amplitude of the phase current, and β is the shift angle between the m.m.f. generated by rotor and stator windings. The rotor winding coefficient is estimated by equation 2.4.2 as well.

To simplify the analysis, the rotor winding is supposed to be same with the stator winding (same winding type and same winding turn number). Equation 2.4.4 is transformed into:

$$F_r(\theta) = -\frac{m}{\pi}\frac{n_s k_{w1}\hat{\imath}_r'}{p}\cos(p\theta-\beta) \quad \text{with} \quad \hat{\imath}_r' = \frac{m_r n_{rr}k_{w1}^r}{m n_s k_{w1}}\hat{\imath}_r \quad 2.4.5$$

The total m.m.f. in the motor is assumed to be the superposition of the m.m.f. generated by the stator and the rotor windings:

$$F(\theta) = F_s(\theta) + F_r(\theta) = \frac{m}{\pi}\frac{n_s k_{w1}\hat{\imath}_m}{p}\cos(p\theta-\alpha) \quad 2.4.6$$
$$\bar{\imath}_m = \bar{\imath}_s - \bar{\imath}_r'$$

The current vector $\bar{\imath}_m$ is regarded as the magnetizing current in the stator winding which generates the magnetic flux $\bar{\varphi}_g$ passing through the air-gap. α is the electrical angle between $\bar{\imath}_s$ and $\bar{\imath}_m$, and $\hat{\imath}_m$ is the amplitude of $\bar{\imath}_m$. The flux $\bar{\varphi}_g$ is determined by the magnetizing current, motor geometry and core magnetic property.

- ***Phase voltage expression***

The stator and rotor phase voltages under steady state are described in equation 2.4.7-2.4.8. The rotor phase voltage is regarded to be zero as a result of the cage structure (in Figure 2.4.2).

$$\bar{V}_s = R_s\bar{\imath}_s + j\omega_s L_s\bar{\imath}_s + j\omega_s n_s k_{w1}\bar{\varphi}_g \quad 2.4.7$$

$$\bar{V}_{rr} = R_r\bar{\imath}_r + js\omega_s L_r\bar{\imath}_r + js\omega_s n_{rr}k_{w1}^r\bar{\varphi}_g = 0 \quad 2.4.8$$

Where:
- R_s: the stator phase resistance;
- R_r: the rotor phase resistance;
- ω_s: the electrical pulsation;
- s: the slip ratio.

The rotor winding is again assumed to be same as the stator winding, then equation 2.4.8 is transformed into:

$$R_r'\bar{\imath}_r' + js\omega_s L_r'\bar{\imath}_r' + js\omega_s n_s k_{w1}\bar{\varphi}_g = 0 \quad 2.4.9$$

$$R'_r = k_{rs}R_r,\ L'_r = k_{rs}L_r,\ \ \bar{\imath}'_r = k'_{rs}\bar{\imath}_r$$

$$\text{With } k_{rs} = \frac{m}{m_r}\left(\frac{n_s k_{w1}}{n_{rr}k^r_{w1}}\right)^2\ k'_{rs} = \frac{m_r n_{rr} k^r_{w1}}{m n_s k_{w1}}$$

Equation 2.4.9 is transformed to equation 2.4.10, providing that stator and rotor winding currents have the same electrical pulsation.

$$\frac{R'_r}{s}\bar{\imath}'_r + j\omega_s L'_r \bar{\imath}'_r + j\omega_s n_s k_{w1}\bar{\varphi}_g = 0 \qquad 2.4.10$$

Equation 2.4.7 and 2.4.10 could be simplified as equation 2.4.11 when the flux linkage is expressed as the product of the magnetizing current and an equivalent inductance.

$$\bar{V}_s = R_s\bar{\imath}_s + j\omega_s L_s\bar{\imath}_s + \bar{V}_r$$

$$\frac{R'_r}{s}\bar{\imath}'_r + j\omega_s L'_r\bar{\imath}'_r + \bar{V}_r = 0 \qquad 2.4.11$$

$$\text{With } \bar{V}_r = j\omega_s L_m\bar{\imath}_m$$

Where V_r represents the phase e.m.f., L_m is defined as the magnetizing inductance, and the value of this inductance varies with the magnetizing current as a result of core saturations.

- ***Lumped parameter circuit***

Lumped equivalent circuit of induction machines is described in Figure 2.4.3. Note that this circuit represents one phase of the three-phase electric machine. Under balanced three-phase feeding condition, the electromagnetic power converted in the air-gap is expressed by the equivalent parameters in equation 2.4.12.

$$P_{ag} = \frac{m}{2}\frac{R'_r}{s}\hat{\imath}'^2_r \qquad 2.4.12$$

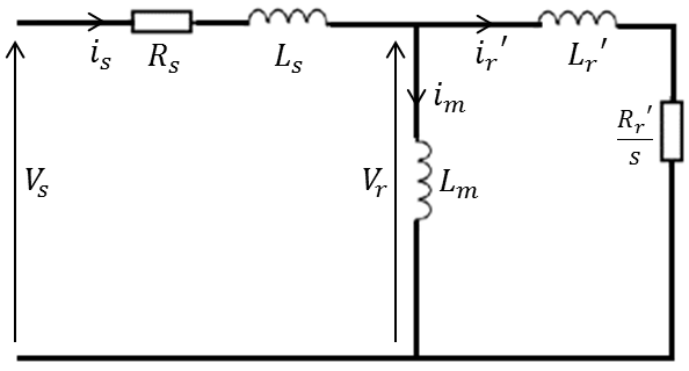

Figure 2.4.3 Lumped parameter circuit

This item is divided into two parts: rotor copper losses and the mechanical power. From equation 2.4.10, the rotor copper losses are:

$$P_{js\_r} = \frac{m}{2} R_r' \hat{\imath}_r'^{\,2} \qquad 2.4.13$$

With equation 2.4.12-13, the mechanical power and the electromagnetic torque could be deduced:

$$P_m = P_{ag} - P_{js\_r} = \frac{m}{2}\frac{R_r'}{s}(1-s)\hat{\imath}_r'^{\,2}$$
$$T_{em} = \frac{P_m}{\Omega_r} = \frac{pm}{2}\frac{R_r'}{s\omega_s}\hat{\imath}_r'^{\,2} \qquad 2.4.14$$

The power factor of IMs is defined as the cosine value of the shift angle between the phase voltage $\bar{V}_s$ and the phase current $\bar{\imath}_s$. The stator copper losses are quantified by the stator phase resistance.

The lumped parameter circuit is an explicit way to quantify the electrical behaviours by the equivalent parameters. And it's easy to combine the circuit with other electromagnetic models. This circuit is often applied in the modeling and control designs of electromagnetic devices and electrical networks. The lumped parameter circuit could be transformed into other forms according to different demands, for example the magnetizing resistance could be added to quantify the core losses ([BONA10]). The above circuit will be used to explain the electrical behaviours of IMs in the analytical model.

- ***Vector presentation***

The phasor relationship between electrical elements in the lumped parameter circuit is shown in the following vector diagram. The diagram shows that when all the equivalent parameters in the lumped circuit ($R_s, L_s, L_m, R_r', L_r', s, \omega_s$) are known, all the other electrical elements could be solved with only one of them described. In the vector diagram, axis *d* and axis *q* are remarked.

Among all the equivalent parameters, the value of the magnetizing inductance is influenced by the value of the magnetizing current, and the values of the rotor phase resistance and inductance are influenced by the rotor flux frequency (slip ratio). The three parameters are influenced by electrical controls, and their calculations can be found in the next sections. The calculations of the other parameters can be found in Appendix 1.

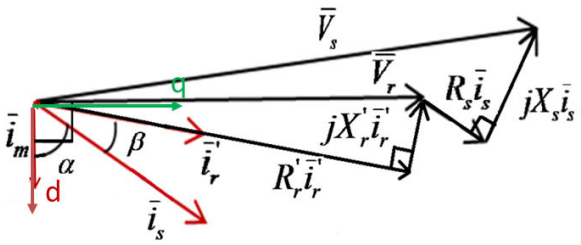

Figure 2.4.4 Vector diagram of IMs

2.4.2 Rotor impedance calculation with skin effect considered

Lipo has proposed the analytical formulas to determine the rotor a.c. impedance, which were deduced directly from Maxwell's equations ([LIPO04]). They are widely used in the analytical models. Unfortunately, it works only with rectangular bar shape. Instead, we take another numerical approach to calculate the rotor bar resistance and slot leakage inductance ([BONA10] [BOCL11]).

To begin, several hypothese are taken:

- Infinite permeability in iron cores ([BONA10]);
- Magnetic field lines (rotor slot leakage flux) parallel with axe *x* (see Figure 2.4.5);
- Resistance and leakage inductance of cage ring neglected;

With this approach, one cage bar cross section is decomposed by *N* thin layers along the *y* axis. The width of the *k*th layer is assigned as w_k, with the height assigned as h_k.

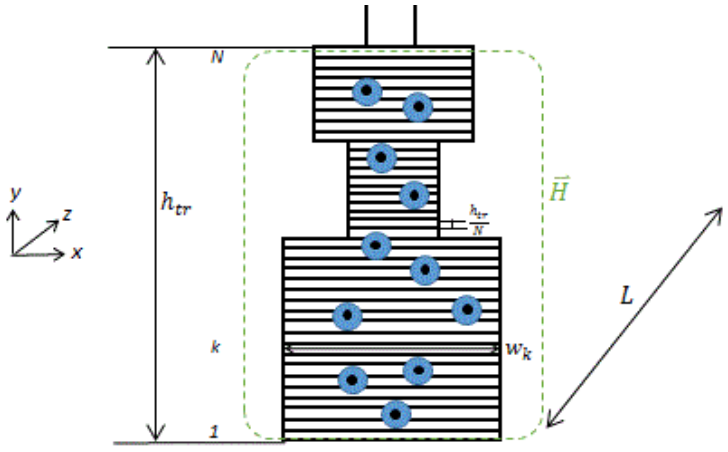

Figure 2.4.5 Multi-layer decomposition of one rotor bar

An identical end-to-end electromotive force $\bar{V}$ is applied to all conductor layers:

$$\bar{V} = R_k \bar{\imath}_k + j\omega_r \bar{\Lambda}_k \qquad 2.4.15$$

Where R_k is the resistance of the k_{th} layer, $\bar{\Lambda}_k$ is the leakage flux passing through bar section below the height h_k, and ω_r the rotor passing flux frequency with respect to the rotary frequency. They are expressed by the following equations.

$$R_k = \rho_{Al} \frac{L}{w_k h_k} \qquad 2.4.16$$

$$\omega_r = s\omega_s \qquad 2.4.17$$

From Faraday's Law:

$$\overline{\Lambda}_k - \overline{\Lambda}_{k-1} = \mu_0 L h_k \overline{\mathrm{H}}_k \qquad 2.4.18$$

Where:
- ρ_{Al}: the resistivity of rotor cage in aluminum;
- L: motor length;
- s: slip ratio;
- ω_s: feeding pulsation;
- $\overline{H}_k$: the magnetic field in the k_{th} layer.

From Ampere's Law, the magnetic field $\overline{H}_k$ can be expressed by induced currents in layers below the k_{th} layer (k_{th} layer included).

$$\overline{H}_k w_k = \sum_{j=1}^{k} \bar{\imath}_j \qquad 2.4.19$$

With equation 2.4.15-2.4.19, the following phasor relation between adjacent layers is found:

$$\bar{\imath}_k = \frac{w_k}{w_{k-1}} \bar{\imath}_{k-1} + j\omega_r \frac{\mu_0}{\rho_b} {h_k}^2 \sum_{j=1}^{k-1} \bar{\imath}_j \qquad 2.4.20$$

With the awareness of the current in the first layer (for example, $\bar{\imath}_1$ could be assigned to a unit value), the currents in all the other layers are found. And the total current in the bar is the sum of currents in all these thin layers:

$$\bar{\imath}_b = \sum_{j=1}^{N} \bar{\imath}_j \qquad 2.4.21$$

From the energy conversion point, the a.c. resistance of the cage bar R_{bar} and the slot leakage inductance λ_{slr} are calculated by equation 2.4.22-2.4.23.

$$P_{js}^{bar} = \sum_{k=1}^{N} R_k {\bar{\imath}_k}^2 = R_{bar} {\hat{\imath}_b}^2 \qquad 2.4.22$$

$$Q^{slot} = \frac{1}{2}\mu_0 \frac{h_{tr}}{N} \sum_{k=1}^{N} w_k {\overline{H}_k}^2 = \frac{1}{2}\lambda_{slr} {\hat{\imath}_b}^2 \qquad 2.4.23$$

A few remarks of this approach are taken:
- only the slot leakage inductance is taken into account;
- to treat a double cage rotor, we have to consider that the current in the empty slot layers between the upper and lower cage is equal to zero;
- this method has not been validated in an IM with closed opening slots yet.

As mentioned in Subsection 2.4.1, the cage is treated as a multi-phase winding with $\frac{n_r}{p}$ phases, each phase has $\frac{1}{2}$ coil turn (one conductor per phase). In Figure 2.4.6, an electrical circuit and the corresponding vector diagram are presented to describe the phasor relation between the currents passing through neighbouring bars and the connecting ring segments. The cage geometry is considered symmetric, and only two bars are treated in this case. Several symbols are assigned:

- R_{bar}: the a.c. resistance of the bar;
- λ_{slr}: the slot leakage inductance;
- i_{bi}: the current passing through the i_{th} bar;
- R_{endr}: the resistance of the connecting ring segment (with skin effect neglected);
- L_{endr}: the inductance of the connecting ring segment (see Appendix 1);
- i_{endri} : the current passing through the i_{th} ring section.

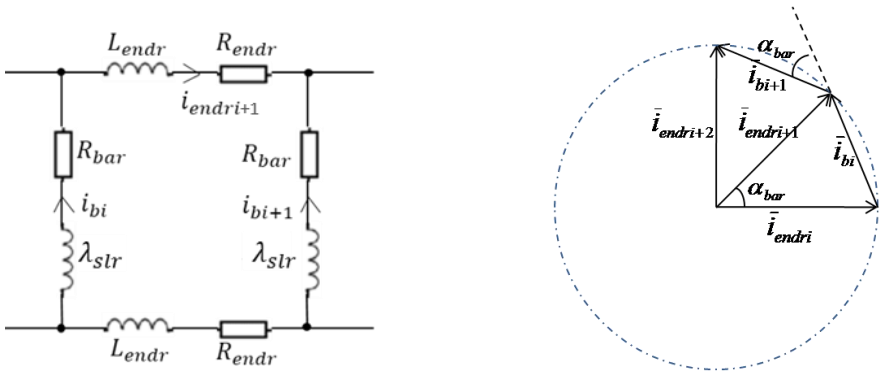

(a) (b)

Figure 2.4.6 Equivalent circuit of the cage (a) vector diagram of the circuit (b)

Under the hypothesis that the e.m.f. distribution at the end of rotor bars is sinusoidal with the angular pulsation $\frac{p}{2\pi}$ ($\frac{n_r}{p}$ phase winding), the amplitude of the currents in the ring sections is defined as $\hat{\imath}_{endr}$, the electrical angle α_{bar} between current $\bar{\imath}_{endri}$ and current $\bar{\imath}_{endri+1}$ is:

$$\alpha_{bar} = \frac{2\pi p}{n_r} \tag{2.4.24}$$

The current $\bar{\imath}_{bi+1}$ is the difference between currents in neighbouring ring segments:

$$\hat{\imath}_{bi} = |\bar{\imath}_{endri} - \bar{\imath}_{endri+1}| = 2\hat{\imath}_{endr}\, sin\left(\frac{\alpha_{bar}}{2}\right) \tag{2.4.25}$$

The bar and its connecting ring segments could be integrated into an equivalent bar with the resistance R_b, and the relationship between them could be deduced by:

$$\begin{aligned} R_b\hat{\imath}_b^2 &= R_{bar}\hat{\imath}_b^2 + 2R_{endr}\hat{\imath}_{endr}^2 \\ R_b &= R_{bar} + \frac{R_{endr}}{2sin^2\left(\frac{\alpha_{bar}}{2}\right)} \end{aligned} \tag{2.4.26}$$

The rotor phase resistance is:

$$R_r = p\frac{R_b}{p} = R_b \tag{2.4.27}$$

Similarly, the inductance of the equivalent bar is:

$$L_b = \lambda_{slr} + \frac{L_{endr}}{2sin^2\left(\frac{\alpha_{bar}}{2}\right)} \tag{2.4.28}$$

And the rotor phase inductance L_r is:

$$L_r = L_b + L_{dr} + L_{zr} \tag{2.4.29}$$

Where L_{dr} is the rotor differential leakage inductance, and L_{zr} is the zig-zag inductance.The calculations of these leakage inductances could be found in Appendix 1.1.

2.4.3 Air-gap induction calculation with iron saturation considered

To consider the iron saturation, the magnetizing inductance will not be computed with saturation coefficient which is deduced from the phase passing through flux ([ALGE65]). Instead, the determination of the air-gap flux density as the function of the magnetic current i_m is discussed with the following approach. The m.m.f. drops in different parts of the motor are investigated. In the analytical model, the electromagnetic behaviours of the IM are assumed to be anti-symmetric.

As mentioned in Subsection 2.4.1, the exciting m.m.f. in the motor is assumed to be the superposition of the m.m.f. generated by the stator and the rotor windings:

$$F(\theta) = F_s(\theta) + F_r(\theta) = \frac{m}{\pi}\frac{n_s k_{w1}\hat{\imath}_m}{p}\cos(p\theta - \alpha) \tag{2.4.30}$$

From Hopkinson's Law, the relation between m.m.f. drops in different parts of motor is:

$$F(\theta) = F_g(\theta) + F_{ts,r}(\theta) + \frac{1}{2}F_{ys,r}(\theta) \tag{2.4.31}$$

Where F_g is the m.m.f. drop in the air-gap, $F_{ts,r}$ are the m.m.f. drops in the stator and rotor teeth, and $F_{ys,r}$ are the mmf drops in the stator and rotor yokes (see Figure 2.4.7).

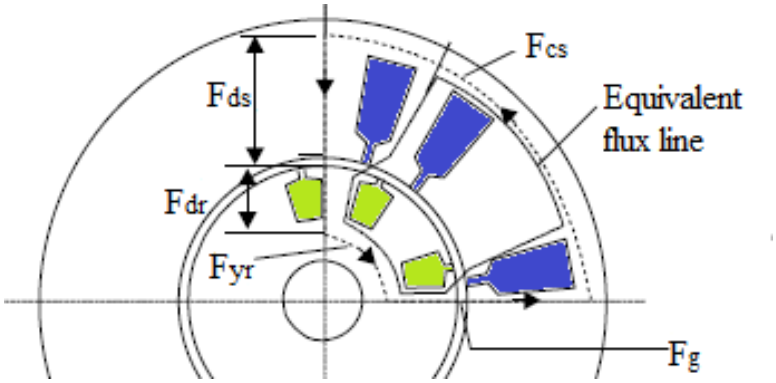

Figure 2.4.7 Equivalent magnetic field lines in IM

- ***M.m.f. drop in the air-gap***

The m.m.f. drop in the air-gap is expressed by the following formula:

$$F_g(\theta) = \frac{k_c g}{\mu_0} B_g(\theta) \qquad 2.4.32$$

Where $B_g(\theta)$ is the flux density in the air-gap at the electrical position θ, and k_c the Carter coefficient which describes the ratio between the fundamental of air-gap flux density and the real air-gap flux density.

$$k_c = k_{cs} k_{cr} = \frac{\tau_s}{\tau_s - \frac{{b_{os}}^2}{5g + b_{os}}} \frac{\tau_r}{\tau_r - \frac{{b_{or}}^2}{5g + b_{or}}} \qquad 2.4.33$$

Where τ_r indicates the number of coil span pitch of rotor, and b_{or} indicates the opening width of the rotor bar. The coil span pitch of rotor is defined by:

$$\tau_r = \frac{\pi D_r}{n_r} \qquad 2.4.34$$

Where D_r is the outer radius of rotor, and n_r the rotor bar number.

- ***M.m.f. drop in the teeth***

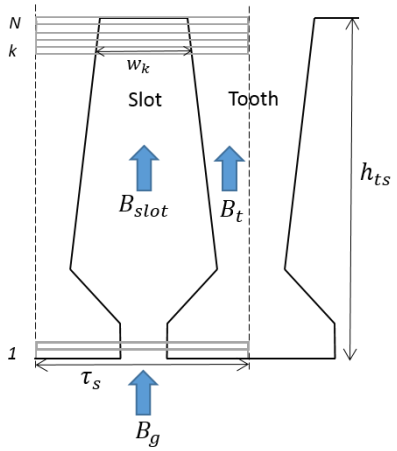

Figure 2.4.8 Flux distribution in one slot pitch

Firstly, we assume that all the flux per slot pitch goes radially through the teeth and the slot as shown in Figure 2.4.8. One slot is divided by N layers within the radial direction when its form is not rectangular. With flux conservation law, the following relation is deduced then:

$$B_g(\theta)\tau_s = B_{slotk}w_k + B_{tk}(\tau_s - w_k) + B_{tk}(1 - k_{ir})w_k \qquad 2.4.35$$

Where:
- B_{slotk}: the induction in the k_{th} layer of the slot (Figure 2.4.8);
- B_{tk}: the induction in the k_{th} layer of the tooth;
- w_k: the width of the k_{th} layer of the slot;
- k_{ir}: the lamination pack coefficient.

In our case, the lamination pack coefficient is assumed to be around 0.95. The last term refers to the flux shunt effect owing to the slot and the air between the teeth laminations.

With the equipotential hypothesis applied in each tangential layer, the relation between B_{slotk} and B_{tk} is deduced by:

$$B_{slotk} = \mu_0 BH^{-1}(B_{tk}) \qquad 2.4.36$$

Where BH^{-1} is the inverse function of function BH.

From [DAGU13], there are mainly two leakage fluxes in the flux path from the air-gap to the stator and rotor teeth: the radial leakage flux which passes through adjacent slot and the tangential leakage flux as a result of the self-inductance effect of coils in the slot. While the first one is modeled in equation 2.4.35, and the latter one is defined as slot leakage inductance in Appendix 1.1.

The m.m.f. drop in the stator tooth is expressed in the following equation 2.4.37.

$$F_{ts}(\theta) = \sum_{k=1}^{N} \frac{B_{slotk}}{\mu_0} \frac{h_{ts}}{N} \qquad 2.4.37$$

Where h_{ts} represents the stator slot height. The m.m.f. drop in the rotor tooth is calculated with the same approach.

- ***M.m.f. drop in the yokes***

By neglecting the radial flux leakage, and with the Faraday's Law, the flux density in the stator and the rotor yoke could be expressed by:

$$B_{ys,r}(\theta) = \frac{D_{ys,r}}{4h_{ys,r}} \int_{\theta}^{\theta+\pi} B_g(\vartheta)\, d\vartheta \qquad 2.4.38$$

Where:
- D_{ys}: mean diameter of the stator yoke;
- D_{yr}: mean diameter of the rotor yoke;
- h_{ys}: stator yoke height;
- h_{yr}: rotor yoke height.

The m.m.f. drops in stator and rotor yokes are then deduced by:

$$F_{ys,r}(\theta) = \frac{D_{ys,r}}{2} \int_{\theta}^{\theta+\pi} BH^{-1}\left(B_{ys,r}(\vartheta)\right) d\vartheta \qquad 2.4.39$$

The fundamental of the air-gap induction $\hat{B}_1$ (along *d*-axis) and the flux passing through one stator phase is deduced by equation 2.4.40.

$$\hat{B}_1 = \frac{2}{\pi} \int_0^{\pi} B_g(\vartheta) cos(\vartheta - \alpha)\, d\vartheta$$
$$\widehat{\Psi}_s = \frac{n_s k_{w1} D_{ag} L \hat{B}_1}{p} \qquad 2.4.40$$

Where D_{ag} is the air-gap diameter, and *L* is the motor length. The integration operator in equation 2.4.38-2.4.40 is realized in a discrete way.

2.4.4 Solution of the electromagnetic model

In the last subsection, the nonlinear relationship between the magnetizing current and the air-gap induction distribution are established. To solve the nonlinear system, a numerical method is applied. One pole arc is divided into *K* intervals θ_i (see Figure 2.4.9, *K* is taken largely higher than the slot number per pole: $K \geq \frac{20\max(n_e, n_r)}{2p}$). Within each interval θ_i, the air-gap flux density B_{gi} is supposed to be uniform. A nonlinear function *W* is defined to describe the relations between the *K* variables $[B_{g1}, \cdots, B_{gK}]$ and the exciting m.m.f. $F([\theta_1, \cdots, \theta_K])$:

$$F([\theta_1, \cdots, \theta_K]) = W\left([B_{g1}, \cdots, B_{gK}]\right) = \frac{m}{\pi} \frac{n_s k_{w1} \hat{\imath}_m}{p} \cos(p([\theta_1, \cdots, \theta_K]) - \alpha) \qquad 2.4.41$$

Where IM geometries and core magnetic properties are concerned in the function *W*.

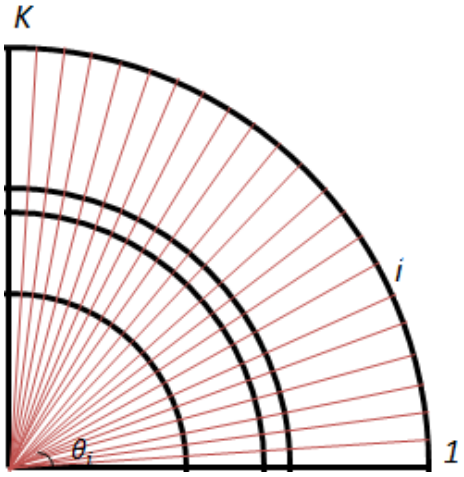

Figure 2.4.9 Pole arc decomposed with *K* intervals

In Subsection 2.4.1-2, the equivalent parameters except the magnetizing inductance are deduced with the awareness of the machine geometry, the electrical pulsation and the slip ratio. These items are assigned as the input of the electromagnetic model. In equation 2.4.41, two other variables are unknown: the amplitude of the magnetizing current $\hat{\imath}_m$, and the electrical angle between $\bar{\imath}_m$ and $\bar{\imath}_s$. To solve the system, additional equations should be developed.

The phase e.m.f. can be found with Faraday's law, or by equation 2.4.11. Then the following equation 2.4.42 is developed:

$$\hat{V}_r = n_s k_{w1} \omega_s \hat{\Psi}_s = \left| \frac{R'_r}{s} \bar{\imath}'_r + j\omega_s L'_r \bar{\imath}'_r \right| = \hat{\imath}'_r \sqrt{\left(\frac{R'_r}{s}\right)^2 + (\omega_s L'_r)^2} \qquad 2.4.42$$

And from the vector diagram in Figure 2.4.4, the following equations are deduced:

$$\begin{aligned} \hat{\imath}'_r cos(\beta) + \hat{\imath}_m cos(\alpha) &= \hat{\imath}_s \\ \hat{\imath}'_r sin(\beta) - \hat{\imath}_m sin(\alpha) &= 0 \\ \beta + \alpha + tan^{-1}\left(\frac{\omega_s L'_r}{R'_r}\right) &= \frac{\pi}{2} \end{aligned} \qquad 2.4.43$$

Combining equations 2.4.41-43, the inputs of the model are chosen as: motor geometries, the slip ratio, electrical pulsation, and the stator phase current $\hat{\imath}_s$. The variables in the model are: air-gap induction distribution$\left[B_{g1}, \cdots, B_{gK}\right]$, the magnetizing current amplitude $\hat{\imath}_m$, the rotor phase current amplitude $\hat{\imath}'_r$, and the shift angles α and β.

In some design cases, when the rotation speed and the torque are specified, the inputs of the model are chosen as: motor geometries, the slip ratio, rotation speed, and the electromagnetic torque. Then from equation 2.4.13, the rotor phase current amplitude $\hat{\imath}'_r$ could be found. And the variables in the model are: air-gap induction distribution$\left[B_{g1}, \cdots, B_{gK}\right]$, the magnetizing current amplitude $\hat{\imath}_m$, the stator phase current amplitude $\hat{\imath}_s$, and the shift angles α and β.

The model could be solved by numerical approaches such as Newton-Raphson method and Secant method. With the solved model, the electrical and electromagnetic behaviours could be treated, such as phase voltage, power factor, slot current density, etc. The procedure of the model is resumed in Figure 2.4.10.

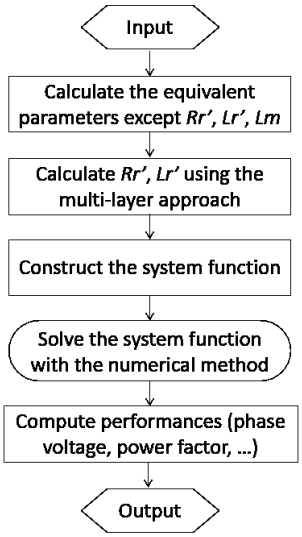

Figure 2.4.10 Flow chart of the electromagnetic model of IMs

A semi-analytical electromagnetic model of IMs was described in this section. The principles of the lumped parameter circuit are applied for IMs. The equivalent parameters except the rotor resistance, the rotor impedance, and the magnetizing inductance are computed with analytical formulas. The rotor a.c. impedance is calculated with a multi-layer approach, which is valid for different bar geometries. The saturation in teeth and yokes is investigated by constructing the nonlinear relations between the air-gap induction distribution and the exciting m.m.f. With the additional relations derived from the vector diagram of the lumped circuit, the nonlinear system is constructed. With numerical methods, the system could be solved. The validations of the methods to consider the rotor a.c. resistance and the core saturation will be presented in Chapter 3.

2.5 Electromagnetic model of Synchronous Reluctant Machines

The electromagnetic model of SynRMs will be described in this section. Physically, IMs generates the electromagnetic torque due to the electromagnetic interactions between stator and rotor winding currents, while SynRMs generates the torque as a result of magnetic reluctance effect. A lumped parameter circuit, is not enough to compute electromagnetic behaviours for SynRMs without rotor damper winding. The *dq* axis representation (as introduced in Section 2.2) is applied in the SynRM analytical model. We start from some electrical definitions in the model.

2.5.1 Vector presentation

Dq phasor is a common mathematical approach for the analytical modelling of synchronous machine family ([FIKU09]). For pure SynRMs, the *q*-axis is defined as along the radial direction of the rotor air barriers (see Figure 2.5.1 (a)). In Figure 2.5.1 (b), the vector diagram is presented with the symbols defined as:

- $\bar{V}_s$: stator phase voltage;
- $\bar{V}_r$: stator phase e.m.f.;
- $\bar{\imath}_s$: stator phase current;
- $\bar{\Psi}_m$: magnetic flux linkage passing through the air-gap per phase;
- $\bar{\Psi}_s$: flux linkage passing through the stator winding per phase;
- L_s: stator phase leakage inductance;
- ω_s: feeding electrical pulsation;
- R_s: stator phase resistance;
- α: shift angle between stator current and *d* axis, which is called current angle;
- φ: shift angle between magnetic flux and *d* axis, which is called flux angle.

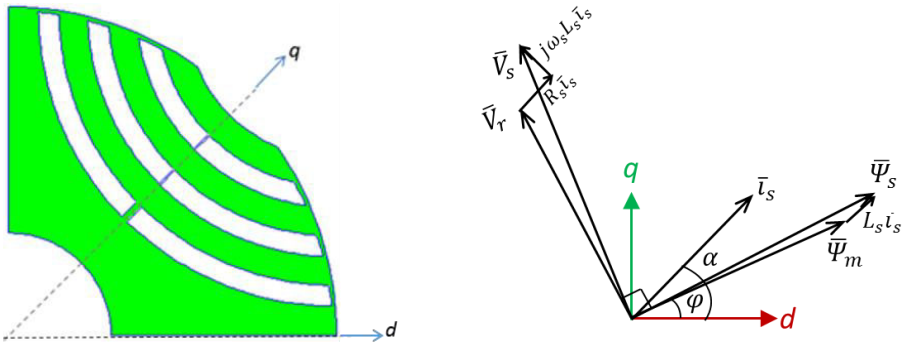

(a) (b)

Figure 2.5.1 (a) Determination of *d*-*q* axis by rotor barrier position
(b) Vector diagram of SRM in *d*-*q* coordinate

Stator phase e.m.f. $\bar{E}_r$, phase voltage $\bar{V}_s$, the electromagnetic torque and the power factor could be expressed by equation 2.5.1.

$$\bar{E}_r = j\omega_s \bar{\Psi}_m$$

$$\bar{V}_s = \bar{E}_r + j\omega_s L_s \bar{\imath}_s + R_s \bar{\imath}_s$$

$$T_{em} = \frac{3}{2} p(\bar{\Psi}_m \times \bar{\imath}_m) = \frac{3}{2} p\left(\hat{\Psi}_{md} \hat{\imath}_{sq} - \hat{\Psi}_{mq} \hat{\imath}_{sd}\right) \qquad 2.5.1$$

$$PF = cos\left(\frac{\pi}{2} + \varphi - \alpha - cos^{-1}\left(\frac{\bar{V}_s \cdot \bar{V}_r}{\hat{V}_s \hat{V}_r}\right)\right)$$

With $\varphi = tan^{-1}\left(\frac{\hat{\Psi}_{mq}}{\hat{\Psi}_{md}}\right), \hat{\Psi}_{md} = \hat{\Psi}_m \cos(\varphi), \hat{\Psi}_{mq} = \hat{\Psi}_m \sin(\varphi)$

The leakage inductances along *d*-axis and *q*-axis are assumed to be equivalent when the influences of the bridges along *q*-axis are neglected. From the above formulas, the air-gap passing through magnetic flux $\bar{\Psi}_m$, the feeding current amplitude, angle and pulsation, and phase resistance and inductance are required to estimate SynRM electrical behaviours. The feeding current $\bar{\imath}_s$ ($\hat{\imath}_s, \omega_s$ and α) is one of the analytical model inputs, and the phase resistance and inductance could be calculated by analytical formulas in Appendix 1.2. In the next subsection, the calculation of the magnetic flux passing through the air-gap will be introduced.

2.5.2 Air-gap induction calculation with iron saturation considered

Like the IM analytical model, the determination of the air-gap flux density as function of the exciting m.m.f. is discussed in this subsection.

- ***M.m.f. of the a.c. winding***

For SynRMs, the exciting m.m.f. is produced by stator winding currents, which is expressed in equation 2.5.2.

$$F(\theta) = \frac{3}{\pi}\frac{n_s k_{w1}\hat{\imath}_s}{p}\cos(p\theta - \alpha) \qquad 2.5.2$$

The variables n_s, p are the same ones as those used in the IM model, with only the stator fundamental winding coefficient considered in k_{w1}. θ is the mechanical position with respect to the *d*-axis.

Similarly, the studied part of the SynRM is assumed to be anti-symmetric. The modeled pole arc is decomposed into two parts: part *I* corresponds to the positions where the air-gap facing to tangential bridges (black regions in Figure 2.5.2), and part *II* includes the rest part.

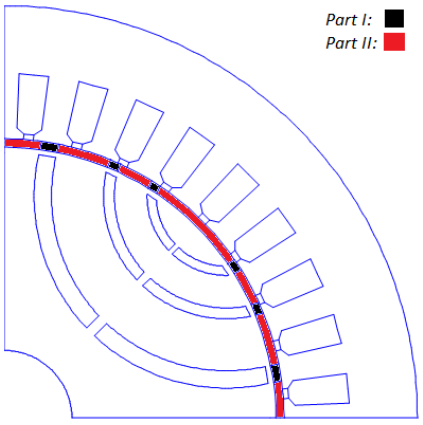

Figure 2.5.2 Decomposition of the pole arc according to the air-gap position

Now we start from studying the air-gap induction in region part *I*.

- ***Tangential bridge region***

Before studying the tangential bridge region, the concerning symbols are assigned as:

-$B_g(\theta)$: air-gap induction at the angular position θ;
-D_{ag}: mean air-gap diameter;
-h_{tb}: tangential bridge height;
-B_{tb}: induction along the tangential direction in the bridge;
-ϕ_{tb}: flux passing through the tangential bridge along the tangential direction;
-D_{tb}: mean diameter of the tangential bridge;
-$H_{tb}(\vartheta)$: field intensity along the tangential direction in the bridge at the angular position ϑ;
-$H_g(\theta)$: field intensity field in the air-gap at the angular position θ;
-$F(\theta)$: exciting m.m.f. at the angular position θ;
-$F_g(\theta)$: m.m.f. drop in the air-gap at the angular position θ;
-θ_f: angular position of the front of the tangential bridge;
-θ_b: angular position of the back of the tangential bridge;
-g: air-gap width;
-k_c: Carter coefficient;
-L: motor length.

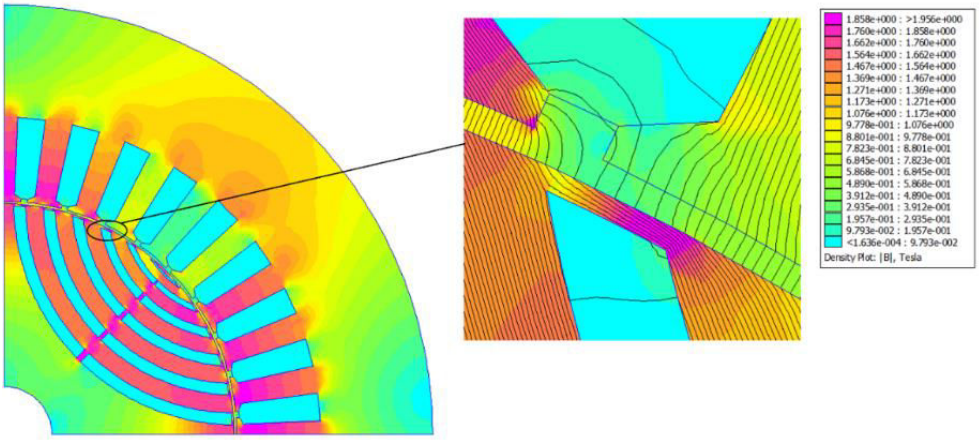

(a)

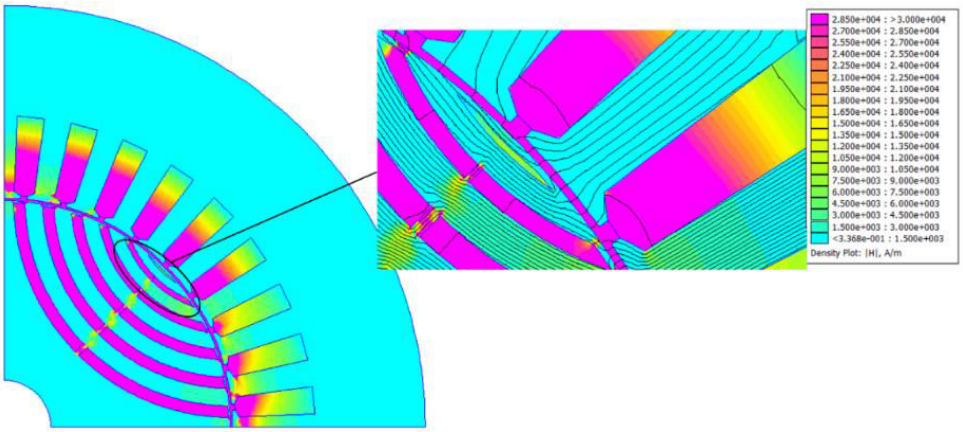

(b)

Figure 2.5.3 Magnetic field and flux density around the tangential bridge (a) and the radial bridge (b) modeled by FEA tool (with current density $\hat{j}_s = 4A \cdot mm^{-2}$ and current angle $\alpha = 45°$)

In Figure 2.5.3 (a), the magnetic field around a tangential bridge is described with FEA tool when the SynRM is fed by current density $\hat{j}_s$ $(4A \cdot mm^{-2})$ and current angle $(45°)$. From the

modelling results, the leakage flux passing from the tangential bridge to the neighbouring barrier is negligible.

With flux conversation law applied in the bridge cross-section (see Figure 2.5.4), the relation between inductions in the air-gap and in the bridge is deduced in equation 2.5.3. The direction of the magnetic field in the air-gap is supposed from the rotor to the stator, when the direction of magnetic field in bridge is assumed to be from the front to the back of bridge.

$$B_g(\theta)\frac{D_{ag}}{2}d\theta = -h_{tb}dB_{tb} \qquad 2.5.3$$

From Ampere's law, a magnetic circuit is chosen to deduce the relation between current density in the air-gap and in the bridge (see the light blue circuit in Figure 2.5.4):

$$\int_{\theta}^{\theta+d\theta} H_{tb}(\vartheta)\frac{D_{tb}}{2}d\vartheta - \Big(F_g(\theta+d\theta) - F_g(\theta)\Big) + \Big(F(\theta+d\theta) - F(\theta)\Big) = 0 \qquad 2.5.4$$

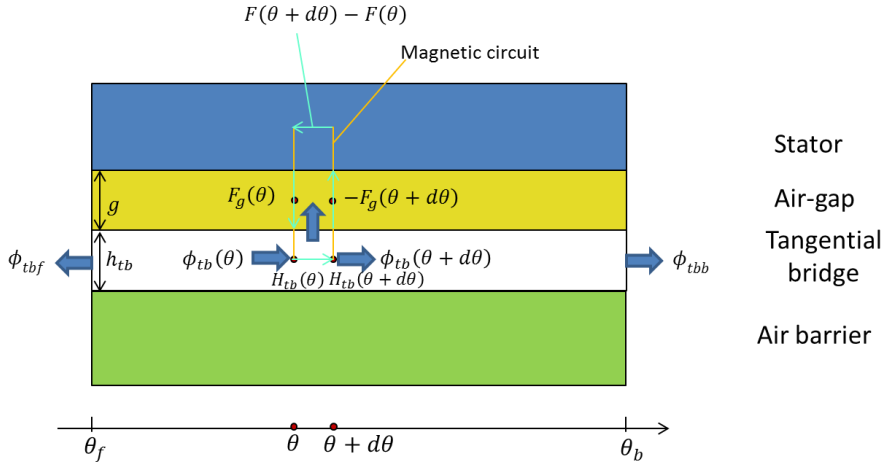

Figure 2.5.4 Magnetic circuit and flux path in the tangential bridge region

In the chosen magnetic circuit, the m.m.f. drops in stator teeth and yokes are negligible compared with the m.m.f. drops in the air-gap and the tangential bridge. When the previous equation is derived, it is transformed into equation 2.5.5 with the magnetic field in the air-gap described in equation 2.4.32.

$$H_{tb}(\theta) - \frac{2gk_c}{D_{tb}}\frac{dH_g}{d\theta} = -\frac{2}{D_{tb}}\frac{dF}{d\theta} \qquad 2.5.5$$

The expression of the Carter coefficient can be found in equation 2.4.33, with the rotor Carter coefficient regarded as unit for SynRMs. From equation 2.5.3-2.5.5 and with magnetic property of iron material, a differential equation with tangential induction in the bridge taken as variable is found:

$$BH^{-1}\left(B_{tb}(\theta)\right)+\frac{2gk_ch_{tb}}{\mu_0 D_{tb}R_g}\frac{d^2B_{tb}}{d\theta^2}=-\frac{2}{D_{tb}}\frac{dF}{d\theta} \quad 2.5.6$$

In order to solve the differential equation, boundary conditions derived from equation 2.5.3 are imposed:

$$\frac{dB_{tb}}{d\theta}|_{\theta=\theta_f}=-\frac{D_{ag}}{2h_{tb}}B_g(\theta_f)$$
$$\frac{dB_{tb}}{d\theta}|_{\theta=\theta_b}=-\frac{D_{ag}}{2h_{tb}}B_g(\theta_b) \quad 2.5.7$$

Since the nonlinear function *BH* (iron saturation considered) appears in the differential equation (equation 2.5.6) subject to Neumann boundary condition (equation 2.5.7), it is difficult to find analytical solutions. Instead, numerical solutions, such as Secant method is proposed to be applied in this case.

In part *I*, the relations between B_{tb} and B_g are constructed from equation 2.5.3. Besides, the fluxes passing from the front and the back of bridge to rotor yokes are expressed by:

$$\Phi_{tbf}=-Lh_{tb}B_{tb}(\theta_f)$$
$$\Phi_{tbb}=Lh_{tb}B_{tb}(\theta_b) \quad 2.5.8$$

Where the direction of the flux is defined to be from the tangential bridge to neighbouring yokes.

- ***Rotor tooth region***

In part *II*, similarly to the magnetic circuit described in the IM model, a new one from the stator to the rotor is constructed as:

$$F(\theta)=F_g(\theta)+F_{ts}(\theta)+\frac{1}{2}F_{ys}(\theta)+\frac{1}{2}F_r(\theta) \quad 2.5.9$$

Where F_g is the m.m.f. drop in the air-gap, F_{ts} is the m.m.f. drop in the stator tooth, F_{ys} is the m.m.f. drop in the stator yoke, and F_r is the m.m.f. drop in the rotor. The part of the magnetic circuit from the stator yoke to the stator tooth, and from the tooth to the air-gap is similar to the IM model. The calculations of $F_g(\theta)$, $F_{ts}(\theta)$, $F_{ys}(\theta)$ are the same as the ones in the IM model (see Subsection 2.4.3). The flux path is different in the rotor. The calculation of the m.m.f. drop in the rotor will be discussed as following.

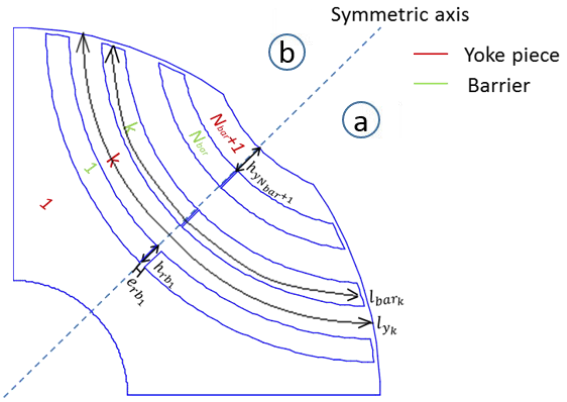

Figure 2.5.5 Number of rotor barriers and yoke pieces, assignment of some barrier dimensions, and decomposition of one pole by the symmetric axis

To simplify the analysis, the rotor is divided into two symmetric sections with the symmetric axis (q-axis): section a and b. As shown in Figure 2.5.5, the barriers and the teeth are numbered by the following symbols:

- N_{bar}: rotor barrier number per pole;
- y_1: the rotor yoke nearest to the shaft;
- rb_1: the barrier nearest to the shaft;
- $y_{N_{bar}+1}$: the rotor yoke farest to the shaft;
- $rb_{N_{bar}}$: the barrier farest to the shaft;
- y_k: the k_{th} rotor yoke (it is called as rotor tooth sometimes);
- rb_k: the k_{th} barrier.

And several dimensions about barriers and teeth are assigned as:

- e_{rb_k}: radial bridge width in the the k_{th} barrier (when a barrier is with two or more radial bridges, e_{rb_k} is the sum of all these bridge widthes);
- h_{rb_k}: the k_{th} barrier height;
- h_{y_k}: the k_{th} yoke height;
- l_{y_k}: mean arc perimeter of the k_{th} rotor yoke;
- l_{bar_k}: mean arc perimeter of the k_{th} barrier;
- $\theta_{fk+1,a}$: the angular position (at section a) of the front of the tangential bridge neighbouring the $k+1_{th}$ barrier (as shown in Figure 2.5.6);
- $\theta_{bk,a}$: the angular position (at section a) of the back of the tangential bridge at the k_{th} barrier.

The m.m.f. drop in the rotor F_r is described in Figure 2.5.6. In order to simplify the calculations, the m.m.f. drop F_r is assumed to be uniform within each yoke piece (the equi-potential hypothesis has been applied in the cross-section of the flux lines, see Figure 2.5.3 (b)). From Figure 2.5.6, the magnetic lines pass across half of the yoke piece, and penetrate the neighbouring radial bridges (for the barriers without radial bridge, the flux lines penetrate the air barriers uniformly). Then they pass though the yoke piece y_1, to the neighbouring pole rotor. For the angular position θ between k_{th} and $k+1_{th}$ air barrier and at section a, the m.m.f. drop in the rotor (as the green line in Figure 2.5.6) could be expressed by equation 2.5.10.

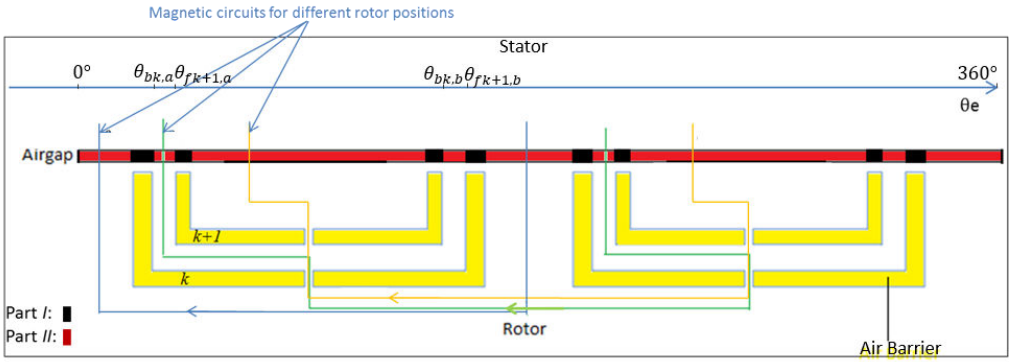

Figure 2.5.6 The magnetic circuits considered in the rotor yoke

$$\frac{1}{2}F_r(\theta) = \sum_{j=1}^{k} H_{rb_j} h_{rb_j} + \int_0^{\frac{l_{y_k}}{2}} H_{y_1}(x)dx + \int_{\frac{l_{y_k}}{2}}^{l_{y_k}} H_{y_{k+1}}(x)dx \qquad 2.5.10$$

$$(\theta_{bk,a} < \theta < \theta_{fk+1,a})$$

Where H_{rb_j} is the mean field intensity at the radial bridge of the j_{th} barrier, $H_{y_1}(x)$ is the field intensity at position x of the considered arc in the 1_{st} yoke piece, and $H_{y_{k+1}}(x)$ is the field intensity at position x of the considered arc in the $k+1_{th}$ yoke. The direction of the field intensity H_{rb} is considered as the radial direction from the inner to the outer face of the rotor, while the direction of H_y is considered as the tangential direction from section b to section a. The details about the x-axis and the magnetic field direction is indicated in Figure 2.5.7.

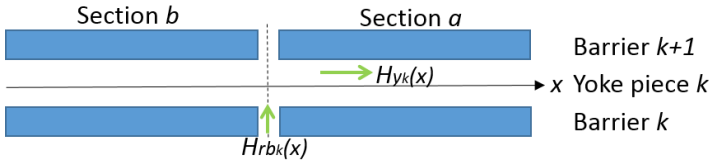

Figure 2.5.7 The definition of the magnetic field direction in the yokes and radial barriers

Similarly, for the angular position between k_{th} and $k+1_{th}$ air barrier and at section b, the m.m.f. drop in the rotor is defined as:

$$\frac{1}{2}F_r(\theta) = \sum_{j=1}^{k} H_{bar_j} h_{bar_j} - \int_0^{\frac{l_{y_k}}{2}} H_{y_k}(x)dx + \int_0^{\frac{l_{y_1}}{2}} H_{y_1}(x)dx \qquad 2.5.11$$

$$(\theta_{bk,b} < \theta < \theta_{fk+1,b})$$

For the angular position at 1_{st} rotor tooth and at section a (see the blue line in Figure 2.5.6), the m.m.f. drop F_r is deduced by equation 2.5.12.

$$\frac{1}{2}F_r(\theta) = \int_0^{\frac{l_{y_1}}{2}} H_{y_1}(x)dx \qquad (0° < \theta < \theta_{f1,a}) \qquad 2.5.12$$

For the angular position at 1_{st} rotor tooth and at section b, it is defined as:

$$\frac{1}{2}F_r(\theta) = \int_{\frac{l_{y_1}}{2}}^{l_{y_1}} H_{y_1}(x)dx \qquad (\theta_{b1,b} < \theta < 360°) \qquad 2.5.13$$

Now we discuss the methods to compute the field intensity in the yokes and the radial bridges. With conservation law applied in the $k+1_{th}$ tooth (yoke piece between barrier k and $k+1$), the relation between fluxes from different components is found in equation 2.5.14.

$$\Phi_{bar_{k+1}} - \Phi_{bar_k} = \Phi_{rb_k} - \Phi_{rb_{k+1}} - \Phi_{ag_k,a} - \Phi_{ag_k,b} + \Phi_{tbf_k,b} + \Phi_{tbf_{k+1},a} + \Phi_{tbb_k,a} + \Phi_{tbb_{k+1},b} \qquad 2.5.14$$

Where:

- Φ_{bar_k}: the flux passing through the k_{th} barrier, the direction is as defined in Figure 2.5.8;
- Φ_{rb_k}: the flux passing through the radial bridge in the k_{th} barrier;
- $\Phi_{ag_{k+1},a}$: the flux passing from the $k+1_{th}$ yoke at section a to the neighbouring air-gap;
- $\Phi_{tbf_k,b}$: the flux passing from the front of the tangential bridge in the k_{th} barrier to the yoke at section b;
- $\Phi_{tbb_k,a}$: the flux passing from the back of the tangential bridge in the k_{th} barrier to the yoke at part a.

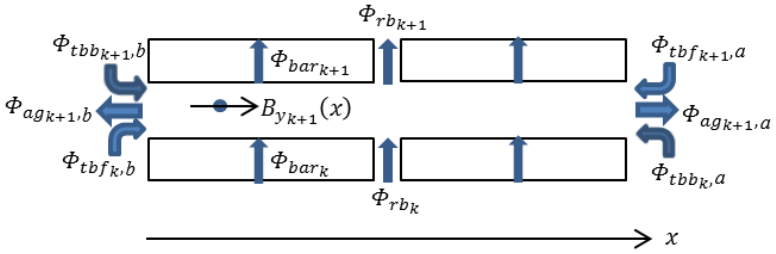

Figure 2.5.8 Flux distribution in the $k+1_{th}$ tooth

In a similar way, for the yoke piece N_{bar+1}, the relation between fluxes is:

$$-\Phi_{bar_{N_{bar}}} = \Phi_{rb_{N_{bar}}} - \Phi_{ag_{N_{bar}+1},a} - \Phi_{ag_{N_{bar}+1},b} + \Phi_{tbf_{N_{bar}},b} + \Phi_{tbb_{N_{bar}},a} \qquad 2.5.15$$

Combining equation 2.5.14-2.5.15, the differential relation between the fluxes passing through adjacent barriers could be resumed as:

$$A\begin{bmatrix}\Phi_{bar_{N_{bar}}}\\ \vdots \\ \Phi_{bar_1}\end{bmatrix} = B\begin{bmatrix}\Phi_{rb_{N_{bar}}}\\ \vdots \\ \Phi_{rb_1}\end{bmatrix} + C\begin{bmatrix}\Phi_{ag_{N_{bar}+1},a}\\ \vdots \\ \Phi_{ag_2,a}\end{bmatrix} + D\begin{bmatrix}\Phi_{ag_{N_{bar}+1},b}\\ \vdots \\ \Phi_{ag_2,b}\end{bmatrix} + E\begin{bmatrix}\Phi_{tbf_{N_{bar}},a}\\ \vdots \\ \Phi_{tbf_1,a}\end{bmatrix} + F\begin{bmatrix}\Phi_{tbf_{N_{bar}},b}\\ \vdots \\ \Phi_{tbf_1,b}\end{bmatrix} + G\begin{bmatrix}\Phi_{tbb_{N_{bar}},a}\\ \vdots \\ \Phi_{tbb_1,a}\end{bmatrix} + H\begin{bmatrix}\Phi_{tbb_{N_{bar}},a}\\ \vdots \\ \Phi_{tbb_1,a}\end{bmatrix} \quad 2.5.16$$

Where A, B, C, D, E, F, G, H are constant square matrices which could be deduced from equation 2.5.14-2.5.15.

The expressions of flux Φ_{tbf} and Φ_{tbb} can be found in equation 2.5.8. And the flux Φ_{ag} is deduced from the air-gap induction:

$$\Phi_{ag_{k+1},a} = L\frac{D_{ag}}{2}\int_{\theta\subset\theta_{ag_{k+1},a}} B_g(\theta)\,d\theta \quad 2.5.17$$

With the equi-potential hypothesis imposed in each barrier and its adjacent radial bridge, the relation between the induction in the air barrier $B_{bar_k}$and the radial bridge B_{rb_k} is deduced in equation 2.5.18. This hypothesis is validated by the numerical analysis, as shown in Figure 2.5.3 (b).

$$BH^{-1}\left(B_{rb_k}\right) = \frac{B_{bar_k}}{\mu_0} \quad 2.5.18$$

And the flux Φ_{bar_k} and Φ_{rb_k} could be expressed by:

$$\Phi_{bar_k} = L(l_{bar_k} - e_{rb_k})B_{bar_k}$$
$$\Phi_{rb_k} = Le_{rb_k}B_{rb_k} \quad 2.5.19$$

The induction vector $\left[B_{rb_{N_{bar}}} \cdots B_{rb_1}\right]$ is set as the variables in the analytical model.

Always keep in mind that we want to calculate the m.m.f. drop F_r. The field intensity in the radial bridge $H_{rb_k}$is found from equation 2.5.18-2.5.19. Now we give the expressions of the induction in the yokes. With flux conservation law and equipotential hypothesis applied in the cross--section of the position x in the $k+1_{th}$ yoke, the yoke induction $B_{y_{k+1,a}}(x)$ (the position is at section *a*) is expressed by equation 2.5.20.

$$B_{y_{k+1,a}}(x)Lh_{y_{k+1}} = -\Phi_{tbb_k,a} - \Phi_{tbf_{k+1},a} + \Phi_{ag_{k+1},a} \quad 2.5.20$$

$$-L\int_{x}^{l_{bar_k}} B_{bar_k}\,dl + L\int_{x}^{l_{bar_{k+1}}} B_{bar_{k+1}}\,dl$$

Similarly, the yoke induction $B_{y_{k+1,b}}(x)$ (the position is at section *b*) is deduced as:

$$\begin{aligned} B_{y_{k+1,b}}(x)Lh_{y_{k+1}} &= \Phi_{tbf_k,b}+\Phi_{tbb_{k+1},b}-\Phi_{ag_{k+1},b} \\ &+L\int_{0}^{x} B_{bar_k}\,dl - L\int_{0}^{x} B_{bar_{k+1}}\,dl \end{aligned} \quad 2.5.21$$

The induction in the first yoke $B_{y_{1,a}}(x)$ (the position is at section *a*) is deduced as:

$$B_{y_{1,a}}(x)Lh_{y_1} = -\Phi_{tbf_k,b}+\Phi_{ag_1,a} + L\int_{x}^{l_{bar_1}} B_{bar_1}\,dl \quad 2.5.22$$

And the induction $B_{y_{1,b}}(x)$ (the position is at section *b*) is deduced as:

$$B_{y_{1,b}}(x)Lh_{y_1} = \Phi_{tbb_1,a}-\Phi_{ag_1,b} - L\int_{0}^{x} B_{bar_1}\,dl \quad 2.5.23$$

The induction in the last yoke $B_{y_{N_{bar}+1}}(x)$ (the position is at section *a*) is deduced by equation 2.5.24.

$$B_{y_{N_{bar}+1}}(x)Lh_{y_1} = -\Phi_{tbb_{N_{bar}},a}+\Phi_{ag_{N_{bar}+1},a} - L\int_{x}^{l_{bar_{N_{bar}}}} B_{bar_{N_{bar}}}\,dl \quad 2.5.24$$

And the induction $B_{y_{N_{bar}+1}}(x)$ (the position is at section *b*) is deduced as:

$$B_{y_{N_{bar}+1}}(x)Lh_{y_1} = \Phi_{tbf_{N_{bar}},b}-\Phi_{ag_{N_{bar}+1},b} + L\int_{0}^{x} B_{bar_{N_{bar}}}\,dl \quad 2.5.25$$

With equation 2.5.20-2.5.25 and the given magnetic property, the field intensity in all the yokes are described.

2.5.3 Solution of the electromagnetic model

The rotor is divided into two parts. In part *I*, the relationship between the inductions in the air-gap and the adjacent tangential bridge are considered. Then the differential equation (equation 2.5.6) with the variable induction in the tangential bridge is deduced. The boundary conditions (equation 2.5.7) gives the relation between the induction in part *I* and part *II*. The differential equation is applied in a discrete way. Each tangential bridge is divided into K_{tb} segments along the tangential direction. Within each segment, the induction is assumed to be uniform. The inductions in the tangential bridge are set as variables, which means that there are $2K_{tb}N_{bar}$ variables in part *II*. With the differential equation, $2(K_{tb}-2)N_{bar}$ equations are constructed. And with the limit conditions, $4N_{bar}$ equations are constructed.

In part *II*, the relations between the air-gap and the exciting m.m.f. are constructed. Similarly to the IM model, the pole arc is divided into *K* segments. The air-gap inductions are set as variables. As the nonlinear relations are sophisticated (with many integrations and nonlinear operators), the induction in the radial bridge $\left[B_{rb_{N_{bar}}} \cdots B_{rb_1}\right]$ are added as the variables to accelerate the solving time. There are $K + N_{bar}$ variables in part *II*. With equation 2.5.10-2.5.25, $K + N_{bar}$ equations could be constructed.

In the analytical model, the motor geometry and control parameters ($\hat{\imath}_s, \omega_s$ and α) are set as inputs. The model will be solved by numerical methods. When the system is solved, the induction in the air-gap and the tangential bridge are deduced. Besides, the induction distribution in the stator and rotor yokes can be deduced as well. From equations 2.5.1, the magnetic flux along *d* and *q* axis should be deduced in order to estimate the electromagnetic behaviours. They could be expressed by the air-gap induction distribution:

$$\begin{aligned} \hat{\Psi}_{md} &= \frac{2n_s k_{w1} D_{ag} L}{\pi p} \int_0^{\pi} B_g(\vartheta) cos(\vartheta)\, d\vartheta \\ \hat{\Psi}_{mq} &= \frac{2n_s k_{w1} D_{ag} L}{\pi p} \int_0^{\pi} B_g(\vartheta) sin(\vartheta)\, d\vartheta \end{aligned} \qquad 2.5.26$$

When the rotation speed and the torque are specified, the input variables are chosen as the motor geometry, the current angle α, the electrical pulsation ω_s and the required torque. Except the $(2K_{tb}+1)N_{bar} + K$ variables, the feeding current amplitude $\hat{\imath}_s$ is added as variable.

In this section, the electromagnetic model of SynRM was discussed. The *dq* phasor is applied in the model, and the air-gap induction distribution is required to deduce the electrical behaviours. Similarly to the IM model, the nonlinear relations between the air-gap induction and the exciting m.m.f. are constructed. Besides, the relations between the tangential bridge induction, the exciting m.m.f. and the air-gap induction are established. The model is solved by numerical methods. Compared with the IM model, the computation time is larger as the variable number is higher in the tangential bridge region and the yoke region. And it takes much more time to solve the nonlinear differential equation. The slot opening and winding harmonic orders are neglected in the analytical model ([BBBD09]), the computed torque is considered as an average torque, and the torque distortion could not be estimated. The calculation of the motor losses will be discussed in Section 2.6.

This analytical model is applicable for several types of rotor geometry:

- Rotors with or without air-gap open angles;
- Rotors without tangential bridges or with several tangential bridges per barrier;
- Rotors with different numbers of barriers per pole.

The validations of the model applied in different kinds of rotors will be presented in the next chapter.

2.6 Loss model of traction system

In this section, a model to evaluate most of the energy losses in the power train of VE is presented. The total energy losses in the traction system are made up with losses in different power components including:

- Losses in the power converter
- Losses in the conducting wires (conduction losses)
- Losses in the studied electric motors

Analytical formulas to estimate steady state losses in each component will be detailed in the following sections. Steady state indicates that the motor rotates at a constant speed.

2.6.1 Losses in the power converter

As mentioned in the introduction, the EM is fed by a three-phase PWM converter (as shown in Figure 2.6.1). Usually, a 3-phase power converter is composed by six IGBT modules and six diodes. It is supplied by a d.c. battery with voltage V_{DC}, and the output current i_a and voltage U_{ab} are supposed to be sinusoidal (fundamental wave considered). Some basic principles of power converters are presented hereafter.

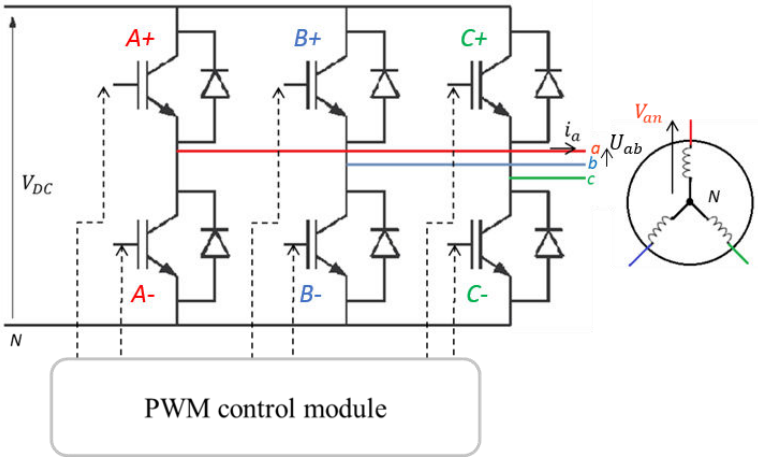

Figure 2.6.1 Electric scheme of the power converter

PWM, or pulse-width modulation, is widely used in the motor control. In PWM control, a rectangular pulse wave is modulated, which results in the variation of the average value of the waveform. The PWM signal is generated by the intersect method, in which a carrier wave (triangle waveform curve in blue in Figure 2.6.2 (a)) and a comparator (reference signal in red) are required. When the value of the reference signal is higher than the modulation amplitude, the modulated PWM signal is in the high state ("1"), otherwise it is in the low state ("0"), as shown in Figure 2.6.2 (a). In power electronics, the frequency of this carrier wave f_c is defined as the sampling frequency, the ratio m between the carrier wave amplitude and the reference signal amplitude V_{ref} is called modulation depth, and the ratio r between f_c and the frequency of reference signal is called modulation index. To assure the normal operation of the converter, the sampling frequency should be much higher than the reference signal frequency, which means the modulation index should be much higher than 1. The above principles work on one interruptor, the state of other interrupters should be considered in a three-phase inverter. The upper and

lower interruptors in the same phase switch alternatively: 0 if the phase winding connects to the negative potential (e.g. A+ off and A- on), else 1 (e.g. A+ on and A- off). For the three-phase inverter, there are eight possible logical states. However, the states that all phase windings are on the negative and positive potentials, are the default states. Six effective states exist in the inverter control, this kind of control method are so-called space vector modulation ([HABO90]). For example, the state vector [0 0 1] represents that A-, B- and C+ is on. Similarly as Subsection 2.3.3, we define a voltage vector $\vec{u} = u_a\vec{a} + u_b\vec{b} + u_c\vec{c}$ under the stator-fixed $\alpha\beta$ coordinator. As shown in Figure 2.6.2 (b), there are six basic state vectors, and the reference signal in each phase interruptors could be represented by a voltage vector $\vec{u}_{ref}$ under the same frame. Figure 2.6.2 (c) shows some typical signal curves in the three-phase motor drive. The details of the space vector modulation could be found in [YUFI98] [GIRI13].

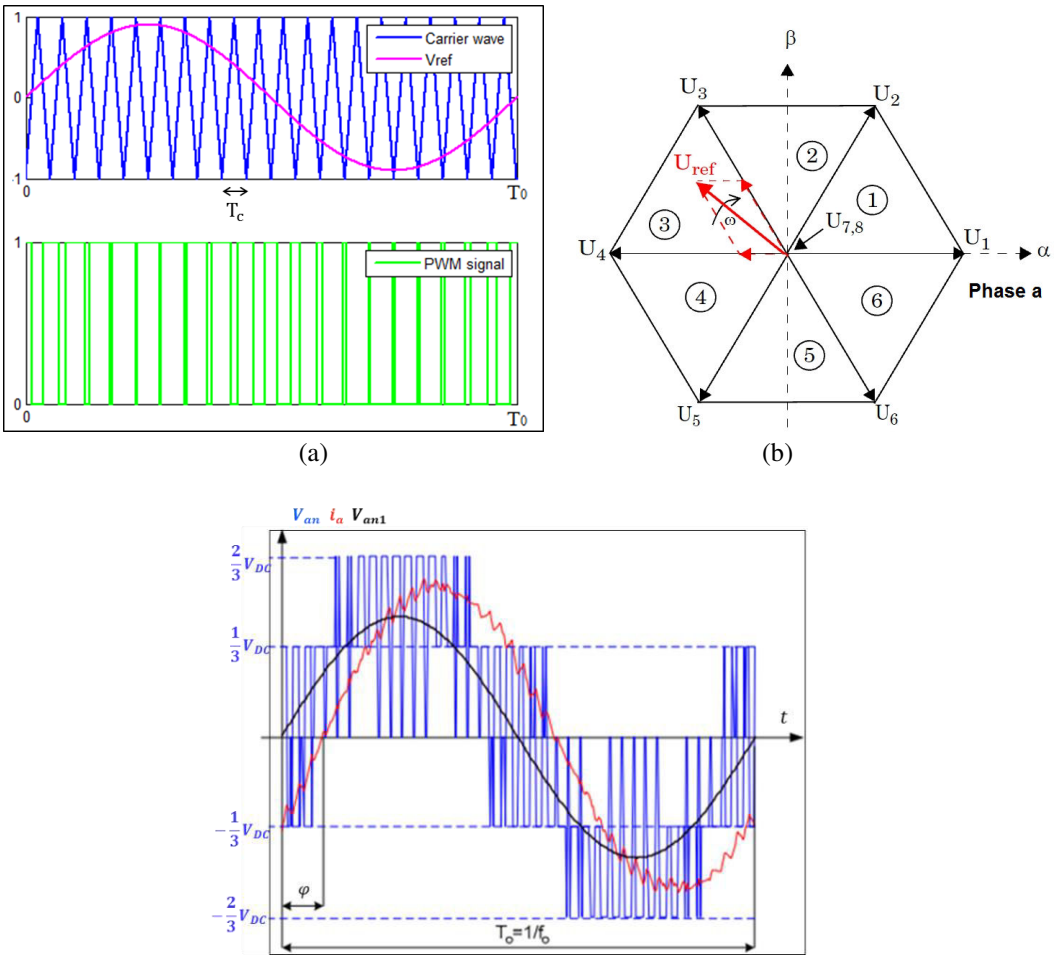

(a) (b)

(c)

Figure 2.6.2 (a) Generation of the PWM pulse corresponding to a given signal by a simple intersected PWM over one interruptor (b) general scheme of space vector control on three-phase inverter ([GIRI13]) (c) three-phase AC motor drive – typical signals

In our case, the fundamental of the output voltage should be lower than V_{DC}. And the nominal current and voltage are considered as the fundamentals of modulated waves. The modulation index should be no less than 10 (*e.g*: the carrier wave frequency should be higher than 500 Hz

for a four-pole IM rotates at 1500 *rpm*). Before introducing the loss model, several electrical parameters in the converter are defined:

Output phase current: $i_a(t) = \hat{I}sin(\omega_0 t - \varphi)$

Reference voltage: $V_{ref}(t) = V_{an1}(t) = msin(\omega_0 t)$

IGBT turn-on and turn-off state function: $\tau_{IGBT}(t) = \frac{1}{2}\left(1 + V_{ref}(t)\right) = \frac{1}{2}\left(1 + msin(\omega_0 t)\right)$

On-state voltage of IGBT: $v_{CE}(t) = V_{CE0} + R_{CE} i(t)$

Diode turn-on and turn-off state function: $\tau_D(t) = \frac{1}{2}\left(1 - V_{ref}(t)\right) = \frac{1}{2}\left(1 - msin(\omega_0 t)\right)$

On-state voltage of diode: $v_D(t) = V_{D0} + R_D i(t)$

Where V_{CE0} is the maximum collector-emitter voltage under "open" state, and R_{CE} is collector-emitter resistance. These characteristic parameters of IGBTs are influenced by operating temperatures. Similarly, V_{D0} indicates the diode threshold voltage, and R_D indicates the diode junction resistance.

Function τ is the IGBT state function. When IGBT is turned on, τ is assigned as unit, otherwise τ assigned as zero. From the sampling theorem ([TRZY10]), the state function can be regarded as the extrapolation from the intersection of the carrier wave with reference voltage V_{ref}.

The power dissipated in the converter comes from the imperfection of components: IGBTs and diodes.

- ***Power dissipated in the IGBT***

The power dissipated by IGBTs is mainly from conduction and switching losses ([INFI06]). The conduction losses occur when the IGBT conducts. And the calculation of these losses is deduced in equation 2.6.1.

$$P_{cond\_IGBT} = \frac{1}{T_0}\int_0^{\frac{T_0}{2}} v_{CE}(t)\, i_a(t)\tau_{IGBT}(t)dt = \frac{\hat{I}}{2}\left(\frac{V_{CE0}}{\pi} + R_{CE}\frac{\hat{I}}{4}\right) + m\hat{I}cos\varphi\left(\frac{V_{CE0}}{8} + \frac{R_{CE}\hat{I}}{3\pi}\right) \quad 2.6.1$$

From equation 2.6.1, the IGBT conduction losses are determined by the modulation depth, the output phase current amplitude and the output power factor of the converter.

Switching losses of IGBT are generated at the state of switching instants. They can be expressed as the integration of all turn-on and turn-off energies:

$$P_{sw\_IGBT} = \frac{f_c}{T_0}\int_0^{\frac{T_0}{2}} \left(W_{on}(t,\hat{I}) + W_{off}(t,\hat{I})\right) dt \qquad 2.6.2$$

From the measured turn-on and turn-off energy dissipation per switching pulse, the energy of the single switching event is assumed to be linear with output current (± 20% error). As a result, the switching losses could be estimated from the nominal switching energy W_{on_IGBT}, W_{off_IGBT} at nominal output current I_{nom} (given in the component datasheet). Then the final expression of switching losses could be found in equation 2.6.3.

$$P_{sw\_IGBT} = \frac{rf_c}{\pi}\frac{V_{DC}\hat{I}}{V_{nom}I_{nom}}\left(W_{on\_IGBT} + W_{off\_IGBT}\right) \qquad 2.6.3$$

From equation 2.6.3, the switching losses in IGBT depend on the output current amplitude and the modulation index. Finally, the total losses dissipated in an IGBT are the sum of these two losses:

$$P_{IGBT} = P_{cond\_IGBT} + P_{sw\_IGBT} \qquad 2.6.4$$

- ***Power dissipated in the diode***

The power dissipated in a diode comes from conduction and switching losses as well. The conduction losses are deduced in equation 2.6.5.

$$\begin{aligned} P_{cond\_D} &= \frac{1}{T_0}\int_0^{\frac{T_0}{2}} v_D(t)i(t)\tau_D(t)dt \\ &= \frac{\hat{I}}{2}\left(\frac{V_{D0}}{\pi} + \frac{R_D\hat{I}}{4}\right) - m\hat{I}\cos\varphi\left(\frac{V_{D0}}{8} + \frac{R_D\hat{I}}{3\pi}\right) \end{aligned} \qquad 2.6.5$$

And the switching losses in a diode are expressed by the following formula when the turn-on energy losses of diodes are negligible:

$$P_{sw\_D} = \frac{rf_c}{\pi}\frac{V_{DC}}{V_{nom}}W_{rec}(\hat{I}) \qquad 2.6.6$$

For the diode, the turn-off energy at a certain current is estimated by the following equation:

$$W_{rec}(\hat{I}) = W_{rec\_D}\left(0.45\frac{\hat{I}}{I_{nom}} + 0.55\right) \qquad 2.6.7$$

Where W_{rec_D} represents the diode recovery energy at nominal current. In equation 2.6.7, the constant coefficients may vary for different types of diode. And the final expression of switching losses in a diode should be:

$$P_{sw\_D} = \frac{rf_c}{\pi}\frac{V_{DC}}{V_{nom}}W_{rec\_D}\left(0.45\frac{\hat{I}}{I_{nom}} + 0.55\right) \qquad 2.6.8$$

The total losses of a diode are the sum of these two kinds of losses:

$$P_D = P_{cond\_D} + P_{sw\_D} \tag{2.6.9}$$

The total losses in the power converter are made up by all these losses:

$$P_{inv} = 6(P_{IGBT} + P_D) \tag{2.6.10}$$

This analytical model gives approximate calculations of steady-state conduction and switching losses of IGBT and inverse diodes in the power converter.

2.6.2 Conduction losses

The conduction losses are defined as the sum of copper losses in all the conducting wires, such as in the conducting cables between the converter and the motor, and the ones between the battery and the converter. D.c. and a.c. losses in the cables are both included.

$$\begin{aligned} P_{cond} &= P_{cond\_dc} + P_{cond\_ac} \\ &= \rho_{Cu} \frac{l_{dc}}{S_{dc}} {I_{dc}}^2 + K_{se} \rho_{Cu} \frac{l_{ac}}{4S_{ac}} \hat{I}^2 \end{aligned} \tag{2.6.11}$$

Where:

- l_{dc}, S_{dc}: the total length and effective cross section area of conducting wires passing through d.c. currents;
- l_{ac}, S_{ac}: the total length and effective cross section area of conducting wires passing through a.c. currents;
- I_{dc}, $\hat{I}$: the amplitudes of d.c. and a.c. currents;
- ρ_{Cu}: the resistivity of copper;
- K_{se}: the skin effect coefficient for a conducting wire containing n identical conductors ([GREL89]):

$$k_R = \lambda \frac{\sinh(2\lambda) + \sin(2\lambda)}{\cosh(2\lambda) - \cos(2\lambda)} + 2\lambda^2 \frac{n^2 - 1}{3} \frac{\sinh(2\lambda) - \sin(2\lambda)}{\cosh(2\lambda) + \cos(2\lambda)} \tag{2.6.12}$$

Where λ is the reduced height of conductor ($\lambda = \frac{h}{\delta}$), in which h is the conductor height and δ is the skin depth:

$$\delta = \frac{1}{\sqrt{\sigma_{Cu} \mu_{Cu} \pi f}} \tag{2.6.13}$$

Where σ_{Cu} and μ_{Cu} are the conductivity and permeability of copper, and f the ac current frequency.

As the resistivity (conductivity) of material is influenced by temperature, the conduction losses increase while the ambient temperature arises. Proper electrical and thermal design helps reducing conduction losses and avoiding overheating in the traction system.

2.6.3 Losses in electric machines

From [BONA10], the total losses in EMs are made up by three kinds of losses which determine the efficiency of energy conversion of the motor:

- Winding losses

Winding losses, or copper losses, occur in motor windings as a result of electrical feeding and field penetration. They are assumed to be major part of motor losses at low and medium rotation speeds when the iron and friction losses are relatively low. In order to prevent important penetration and proximity effects at high rotation speed, motor designers should take care in choosing the winding wire number and diameter ([GREL89]). Litz wires could be designed to reduce skin effect losses and proximity effect losses in conductors used at frequencies up to around 1MHz.

- Iron losses

Iron losses, or core losses, are defined as the power that the core dissipates when imposing a changing magnetic field. The losses are often assumed to be in three categories ([BOCL11]):

1) Hysteresis losses – Losses due to the hysteresis in ferromagnetic materials.
2) Eddy current losses – Losses due to the eddy current induced in cores.
3) Excess losses – This category includes any losses in addition to hysteresis and eddy current losses. It is more difficult to estimate excess losses than the other two items.

In industry, core pieces are usually laminated to reduce eddy current losses.

- Mechanical losses

Mechanical losses include friction losses and windage losses:

1) Friction losses – Losses generated by the friction force between rotor and shaft.
2) Windage losses – Losses generated by the friction force between air and the rotor in the air-gap. This losses depend essentially on the type of cooling system applied. This item should be considered in air cooling system, while it could be taken off with other kinds of cooling system. In our case, the air cooling system is common according to the machine power range ([BONA10]).

The losses in the motor are defined as the sum of these three losses:

$$P_m = P_{wind} + P_{core} + P_{mech} \qquad 2.6.14$$

In this section, the analytical models to calculate the total losses in IMs and SynRMs will be discussed separately.

I. Induction motor

- ***Winding losses***

For IMs, the winding losses include copper losses in the stator windings, and in the rotor cages. With the help of lumped parameters, the winding losses are expressed in equation 2.6.15.

$$P_{wind\_IM} = \frac{3}{2}\left(R_s \hat{\imath}_s{}^2 + R_r' \hat{\imath}_r'{}^2\right) \qquad 2.6.15$$

The stator and rotor phase resistances, R_s and $R_r{}'$ were described in Section 2.4. $\hat{I}_s$ and $\hat{I}_r{}'$ are amplitudes of stator and rotor phase currents.

- ***Core losses***

Core losses are the total iron losses in the machine, including stator teeth and yokes, rotor teeth and yokes. Boglietti in [BCLP03] proposed an analytical model to calculate iron losses in a piece of iron for a sinusoidal induction:

$$\begin{aligned} P_{iron} &= k_H f \hat{B}^{\alpha_{ir}+\beta_{ir}\hat{B}} + k_{ec} f^{1.5} \hat{B}^2 \frac{\sinh\left(\gamma\sqrt{f}\right) - \sin\left(\gamma\sqrt{f}\right)}{\cosh\left(\gamma\sqrt{f}\right) - \cos\left(\gamma\sqrt{f}\right)} + k_{exc} f^{1.5} \hat{B}^{1.5} \\ &= P_{hys} + P_{ec} + P_{exc} \end{aligned} \qquad 2.6.16$$

Where f indicates the induction frequency, $\hat{B}$ indicates the induction amplitude, and the unit of P_{iron} in equation 2.6.16 is $[W/kg]$. The left parameters are assumed to be constant for a defined material, k_H, α_{ir} and β_{ir} refer to the hysteresis loss (P_{hys}) coefficients, k_{ec} refers to eddy current loss (P_{ec}) coefficient, and k_{exc} refers to excess loss (P_{exc}) coefficient. The value of these parameters for material M330-35 are identified in the following Table 2.6.1.

Parameter	k_H	α_{ir}	β_{ir}	k_{EC}	γ	k_{EXC}
Value	0.022	2	0	0.3873	6.04e-4	0

Table 2.6.1 Value of iron loss parameters for material M330-35

The influences of induction frequency and amplitude on precision of equation 2.6.16 are shown in Figure 2.6.3. The relative error of analytical formula is between -35% and +12%. For an induction distribution with lower frequency and lower amplitude, the relative error seems to be higher than inductions with high frequency and high amplitude. As the relation between them is not absolutely linear, the error could not be compensated by one simple correction coefficient. A curve fitting method may be applied to correct it. And this error is assumed as excess losses which has not been considered in the formula (k_{exc}=0).

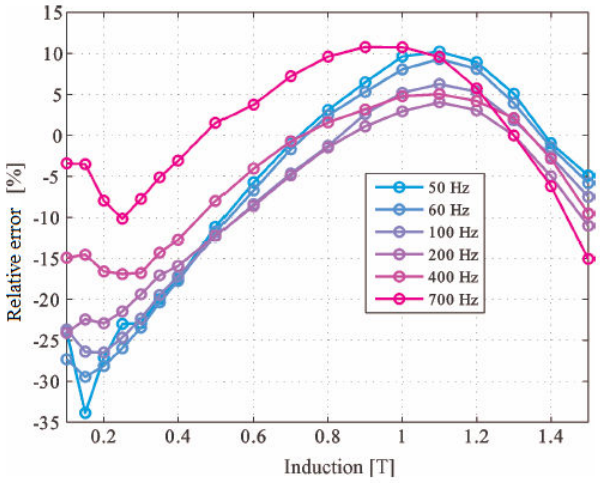

Figure 2.6.3 Influences of induction frequency and amplitude on the precision of the formula to calculate iron losses ([JANN10])

In order to calculate core losses, the induction distributions in the teeth and yokes are required. They are deduced from equation 2.4.35 and 2.4.38, with the awareness of the air-gap induction distribution. That means the core loss calculation is a post-operation of electromagnetic modelling.

As a result of the magnetic saturation, the induction distribution in the cores is not sinusoidal. The author in [JANN10] has proposed a method to consider the influence of the saturation. This method is based on the equation 2.6.16, the eddy current losses of different induction harmonic order are accumulated after the induction distribution was decomposed by FFT (Fast Fourrier Transformation). The hysteresis losses are determined by the induction amplitude. This method has been validated by *Loss Surface* (a numerical tool to calculate iron losses which is incorporated with "FLUX2D" [GAUT05]), equation 2.6.16 is transformed into (for M330-35, the excess losses are neglected):

$$P_{iron} = k_H f \hat{B}^{\alpha_{ir}+\beta_{ir}\hat{B}} + k_{ec} \sum_{h=1}^{\infty} (hf)^{1.5} \hat{B}_h{}^2 \frac{\sinh\left(\gamma\sqrt{hf}\right) - \sin\left(\gamma\sqrt{hf}\right)}{\cosh\left(\gamma\sqrt{hf}\right) - \cos\left(\gamma\sqrt{hf}\right)} \qquad 2.6.17$$

$$= P_{hys} + P_{ec}$$

Where h represents the harmonic order, and $\hat{B}_h$ the amplitude of induction in h_{th} order, and the other parameters are the same with those in equation 2.6.16. Equation 2.6.17 is applied on the stator teeth and yokes, rotor teeth and yokes. The core losses are expressed by:

$$P_{core} = P_{iron}(f_s, B_{ds})m_{ds} + P_{iron}(f_s, B_{ys})m_{ys} + P_{iron}(f_r, B_{dr})m_{dr} + P_{iron}(f_r, B_{yr})m_{yr} \qquad 2.6.18$$

Where the fundamental frequency in stator cores is equal to the feeding frequency, and the fundamental frequency in rotor depends on slip ratio ($f_r = sf_s$). $B_{ds}, B_{ys}, B_{dr}, B_{yr}$ are induction distribution in stator teeth and yokes, rotor teeth and yokes, $m_{ds}, m_{ys}, m_{dr}, m_{yr}$ are the mass of stator teeth and yokes, rotor teeth and yokes respectively.

Authors in [BCIP10] has investigated the influence of non-sinusoidal feedings from PWM converter on iron losses, and has proposed a formula to take it into consideration:

$$P_{iron\_PWM} = \eta^{\alpha_{ir}} P_{hys} + \chi^2 P_{ec}$$
$$\text{With } \eta = \frac{V_{av}}{V_{av,fond}}, \chi = \frac{V_{rms}}{V_{rms,fond}} \quad 2.6.19$$

P_{hys}, P_{ec} are hysteresis and eddy current losses calculated from equation 2.6.17 with sinusoidal feeding assumption. η is the ratio between average value of converter output phase voltage (V_{av}) and that of fundamental voltage $V_{av,fond}$. χ is the ratio between RMS value of converter output phase voltage and that of fundamental voltage. The research work of Dr. Jannot ([JANN10]) has proved that the two ratios χ, η are determined by the modulation depth and indice. With the modulation depth fixed, the reduction of the modulation indice decreases values of χ and η. With the modulation indice fixed, the reduction of the modulation depth decreases χ but increases η, which means that hysteresis losses decline and eddy current losses raise. From this conclusion, designers could optimize motor iron losses by adjusting modulation depth and indice. When the modulation indice is assigned to be unit, both two ratios approach to one.

- ***Mechanical losses***

As the air cooling system is applied in the traction system, the windage losses should be considered. They can be found in the following formula proposed by [VRAN68]:

$$P_{windage} = \frac{1}{2} \frac{\rho_{air} S_{air} {V_p}^3}{\eta_{air}} \quad 2.6.20$$

Where:
- η_{air}: the ventilator efficiency, which depends on the flow type (laminar or turbulent);
- ρ_{air}: the air density;
- S_{air}: the rotor surface area in contact with the air-gap;
- V_p: the rotor peripheral speed.

The losses from the frictions between the rotor and the shaft, are included in the analytical model as well. This item could be supposed as the mechanical power due to the viscous resistant torque, as shown in the following equation.

$$P_{fric} = T_r \Omega = C_v \Omega^2 \quad 2.6.21$$

Where C_v is the viscous friction coefficient, Ω is the angular velocity of the rotor with unit *rad/sec* and R_r the external radius of rotor. Here we take the hypothesis that the viscous friction coefficient of IM is identical with the one in a reference motor.

The mechanical losses are defined as the sum of windage losses and friction losses:

$$P_{mech} = P_{windage} + P_{fric} \quad 2.6.22$$

The constant parameters appeared in equation 2.6.20-2.6.21 are detailed in the following table.

Parameter	Value
η_{air}	65%
C_v [N·m·s/rad]	0.00109
ρ_{air} [kg/m³]	1

Table 2.6.2 Value of constant parameters appeared in mechanical loss calculation

II. Synchronous reluctance motor

- ***Winding losses***

Unlike IMs, SynRMs generate electromagnetic torque through the phenomenon of magnetic reluctance. There are no copper losses in the rotor, and only the stator copper losses are counted.

$$P_{w\_IM} = \frac{3}{2} R_s \hat{i}_s^{\,2} \tag{2.6.23}$$

- ***Core losses***

The calculation of core losses in SynRM stator are similar to the one in IM stator (see equation 2.6.16-2.6.19).

From [GREL89], eddy current loops in rotor yokes are induced by space harmonic magnetic field due to stator slots and rotor barriers. Eddy current losses in the rotor are defined. Firstly, the skin effect depth of rotor yokes is defined as:

$$\delta_{shm} = \frac{1}{2\pi} \sqrt{\frac{10^7}{\sigma_{shm} \mu_{shm} f_{slot}}} \tag{2.6.24}$$

Where σ_{shm} and μ_{shm} are conductivity and permeability of sheet metal, and f_{slot} is the stator slot geometry variation frequency on rotor:

$$f_{slot} = \frac{V_p}{\tau_{sl}} = \frac{\frac{2\pi N_{rot}}{60} \frac{D_g}{2}}{\frac{2\pi}{n_e} \frac{D_g}{2}} = \frac{N_{rot} n_e}{60} \tag{2.6.25}$$

Where:

-V_p: rotor peripheral speed;

-τ_{sl}: stator slot pitch;

-N_{rot}: rotor rotation velocity [*tr/min*];

-D_g: average diameter of the air-gap;

-n_e: stator slot number.

In the analytical model, only eddy current losses are considered:

$$P_{iron\_SynRM\_rot} = 2pK_s K_s' V_p^{\,1.5} \tau_{sl} \sum_{j=1}^{2n_{barr}+1} \left(B_{g_{av}}(j)\right)^2 S_{yr}(j) \tag{2.6.26}$$

Where:

-p: pole pair number;

-n_{barr}: barrier number per pole;

-K_s: metal sheet skin effect coefficient: $K_s = \frac{1}{32\pi}\sqrt{\frac{10^7\sigma_{shm}}{\mu_{shm}}}$;

-$B_{g_{av}}(j)$: average induction in the air-gap with positions facing to j_{th} piece of yoke;

-$S_{yr}(j)$: cross section of j_{th} piece of yoke, which is perpendicular with radial direction;

-K_s': metal sheet lamination coefficient, and could be expressed by the following polynomial based on the ratio X between the lamination thickness e_{shm} and the yoke skin effect depth δ_{shm}:

$$K_s' \cong 0.015 - 0.023X + 0.044X^2 - 0.0065X^3 + 3.9e^{-4}X^4 - 9.3e^{-6}X^5 + 2.92e^{-8}X^6 \quad 2.6.27$$

$$\text{With } X = \frac{e_{shm}}{\delta_{shm}}$$

The following figure shows that K_s' increases with ratio X when the value of X is not too high, rotor with a thinner yoke consumes less iron losses. Analytical formula in 2.7.26-27 to consider iron losses in the rotor of SynRM has been validated by Dr. Prieto in his thesis work [PRIE15]. And the error is between +31% and +32%.

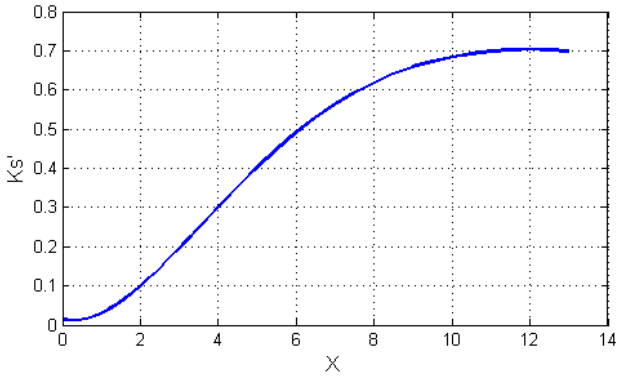

Figure 2.6.4 Relation between ratio X and coefficient K_s'

- ***Mechanical losses***

Since the SynRM is designed with similar air cooling system with the IM (the same power specifications imposed on the two kinds of EMs), the mechanical losses could be expressed by the same formulas with IM (see equation 2.6.20-2.6.22).

The loss models of IMs and SynRM were developed in this subsection. The analytical formulas of the winding losses, the core losses and the mechanical losses were described separately.

2.6.4 Definition of energy efficiency of system

The power transmission chain in the traction system is presented in Figure 2.6.5: the EM working at motor mode is with solid lines, and at generator mode with dashed lines. The system

energy efficiency is defined as the ratio between the useful mechanical power absorbed by gear side and the total energy power consumed by the system (torque and rotation speed given):

$$P_{loss}(T_{em},\Omega) = P_{inv} + P_{cond} + P_{iron} + P_{wind}$$
$$\eta_{sys}(T_{em},\Omega) = \frac{T_{em}\Omega - P_{mech}}{P_{loss}(T_{em},\Omega) + T_{em}\Omega} \quad 2.6.28$$

Where T_{em} is the electromagnetic torque provided by the motor, Ω is the rotor velocity, and $P_{loss}(T_{em},\Omega)$ is the total energy losses at some working point. The energy efficiency over the driving cycle is defined as the average efficiency at all the working points of the driving specification:

$$\eta_{dc} = \frac{\sum_{j=1}^{N_{wp}}(T_{emj}\Omega_j - P_{mechj})w_j}{\sum_{j=1}^{N_{wp}}(P_{lossj}(T_{emj},\Omega_j) + T_{emj}\Omega_j)w_j} \quad 2.6.29$$

Where N_{wp} is the total number of working points in the driving cycle (which will be served in Chapter 4), (T_{emj},Ω_j) represents j_{th} working point in the cycle considered, and w_j is the weight of the j_{th} working point.

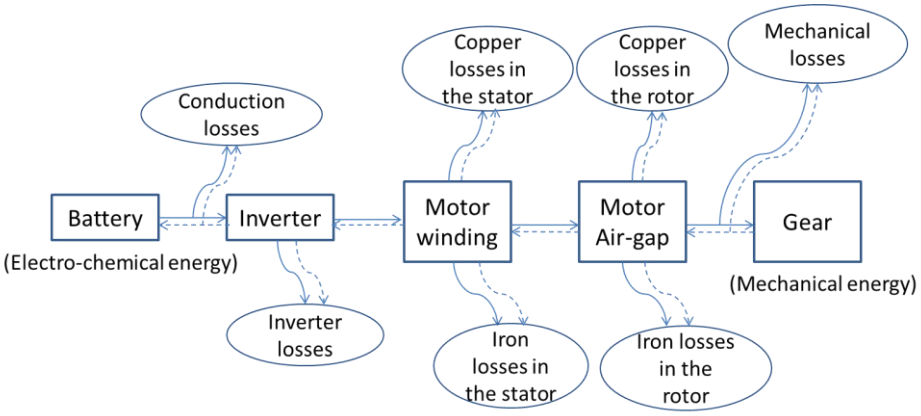

Figure 2.6.5 Power transmission in the traction system

In this section, an analytical method to quantify steady-state losses occurring in the inverter, in the conducting wire and in the motors has been discussed. In the converter, the losses in the IGBT and diodes are taken into consideration respectively. As in the conducting wires, the copper losses are calculated with the skin effect considered. And the losses in the motor (IMs and SynRMs) contain three categories: winding losses, core losses and mechanical losses. As both motors are assumed with the same kind of cooling system and mechanical frame, the calculations of mechanical losses are the same. Copper losses in IM rotor are defined, while the calculations of iron losses in SynRM rotor are considered.

2.7 Cost model of traction system

The following model estimates initial cost of traction system which includes:

- Commercial cost of d.c. battery

- Commercial cost of power electronics
- Manufacturing cost of electric motor

As this thesis concentrates on the design of electric motor for VE applications, the cost of EM is assumed as manufacturing cost but not commercial cost.

2.7.1 D.C. battery cost

The d.c. battery is no doubt the most important component in the whole traction system, it is difficult to estimate the precise cost of the dc battery as the semiconductor industry is ever-changing nowadays. From [NYNI15], the costs of lithium-ion batteries are coming down approximately 14% annually between 2007 and 2014, from above 1000 $ per kWh to around 410 $ per kWh. Furthermore, the cost of battery packs used by leading vehicle manufacturers is even lower, at around 200~300 $ per kWh in 2014. Here, we take the most recent unit price. For a certain battery power and volume, the number of cells in the pack has substantial effects on its price, which would change pack voltage and the maximum output current (see Figure 2.7.1). These effects are illustrated for a lithium-ion battery providing about 32 km electric range with 60 kW power. The battery cost increases by 15% in changing d.c. voltage from 190V to 380V, while the maximum current change oppositely. As a result of this offsetting effect on the total cost of the electric powertrain, the EM design is required to determine optimum d.c. voltage at rated power.

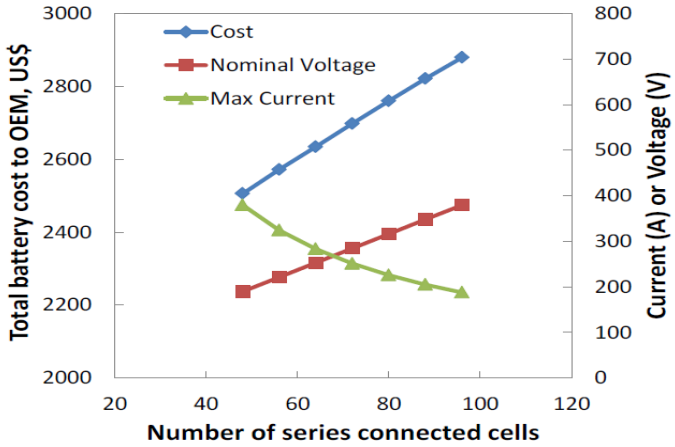

Figure 2.7.1 The effect of the number of series-connected lithium-ion cells, 60-kW with 8 kWh total energy ([NGBD12])

2.7.2 Converter cost

The fast development of semi-conductor technologies reduces the power converter cost applied in EV domains as well. However, the converter cost is still steady compared with the battery cost. In our case, a three phase IGBT-based converter is applied. The commercial cost of IGBTs, which are considered as the critical components in the converter, is determined by its nominal current. The IGBT cost has a nature linear relation with its nominal current. As a result, one could say that when the power range is fixed, the converter cost is determined by the caliber of converter output current, which could be proved in Figure 2.7.2.

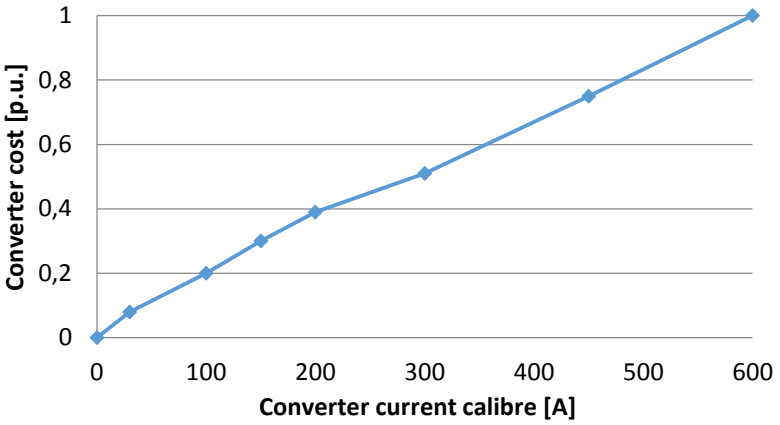

Figure 2.7.2 Impact of output current caliber on converter cost ([PRIE15])

2.7.3 EM cost

The total manufacturing cost of electric motors depends mainly on two parts: material cost (around 35%) and labour cost (around 25%) ([SAMA13]).

The material cost is the cost of different materials in the motor, which are aluminum, copper and sheet metal for IM:

$$TC_{M\_IM} = \gamma_{Al} m_{Al} + \gamma_{Cu} m_{Cu} + \gamma_{ir} m_{ir}$$

$$m_{Al} = \rho_{Al}\left(L n_r h_{tr} b_{ar} + 2\pi D_{ring} h_{ring} b_{ring}\right)$$

$$m_{Cu} = \rho_{Cu}\left(L K_{fill} b_{as} h_{ts} + 2 l_{endw} p_{endw}\right) \qquad 2.7.1$$

$$m_{shm} = \rho_{shm} L \left(\pi \frac{\left({D_{ext}}^2 - {D_s}^2 + {D_r}^2 - {D_{in}}^2\right)}{4} - n_r h_{tr} b_{ar} - n_e h_{ts} b_{as}\right)$$

Where:

- $\gamma_{Cu}, \gamma_{Al}, \gamma_{shm}$: unit cost on copper, aluminum and sheet metal with unit [*€/kg*];
- ρ_{Cu}, ρ_{Al}, ρ_{shm} : material mass per unit volume on copper, aluminum and sheet metal with unit [kg/m^3];
- n_r: bar number in rotor cage;
- L: motor length;
- n_e: stator slot number in stator;
- h_{ts}, h_{tr}: stator and rotor slot heights;
- b_{as}, b_{ar}: stator and rotor slot widths;
- $D_{ring}, h_{ring}, b_{ring}$: rotor ring mean diameter, ring height and width;
- K_{fill}: slot filling factor which describes the ratio between the coil cross section in each slot and slot section;
- l_{endw}, p_{endw} : average length and cross section perimeter of stator end-winding;
- D_{ext}, D_{in}: external and inner diameters of motor;
- D_s, D_r: inner diameter of stator and outer diameter of rotor.

For SynRM, only copper and metal sheet are counted in a similar way.

The labour cost is evaluated from three categories: labour costs of stator and rotor fabrication, workforce cost of stator coiling.

$$TC_L = {TC_L}^s + {TC_L}^r + {TC_L}^{coil} \tag{2.7.2}$$

The stator labour cost is defined as the total cost of pressing, profiling, slotting, soldering and stacking of stator:

$$\begin{aligned} TC_L^s &= TC_L^{pres}(L) + TC_L^{prof}(L) + TC_L^{slot}(L) + TC_L^{sold}(L) + TC_L^{stack} \\ &= \gamma_L^s L + \gamma_{n_e}^s n_e \end{aligned} \tag{2.7.3}$$

Where γ_L^s represents motor length coefficient on stator labour cost, and $\gamma_{n_e}^s$ represents stator slot number coefficient on stator labour cost. As shown in equation 2.7.3, the stator labour cost is proportional with motor length and slot number. Similarly, the rotor labour cost is proportional with motor length and bar number (IM) or barrier number (SynRM) as well. The workforce cost of stator coiling concludes the costs of winding, wire wiping, wire conjugation, section opening, wire isolation and wedging:

$$\begin{aligned} TC_L^{coil} = TC_L^{wd}(n_c, n_e) + TC_L^{wp}(n_e) + TC_L^{cj}(n_e) + TC_L^{op}(n_e) + TC_L^{is}(n_e) \\ + TC_L^{wg}(n_e) = \gamma_{n_e}^{coil} n_e + \gamma_{n_c}^{coil} n_c \end{aligned} \tag{2.7.4}$$

Where $\gamma_{n_e}^{coil}$ represents stator slot number on workforce cost of stator coiling, and $\gamma_{n_c}^{coil}$ represents the number of conductors per slot coefficient on workforce cost of stator coiling. From equation 2.7.4, the stator workforce cost is mainly proportional with stator slot number and number of conductors per slot. Above all, the total manufacturing cost is estimated in equation 2.7.5.

$$TC_{Mot} \cong \frac{TC_M + TC_L}{60\%} \tag{2.7.5}$$

A coarse analytical model is introduced to estimate initial cost of traction system, while some other components such as converter and motor cooling systems, control systems and associated mechanical devices are not considered.

2.8 Mechanical model of SynRMs

A complete mechanical model refers to the following issues:

- critical rotation speed,
- noise and vibration modes,
- mechanical stresses in the shaft,
- rotor deformation, displacement,
- bearing system,
- inertia calculation,
- …

In our case, critical rotation speed, mechanical stresses and rotor deformation are the items involved in the motor pre-sizing. From [SPIN97], the relation between the critical speed Ω_{cri} and the maximum speed of driving cycle Ω_{max} is assumed to be linear:

$$\Omega_{cri} = \frac{\Omega_{max}}{\beta} \qquad 2.8.1$$

$$\text{With} \quad \beta = 0.7$$

For SynRM stators, as their structures are similar to IM stators, the same mechanical constraints are imposed in the design procedure. As discussed in the introduction, the tangential and radial bridges of SynRM make the rotor piece high probably deform while it rotates at high speed. And the accurate criteria to avoid the rotor deformation at high speed have not been discussed in detail by literatures. In some literatures such as [LJKL04], mechanical constraints on rotor bridges have been discussed by using FEA methods. However, an analytical model to investigate rotor deformation at high rotation speed should be introduced and used in the SynRM design. Here, we adapt a relatively simple mechanical model proposed by [KOEC13] to evaluate the rotor rigidity. This model is based on some basic theories from solid mechanics. We will start from some basic knowledge applied in the model.

- ***Stiffness***

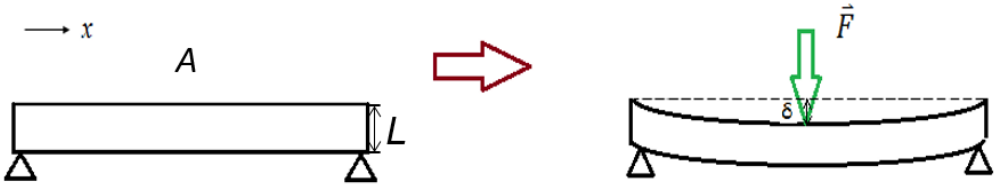

Figure 2.8.1 Reaction of an object with single degree of freedom to an imposed force

Stiffness is the object ability to resist the deformation in response to an imposed force. For an elastic body subjected to a uniaxial tensile stress, the stiffness gives the relationship between the applied pressure and the deformation generated:

$$k = \frac{F}{\delta} \qquad 2.8.2$$

Where F is the applied force, δ is the displacement produced by the force along the same direction as the force, and the stiffness k is measured in [N/m]. With the assumption that the pressure is uniformly distributed along x-axis (in Figure 2.8.1), the expression of stiffness could be deduced from the object geometries and its material property:

$$k = \frac{AE}{L} \qquad 2.8.3$$

Where A is the cross section area of the object, L is the object length along the force direction and E is the Young's modulus (or material elastic modulus). Young's modulus is an intrinsic

property of the material, and stiffness is an extensive property of solid object dependent on both the material and the shape.

- ***Relation of forces***

In order to simplify the analysis, we assume a SynRM rotor with a single barrier per pole firstly, as shown in Figure 2.8.2. The barrier is divided by two symmetric radial bridges into three pieces. When the motor rotates at a given speed, a centrifugal force F_G is imposed at the center of the metal piece at the outer side (section in grey). To balance this centrifugal force, there are forces F_{rad}, F_{tg} imposed to radial bridges and tangential bridges, from the rotor piece at the inner side (section in green) which is considered undeformed. As there are two tangential and two radial bridges, the following relation is deduced:

$$F_G = 2F_{tg}cos\theta_{tg} + 2F_{rad}cos\theta_{rad} = M_{sec}R_G{\Omega_{cri}}^2 \qquad 2.8.4$$

Where:

- M_{sec}: the mass of the rotor piece imposed by centrifugal force (region in grey in Figure 2.8.2);
- R_G: the radius of this rotor piece;
- Ω_{cri}: the critical rotation speed;
- θ_{tg}: the angle between tangential bridge and symmetric axis of one rotor pole;
- θ_{rad}: the angle between radial bridge and symmetric axe.

In the case with single or triple radial bridges per barrier, equation 2.8.4 should be modified to satisfy the force balance condition.

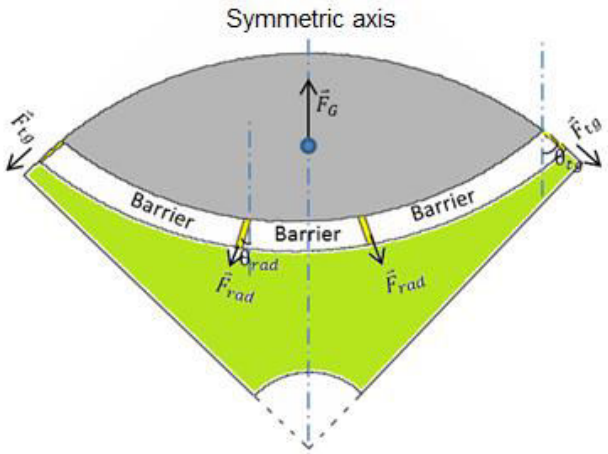

Figure 2.8.2 Forces imposed to the bridges and to the rotor core

- ***Relation between displacements of radial and tangential bridges***

Due to the rigidity of metal sheet, the projection of displacement in each bridge to the symmetric axis is supposed to be identical. The relation of displacements in different bridges could be found in the following formula.

$$\frac{\delta_{rad}}{cos\theta_{rad}} = \frac{\delta_{tg}}{cos\theta_{tg}} \qquad 2.8.5$$

Where δ_{rad} is the displacement of radial bridges resisting $\vec{F}_{rad}$, and δ_{tg} is the displacement of radial bridges resisting $\vec{F}_{tg}$.

- ***Nominal stresses***

Combining equation 2.8.2-2.8.5, the following relations are found:

$$F_{rad} = \frac{F_G}{2}\frac{cos\theta_{rad}}{cos^2\theta_{rad} + \frac{k_{tg}}{k_{rad}}cos^2\theta_{tg}}$$

$$F_{tg} = F_{rad}\frac{k_{tg}cos\theta_{tg}}{k_{rad}cos\theta_{rad}} \qquad 2.8.6$$

$$k_{rad} = E_{shm}\frac{e_{rad}L}{l_{rad}} \qquad k_{tg} = E_{shm}\frac{e_{tg}L}{l_{tg}}$$

Where k_{rad} and k_{tg} represent stiffnesses of radial and tangential bridges repectively, and E_{shm} is the sheet metal elastic modulus. The nominal stresses in tangential and radial bridges could be expressed as:

$$\sigma_{nom_{rad}} = \frac{F_{rad}}{A_{rad}} = \frac{F_G}{2e_{rad}L}\frac{cos\theta_{rad}}{cos^2\theta_{rad} + \frac{k_{tg}}{k_{rad}}cos^2\theta_{tg}} \qquad 2.8.7$$

$$\sigma_{nom_{tg}} = \frac{F_{tg}}{A_{tg}} = \sigma_{nom_{rad}}\frac{e_{rad}}{e_{tg}}\frac{k_{tg}cos\theta_{tg}}{k_{rad}cos\theta_{rad}}$$

Equation 2.8.6-2.8.7 show that the nominal forces and stresses imposed on bridges depend only on the ratio between the stiffness of tangential bridge and that of radial bridge.

- ***Fatigue properties***

In industry, fatigue properties should be investigated to assure the cycle life of products. In our case, the rotor may rotate at a large range of speed in a short time, which would generate stress peaks and break the bridges. As a result, despite the nominal stresses imposed on bridges, the fatigue stresses should be studied as well. Fatigue stresses are determined by nominal stresses and concentration coefficient k_t:

$$\sigma_{fat} = k_t\sigma_{nom} \qquad 2.8.8$$

While the concentration coefficient k_t depends on the ratio between the width of bridges e_{rad} (e_{tg}) and the radius of connection arc $R_{C_{tg}}$ ($R_{C_{rad}}$) as shown in Figure 2.8.3. Generally, k_t is larger than unit, and higher the ratios $\frac{e_{rad}}{R_{C_{rad}}}$ ($\frac{e_{tg}}{R_{C_{tg}}}$), higher the concentration coefficient is.

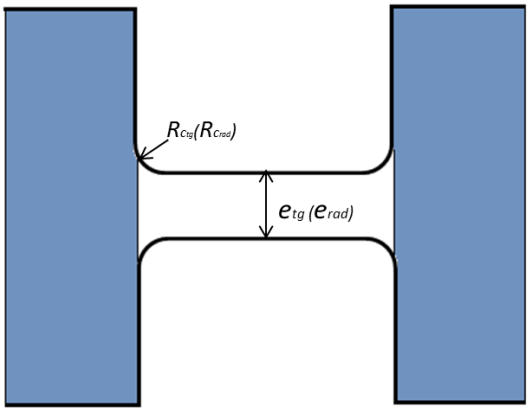

Figure 2.8.3 Dimenisions of the connection arc between the bridge and the core

The connection arcs are not designed in the motor pre-sizing step, we assume that the ratios $\frac{e_{rad}}{R_{C_{rad}}}$ ($\frac{e_{tg}}{R_{C_{tg}}}$) are around 4 and k_t is nearly 1.8 from [PRIE15].

- ***Security factors***

Security factors indicate the industrial tolerance of maximum nominal and fatigue stresses on materials. They could be expressed by the following equations:

$$S_E = \frac{Y_{shm}}{max\left(\sigma_{nom_{rad}}, \sigma_{nom_{tg}}\right)} \qquad S_F = \frac{\sigma_{shm}}{max\left(\sigma_{fat_{rad}}, \sigma_{fat_{tg}}\right)} \qquad 2.8.9$$

Where Y_{shm} is the yield steel strength, and σ_{shm} is the fatigue strength. In our case, the security factor value should be no less than 1.5 from [KOEC13].

In the case with several barriers per pole, the security factor of bridges neighbouring each barriers should be evaluated separately. To simplify the analysis, each barrier is studied exclusively, by neglecting the presence of other barriers.

In this section, a simple analytical model to investigate the rigidity of SynRM rotor is introduced with several hypotheses taken. The influences of the mechanical tensors on the steel magnetic behaviors are neglected. The coupling between the mechanical and electromagnetic models ([DANI13][BEDA15]) is an interesting topic for the future research. The validation of this analytical model by finite element tool will be carried out in Chapter 3. The constraint of security factors will be implemented in the SynRM design.

2.9 General scheme of the multi-physical model

As introduced in the introduction, the multi-physical model estimates the electromagnetic performances of IMs and SynRMs, the energetic performance of the whole traction system, the economic performance of the system, and the mechanical performance of SynRMs. The input and output variables, and the couplings between different models are resumed in the following Figure 2.9.1.

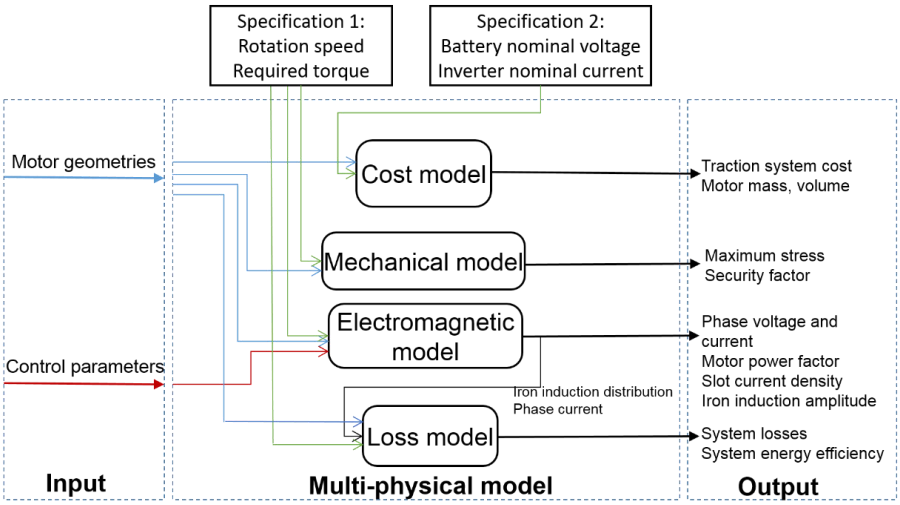

Figure 2.9.1 General scheme of the multi-physical modelling

The above model will be applied in the traction system optimization. In the direct optimization procedure, the input variables will be optimized, while the outputs serve as optimization constraints and objectives. The details of the optimization methodology will be discussed in Chapter 4.

2.10 Conclusions

The multi-physical modelling of a traction system has been presented in this chapter, which includes electromagnetic, energetic, economic and mechanical modellings. Before introducing the applied models, reviews of different modelling technologies have been made. Considering the design applications, all the models except electromagnetic models are purely analytical, and the last one is semi-analytical. The couplings between different models, and the input and output of the model have been described as well.

The electromagnetic models evaluate the electromagnetic performances of IMs and SynRMs. In the models, with the awareness of motor geometries and control states, the steady-state induction distribution in the air-gap is solved firstly. For IMs, the model is deduced with the help of a lumped parameter circuit. The equivalent parameters except magnetizing inductance are computed firstly. The rotor a.c. resistance and inductance are calculated with a numerical approach, which is applicable for any rotor bar geometry. A closed magnetic circuit is modeled from the stator yokes to the rotor yokes, passing through the stator teeth, the air-gap and the rotor teeth. With several hypotheses and Maxwell's law, the relations between the inductions in the air-gap, the yokes and the teeth are established. The induction distribution in the air-gap is solved with numerical methods. The lumped-parameter model is not suitable for the SynRM if there is no damper winding in the rotor. The *dq* space phasor is then applied. Similarly to the IM model, the magnetic circuit and Maxwell's law are applied to deduce the induction distribution in the air-gap. For the air-gap region facing to the rotor tangential bridges, the magnetic circuit is treated separately with other regions, with several assumptions taken. With the solved induction in the air-gap, other performances such as the phase voltage and current, the power factor, the slot current density and maximum iron induction could be deduced.

The loss model estimates the steady-state losses occurring in the converter, the conducting wires and the EMs. The converter losses include switching losses and conducting losses of the IGBTs and the diodes. The copper losses occurring in the conducting wires are considered with skin effect. The losses in the motor include winding losses, core losses and mechanical losses. The core loss calculations require the induction distribution in the yokes and the teeth, which are the outputs of the electromagnetic model. The core losses are computed under frequency frame instead of dynamic one, with the influences of the iron saturation and PMW control considered. The energy efficiency of the traction system was described. Electrical drive loss modelling is a post-processing of the electromagnetic model, as losses in the EM are deduced from the solutions of electromagnetic model (the phase voltage and current, and the induction distribution in the cores).

In the economic model, the commercial costs of d.c. batteries and power converters have been investigated. The d.c. battery cost decreases annually due to the ever-changing semiconductor industry, while the commercial costs of converters are relatively steady. Both of two items are influenced by the electrical capacities of batteries and converters. A coarse analytical model to estimate the manufacturing costs of EMs has been presented, which demands the geometrical parameters of the EM.

The mechanical model estimates the nominal and fatigue stresses applied in the tangential and radial bridges of the SynRM at the critical rotation speed. The security factor of stresses will be served as design criteria.

The validations of the electromagnetic and the mechanical models with finite element methods will be presented in the next chapter.

2.11 References

[ALGE65] Philip L. Alger, *The Nature of Induction Machines*, Gordon and Breach, New York, Aug. 1965.

[ALIS98] M. B. Allen and E. L. Isaacson, *Numerical analysis for applied science*, New York: Wiley, 1998.

[AMKR10] M. Amrhein and P. T. Krein, "Induction machine modeling approach based on 3-d magnetic equivalent circuit framework," *IEEE Transactions on Energy Conversion*, vol. 25, no. 2, pp. 339–347, Jun. 2010.

[BBBD09] N. Bianchi, S. Bolognani, D. Bon, and M. Dai Pre, "Rotor flux-barrier design for torque ripple reduction in synchronous reluctance and pm-assisted synchronous reluctance motors," *IEEE Transactions on Industry Applications*, vol. 45, no. 3, pp. 921–928, 2009.

[BCIP10] A. Boglietti, A. Cavagnino, D. M. Ionel, M. Popescu, D. A. Staton, and S. Vaschetto, "A general model to predict the iron losses in pwm inverter-fed induction motors," *IEEE Transactions on Industry Applications*, vol. 46, no. 5, pp. 1882–1890, Sep. 2010.

[BCLP03] A. Boglietti, A. Cavagnino, M. Lazzari, and M. Pastorelli, "Predicting iron losses in soft magnetic materials with arbitrary voltage supply: an engineering approach," *IEEE Transactions on Magnetics*, vol. 39, no. 2, pp. 981–989, Mar. 2003.

[BEDA15] L. Bernard and L. Daniel, "Effect of Stress on Magnetic Hysteresis Losses in a Switched Reluctance Motor: Application to Stator and Rotor Shrink Fitting," *IEEE Transactions on Magnetics*, vol. 51, no. 9, pp. 1–13, Sep. 2015.

[BENH96] A. Benhama, "Computation of electromagnetic forces from finite element field solutions," 1996, vol. 1996, pp. 247–252.

[BIBO97] N. Bianchi and S. Bolognani, "Design procedure of a vector controlled induction motor for flux-weakening operations," in *Industry Applications Conference, 1997. Thirty-Second IAS Annual Meeting, IAS '97., Conference Record of the 1997 IEEE*, 1997, vol. 1, pp. 104–111 vol.1.

[BOCL11] A. Boglietti, A. Cavagnino, and M. Lazzari, "Computational algorithms for induction motor equivalent circuit parameter determination, part ii: skin effect and magnetizing characteristics," *IEEE Transactions on Industrial Electronics*, vol. 58, no. 9, pp. 3734–3740, Sep. 2011.

[BONA10] I. Boldea and S. A. Nasar, *The induction machines design handbook*, 2nd ed. Boca Raton, FL: CRC Press/Taylor & Francis, 2010.

[DANI13] L. Daniel, "An Analytical Model for the Effect of Multiaxial Stress on the Magnetic Susceptibility of Ferromagnetic Materials," *IEEE Transactions on Magnetics*, vol. 49, no. 5, pp. 2037–2040, May. 2013.

[FIKU09] A. E. Fitzgerald, C. Kingsley, and S. D. Umans, *Electric machinery*, 6. ed., international ed., Boston, Mass.: McGraw-Hill, 2009.

[GAUT05] T. Gautreau, "Estimation des pertes fer dans les machines electriques: Modèle d'hystéresis Loss Surface et applications aux machines synchrones à aimants," 2005.

[GIRI13] F. Giri, Ed., AC electric motors control: advanced design techniques and applications, 1. ed. Chichester: Wiley, 2013.

[GREL89] G. Grellet, *Pertes dans les machines tournantes,* Techniques d'ingénieurs, 1989.

[HABO90] P. G. Handley and J. T. Boys, "Space vector modulation: an engineering review," in Power Electronics and Variable-Speed Drives, 1991., Fourth International Conference on, 1990, pp. 87–91.

[HABU12] W. H. Hayt and J. A. Buck, *Engineering electromagnetics*, 8th ed. New York, NY: McGraw-Hill, 2012.

[INFI06] Infineon, “Dimensioning program IPOSIM for loss and thermal calculation of Infineon IGBT modules,” Technical Documentation, 2006.

[JANN10] X. Jannot, “Modélisation et optimisation d’un ensemble convertisseur-machine,” Thesis (Supélec), 2010.

[KOEC13] S. Koechlin, “Synchronous rotros mechanical dimensioning,” Document Leroy-Somer, 2013.

[LEVI95] E. Levi, “Impact of iron loss on behavior of vector controlled induction machines,” *IEEE Transactions on Industry Applications*, vol. 31, no. 6, pp. 1287–1296, Dec. 1995.

[LIPO04] T. A. Lipo, *Introduction to AC machine design*, Wisconsin Power Electronics Research Center, University of Wisconsin, 2004.

[LJKL04] E. Lovelace, T. Jahns, T. Keim, and J. Lang, “Mechanical design considerations for conventionally laminated, high-speed, interior pm synchronous machine rotors,” *IEEE Transactions on Industry Applications*, vol. 40, no. 3, pp. 806–812, May. 2004.

[LURR02] T. Lubin, H. Razik, and A. Rezzoug, “Magnetic saturation effects on the control of a synchronous reluctance machine,” *IEEE Transactions on Energy Conversion*, vol. 17, no. 3, pp. 356–362, Sep. 2002.

[MCCL99] C. I. McClay, “A comparison of time-stepped finite-element techniques for the calculation of losses in cage induction motors,” 1999, vol. 1999, pp. 35–39.

[MEEK10] D. Meeker, “Finite Element Method Magnetics Version 4.2: User’s Manual,” FEMM, Oct-2010.

[NGBD12] P. Nelson, K. Gallagher, I. Bloom, and D. Dees, “Modeling the performance and cost of lithium-ion batteries for electric-drive vehicles, Second Edition,” 2012.

[NYNI15] B. Nykvist and M. Nilsson, “Rapidly falling costs of battery packs for electric vehicles,” *Nature Climate Change*, vol. 5, no. 4, pp. 329–332, Mar. 2015.

[OSTO89] V. Ostović, *Dynamics of Saturated Electric Machines*, New York, NY: Springer New York, 1989.

[PARK29] R. H. Park, “Two-reaction theory of synchronous machines generalized method of analysis-part I,” *American Institute of Electrical Engineers, Transactions of the*, vol. 48, no. 3, pp. 716–727, Jul. 1929.

[PCFB03] G. Pugsley, C. Chillet, A. Fonseca, and A.-L. Bui-Van, “New modeling methodology for induction machine efficiency mapping for hybrid vehicles,” 2003, vol. 2, pp. 776–781.

[PDVJ14] D. Prieto, P. Dessante, J.-C. Vannier, X. Jannot, and J. Saint-Michel, “Analytical model for a saturated Permanent Magnet Assisted Synchronous Reluctance Motor,” in *Electrical Machines (ICEM), 2014 International Conference on*, 2014, pp. 72–78.

[PERH02] J. Perho, *Reluctance network for analysing induction machines*, Helsinki: Finnish Acad. of Technology, 2002.

[PNMS09] J. Pyrhönen, J. Nerg, A. Mikkola, J. Sopanen, and T. Aho, “Electromagnetic and mechanical design aspects of a high-speed solid-rotor induction machine with no separate copper electric circuit in the megawatt range,” *Electrical Engineering*, vol. 91, no. 1, pp. 35–49, Jun. 2009.

[PRIE15] D. Prieto, “Modélisation et optimisation des machines synchro-réluctantes à aimants permanents et de leur électronique,” 2015.

[RARI97] C. B. Rasmussen and E. Ritchie, “A magnetic equivalent circuit approach for predicting PM motor performance,” 1997, vol. 1, pp. 10–17.

[SALO95] S. J. Salon, *Finite Element Analysis of Electrical Machines*, Boston, MA: Springer US, 1995.

[SAMA13] D. Samarkanov, “Techno-economic multi-objective optimization of induction machines,” 2013.

[SARM79] M. S. Sarma, *Synchronous machines: their theory, stability, and excitation systems*, New York: Gordon and Breach, 1979.

[SBLO10] A. Stermecki, O. Biro, H. Lang, G. Ofner, and K. Preis, "Analysis of synchronous generator end-winding deformations using 3-D time-harmonic FEM," 2010, pp. 1–5.

[SKCB07] S. D. Sudhoff, B. T. Kuhn, K. A. Corzine, and B. T. Branecky, "Magnetic Equivalent Circuit Modeling of Induction Motors," *IEEE Transactions on Energy Conversion*, vol. 22, no. 2, pp. 259–270, Jun. 2007.

[SPIN97] G. Spinnler, *Conception des machines: principes et applications*, Lausanne, Suisse: Presses polytechniques et universitaires romandes, 1997.

[TBDB14] A. Tessarolo, C. Bruzzese, M. Degano, and L. Branz, "Analytical modeling of split-phase synchronous reluctance machines," 2014, pp. 3190–3196.

[TRZY10] A. Trzynadlowski, *Introduction to modern power electronics*, 2nd ed. Hoboken, N.J: John Wiley & Sons, 2010.

[VANN07] J.-C. Vannier, "Conversion électromécanique," Polycopié Supélec, 2007.

[VRAN68] J. E. Vrancrik, "Prediction of Windage Power Loss in Alternators," NASA-Langey, Report No. TND-4849, 1968.

[XXLN90] L. Xu, X. Xu, T. A. Lipo, and D. W. Novotny, "Vector control of a synchronous reluctance motor including saturation and iron loss," 1990, pp. 359–364.

[YUFI98] Z. Yu and D. Figoli, "AC Induction Motor Control Using Constant V/Hz Principle and Space Vector PWM Technique with TMS320C240." Texas Instruments Incorporated, Apr-1998.

[ZHPH13] K. Zhou, J. Pries, and H. Hofmann, "Computationally-efficient 3D finite-element-based dynamic thermal models of electric machines," 2013, pp. 839–846.

Chapter 3 Validation by FEA Methods

Chapter 3 Validation by FEA methods

3.1 Introduction

The validations of IM and SynRM electromagnetic models, and the SynRM mechanical model will be carried out in this chapter with FEA methods.

- ***Induction Machines***

Since the static FEA method could not model the induced currents in the rotor, harmonic and time-domain FEA methods are usually applied in IM numerical analysis. Harmonic and transient FEA analysis, especially the latter one, are more calculation time-consuming than static FEA analysis ([SALO95]). Authors in [ALBB09] have proposed a method to extract equivalent parameters of the lumped parameter circuit from 2D harmonic FEA computations. We will apply this method to validate the equivalent parameters directly. The transient FEA method will be applied to verify electrical performances at several working points. Besides, a method combining the analytical model and the static FEA analysis will be presented. The electromagnetic performances of the analytical model and the novel method will be compared with variable slip ratio and stator current amplitude. The analytical error will be quantified and analyzed.

- ***Synchronous Reluctant Machines***

With the method proposed by authors in [BAPM07], few static FEA solutions are required in the analysis of saturated synchronous machines, which allows the computation of the average torque and the main torque harmonics. This method will be used in the validation of the SynRM analytical model from the performances such as the phase voltage, the power factor and so on (the torque ripple excluded). This analysis will be carried out in several different rotors. The analytical and numerical performances will be compared with various current angles and stator current amplitudes, and the analytical error will be analyzed.

The mechanical model is used to investigate the maximum stresses applied on the SynRM bridges. The stress distribution could be obtained from two-dimensional finite element analysis for linear elasticity ([BRSU92] [FALK91]), and the average stress in each bridge will be compared with the analytical calculations.

3.2 Validations of IM electromagnetic model

In this section, the validations of IM analytical model will be carried out. We start from the equivalent parameter validations.

3.2.1 Equivalent parameter validations

- ***Validations of the rotor bar resistance and inductance***

The frequency in the harmonic FEA scenario is set to be the slip frequency (the rotor current frequency). In the analytical model, the multi-layer method is applied to consider the a.c. impedance of the rotor bar. In FEA simulations, the bar resistance R_{bar} and slot inductance L_{slr} are deduced from:

$$R_{bar} = \frac{P_{bar}}{i_{bar}^2}$$
$$L_{slr} = \frac{2W_{bar}}{i_{bar}^2} \qquad 3.2.1$$

Where P_{bar} is the resistive loss in the bar, i_{bar} is the current passing through the bar, and W_{bar} is the magnetic field coenergy in the bar.

The resistance and inductance of a rectangular rotor bar calculated from analytical and numerical models are compared in Figure 3.2.1. The computed inductance is supposed as the rotor slot leakage inductance in the analytical model. The a.c. resistance increases with the bar current frequency, while the inductance decreases. The bar resistance error is negligible when the rotor current frequency is below 100Hz. The inductance error of the analytical model is steady with the frequency and tolerable (<=7%).

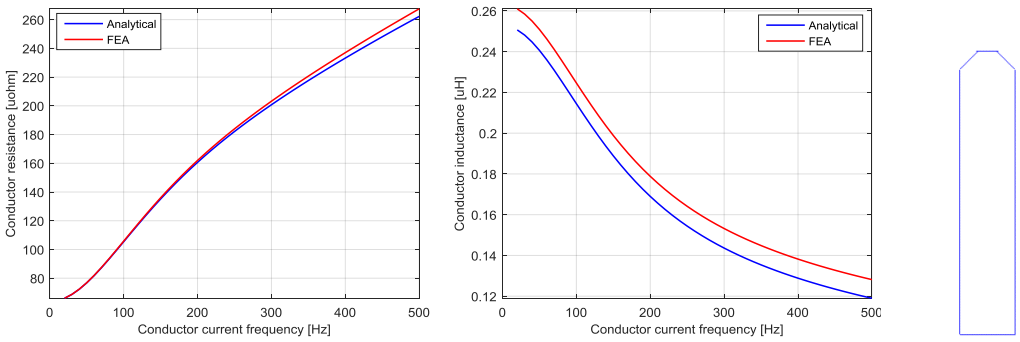

(a) (b) (c)

Figure 3.2.1 Comparisons of resistance (a) and inductance (b) of a rectangular rotor conductor (c) in the analytical and numerical models

Similar comparisons are applied in a non-rectangular bar shape (as shown in Figure 3.2.2). The resistance error is still negligible when the rotor current frequency is below 100 Hz, and the inductance error is still tolerable. The analytical error mainly comes from the hypothesis of an infinite permeability of the rotor teeth.

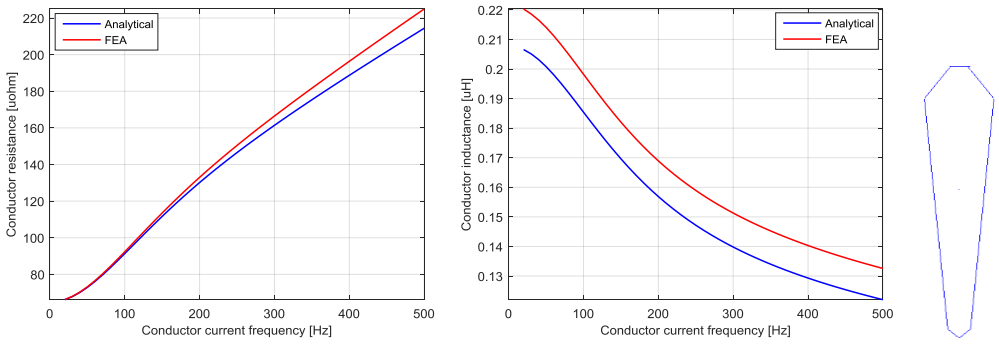

(a) (b) (c)

Figure 3.2.2 Comparisons of resistance (a) and inductance (b) of a non-rectangular rotor conductor (c) in the analytical and numerical models

The above results have shown that the multi-layer method is reliable and valid with an arbitrary bar shape.

- ***Validations of the magnetizing inductance***

The calculation of the magnetizing inductance is validated with static FEA simulations at no-load. In this case the *d*-axis is set to be along the phase *a*-axis, and the flux linkage passing through d-axis and the equivalent current along d-axis are expressed by:

$$\Lambda_d = \frac{2}{3}\left(\Lambda_a - \frac{1}{2}\Lambda_b - \frac{1}{2}\Lambda_c\right)$$
$$i_d = \frac{2}{3}\left(i_a - \frac{1}{2}i_b - \frac{1}{2}i_c\right) \quad 3.2.2$$

Where i_a, i_b, i_c are phase currents, and the magnetizing inductance at no-load is:

$$L_m = \frac{\Lambda_d}{i_d} \quad 3.2.3$$

The validated motor is predefined firstly. The motor geometrical variables are defined as:
-p: pole pair number;
-n_c: conductor number per slot;
-n_e: stator slot number;
-n_r: rotor bar number;
-L: motor length;
-g: air-gap width;
-h_{ts}: stator tooth height;
-h_{ys}: stator yoke height;
-h_{tr}: rotor tooth height;
-h_{yr}: rotor yoke height;
-γ_{ts}: stator tooth concentration coefficient;
-γ_{tr}: rotor tooth concentration coefficient;
-D_{ir}: shaft diameter.

Most variables are remarked in Figure 3.2.3, stator and rotor tooth concentration coefficients are supposed to be the ratio between the teeth width and the slot width:

$$\tau_{ts} = \frac{b_{ts}}{b_s} \quad \tau_{tr} = \frac{b_{tr}}{b_r} \tag{3.2.4}$$

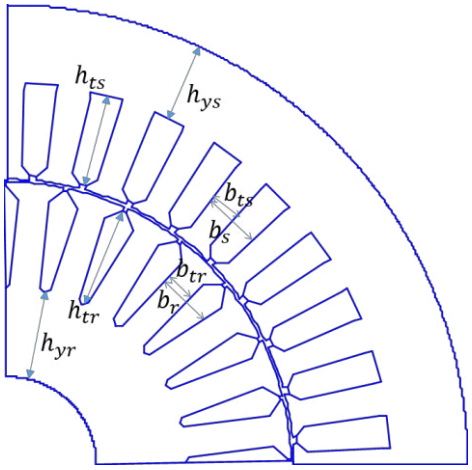

Figure 3.2.3 The description of geometrical varaibles in an IM

And the variables are assigned in Table 3.2.3.

L[mm]	g[mm]	h_{ts}[mm]	h_{ys}[mm]	h_{tr}[mm]	h_{yr}[mm]	γ_{ts}	γ_{tr}	n_c	n_e	n_r
100	0.4	13.6	11	15	12.6	0.5	0.52	40	36	28
p	D_{ir}[mm]									
2	25									

Table 3.2.1 Geometrical dimensions of the IM at no-load test

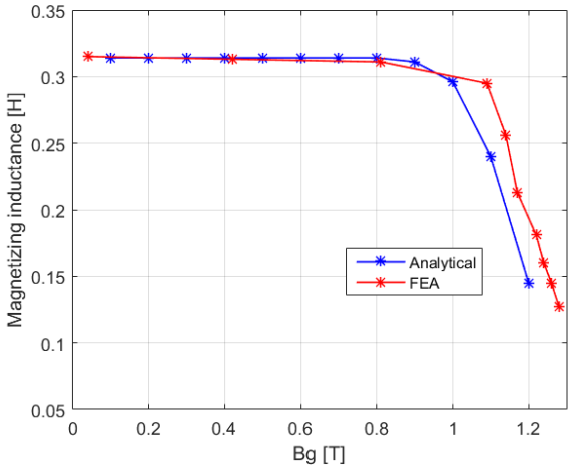

Figure 3.2.4 Magnetizing inductance comparisons between the analytical and numerical models

The magnetizing inductances calculated from the analytical and numerical models are compared in Figure 3.2.4. The inductance decreases when the flux density in the air-gap increases. The analytical error is low when the air-gap induction amplitude is below 1.1 Tesla. It proves that the analytical model is reliable in considering the magnetizing inductance when the motor

does not saturate heavily, and the error comes from the neglect of teeth defluxing ([LIUW07]) and third harmonic flux modulation ([BONA10]).

3.2.2 Performance validations with transient FEA simulations

As the transient FEA is the most accurate and the most straightforward method for the induction motor modeling, the analytical model will be validated with the transient FEA simulations, included in the software "FLUX2D" ([FLUX06]). The transient analysis in "FLUX2D" is carried out with a constant rotation speed. The electrical drive circuits are added and paired with the electromagnetic analysis. The voltage sources are defined with a time-varying sinusoidal waveform. In the transient analysis, the torque is not constant due to the influences of the cogging torque, we take the average value during a large time range (at least 10 periods). The modeled motor is the same as the one described in Subsection 3.2.1. The rotation speed is fixed at 1500rpm, and the efficient phase voltage is fixed to 380V. Due to the limit of computation efforts, we have only chosen 5 working points. The comparisons of phase voltage, phase current, electric power and power factor are shown in Table 3.2.2.

Slip ratio	0.01	0.02	0.03	0.04	0.05
Phase voltage (Analytical) [V]	380	380	380	380	380
Phase voltage (FEA) [V]	380	380	380	380	380
Absolute error %	0				
Phase current (Analytical) [A]	4.9	5	5.6	6.5	7.3
Phase current (FEA) [A]	5.3	5.3	5.9	6.6	7.3
Absolute error %	4				
Torque (Analytical) [Nm]	3.3	6.7	9.8	13	16.2
Torque (FEA) [Nm]	3	6.6	10	13.2	16.5
Absolute error %	4				
Electric power (Analytical) [kW]	0.57	1.2	1.9	2.3	3
Electric power (FEA) [kW]	0.6	1.3	2	2.4	3.2
Absolute error %	6				
Power factor (Analytical)	0.26	0.48	0.64	0.73	0.8
Power factor (FEA)	0.25	0.46	0.63	0.74	0.79
Absolute error %	3				

Table 3.2.2 IM electromagnetic performance comparisons between the analytical and the transient FEA models

As the electrical circuits are added, the stator copper losses are considered in the transient model, and the analytical model as well (which are not considered in the static and frequency FEA models). However, the above computation takes nearly 4 hours in the transient FEA model and less than 5 seconds in the analytical model. The comparison results have shown that the analytical model is accurate enough for the motor designs.

3.2.3 Validation methodology based on analytical and static FEA models

Since the transient FEA model takes large time to compute, other FEA methods are more frequently applied in the numerical modeling. However, harmonic FEA methods take risk in seeking the determination of the effective permeability by taking the field intensity as the sinusoidally varying quantity ([MEEK10]), and static models could not model the bar penetration.

Here, we propose a methodology to model the IMs by combing the static FEA model with the analytical model. In the static scenario, the stator phase currents are firstly imposed. Then the current in each rotor bar is imposed, which has been computed from the analytical model. The general scheme is presented in Figure 3.2.5, and the stator resistance is neglected in the analytical and numerical analysis. The current in the j_{th} bar is expressed in equation 3.2.5.

$$i_{rj} = \frac{1}{k'_{rs}} \hat{\imath}'_r \cos(p(\frac{2\pi}{n_r} - \delta) - \beta) \qquad 3.2.5$$

Where:

- $\hat{\imath}'_r$: rotor phase current amplitude;
- k'_{rs}: rotor transformation coefficient (see equation 2.4.9);
- p: pole pair number;
- n_r: rotor bar number;
- δ: the mechanical angle between the stator current axe and the rotor bar nearest to it;
- β: the phase angle between the stator and rotor currents (see Figure 2.4.4).

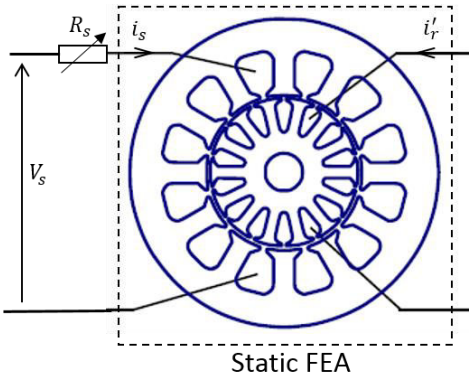

Figure 3.2.5 Static FEA model combined with the analytical one

In Figure 3.2.6, the bar current distributions computed from the analytical and the harmonic model are compared with a current density $\hat{\jmath}_s$ of $5A/mm^2$ and differential frequency of 0.04. To eliminate the saturation influence on the harmonic FEA analysis, both simulations do not consider the core saturation. The results show that bar current distribution of the analytical model is reliable.

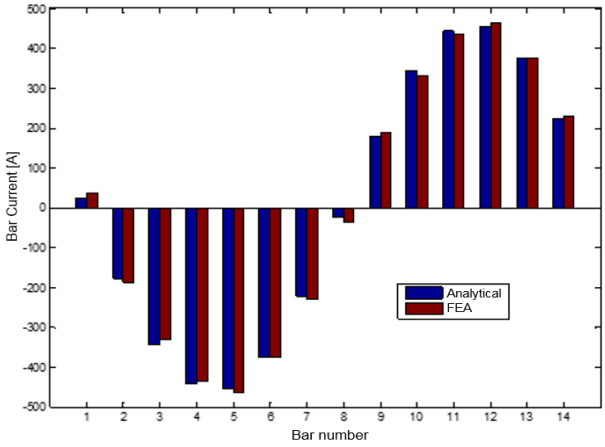

Figure 3.2.6 The comparisons of the rotor bar current distributions calculated from analytical and harmonic FEA models (with current density $\hat{j}_s = 5A/mm^2$ and rotor current frequency $f_r = 4\ Hz$)

With the proposed method, a simulation combining the analytical and numerical analysis was carried out. With the same state parameters, another simulation was realized with a harmonic FEA analysis. Both of two linear simulations were achieved with "FEMM", under the same feeding condition ($\hat{j}_s = 5A/mm^2$ and rotor differential frequency $f_r = 4\ Hz$). The induction distribution and flux lines in the two tests are shown in Figure 3.2.7 (a-b), and the air-gap inductions along the normal direction calculated from the two models are compared in Figure 3.2.7 (c). Generally, the flux lines and the induction distribution in the two tests are similar, and the main error comes from the rotor current difference. However, the error is acceptable for the estimation of motor performances.

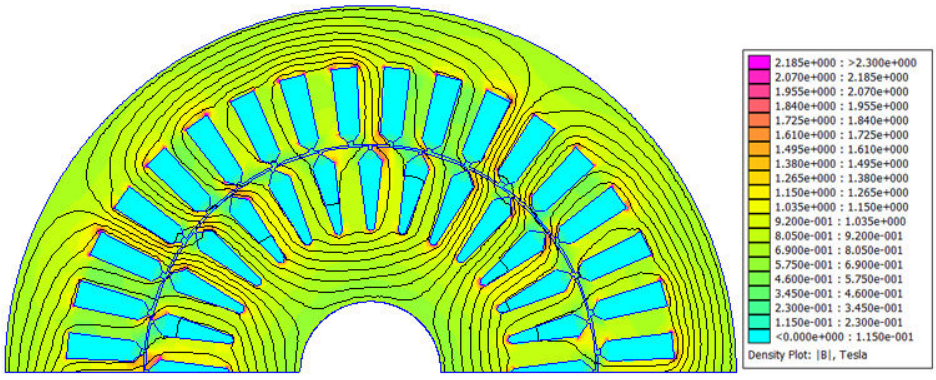

(a)

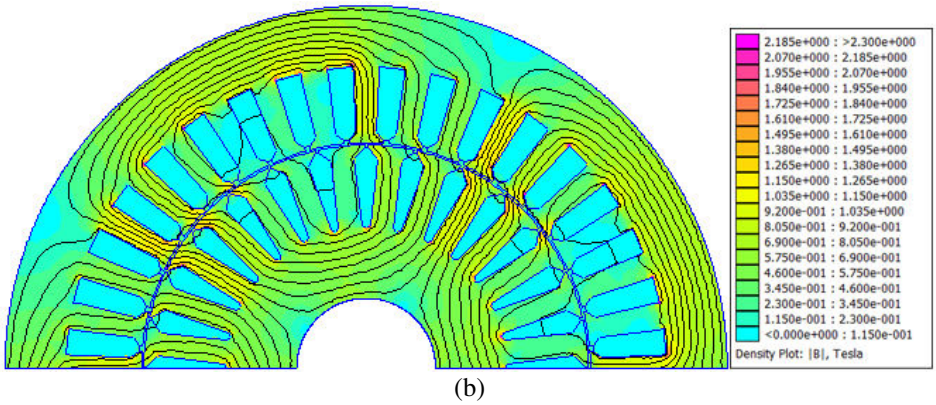

(b)

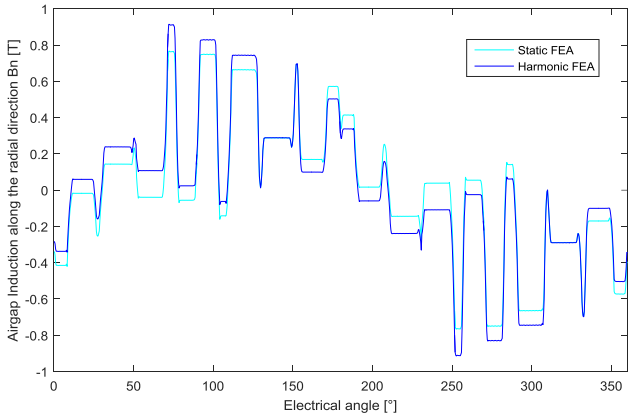

(c)

Figure 3.2.7 The induction distribution in the harmonic FEA simulation (a) and the static FEA simulation (b) with current density $\hat{j}_s = 5A/mm^2$ and rotor current frequency $f_r = 4\ Hz$) (c) comparisons between the airgap inductions along the normal direction calculated from harmonic and static FEA simulations

With static FEA analysis, the phase voltage could be deduced by:

$$U_s = \sqrt{\frac{3}{2}}\omega_s\sqrt{\hat{\Psi}_d^2 + \hat{\Psi}_q^2} \qquad 3.2.6$$

Where ω_s is the electrical pulsation, Ψ_d is the flux linkage along *d*-axis (see equation 3.2.2), and Ψ_q is the flux linkage along *q*-axis. Since the *dq* theory is applicable in all the three-phase alternative motors, the power factor could be deduced from equation 3.2.7.

$$PF = cos\left(tan^{-1}\left(\frac{\hat{\Psi}_d}{\hat{\Psi}_q}\right) - \gamma_a\right) \qquad 3.2.7$$

Where γ_a is the phase *a* current angle.

The simulations with various slip ratio (from 0.001 to 0.9) were realized with the analytical, the static FEA and the harmonic FEA models. The stator phase current is fixed as a constant, and regulated at several levels (the slot current density amplitude $\hat{j}_s = 2.5, 5, 7.5, 10\ A/mm^2$). Both three models took the core saturation into consideration. The motor geometries are the same as the one described in Subsection 3.2.1. The torques computed from the above models are compared in Figure 3.2.8. The difference in low current densities is negligible, while the difference with high phase currents increases as the leakage flux in the cores are influenced by the saturation ([BONA10]). The error (between the analytical and the harmonic FEA models) in the whole slip range is steady and tolerable (<= 5%). And the difference between the analytical and the static FEA models is lower in the whole slip range (<= 3%). The comparisons show that the torques calculated from the analytical model and the model combining analytical and static FEA analysis are accurate and reliable.

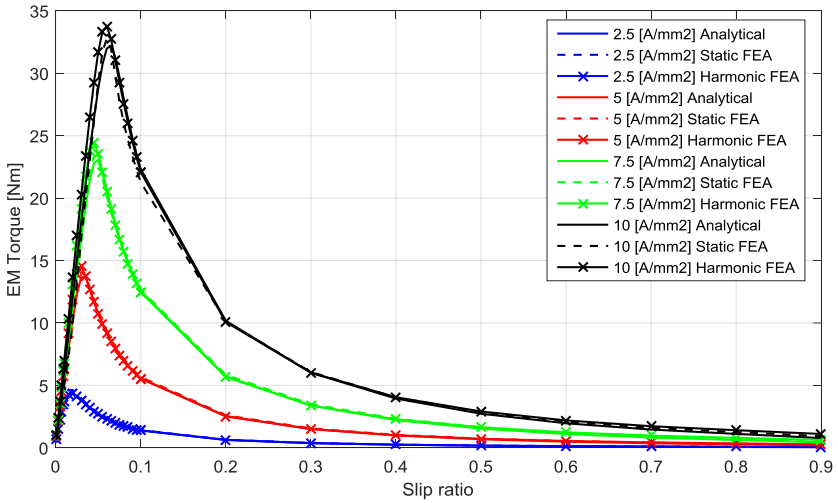

Figure 3.2.8 Comparisons of the electromagnetic torque calculated from analytical and static FEA models with different current supplies and slip ratios

In Figure 3.2.9, the phase voltages calculated from the analytical and the numerical models are compared. One can see that the phase voltage consists within a small slip ratio value, while the value range increases with the phase current. However, the phase voltage is quite different between the no-load phase voltage and the one with a high slip ratio. The error is resumed in Table 3.2.3, and the absolute error is the average value of the errors with different slip ratios and the same current amplitude. It raises with the increase of supply currents, as the leakage inductance is influenced by the core saturation. The error at the lowest slip ratio is the highest, since the motor saturates the most heavily at no-load test. However, the phase voltage error is tolerable for the design application.

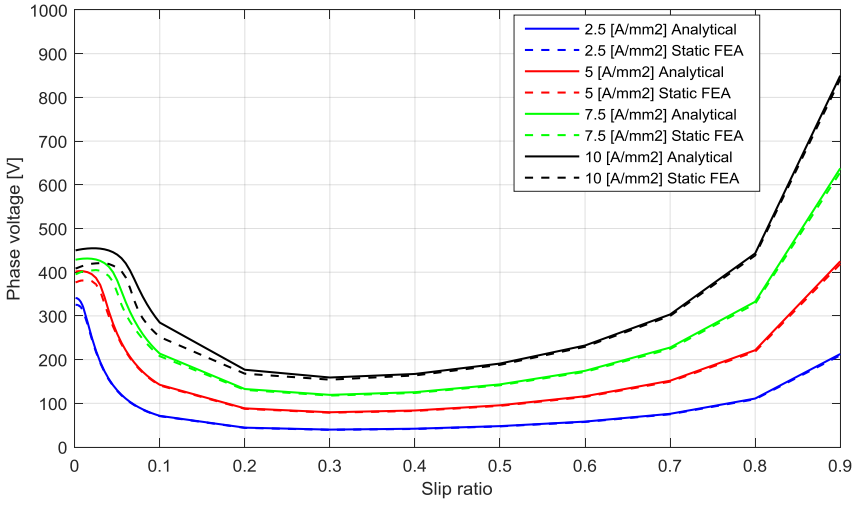

Figure 3.2.9 Comparisons of the effective phase voltages calculated from analytical and static FEA models with different current supplies and slip ratios

Current density J_s	2.5 [A/mm²]	5 [A/mm²]	7.5 [A/mm²]	10 [A/mm²]
Absolute error [%]	1.7	2.7	5	8.6
Maximum error [%]	4.8	6.6	9.5	17
Slip with maximum error	0.0001	0.0001	0.05	0.08
Minimum error [%]	1	1	1.4	1
Slip with minimum error	0.07	0.1	0.4	0.9
Mean absolute error [%]	4.5			

Table 3.2.3 The phase voltage error (including the absolute error the maximum and the minimum errors) in the comparisons between the analytical and the static FEA models

Similarly, the power factors calculated from the two models are compared in Figure 3.2.10. The maximum error occurs at the minimum slip ratio (s = 0.0001), at which the power factor value is quite small (nearly zero). The analytical power factor is accurate from the mean error value (see Table 3.2.4). Compared with harmonic FEA models, the proposed model which combines the analytical and static FEA model takes less time. It estimates the phase voltage and the power factor. However, the precision of the proposed methodology relies on the precision of the imposed state currents.

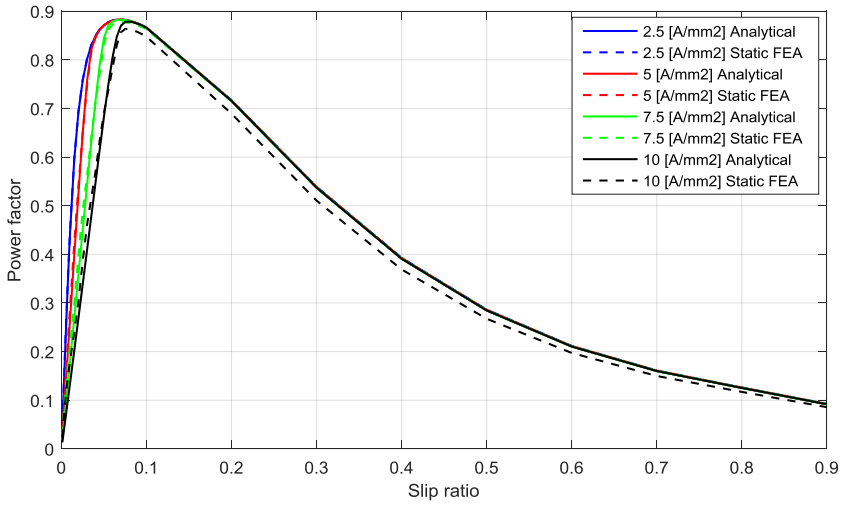

Figure 3.2.10 The comparisons of the power factor calculated from analytical and static FEA models with different current supplies and slip ratios

Current density J_s	2.5 [A/mm²]	5 [A/mm²]	7.5 [A/mm²]	10 [A/mm²]
Absolute error [%]	0.6	2.7	4.9	7.8
Maximum error [%]	7	10	20	30
Slip with maximum error	0.0001	0.0001	0.0001	0.0001
Minimum error [%]	0	0	0	-1.1
Slip with minimum error	0.07	0.1	0.4	0.9
Mean absolute error [%]	4			

Table 3.2.4 The power factor error (including the absolute error the maximum and the minimum errors) in the comparisons between the analytical and the static FEA models

In this section, we have firstly validated the rotor bar resistance and inducance with the harmonic FEA method, and the no-load magnetizing inductance with the static FEA method. The rotor bar impedance error is weak for different bar geometries, and the magnetizing inductance error increases with the saturation but is still tolerable. The transient FEA model was then applied to validate the phase current, the electric power, and the power factor calculated from

the analytical model, within several working points. At last, a new methodology combining the analytical and static FEA analysis has been introduced. The induction distributions in static and harmonic FEA simulations have been compared. With the proposed method, the phase voltage and the power factor are computed. Under different stator current amplitudes and slip ratios, the electrical performances calculated from the analytical, the harmonic FEA, and the proposed models have been compared.

3.3 Validations of the SynRM electromagnetic model

In this section, the SynRM analytical model will be validated with static FEA method.

3.3.1 Validation method based on static FEA model

The rotor saliency and the discrete positions of winding coils induce a high influence of the electromagnetic by rotor position, which brings important torque distortion as shown in Figure 3.3.1. The average torque and the torque ripple are quantified as:

$$T_{av} = \frac{1}{2\pi}\int_0^{2\pi} T(\theta)d\theta$$

$$\eta_{rip} = \frac{T_{max} - T_{min}}{T_{av}} \qquad 3.3.1$$

Where T_{max} and T_{min} are the maximum and the minimum torques for different mechanical positions, when the control parameters are fixed (the shift angle between the phase current vector and the *d*-axis keeps as constant when the rotor rotates).

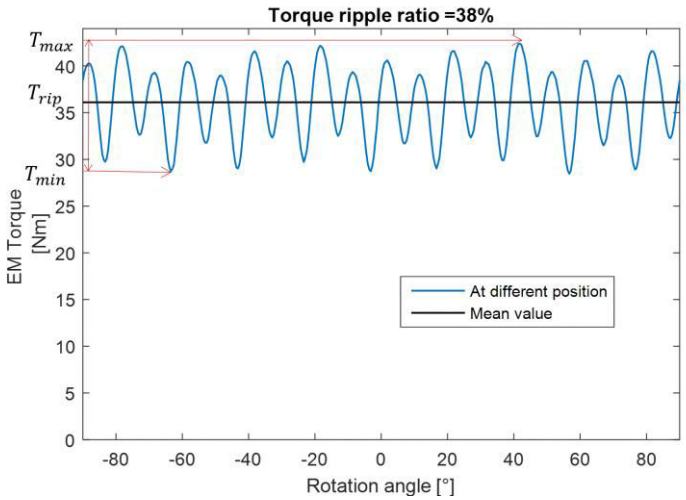

Figure 3.3.1 Torques at different rotor positions (electrical position) and its mean value when the control parameters are fixed, calculated from Maxwell stress tensor in static FEA (with phase current amplitude $\hat{\imath}_s = 15A$ and current angle $\alpha = 60°$)

From [BAPM07], the instantaneous torque under the synchronous reference frame is reported in equation 3.3.2.

$$T(\theta) = \frac{3}{2}p\left(\Psi_d i_q - \Psi_q i_d\right) + \frac{\partial W_m'}{\partial \theta_m} = T_{dq} + \frac{\partial W_m'}{\partial \theta_m} \qquad 3.3.2$$

Where W_m' is the magnetic co-energy, θ_m is the rotor mechanical position, and Ψ_d, i_q, Ψ_q, i_d are the same representations as those in Chapter 2. As currents i_d, i_q are constant under steady state, the derivation of the magnetic co-energy with the rotor position is expressed as:

$$\frac{\partial W_m'}{\partial \theta_m} = \frac{3}{2}p\left(i_d\frac{\partial \Psi_d}{\partial \theta_m} + i_q\frac{\partial \Psi_q}{\partial \theta_m}\right) - \frac{\partial W_m}{\partial \theta_m} \qquad 3.3.3$$

Where W_m represents the magnetic energy. It is proved that the presence of certain torque harmonic (FFT of torque distribution with the rotor position as shown in Figure 3.3.2) orders coincides with the harmonic orders of flux linkages Ψ_d and Ψ_q. The most important harmonic order (18_{th} order) concerns the stator slot number per pair of poles (18 slots). Besides, the phase number and the slot number per pole coincide other harmonic orders.

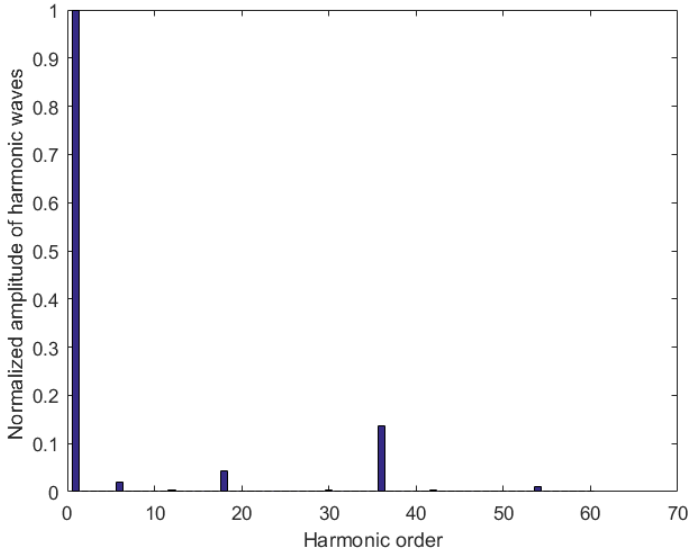

Figure 3.3.2 FFT of the electromagnetic torque taking the rotor position into consideration

However, the variations of flux linkages Ψ_d and Ψ_q are much lower than the variation of their rates of change $\frac{\partial \Psi_d}{\partial \theta_m}$ and $\frac{\partial \Psi_q}{\partial \theta_m}$. The torque ripple is mainly issued in the term $\frac{\partial W_m'}{\partial \theta}$. It is reasonable to consider the term T_{dq} in the calculations of the average torque, since it is slightly influenced by rotor positions. Under static FEM scenario, the comparisons between the T_{dq} value and the precise computation of average torque achieved by Maxwell stress tensor have been validated in a surface-mounted permanent machines and an interior permanent machine ([BAPM07]). The good precision proves that the component T_{dq} imposes slight influences on torque ripple. In order to eliminate the influences of high harmonic orders of flux linkages, authors in [BAPM07] has proposed to compute the value of flux linkages Ψ_d and Ψ_q under four mechanical positions: 0, $\frac{\pi}{12}$, $\frac{\pi}{6}$, $\frac{\pi}{4}$, while the mechanical position indicates the *a*-phase winding position with respect of *d*-axis. The final average torque is calculated from 4 static FEM solutions:

$$T_{av} = \frac{3}{2} p\left(\widehat{\Psi}_d i_q - \widehat{\Psi}_q i_d\right)$$

$$\text{With } \widehat{\Psi}_d = \frac{1}{4}\left(\Psi_d(0) + \Psi_d\left(\frac{\pi}{12}\right) + \Psi_d\left(\frac{\pi}{6}\right) + \Psi_d\left(\frac{\pi}{4}\right)\right) \quad 3.3.4$$

$$\text{and } \widehat{\Psi}_q = \frac{1}{4}\left(\Psi_q(0) + \Psi_q\left(\frac{\pi}{12}\right) + \Psi_q\left(\frac{\pi}{6}\right) + \Psi_q\left(\frac{\pi}{4}\right)\right)$$

And the power factor and phase voltage (with phase resistance neglected) are expressed in equation 3.3.5.

$$PF = cos\left(\frac{\pi}{2} + tan^{-1}\left(\frac{\widehat{\Psi}_q}{\widehat{\Psi}_d}\right) - \alpha\right)$$

$$U_s = \sqrt{\frac{3}{2}}\omega_s\sqrt{\widehat{\Psi}_d^2 + \widehat{\Psi}_q^2} \quad 3.3.5$$

Where α is the current angle (as mentioned in Section 2.5), and ω_s is the electrical pulsation. This method, considered as a "minimum set" method, allows a precise and rapid computation of the average torque with static FEA scenario. It has been adopted in the numerical analysis of permanent magnet synchronous machines and permanent magnet assisted synchronous reluctance machines ([PDDV13]). In the same way, this method will be applied in the validations of the SynRM analytical model.

3.3.2 Validations and characterizations in different geometrical cases

With the proposed static FEA strategy, the analytical model will be validated in several SynRMs with different rotor geometries:

- Rotors with or without radial bridges;
- Rotors with or without air-gap opening air-gaps;
- Rotors with different barrier numbers.

First of all, we define the geometrical dimension variables as:

- p: motor pole pair number;
- L: motor length;
- g: air-gap width;
- h_{ts}: stator tooth height;
- h_{ys}: stator yoke height;
- γ_{ts}: stator tooth concentration coefficient;
- γ_{tr}: rotor tooth concentration coefficient;
- D_r: rotor external diameter;
- N_{bar}: rotor barrier number per pole;
- e_{rb}: radial barrier bridge width: $[e_{rb_1}, \cdots, e_{rb_{N_{bar}}}]$;

- h_{tb}: tangential barrier bridge height;
- $[\beta_1, \cdots, \beta_{N_{bar}}]$: opening angles of the barriers, β_1 is assigned as the opening angle of the barrier nearest to the shaft;
- β_0: air-gap opening angle;
- D_{sh}: shaft diameter;
- D_{dr}: diameter of the barrier nearest to the shaft;
- n_c: conductor number per slot;
- n_e: stator slot number.

The rotor barrier width is given by the symbol b_{br}, while the width of the yoke piece between two barriers is given by b_{tr}. Rotor tooth concentration coefficient γ_{tr} is quantified as:

$$\gamma_{tr} = \frac{b_{tr}}{b_{br} + b_{tr}} \tag{3.3.6}$$

To reduce the variable number, the tooth concentration coefficient is identical for all the rotor teeth. In all the validation cases, the pole number is set to be four, and the single layer distributed winding type is applied. In the first case, the rotor is without radial bridges and air-gap openings as well, and the barrier number per pole is three. In case 2, at the base of the machine geometry in case 1, the barrier number increases to six. In case 3, at the base of the geometry in case 1, the radial bridge is added in each rotor barrier. In case 4, at the base of the geometry in case 1, the air-gap opening is added in each rotor barrier. The four machines are drawn in Figure 3.3.3, with several dimensions shown.

- ***Constraints of barrier positions***

In the research work of Dr. Prieto [PRIE15]), a large set of experiment results has indicated that the barrier positions impose important influences on the torque ripple of SynRMs. It has been concluded that the torque ripple reaches its local maximum value when any barrier span is the integer multiples of the stator slot pitch:

$$\beta_j = k\tau_s \qquad \left(k = 1, 2, 3, \cdots, \frac{n_e}{2p}\right) \ (j = 1, \cdots, N_{bar}) \tag{3.3.7}$$

Where τ_s is the slot opening angle. To assure that the torque ripple approaches the minimum value, all the barrier spans should be avoided in the region with a rayon as one fifth of the stator slot pitch.

$$\beta_j \neq k\tau_s \pm \frac{\tau_s}{5} \tag{3.3.8}$$

The above rules should be respected in determining the opening angles of each barrier, when we try to investigate the influences of rotor geometrical dimensions on the torque ripple.

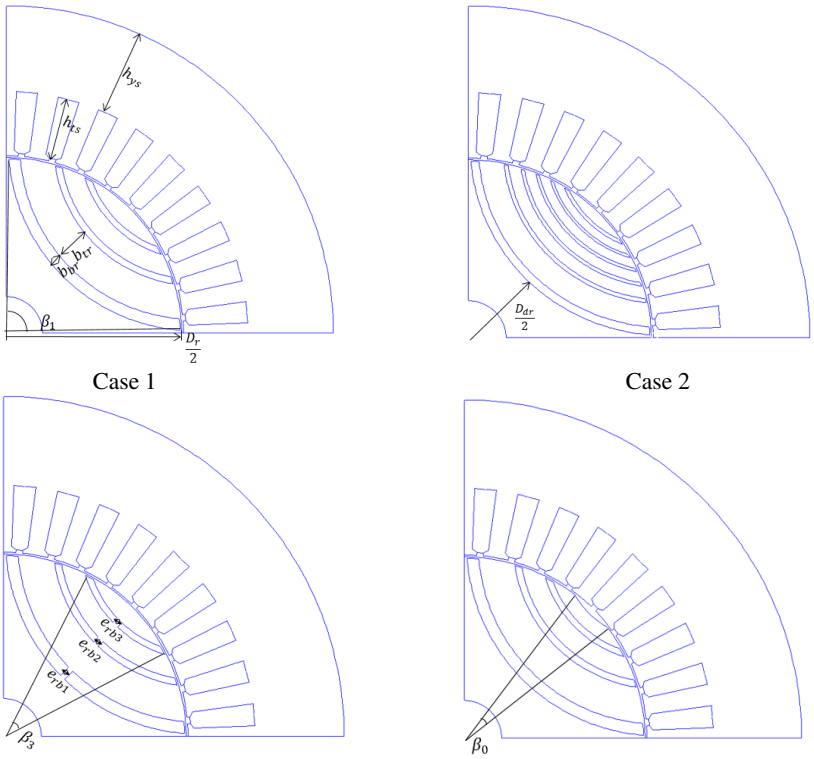

Figure 3.3.3 Motor geometries in four cases

- ***Case 1: Reference machine***

The geometrical dimensions in case 1 are specified in Table 3.3.1.

L[mm]	g[mm]	h_{ts}[mm]	h_{ys}[mm]	γ_{ts}	D_r[mm]	N_{bar}	e_{rb}[mm]	h_{tb}[mm]
160	0.62	20	29.3	0.5	120	3	0	0.8
D_{sh}[mm]	D_{dr}[mm]	γ_{tr}	n_c	n_e	p	β_0	$[\beta_1, \beta_2, \beta_3]$	
25	55	0.75	6	36	2	0°	[88°, 57°, 36°]	

Table 3.3.1 Geometrical dimensions in case 1

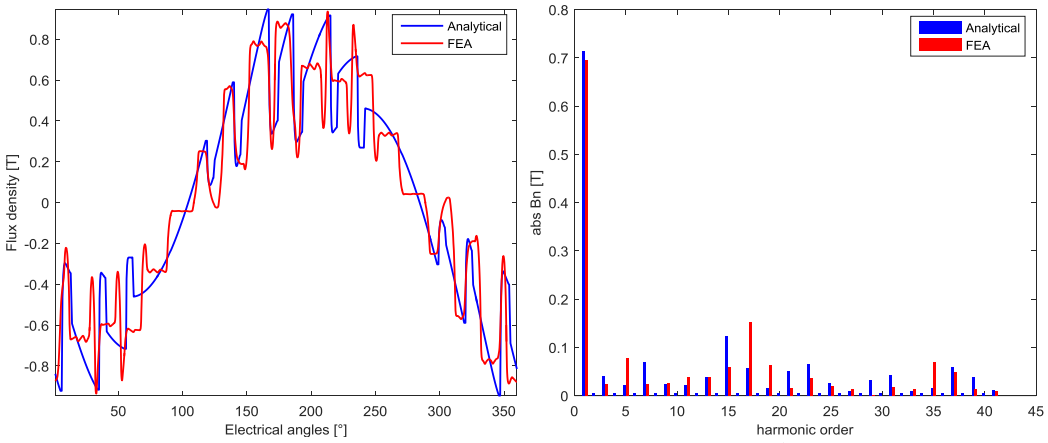

(a) (b)

Figure 3.3.4 Air-gap induction comparisons between the analytical model and FEA (a) harmonic orders of the induction distributions (b) (with current density $\hat{j}_s = 2.5A \cdot mm^{-2}$ and current angle $\alpha = 60°$ for SynRM with the geometry in case 1)

As the induction in the tangential bridge is correlated with the air-gap induction, we measured the tangential induction along the mid cut line of each tangential bridge (as shown in Figure 3.3.5) in the same experiment. From the tangential induction comparisons in Figure 3.3.6, the consistence of curve tendency has proved the reliability of the tangential bridge induction consideration in the analytical model. The error comes from the neglect of barrier and air-gap leakage flux. Generally, the flux density amplitude in the bridges is much higher than that in other parts of the EM.

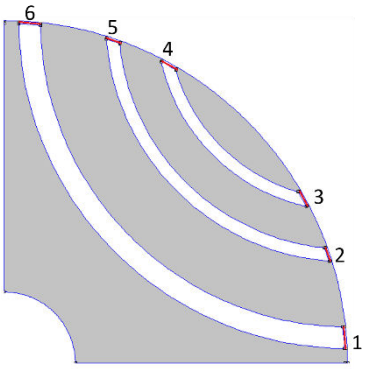

Figure 3.3.5 The mid cut lines of each tangential bridge (red lines) and bridge number

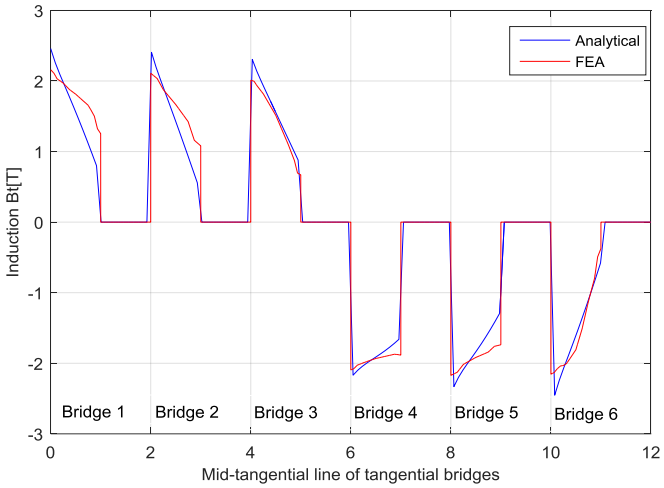

Figure 3.3.6 The comparisons of inductions along the mid cut line of each tangential bridge

Then we have measured the electromagnetic performances under different current supplies with the analytical and numerical model as shown in Table 3.3.2. The saliency ratio is the ratio between the *d*-axis and *q*-axis magnetizing inductances, and the saliency ratio error is higher because the *q*-axis magnetizing inductance calculation in the analytical model is not precise enough. Several leakage fluxes such as the one from the rotor teeth to the tangential bridge (as presented in Figure 3.3.7) are neglected in the analytical model. The estimations of the average torque, the power factor, and the phase voltage are accurate under different current densities.

Current density J_s Current angle α	2.5 [A/mm²] 45°	2.5 [A/mm²] 60°	5 [A/mm²] 45°	5 [A/mm²] 60°
Average torque (FEA) [Nm]	13.9	11.9	35.8	39
Torque (Analytical model) [Nm]	13.9	12.5	33.6	38
Power factor (FEA)	0.57	0.66	0.54	0.66
Power factor (Analytical model)	0.57	0.68	0.58	0.68
Phase voltage (FEA) [V]	171	126	228	204
Phase voltage (Analytical model) [V]	170	129	211	194
Saliency ratio (FEA)	5.3	5.2	4.5	5.2
Saliency ratio (Analytical model)	6.6	6.5	5.8	6.6
Torque ripple (FEA)	35.2%	34.8%	34.9%	33.3%

Table 3.3.2 Electromagnetic performances of the SynRM in case 1

In our case, the torque ripple is relatively high. In order to eliminate the stator winding influence on the torque ripple, the stator geometry and winding structure in all cases are the same.

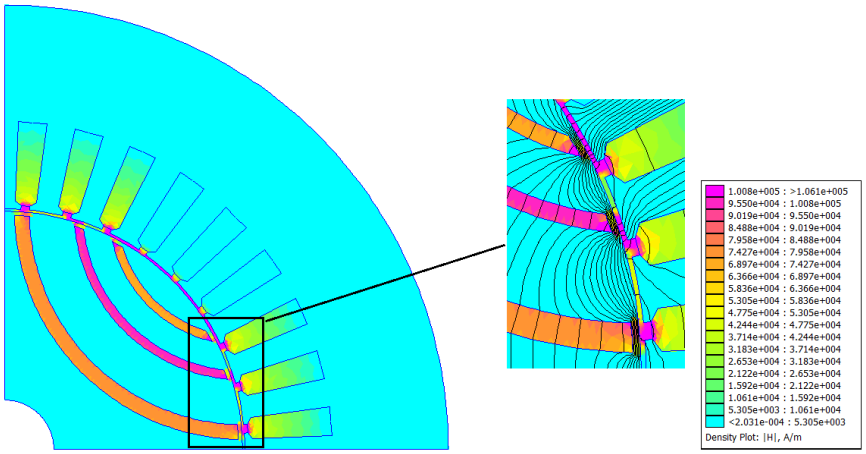

Figure 3.3.7 The magnetic field distribution in the motor when the current angle $\alpha = 90°$

- ***Case 2: With 6 barriers per pole***

In case 2, the barrier number is increased to six per pole. The total barrier width is the same as in case 1, which indicates that the rotor tooth concentration is the same. The opening angle of each barrier has been listed in Table 3.3.3.

β_1	β_2	β_3	β_4	β_5	β_6
88°	67°	56°	46°	36°	26°

Table 3.3.3 Geometrical dimensions in case 1

We compare the air-gap induction in the analytical and numerical model in Figure 3.3.8. With the same current supply, the harmonic order ratio is lower than that in case 1, especially the 13_{th} and 15_{th} order. As the rotor barrier in case 2 is thinner, the barrier span range could be well avoided in the region where the span is the integer multiples of the stator slot pitch. The fundamental inductions in the analytical and harmonic order are quite close, and the value is a bit higher than case 1 as a result of the reduction of the harmonic ratio.

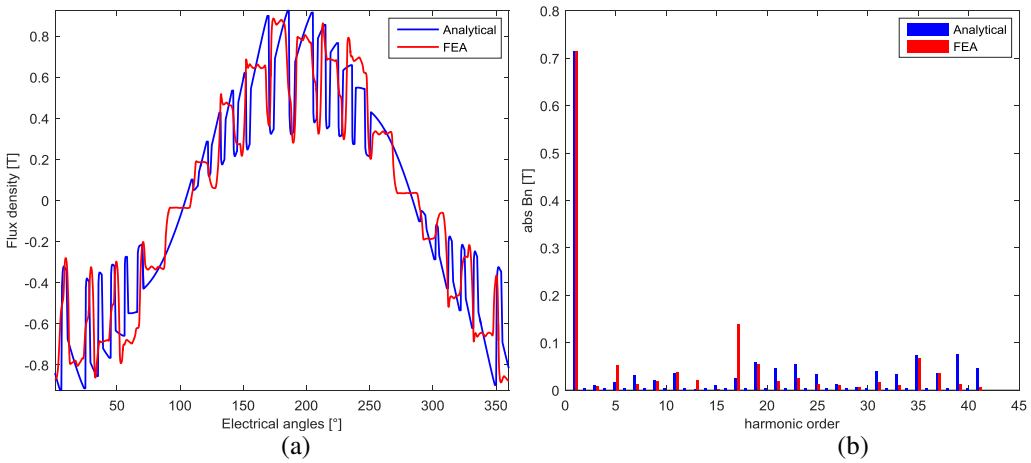

(a) (b)

Figure 3.3.8 Air-gap induction comparisons between the analytical model and FEA (a) harmonic orders of the induction distributions (b) (with current density $\hat{J}_s = 2.5A \cdot mm^{-2}$ and current angle $\alpha = 60°$ for SynRM with the geometry in case 2)

We computed the electromagnetic performances with the same current supplies as in case 1, and the results are listed in Table 3.3.4. As the barrier total width and barrier form is the same, the average torque, the power factor and the phase voltage are close in case 1 and case 2. The precision of the analytical model is still reliable in case 2. The torque ripple is weaker than case 1, which could be proved from the view of harmonic order ratio (lower harmonic ratio means lower torque ripple).

Current density J_s Current angle α	2.5 [A/mm²] 45°	2.5 [A/mm²] 60°	5 [A/mm²] 45°	5 [A/mm²] 60°
Average torque (FEA) [Nm]	13.9	12.3	35.4	38.6
Torque (Analytical model) [Nm]	14	12.9	33.5	38
Power factor (FEA)	0.56	0.66	0.54	0.66
Power factor (Analytical model)	0.57	0.69	0.55	0.68
Phase voltage (FEA) [V]	174	130	230	204
Phase voltage (Analytical model) [V]	173	132	212	194
Saliency ratio (FEA)	5	5.2	4.5	5.1
Saliency ratio (Analytical model)	6.3	6.6	5.7	6.6
Torque ripple	31%	30.3%	32.2%	33.5%

Table 3.3.4 Electromagnetic performances of the SynRM in case 2

- ***Case 3: With radial bridges***

On the base of the geometry in case 1, radial bridges with two millimeter width are added in the middle of each barriers. The air-gap induction distributions in the analytical and the numerical models are compared under the same current supply with the one in case 1 (as shown in Figure 3.3.9). The harmonic induction distribution is nearly the same as case 1, except the third harmonic order is higher (generated by the presence of radial bridge in each barrier).

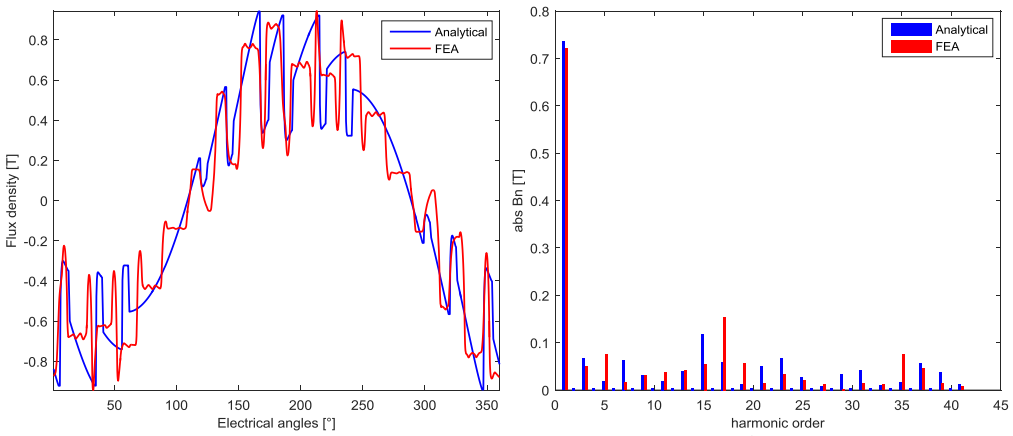

Figure 3.3.9 Air-gap induction comparisons between the analytical model and FEA (a) harmonic orders of the induction distributions (b) (with current density $\hat{J}_s = 2.5A \cdot mm^{-2}$ and current angle $\alpha = 60°$ for SynRM with the geometry in case 3)

In the same experiment, we calculated the induction distribution along the mid-tangential line in the rotor teeth (in Figure 3.3.10) from the analytical and numerical model. From the finite element simulation, the induction has a pic in the middle of the tangential line in Figure 3.3.11, which is influenced by the presence of the radial bridge. The curve tendency in each teeth is consistent in the analytical and numerical analysis, and the average values are close. That assures the reliability of the rotor iron loss estimation in the analytical model (see Section 2.6).

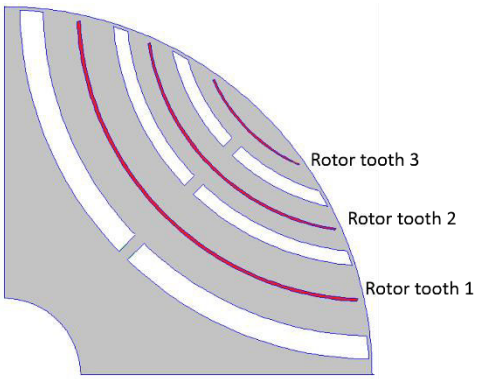

Figure 3.3.10 The mid tangential lines of each rotor tooth (red lines)

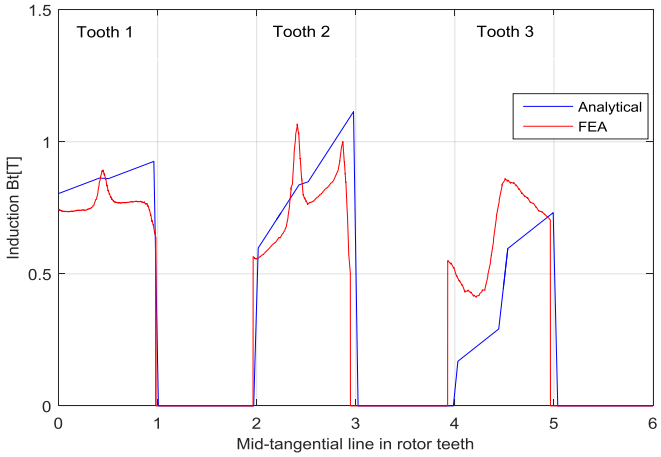

Figure 3.3.11 The comparisons of inductions along the tangential line of each rotor tooth

Similarly, we computed the electromagnetic performances with the same current supplies as in case1 (as shown in Table 3.3.5). The saliency ratio is much lower than that in case 1, as the q-axis magnetizing inductance increases when the radial bridges are added. Therefore, the power factor in case 3 is lower than the one in case 1, and the phase voltage is a bit higher than case 1, which are proved by both analytical and numerical simulations. In this case, the concerned performances are well estimated with the analytical model. The torque ripple is a bit higher than case 1, as the third harmonic order are higher with the presence of the radial bridge.

Current density J_s Current angle α	2.5 [A/mm²] 45°	2.5 [A/mm²] 60°	5 [A/mm²] 45°	5 [A/mm²] 60°
Average torque (FEA) [Nm]	12.7	11.7	33	38
Torque (Analytical model) [Nm]	12.7	12.6	31	37
Power factor (FEA)	0.51	0.59	0.5	0.62
Power factor (Analytical model)	0.52	0.62	0.5	0.64
Phase voltage (FEA) [V]	175	132	229	207
Phase voltage (Analytical model) [V]	172	133	213	197
Saliency ratio (FEA)	3.9	4	3.6	4.3
Saliency ratio (Analytical model)	4.5	4.7	4.3	5.3
Torque ripple	39.2%	38.1%	36.6%	34.9%

Table 3.3.5 Electromagnetic performances of the SynRM in case 3

- ***Case 4: With the air-gap opening***

An air-gap opening angle 25° is added in case 4 on the base of the geometry in case 1. Like in all other cases, we compared the air-gap induction distribution calculated from the analytical and numerical models (as shown in Figure 3.3.12). The coupling of the rotor air-gap opening and the stator winding increases several harmonic orders, such as 5_{th}, 7_{th} and 9_{th} harmonic orders. Thus makes the fundamental induction amplitude decrease compared with the one in case 1, which is identified by both two models.

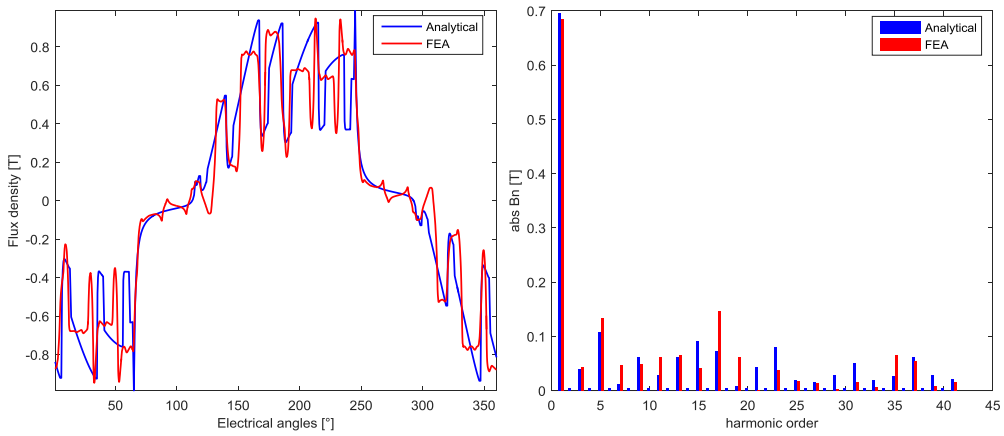

(a) (b)

Figure 3.3.12 Air-gap induction comparisons between the analytical model and FEA (a) harmonic orders of the induction distributions (b) (with current density $\hat{J}_s = 2.5A \cdot mm^{-2}$ and current angle $\alpha = 60°$ for SynRM with the geometry in case 4)

In Table 3.3.6, the electromagnetic performances under several current supplies, including the torque, the power factor, the phase voltage, the saliency ratio and the torque ripple are listed. The added air-gap opening increases the motor saliency ratio, which increases the motor power factor. From the simulations of the analytical and numerical models, the power factor is higher than that in case 1. It is not surprising that the torque ripple increases 25% compared with case 1, which could be proved by the higher harmonic ratio.

Current density J_s Current angle α	2.5 [A/mm²] 45°	2.5 [A/mm²] 60°	5 [A/mm²] 45°	5 [A/mm²] 60°
Average torque (FEA) [Nm]	13.9	11.9	34.2	38
Torque (Analytical model) [Nm]	13.9	12.6	32.7	36.6
Power factor (FEA)	0.58	0.68	0.56	0.68
Power factor (Analytical model)	0.59	0.7	0.57	0.7
Phase voltage (FEA) [V]	167	123	219	195
Phase voltage (Analytical model) [V]	166	125	198	182
Saliency ratio (FEA)	5.4	5.4	4.7	5.3
Saliency ratio (Analytical model)	6.9	6.7	6.1	6.9
Torque ripple	44.5%	41. 8%	45.2%	43.4%

Table 3.3.6 Electromechanical performances of the SynRM in case 4

In this subsection, we have validated the SynRM analytical model with four different rotor geometries. From the comparisons with the numerical simulations, the analytical model is valid with the proposed geometries. Among the estimations of the saliency ratio, the average torque, the phase voltage, and the power factor, the latter three are more accurate. The main error comes from the q-axis magnetizing inductance calculation. To reduce the torque ripple, the barrier span should not be the integer multiples of the slot pitch. The SynRMs with more barriers (when the total barrier width is constant) present lower torque ripple as the span of the single barrier could be completely avoided in the described ranges. However, the radial bridges are indispensable considering the mechanical rigidity. When the barrier bridges are added, the power factor decreases as the saliency ratio decreases. The saliency ratio of the SynRMs increases with the air-gap opening, while important torque ripple appears with the higher harmonic ratio.

3.3.3 The analytical error analysis of the SynRM model

We decided to validate the electromagnetic performances under various current supplies, with the geometry shown in Figure 3.3.13. On the base of the geometry in case 2, the radial bridges are added.

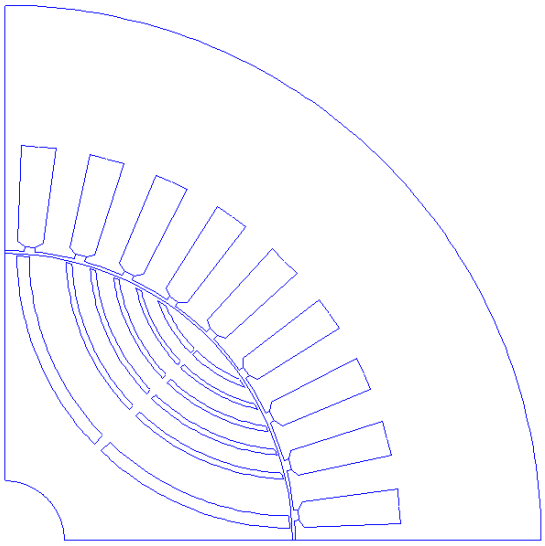

Figure 3.3.13 Motor geometry

The current density varies from 2A/mm² to 10 A/mm², and the current angle varies from 0° to 90°. Both the analytical and numerical models take the core saturation into account. The whole simulation takes 33 minutes in the analytical model, while it takes more than 5 hours in the numerical model.

The average torque vs current angle are calculated from the analytical and numerical models and are compared in Figure 3.3.14. The optimal angle (maximum torque) shifts to higher values as the motor saturates, and the torque is nearly proportional to the supply current's square value.

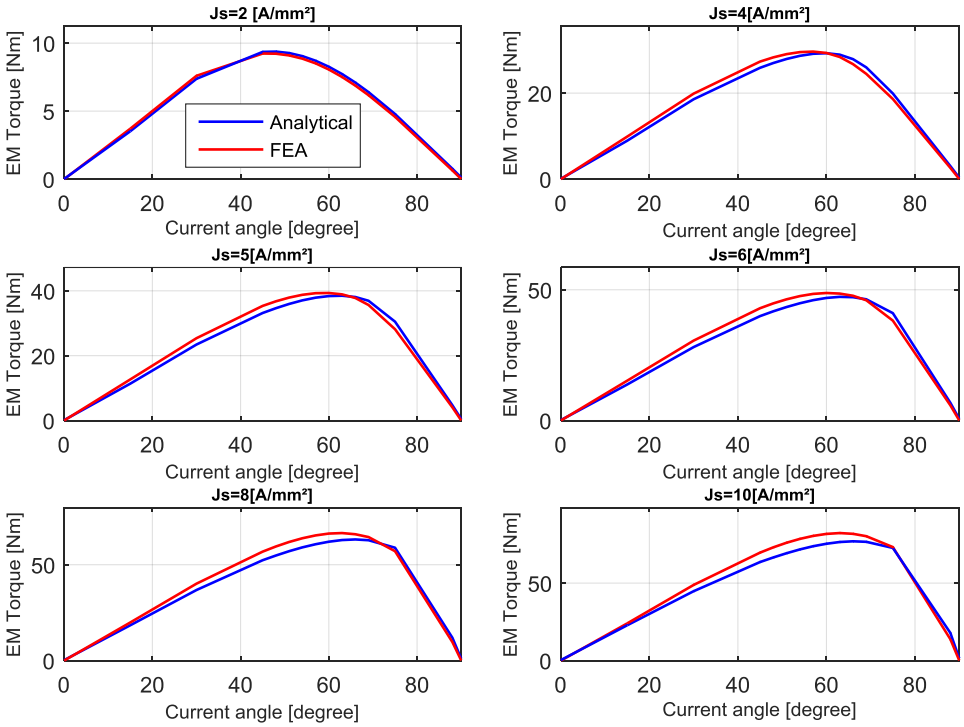

Figure 3.3.14 The comparisons between the average torques calculated from analytical and numerical models with different current supplies

The errors of the average torque estimation from the analytical model are resumed in Table 3.3.7. The absolute error is the average value of the errors with different current angles and the same current amplitude. The optimal operating range of the current angle is between 45° and 80° from the values of torque, power factor and phase voltage. Here we define the key error as the average absolute error at the operating range [45° 80°]. And the mean absolute error is the average value of the absolute errors under different current densities. The absolute error increases with the current density value which is caused by the teeth defluxing and the raising air-gap leakage when the motor is heavily saturated. As the maximum error does not occur at the operating range, the key error is slightly lower that the absolute error. The mean key error is below 5%, which is tolerable in the design applications.

Current density J_s	2 [A/mm²]	4 [A/mm²]	5 [A/mm²]	6 [A/mm²]	8 [A/mm²]	10 [A/mm²]
Absolute error [%]	4.1	5.41	5.81	6.27	7.61	8.64
Maximum error [%]	19.47	16.17	16.28	17.03	23.51	29.56
Angle with maximum error	89°	89°	89°	89°	89°	89°
Minimum error [%]	1.3	-0.2	0.79	0.79	-2.56	-0.74
Angle with minimum error	45°	60°	66°	69°	69°	75°
Key error [%]	3.58	4.69	5.23	5.83	6.72	7.12
Mean absolute error [%]	6.31					
Mean key error [%]	4.69					

Table 3.3.7 The error (including the absolute error, the key error, the maximum and the minimum errors) of the average torque estimation from the analytical model

As shown in Figure 3.3.15, the power factor calculated from analytical and numerical models are compared. The optimal angle of the power factor (the position where the value is maximum) shifts to higher angle when the supply current increases, because the saliency ratio decreases with the core saturation.

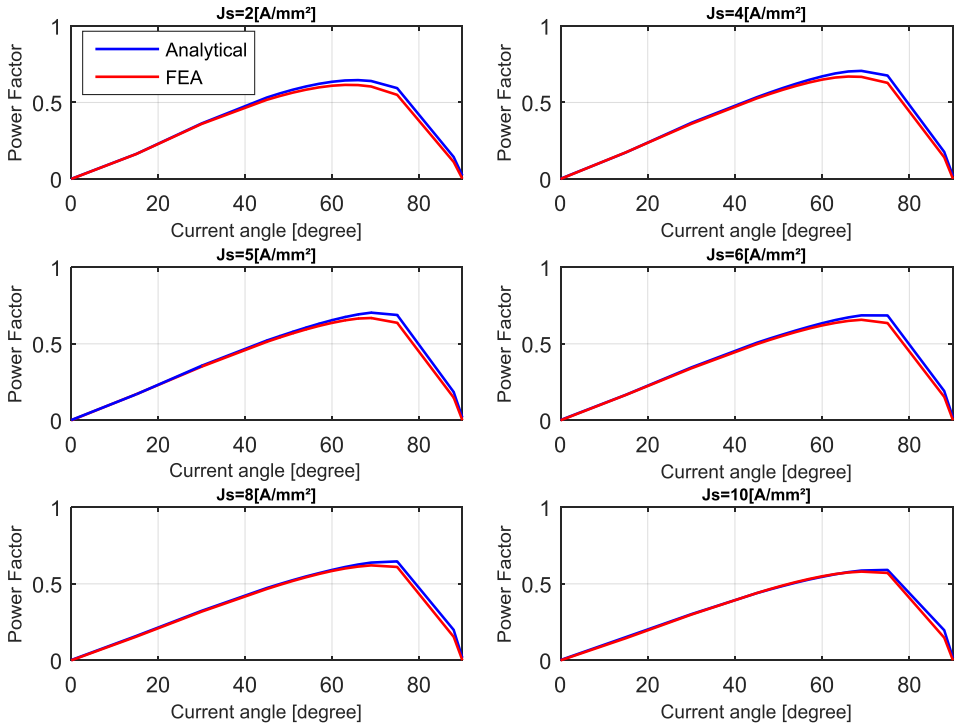

Figure 3.3.15 The comparisons between the power factors calculated from analytical and numerical models with different current supplies

In Table 3.3.8, the power factor error is resumed. The error peaks around 90°, which comes from the q-axis flux estimation. However, the estimation of the power factor in the analytical model is precise enough from the mean absolute error and key error.

Current density J_s	2 [A/mm²]	4 [A/mm²]	5 [A/mm²]	6 [A/mm²]	8 [A/mm²]	10 [A/mm²]
Absolute error [%]	5.83	4.85	4.56	4.38	4.09	3.63
Maximum error [%]	29.48	25.12	24.78	24.98	29.53	32.92
Angle with maximum error	89°	89°	89°	89°	89°	89°
Minimum error [%]	0.41	-0.42	-0.34	0.6	0.93	-0.13
Angle with minimum error	35°	40°	45°	48°	57°	45°
Key error [%]	4.49	3.58	3.25	2.97	1.91	0.86
Mean absolute error [%]	4.56					
Mean key error [%]	2.84					

Table 3.3.8 The error (including the absolute error, the key error, the maximum and the minimum errors) of the power factor estimation from the analytical model

At last, we computed the phase voltage from the analytical and numerical models (in Figure 3.3.16). As the phase voltage is determined by the flux passing through the phase winding, it peaks at $\alpha = 0°$.

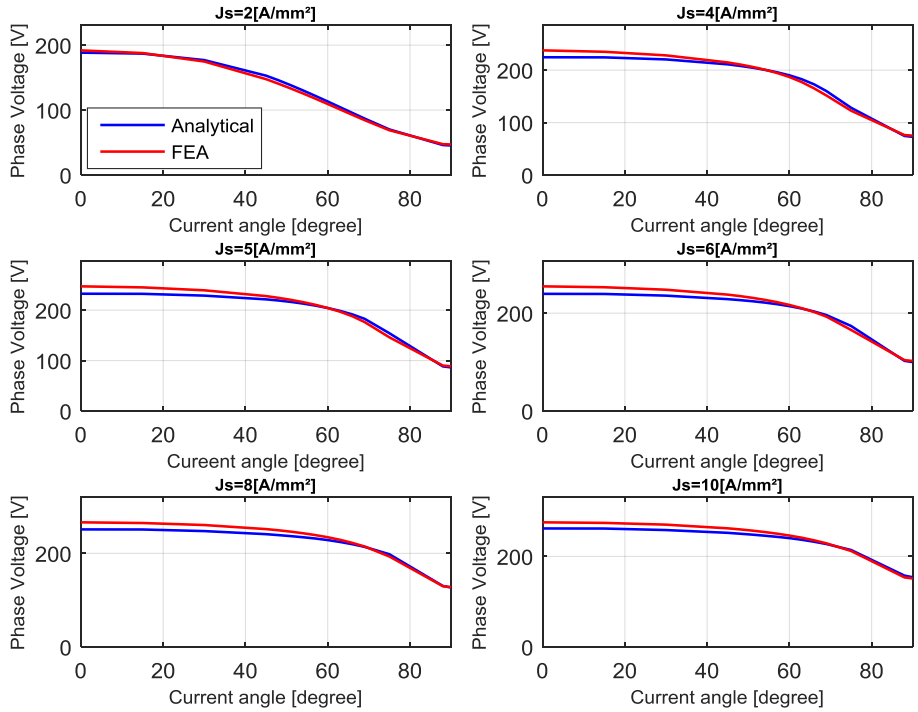

Figure 3.3.16 The comparisons between the efficient phase voltages calculated from analytical and numerical models with different current supplies

The phase voltage error is resumed in Table 3.3.9. The weak maximum error shows that the analytical model is steady in estimating the phase voltage. Both mean absolute and key errors are lower than 5%, which suggested that the analytical phase voltage is accurate for the design applications.

Current density J_s	2 [A/mm²]	4 [A/mm²]	5 [A/mm²]	6 [A/mm²]	8 [A/mm²]	10 [A/mm²]
Absolute error [%]	3.36	2.64	2.52	2.69	2.94	2.74
Maximum error [%]	3.9	5.57	5.55	-5.44	-5.22	-4.55
Angle with maximum error	51°	69°	15°	0°	0°	0°
Minimum error [%]	-0.46	-0.11	-0.03	-0.31	-0.36	-0.68
Angle with minimum error	30°	54°	60°	63°	69°	69°
Key error [%]	2.93	2.41	2.12	2.32	2.76	2.41
Mean absolute error [%]	2.9					
Mean key error [%]	2.4					

Table 3.3.9 The error (including the absolute error, the key error, the maximum and the minimum errors) of the phase voltage estimation from the analytical model

In this section, we have validated the SynRM analytical model by a "minimum set" method based on static FEA method. In four different geometries, the air-gap induction distribution, the induction in the tangential bridges and radial teeth have been compared from the analytical and numerical simulations, which have proved that the model is valid in the proposed geometries. In the same experiments, the electromagnetic performances in different geometries are compared, including the torque ripple measured from FEA simulations. The torque ripple is influenced by barrier spans and the harmonic order ratios. With a certain geometry (which is the initial rotor geometry in the design step), several kinds of errors are studied under various current supplies.

Besides the advantage in computation efforts, the mean errors of the average torque, the power factor and the phase voltage make the analytical model suitable for the machine design applications.

3.4 Validations of the SynRM mechanical model

As stated in Section 2.8, the mechanical model is established to investigate the stresses on the rotor tangential and radial bridges. The stresses computed from the analytical and numerical analysis will be compared in this section. The motor is the same with the one in Subsection 3.3.2. The Von Mises stress distribution from the numerical model is presented in Figure 3.4.1. The stress in the radial and tangential bridges is important, and the barrier with larger span angle gets higher stress, which suggests that the bridge should be arranged wider around the barriers with larger spans. The critical speed has been set to be 12000 rpm.

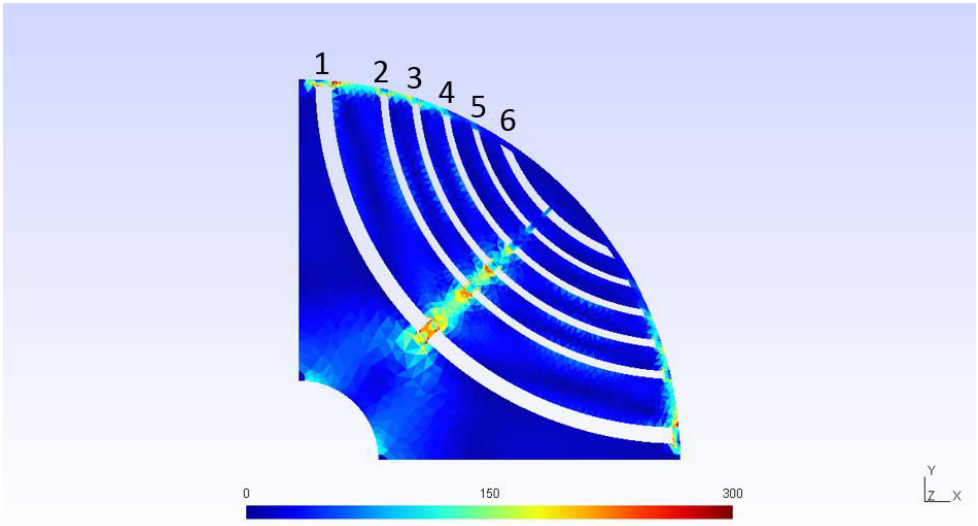

(a)

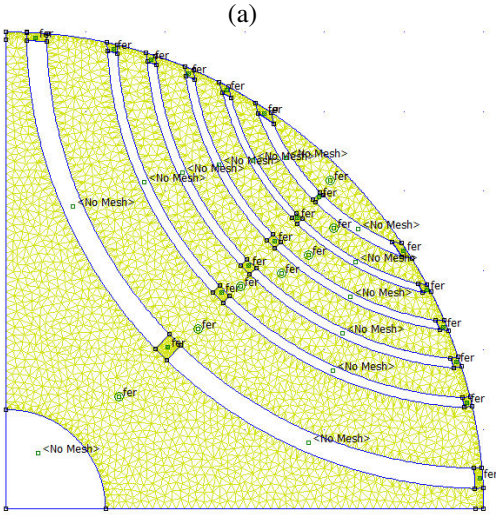

(b)

Figure 3.4.1 The Von Mises stress distribution ([MPa]) of a SynRM with single radial bridge per barrier calculated from the numerical model (calculation code from GeePs) (a) the mesh (1291 nodes) (b)

In Table 3.4.1, the numerical mean stress on each tangential and radial bridges have been listed (the bridge number is noted as in Figure 3.4.1), and the analytical value as well. The mean error of the mechanical model is higher than the one in the electromagnetic model. The maximum stress in the analytical model is higher than the numerical value, since the stress in each bridge is estimated with other neighbouring barriers neglected.

	1	2	3	4	5	6
Numerical average stress on the radial bridge [MPa]	260	200	170	130	100	80
Analytical model stress on the radial bridge [MPa]	304	233	189	140	107	70
Mean error %	12					
Numerical average stress on the tangential bridge [MPa]	200	140	100	80	50	20
Analytical model Stress on the tangential bridge [MPa]	207	122	82	48	25	10
Mean error %	29					
Maximum stress error %	17					

Table 3.4.1 The stresses on the radial and the tangential bridge calculated from numerical and analytical models and the mean error of the analytical model

In this section, the analytical mechanical model has been evaluated by the numerical analysis. Compared with the electromagnetic model, the mechanical model is relatively coarse as it is simple with several hypotheses taken. Since the stress calculations serve as the design constraint, the analytical error is tolerable.

3.5 Conclusions

The IM electromagnetic model was firstly validated in this chapter. The resistance and inductance of rectangular and non-rectangular bars were calculated from the analytical model and the harmonic FEA analysis. The analytical model is valid with different bar shapes according to the analytical error value. The no-load magnetizing inductances calculated from the analytical and numerical methods were compared with different air-gap induction amplitudes. The error is tolerable while the machine is not heavily saturated. Besides the equivalent parameter validation, the analytical model was validated by the transient FEA analysis at several working points since the transient method is effort-consuming. We have proposed a novel method combining the analytical model and the static FEA method. The method calculates the power factor and phase voltage within one simulation, and that could not be realized with harmonic FEA analysis. The analytical model, the harmonic FEA and the proposed method were applied in a defined machine geometry with different current supplies. The average errors of the torque, the power factor and the phase voltage have shown the accuracy and robustness of the IM analytical model.

The SynRM electromagnetic model was validated with a proposed method based on static FEA model. In several kinds of rotor geometries, the induction distribution in the air-gap and the rotor bridges calculated from analytical and numerical models were compared. The results have shown that the analytical model is valid on the proposed geometries. Besides, we have compared and analyzed the electromagnetic performances (the torque, the power factor, the phase voltage and the torque ripple) in different geometries with the same electrical supply. At last, the analytical model was validated with different current supplies in one motor geometry. The analytical error of the average torque, the power factor and the phase voltage was tracked and analyzed. Finally, the SynRM mechanical model was validated with numerical analysis in the same motor with the electromagnetic test. The error is more important than the electromagnetic error, but still tolerable for the design application.

However, the analytical models are surely not accurate for all the applications, for example when the motors are heavily saturated. The sensibility analysis of the analytical model becomes one of interesting future work. In the design procedure, the analytical estimations on the optimized motors should be verified with the proposed numerical analysis.

3.6 References

[ALBB09] L. Alberti, N. Bianchi, and S. Bolognani, "A finite-element procedure to compute variable speed induction machine performance," in *Energy Conversion Congress and Exposition, 2009. ECCE 2009. IEEE*, 2009, pp. 1280–1287.

[BAPM07] N. Bianchi, L. Alberti, M. Popescu, and T. J. E. Miller, "MMF Harmonics Effect on the Embedded FE-Analytical Computation of PM Motors," in *Industry Applications Conference, 2007. 42nd IAS Annual Meeting. Conference Record of the 2007 IEEE*, 2007, pp. 1544–1551.

[BONA10] I. Boldea and S. A. Nasar, *The induction machines design handbook*, 2nd ed. Boca Raton, FL: CRC Press/Taylor & Francis, 2010.

[BRSU92] S. C. Brenner and L.-Y. Sung, "Linear Finite Element Methods for Planar Linear Elasticity," *Mathematics of Computation*, vol. 59, no. 200, p. 321, Oct. 1992.

[FALK91] R. S. Falk, "Nonconforming finite element methods for the equations of linear elasticity," *Mathematics of Computation*, vol. 57, no. 196, pp. 529–529, Jan. 1991.

[FLUX06] 2D Flux, "Induction Machine Calculations in Flux2D," Preflux2D 9.2, 2006.

[LIUW07] T. A. Lipo, University of Wisconsin--Madison, and Wisconsin Power Electronics Research Center, *Introduction to AC machine design*, Madison, WI: Wisconsin Power Electronics Research Center, University of Wisconsin, 2007.

[MEEK10] D. Meeker, "Finite Element Method Magnetics Version 4.2: User's Manual," FEMM, Oct-2010.

[PDDV13] D. Prieto, B. Daguse, P. Dessante, and J.-C. Vannier, "Performance comparison of the permanent magnet assisted synchronous reluctance motor and the double magnet synchronous motor," in *Power Electronics and Applications (EPE), 2013 15th European Conference on*, 2013, pp. 1–7.

[PRIE15] D. Prieto, "Modélisation et optimisation des machines synchro-réluctantes à aimants permanents et de leur électronique," Thesis (CentraleSupélec), Jul-2015.

[SALO95] S. J. Salon, *Finite Element Analysis of Electrical Machines*, Boston, MA: Springer US, 1995.

Chapter 4 Optimization for the traction application

Chapter 4 Optimization for the traction application

4.1 Introduction

Since the studied power train system will be applied in electric vehicles, the driving cycles obtained from real world tests will be discussed and considered as the driving specifications.

The optimization strategy considering geometrical parameters and electrical controls of electric machines will be introduced and applied for both induction and synchronous reluctant machines. The optimization details, such as the design specifications, applied algorithms and different kinds of constraints for two kind of electric machines will be discussed as well. Besides, the optimization results will be validated by finite element analysis at the selected working points. And the torque ripple of the optimized SynRM will be verified by finite element analysis as well.

The optimized IMs and SynRMs for the purpose to reduce the total losses over the driving cycle will be compared following their volume, cost, and electrical performances over the cycle. The Pareto Front obtained from the bi-objective optimization goaling to optimize the total losses and the motor cost, will be compared as well. The comparison results will be resumed and analyzed at last.

4.2 Driving condition specification

Electric machines are designed as an electric vehicle traction engine, which means that they will operate within a wide range of rotation speeds and power. To specify the driving conditions, the driving cycles will be introduced firstly.

4.2.1 Driving cycles

The driving cycle ([BLMB09]), which is made up by hundreds or thousands of data points, is used to represent the vehicle engine speed and power versus time in the real driving world. Various driving cycles are produced for different car types (passenger cars and light trucks for example) under different driving conditions (urban, road, and highway) in different countries. These driving cycles were firstly applied in the assessment of vehicle performances, for example the measurement of fuel consumptions, and polluting emissions. Besides, they are used in the

propulsion system simulations. Recently, the driving cycles were used in EV power system simulations as well. Here, we introduce some most popular driving cycles used in the power train design.

- ***New European Driving Cycle***

The New European Driving Cycle (NEDC) was proposed to assess the pollutant emission level and the fuel consumption in European passenger cars (light trucks excluded) in 1997. The cycle is conducted on a cold vehicle at 20-30°C, with all ancillary loads turned off (air conditioning compressor and fan, lights, heated rear window, etc.). The whole NEDC is composed of 4 repeated ECE-15 urban driving cycles and one extra-urban driving cycle (as shown in Figure 4.2.1). The ECE-15 urban driving cycle was introduced to represent typical driving conditions in large European cities, while the extra-urban driving cycle was designed to represent more aggressive, high speed driving modes. The NEDC is considered to be a bit out of date since it replicates real-world driving conditions and does not consider the modern driving technologies.

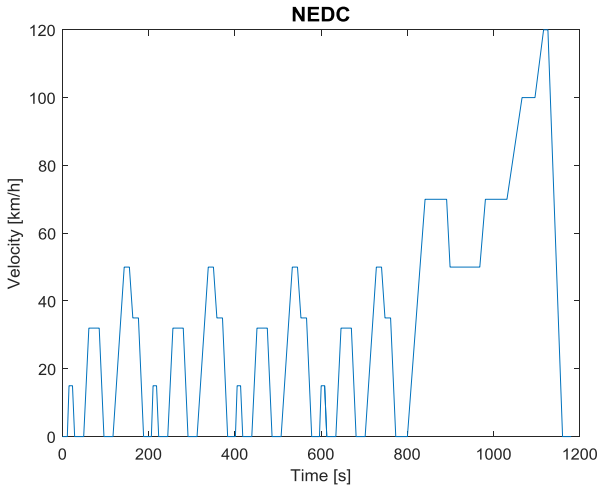

Figure 4.2.1 The New European driving cycle: 4 repeated ECE-15 cycles and one extra-urban cycle

- ***Worldwide harmonized Light vehicles Test Procedures***

The Worldwide harmonized Light vehicles Test Procedures (WLTP) are considered as a global standard for determining the levels of fuel or energy consumptions, polluting emissions and electric range of light-duty vehicles. It is developed by experts from European and Asiatic countries, taking each country's traffic condition and driving characteristic into consideration. Three different test cycles are included in WLTC, which is classified by vehicle power-weight ratio PWr in [$kW/Tonne$]. Most electric cars have power-weight ratios of 40-70 $kW/Tonne$, which belong to Class 3: high-power vehicles with $PWr > 34$. The Class 3 driving cycle includes four driving speed ranges: low, medium, high, and extra high speeds (see Figure 4.2.2). WLTP allows to calculate the optimal shift points with the real power-weight ratio within normalized engine speeds, which are not considered in other kinds of vehicle test procedures. Since the final version will come up in the year of 2017, the current database is not assured as the final one.

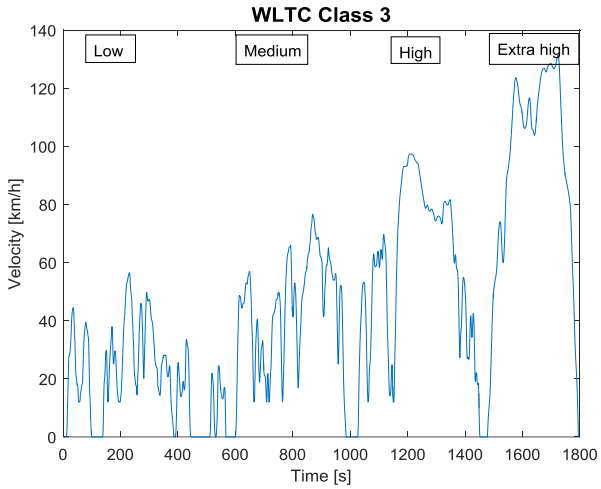

Figure 4.2.2 The WLTC driving cycle for a Class 3 vehicle: low, medium, high and extra high speed ranges

- ***Common Artemis Driving Cycles***

The Common Artemis Driving Cycles (CADCs) were developed within the European Artemis (Assessment and Reliability of Transport Emission Models and Inventory Systems) project ([ANDR04]), based on statistical analysis of a large set of European real world driving patterns. The real world driving cycles based on different driving conditions (urban, congested urban, road, motorway, etc.) and different instrumented vehicles (according to vehicle power to weight ratio) are classified into several driving cycle databases. Then statistical analysis such as Principle Component Analysis (PCA) and data-cluster method were conducted in order to develop one or more representative cycles for recorded conditions ([CRIN89]). In Figure 4.2.3, the Artemis cycle is composed of two urban and one motorway 130 cycles, which considers both light and heavy driving duties.

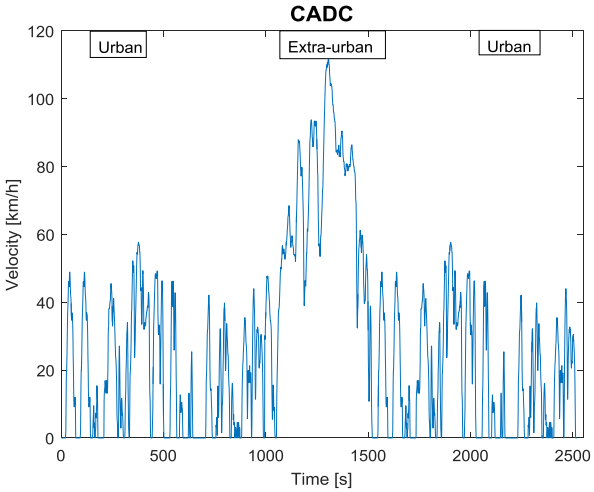

Figure 4.2.3 Common Artemis Driving Cycle: urban, Motorway 130, urban driving conditions

Among them, NEDC are the earliest cycles while WLTP are the latest worldwide cycles. Since the final version of WLTP has not been verified, CADCs are taken into consideration in this study.

4.2.2 Method to select the working points

In Figure 4.2.4, the engine power versus the rotation speed is presented, where the data are tested by some partner manufacturers, following the CADCs (Figure 4.2.3). There are more than two thousand working points in this driving database.

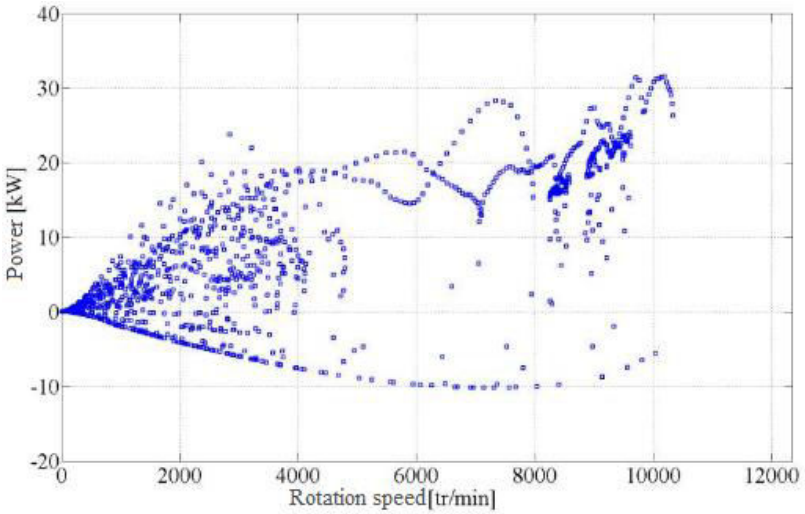

Figure 4.2.4 Electric power measured in a test bench at the referring speeds in the chosen CADC cycle [DAGU13]

As the main objective is to minimize the energy losses in the whole cycle, the losses at each working point in the cycle should be accounted. To avoid a long-term optimization, it is not surprising that one picks some typical working points from the driving cycle to simulate the considered driving conditions. In several literatures, statistical methods to extract representative points have been introduced. For example, authors in [KRCM12] have realized the working point selection with the barycenter method, when the torque-speed plan is cut into several rectangular regions. Here, we choose the method in [DDVV12]. In the power-speed plan, all working points are partitioned with *k-means* clustering method ([DHMO01]) into several clusters. In each cluster, a representative point is selected with the barycenter method. With *k-means* method, working points in the power-speed plan are classified into 12 clusters (they are represented with different colors as shown in Figure 4.2.5): 8 clusters at motor mode, and 4 at brake mode. The representative point is selected and assigned with a weight according to the point number in its cluster (the red-cross points in Figure 4.2.5). Besides, a constant power speed range is defined as the transient cycle boundary (red line). The Constant Power Speed Ratio (CPSR) is the ratio between the highest speed and the lowest speed at rated power, and the cycle in our case requires a CPSR of 5.5:1. This method and the presented data is validated in [DAGU13].

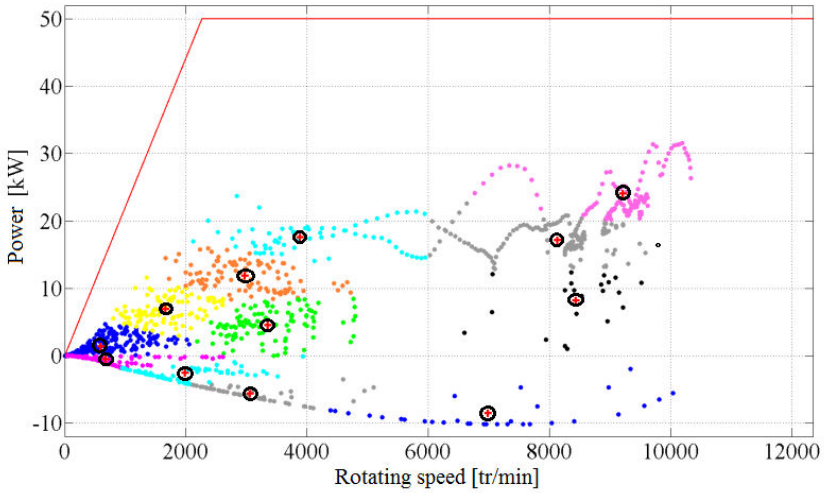

Figure 4.2.5 Cluster partition in the power-speed plan and selection of the barycenter point in each cluster ([DAGU13])

The selected working points and the power speed range of the adopted cycle are listed in Table 4.2.1, two points (at base and highest speeds) in the constant power speed range are selected as the cycle limits (the motor should work at cycle limit points under electrical constraints). These two cycles will serve as the driving specifications in the following sections.

Number	*Speed [tr/min]*	*Torque [Nm]*	*Power [kW]*	*Weight*	
		Motor mode			
1	593	21.74	1.35	439	Working points considered
2	1666	39.55	6.9	193	
3	2970	38.1	11.85	190	
4	3355	12.95	4.55	223	
5	3884	43.15	17.55	95	
6	8134	20.16	17.17	180	
7	8435	9.24	8.16	21	
8	9216	24.93	24.06	120	
		Brake mode			
9	681	-7.15	-0.51	202	
10	1987	-12.5	-2.6	170	
11	3062	-17.62	-5.65	113	
12	6983	-11.66	-8.53	32	
		Power speed range			
13	2263	211	50	-	Cycle limits
14	12350	38.7	50	-	

Table 4.2.1 Data of selected points on motor and brake modes, and the power speed range

We have introduced several types of driving cycles in this section, including NEDC, WLTP and CADC, where the last term was selected in our case. We have decided to reduce the working point number in the real driving cycle for the sake of optimization time. The *k-mean* clustering method is applied to partition the data in the power-speed plan into several clusters, then the

barycenter of each cluster is selected to represent the whole cluster data. Besides, two points on the constant power speed range are used as the transient cycle constraint on the traction engine.

4.3 Optimization Model

In most industrial applications, the global optimization is required since it aims to find the minimum over the whole instance instead of a local minimum. The standard form of a continuous mono-objective optimization problem is described as:

$$\begin{aligned} &\underset{\theta \subseteq \Theta}{minimize} && f(\theta) \\ &subject\ to && g_i(\theta) \leq 0 && (i = 1, \cdots, m) \\ & && h_j(\theta) = 0 && (j = 1, \cdots, p) \end{aligned}$$

Where:

-*f*: the objective function to be minimized;

-θ: the *n*-dimensional variable vector;

-Θ: the variable instance ($\Theta \subseteq \mathbb{R}^n$);

-g_i: the i_{th} inequality constraint function over the variable *x*;

-h_j: the j_{th} equality constraint function.

4.3.1 Global optimization algorithms

Before introducing our optimization models, a review of global optimization methods will be carried out briefly. To treat a global optimization problem, there are mainly two branches of methods:

- Direct optimization methods

Direct optimization methods ([FLOU00] [NEUM04]) aims to find a minimum with the help of some deterministic heuristic (gradient for example). In our case (nonlinear optimization with constraints), the Sequential Quadratic Programming (SQP) ([HOPA95] [NOWR06]) is one of the most popular deterministic methods.

- Stochastic optimization methods

Stochastic optimization methods ([SPAL03]) are applicable in optimization problems with nonlinear objective functions, and nonlinear constraints. It is more likely to find a global optimum with stochastic methods rather than deterministic ones. Since the search methods are stochastic, they take risk to find different optimal solutions in different realizations. Random search methods are popular and they are often associated with metaheuristics ([BDGG09]). Metaheuristics ([GEPO10]) are strategies derived from natural experiences or evolutionary processes, which provide a sufficiently good solution to an optimization problem. Among diverse stochastic methods based on metaheuristics, Evolutionary Computing (EC) approaches are largely applied in energy conversion and mechanical system design cases ([PUGS09][JVMG11][HASS14]). EC approaches exploit a set of metaheuristic techniques based on principles of biological evolution ([EISM03]). In an Evolutionary Algorithm (EA), there are some implementing mechanisms inspired from the biological evolution:

-*Individual*: an individual is a possible solution to the optimization problem.
-*Population*: a population is a set of individuals.
-*Parent*: parents are individuals selected from the population. They mate and produce offspring.
-*Offspring*: the offspring is the next generation of the parent individual.
-*Recombination*: the recombination is the operation that produces offsprings.
-*Mutation*: the mutation is the operation that makes a portion of new individuals flip with some probability. The mutation rate may influence the feasibility of the optimization.
-*Selection*: the selection operation is applied to choose the best individuals when the recent population is judged by the fitness function.
-*Fitness function*: the fitness function is determined by the objective function. Generally, optimization constraints are transformed into penalty terms which are accounted in the fitness function.

As shown in Figure 4.3.1, an Evolutionary Algorithm starts from the population initialization. The initial population is often generated randomly. Then parent individuals are selected from the current population through a fitness function. Through the recombination and mutation operations, the offspring is generated. The population generation loop is repeated until the defined termination condition has been satisfied.

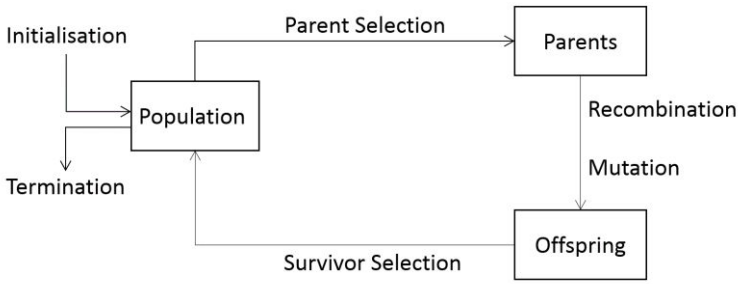

Figure 4.3.1 The general scheme of an Evolutionary algorithm ([EISM03])

EA family includes Genetic algorithm (GA), Evolutionary Programing (EP), Evolutionary Strategy (ES) and so on. The individual is represented by binary strings over a finite alphabet in GAs, finite state machines in classical EPs, and real-valued vectors in ESs ([EISM03]). GA and EP approaches are suitable for solving discrete optimization problems, while ES approaches do better in solving a continuous or a mixed optimization problem. In our case, as the geometrical variables are mostly continuous, ES approaches are better alternatives to other evolutionary algorithms.

- ***Differential Evolution***

Among several ES approaches, Differential Evolution (DE) is simple but powerful ([PRSL05] [CHAK08]). It is combined with direction-based search technique, proposed by Storn and Price in 1997 ([STPR97]). DE maintains the individual and population model, the recombination and mutation operators, and the selection process. The main difference between DE and other ES approaches relies on the determination of the mutation operator.

Here, we take a simple example to show how DE selects individuals. Firstly, we suppose that the i_{th} individual x_i has n dimensions in the search space, which can be expressed as:

$$x_i = (x_{i,1}, x_{i,2}, \cdots, x_{i,n})$$
$$x_{i,j} \in \mathbb{R}, j = 1,2, \cdots, n \qquad 4.3.1$$

The standard mutation operator of DE is composed of three randomly selected individuals from the current population, the selected individuals r_1, r_2, r_3 $(r_1 \neq r_2 \neq r_3 \neq x_i)$ form a simplex like triangle. For individual x_i, its mutant v_i is:

$$v_i = r_1 + F(r_2 - r_3) \qquad 4.3.2$$

Where F is a positive real number. Equation 4.3.2 shows that DE is a direction-based research. After mutation, DE recombines the information of parent individuals x_i and v_i with a uniform recombination operator, to generate the offspring u_i. An integer number j_{rand} is randomly chosen in the range [1, n]. The recombination operator is defined in equation 4.3.3:

$$u_{i,j} = \begin{cases} v_{i,j} & rand \leq C_r \ or \ j = j_{rand} \\ x_{i,j} & otherwise \end{cases} \qquad 4.3.3$$

Where C_r is the recombination probability coefficient which determines the probability that the offspring will inherit genes from the mutant. C_r will be recoded during the generation of the new population following certain rule (such as self-adaptive crossover probability control [QISU05]). Then u_i competes with x_i for surviving in the next generation.

The initialization and the termination criteria might be the same as other ES approaches. DE method is robust, and easy to be implemented, especially into parallel computation. It is chosen to solve the global optimization problem in this work.

- ***Multi-objective optimization***

When there are two or more optimization objectives in an optimization problem, it is called a Multi-objective Optimization Problem (MOP). Usually, the objectives are conflicting, which means that a single solution could not be the optimal in all objectives. From Pareto's theory ([BARR12]), it is more useful to discuss the trade-off relation rather than a single "good" solution when treating a MOP. A solution x_1 is defined to dominate another one x_2 if the solution x_1 is better than x_2 in all objectives, and x_2 is named as a dominated solution. The Pareto Efficient Front represents a group of non-dominated solutions, as shown in Figure 4.3.2 (see the blue line).

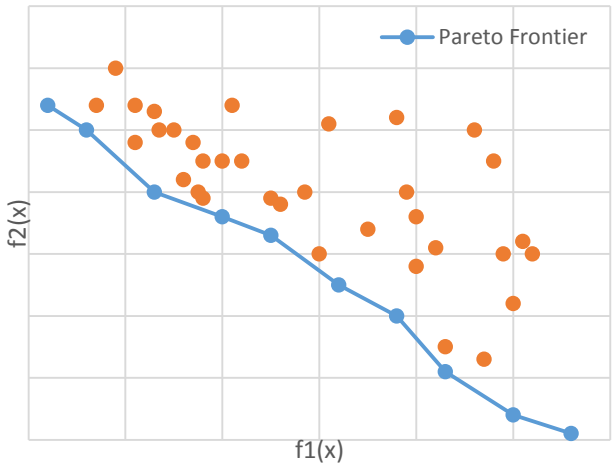

Figure 4.3.2 An example of a Pareto Efficient Front

EA approaches are considered to be efficient in treating MOPs, since they could provide users a group of solutions (individuals) at each iteration. When EA approaches are applied in MOPs, the selection and mutation mechanisms should be adapted in order to prevent all individuals from converging to one direction (in favour of one objective). The selection operator becomes more complicated since the comparison between two individuals is useless here. When the new population is generated, it is ranked with the Pareto rank method or other sophisticated methods in order to find the non-dominated solutions in the current population ([GOLD89]), these non-dominated points will be ranked in rank 1. At each iteration, the individuals are classified by their dominance rank number, and the solutions in rank 1 will be moved to the Pareto dominance set. In our case, the Non-dominated Sorting Genetic Algorithm II (NSGA-II) is applied to embed with the DE method in treating the MOPs ([DPAM02]). It generates the Pareto set with a method based on distance method: crowding distance method. The adapted algorithm process is detailed as a flow chart in Figure 4.3.3.

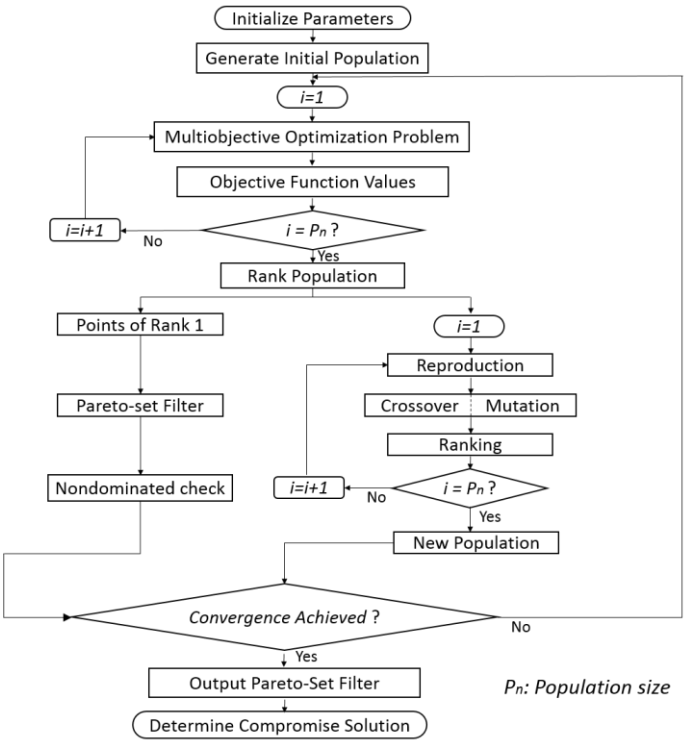

Figure 4.3.3 Detailed multi-objective optimization process using GA approaches

4.3.2 General optimization scheme

In this subsection, we discuss the optimization objectives and the general scheme in our cases. There are two global optimization objectives:

- To minimize the system energy losses in the whole driving cycle

From equation 2.6.28-29, the total energy losses P_{loss_sys} and the energy efficiency η_{dc} in the driving cycle are defined. Here, the minimization of the system losses is named "OBJ1".

- To minimize the EM cost

The minimization of the EM cost is called "OBJ2".

To deal with the mono objective minimization of the system energy losses an intertwined optimization will be carried out. Firstly, a master problem (OPT1) will deal with the optimization of the variables defining the motor geometries. Secondly for each individual of the master problem a second slave optimization (OPT2) will be carried out, minimizing the system losses by dealing with the control parameters (electrical mainly). By separating the main optimization into to simpler one, we will assure that a given motor (an individual characterized by the variables of OPT1) will be controlled in such a way that the total system losses will be minimized. The constraints of OPT1 and OPT2 are named respectively CONT1 and CONT2. To find the total energy losses of an individual, each losses are added for each working point defined in the reduced duty cycle (see Table 4.2.1). The general scheme of the global optimization is presented in Figure 4.3.4. The details of OPT1 and OPT2 including optimization variables and constraints will be discussed in the following sections. The motor cost minimization will be treated by a regular optimization scheme and will be added as a second objective in the multi-objective problem.

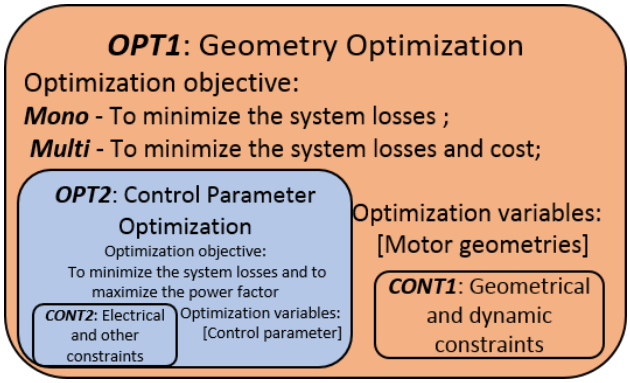

Figure 4.3.4 General optimization scheme

4.3.3 Traction system specification

There are some general specifications for applied traction system including nominal battery voltage, nominal converter current, EM external diameter and so on. They will be imposed on both IM and SynRM designs. Since the focus of the thesis lies on the performance comparisons of optimized IMs and SynRMs applied for EV traction systems, we choose the d.c. battery and the PWM converter. The EM volume constraints are taken from some industrial experiences, and with market favoured sizes. The EM volume constraint on slot current density and core flux density are considered from thermal and magnetic aspects ([BONA10]). The conductor in a wire is described by a constant slot filling factor.

Battery	
Nominal battery voltage	U_{dc} = 440 V
Converter	
Nominal converter current	I_{inv} = 250 A
EM	
Core material	M330-35
Phase number	m = 3
External diameter	D_{ext} <= 260 mm
Motor length	L <= 230 mm
Shaft diameter	D_{int} = 25 mm
Slot current density	J_{max} = 10 A/mm²
Core induction	B_{max} = 2.2 T
Motor Power	P_m <= 50 kW
Three phase configuration	Star
Winding type	Distributed with single layer
Stator slot number per phase per pole	q = 3
Stator slot filling factor	K_{fill} = 0.5
Motor cooling system	Air cooling system

Table 4.3.1 Specifications on battery, power converter and EM sizes

In this section, principle numerical methods to treat a global optimization problem have been reviewed firstly. Differential Evolution method will be applied in our case. Then we discussed the Multi-objective Optimization Problems, in which the Pareto trade-off principle is applied to define the non-dominated solutions. At last, we defined the mono-objective and bi-

objective problems in our case, and proposed an optimization model to solve them. This optimization model will be applied in both IM and SynRM designs. Some general specifications have been defined in designing the EMs applied in the traction system.

4.4 Control parameter optimization (OPT2)

In this section, we discuss the optimization details of the OPT2. OPT2 is named "Control Parameter Optimization" (CPO) in this thesis as well.

Due to the adoption of the PWM techniques in the converter, the EMs could be controlled within a wide range of rotation speed and torque. In our case, a control parameter optimization is defined to minimize the system energy losses and to maximize the power factor in respecting several constraints, for a geometry predefined IM or SynRM at a defined working point (rotation speed and torque). Among them, the system energy losses can be quantified by the parameter: system energy efficiency η_{sys} (which has been illustrated in Subsection 2.6.4). A typical CPO could be described as:

$$\underset{\theta \subseteq \Theta}{maximize} \quad \eta_{sys}(\theta)$$

$$\underset{\theta \subseteq \Theta}{maximize} \quad PF(\theta)$$

$$subject\ to \quad \hat{B}_c(\theta) \leq B_{max} \qquad \text{(Magnetic constraint)}$$

$$I_s(\theta) \leq I_{inv} \qquad U_s(\theta) \leq U_{dc} \qquad \text{(Electrical constraint)}$$

$$J_s(\theta) \leq J_{max} \qquad \text{(Thermal constraint)}$$

Where:
-θ: the optimization variable, there is only one variable in the CPO since the torque and speed values are given;
-$\hat{B}_c$: the amplitude of the induction in the core;
-I_s: the efficient stator phase current;
-U_s: the efficient stator phase voltage;
-J_s: the slot current density amplitude.

A "light" CPO is desired to be applied to reduce the calculation time of the whole optimization, which means that it should contain less optimization objectives and constraints. This bi-objective optimization problem shall be transformed into mono-objective optimization problem. The simplified CPO models of IMs and SynRMs will be introduced in this section.

4.4.1 Induction Machines

We start from the investigation of electrical parameters influences on IMs. With FOC strategy, energy efficiency and power factor are defined in the variable speed drive system. In the analytical model, the reference frame of the analysis is fixed to the magnetizing flux (see Figure 2.4.4), and the control parameters are i_{sd}, i_{sq}.

The influences of electrical parameters on efficiency and power factor are investigated in Figure 4.4.1. With different control parameters, a defined 4-pole IM is tested at three different rotational speeds (593 rpm, 3884 rpm and 9216 rpm) and at the same torque (20 Nm). Stator phase currents are regulated to change the slip ratio and to keep the electromagnetic torque as constant. From Figure 4.4.1(k), the energy efficiency and power factor reach their maximum values with nearly the same electrical parameters at high and medium speed ranges. Meanwhile, the energy efficiency reaches its maximum value with a relatively low power factor at low speed range. If a CPO is realized with the strategy to maximize the energy efficiency, the optimal power factor may be not satisficing enough at low rotation speed range. From Figure 4.4.1(a), the system energy efficiency reaches a maximum value while the phase current amplitude i_s is minimized. However, the power factor with the minimum phase current is not optimal from Figure 4.4.1(b). In the same way, the power factor reaches a maximum value while the phase d-axis current i_{sd} is minimized from Figure 4.4.1(c), while the energy efficiency is still not much degraded from Figure 4.4.1(d). Figure 4.4.1(e-h) show that the phase q-axis current i_{sq} and the phase voltage v_s do not have an interesting relation with neither the energy efficiency nor the power factor. In Figure 4.4.1(i), one could see that the optimal energy efficiency appears with a lower slip ratio when the motor works within medium and high speed range, which proves that the optimal slip ratio decreases with the increase of the motor power ([BONA10]).

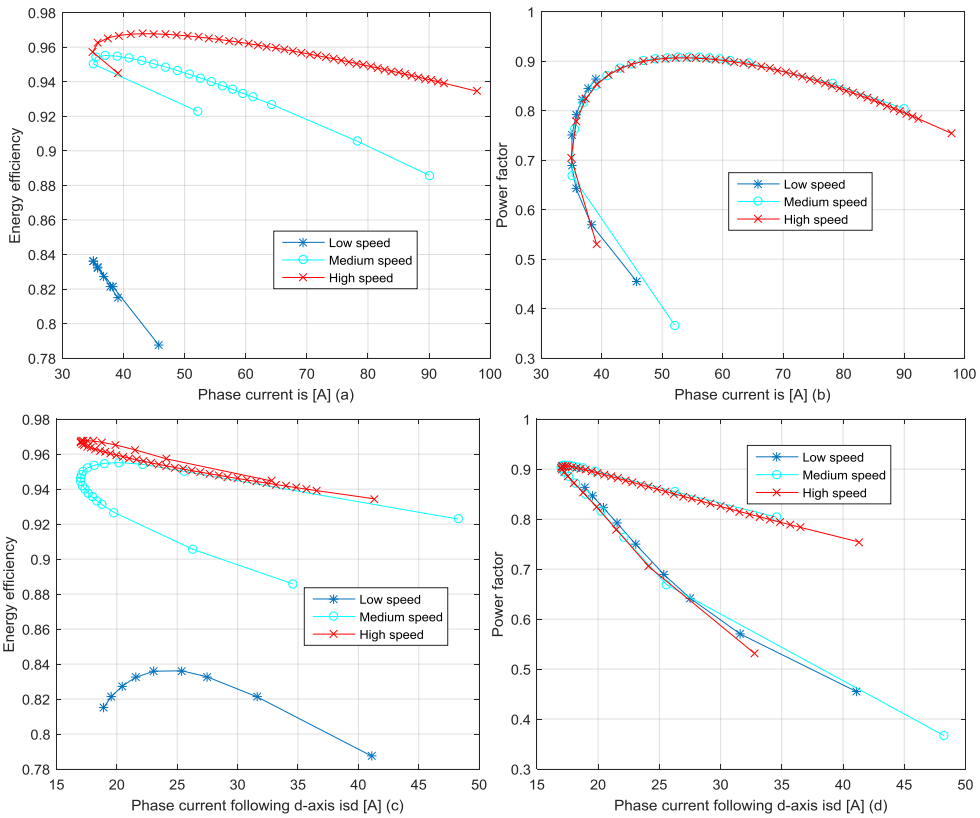

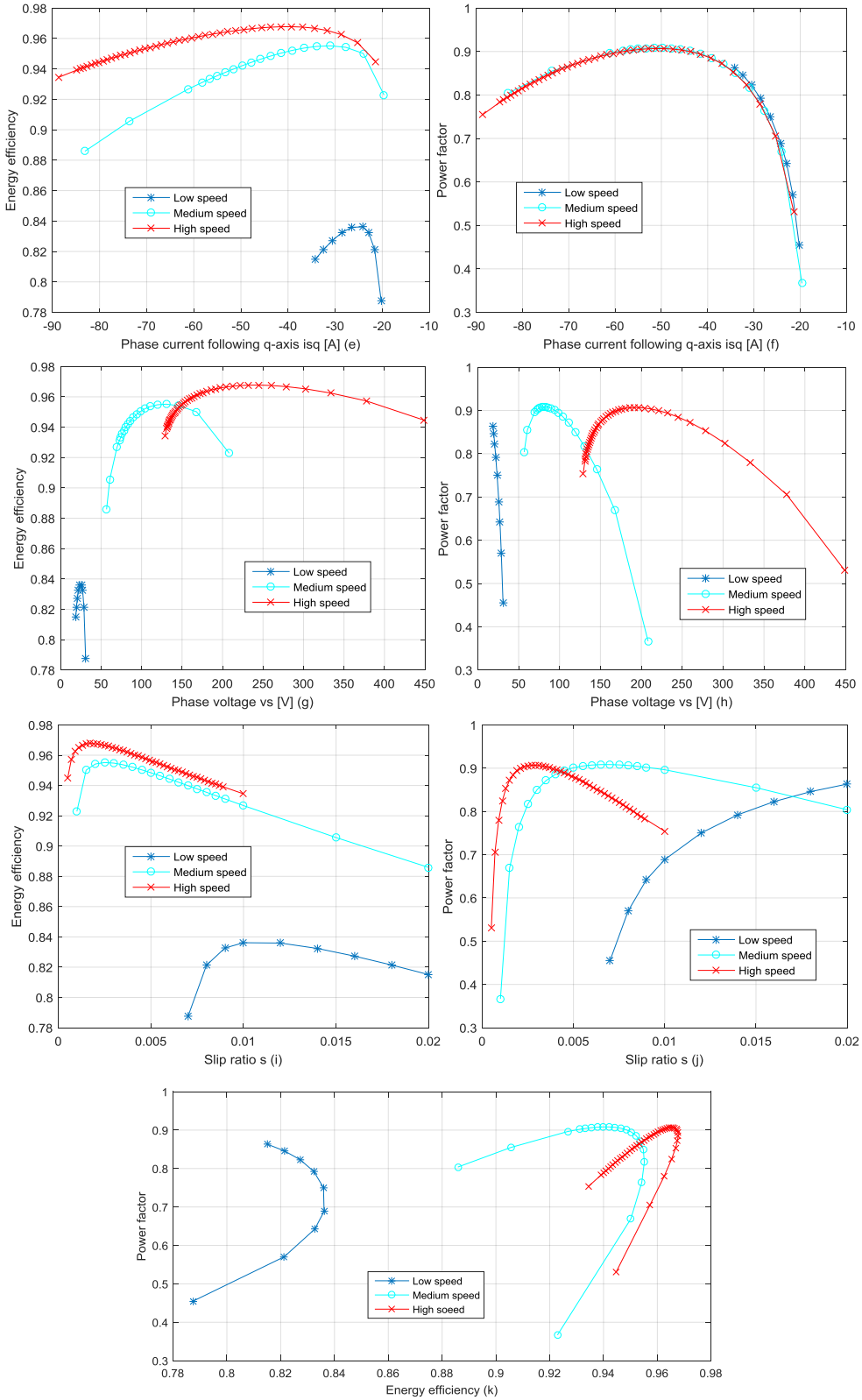

Figure 4.4.1 Influence of control parameters on energy efficiency and power factor: (a, b) stator phase current i_s (c, d) stator phase current following d-axis i_{sd} (e, f) stator phase current following q-axis i_{sq} (g, h) stator phase voltage v_s(i, j) and slip ratio s (k) the relation between energy efficiency and power factor

Searching for the best efficiency is nearly equivalent to minimize the phase current amplitude at medium and high speed ranges. It is observed that the motor power factor is more sensitive to a change in the command parameters than its energy efficiency. So we rather propose to maximize the power factor. This method somehow permits us to have a good energy efficiency (almost optimal) and an optimal power factor for the mono-objective optimization. The slip ratio is chosen as the optimization variable since its variation range is small and aware. The constraint on stator phase amplitude is removed from the initial optimization since one could see that the optimal point is around the minimum stator current. As a result, the IM CPO model is composed with two steps:

Step1: Optimization

$$\underset{s\subseteq \Theta}{maximize} \quad PF(s)$$

$$subject\ to \quad \hat{B}_c(s) \le B_{max}$$

$$U_s(s) \le U_{dc}$$

$$J_s(s) \le J_{max}$$

If the optimization successes, Continue;

Else, Break and $OUTPUT = PENALTY$ *;*

Step2: Verification

$$\text{If } I_s(s_{opt}) \le I_{inv},\ OUTPUT = P_{loss}(s_{opt})$$

Else, End and $OUTPUT = PENALTY$.

The Sequential Quadratic Programming (SQP) method is applied in STEP1. It is a kind of deterministic method to solve nonlinear optimization problems, which has been applied since the late 1970s ([BOTO00]). SQP method has been successfully implemented in many computation softwares, such as Matlab, Scilab, and so on. The analytical models are constructed with Matlab, so we have used the Matlab implementation of the SQP algorithm. When the CPO successes (which is indicated by the SQP feedback), the minimum system losses gives the objective function value. Else, the predefined penalty value is used instead of the loss value.

4.4.2 Synchronous Reluctant Machines

Now a similar research is conducted in a defined 4-pole SynRM, at the same test points as the IM. The d-q axis is defined as in Figure 2.5.1. Stator current angle is regulated to change the phase current and to keep the electromagnetic torque as constant. From Figure 4.4.2(k), the system energy efficiency and motor power factor reach their maximum values nearly simultaneously within low, medium and high speed ranges. It is observed that the system energy efficiency reaches a maximum value while the phase current amplitude i_s is minimized, in Figure 4.4.2 (a). Meanwhile, the power factor value is not much degraded with the minimum phase current. From Figure 4.4.2 (c-h), the d-axis and q-axis phase currents, and stator phase voltage do not have an obvious relation with the optimal energy efficiency and power factor. From Figure 4.4.2 (i-j),

one could see that the optimal energy efficiency and power factor appear at the current angle range: [45° 90°].

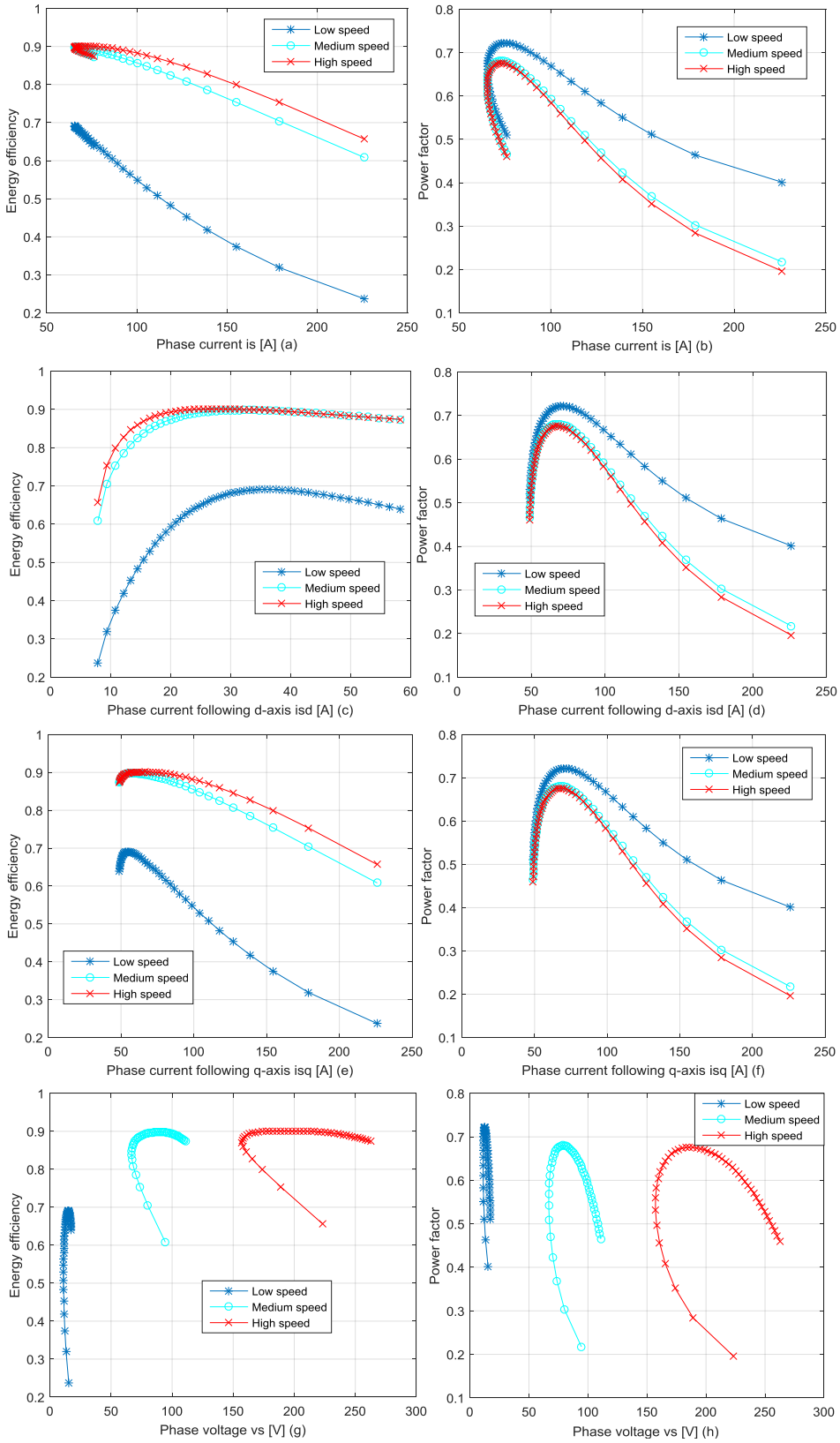

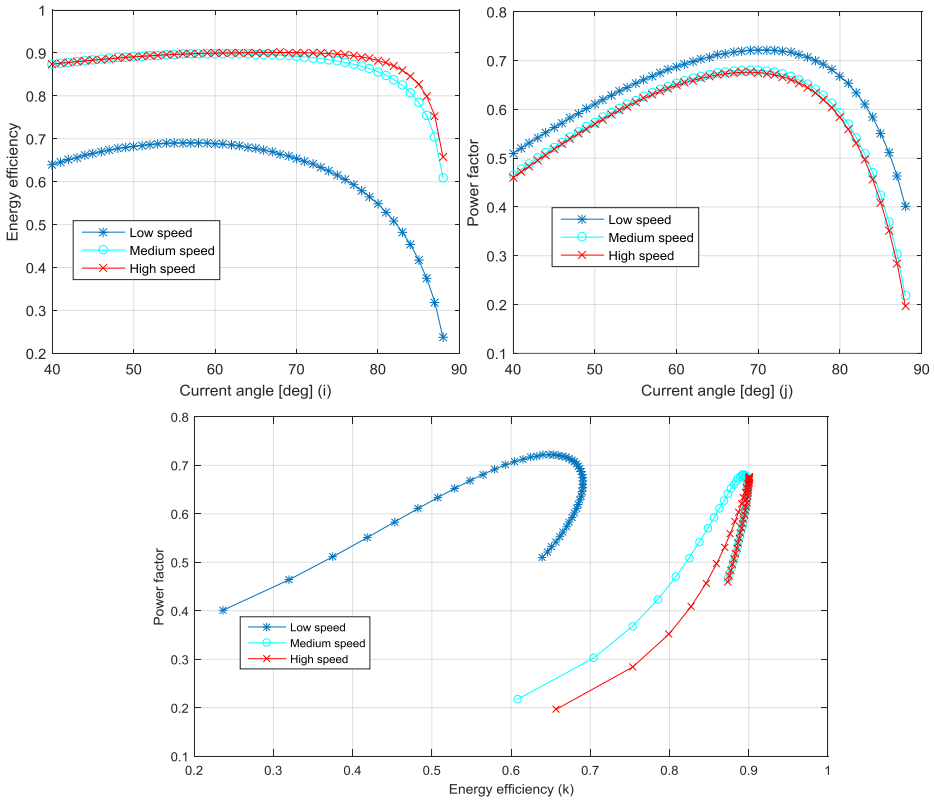

Figure 4.4.2 Influence of control parameters on energy efficiency and power factor: (a, b) stator phase current i_s (c, d) stator phase current following d-axis i_{sd} (e, f) stator phase current current following q-axis i_{sq} (g, h) stator phase voltage v_s (i, j) and current angle (k) the relation between energy efficiency and power factor

With the above observations, we decide to set the current angle as the variable, and to set the system energy efficiency as the optimization objective, since the power factor is nearly maximized when the energy efficiency is maximized. Thus, the SynRM CPO is described as:

$$\underset{\alpha \subseteq \Theta}{maximize} \quad \eta(\alpha)$$

$$subject\ to \quad \hat{B}_c(\alpha) \leq B_{max}$$

$$U_s(\alpha) \leq U_{dc}$$

$$J_s(\alpha) \leq J_{max}$$

As with the IM CPO model, the stator phase current will be verified in STEP2. And the SQP method is adopted in the SynRM CPO model as well.

4.4.3 Incorporation with the analytical model

In order to save the calculation time, we propose to take the solution of each iteration in the analytical model as the initial point for the next iteration. The general flow chart of a complete CPO incorporated with the EM analytical model is described in Figure 4.4.3. The CPO will be carried out at each working point of the reduced driving cycle.

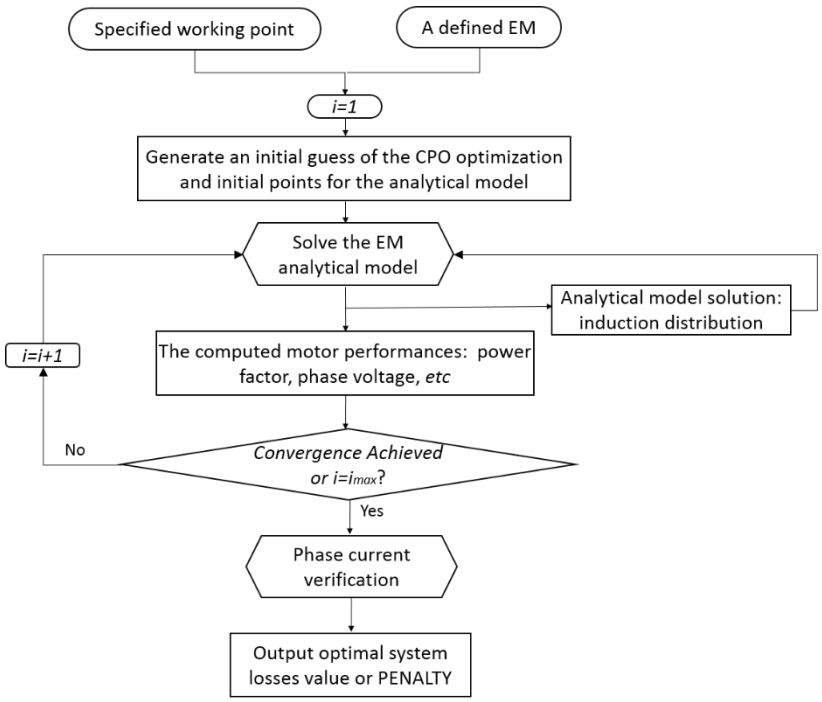

Figure 4.4.3 Flow chart of the Control Parameter Optimization incorporated with EM analytical model

4.4.4 CPO application over the cycle limits

As mentioned in Section 4.2, the EMs should be evaluated if they could work at the maximum speed and at the maximum torque of the driving cycle, while respecting the electrical constraints (thermal and electromagnetic constraints neglected). We define it as one constraint in OPT1. The CPO is applied here to define the dynamic constraint value. It is divided into two steps to get the constraint value for a defined EM: the phase current is minimized with SQP method, and then the optimal phase current is compared with the nominal current. The dynamic constraint function is realized as:

Step1: Optimization

$$\underset{\theta \subseteq \Theta}{minimize} \quad I_s(\theta)$$

$$subject\ to \quad U_s(\theta) \leq U_{dc}$$

If the optimization successes, Continue;

Else, Break and $OUTPUT = 1$ *;*

Step2: Verification

$$\text{If } I_s(s_{opt}) \leq I_{inv},\ OUTPUT = -1$$

Else, End and $OUTPUT = 1$.

In this section, we have discussed the control parameter optimization with the objective to maximize the system energy efficiency and the EM power factor. A control parameter research

have been realized in order to observe the influence of these parameters on the energy efficiency and the power factor, at different speeds. Besides, we proposed a strategy to embed the analytical model with the CPO, which accelerates the optimization speed, especially for SynRMs. The dynamic constraint in OPT1 was discussed at last as the CPO methodology is applied in the constraint function.

4.5 Induction Motor Optimization

Since the OPT2 optimization of IMs has been presented in Section 4.4, we will discuss the optimization variables and constraints of OPT1 in this section.

4.5.1 Optimization Variables and Constraints

As we concentrate on designing an IM from electrical and magnetic aspects, the electrical variables such as pole number, and magnetic variables such as slot sizing and core height should be defined. Ten optimization variables and their bounds are detailed in Table 4.5.1. The variables are chosen according to the literatures ([PUGS09]) which have carried out some sensibility research on the IM geometrical variables. Some variable boundaries are determined from some literatures ([BONA10]) such as the air-gap width and the tooth concentration ratio, and others are taken from industrial experiences.

Variable	***Bound***
Motor length L [mm]	[140 230]
Air-gap width g [mm]	[0.5 2]
Winding turn number per phase n_s	[24 60]
Rotor bar number per pole pair N_r/p	[14 18]
Stator tooth height h_{ts} [mm]	[10 40]
Rotor tooth height h_{tr} [mm]	[10 40]
Stator yoke height h_{ys} [mm]	[10 40]
Rotor yoke height h_{yr} [mm]	[10 40]
Stator tooth concentration ratio τ_{ts}	[0.4 0.6]
Rotor tooth concentration ratio τ_{tr}	[0.4 0.6]

Table 4.5.1 Optimization variables and their boundary values for IM design

Besides, there is a constraint imposed on the tooth height to ensure the tooth mechanical rigidity:

$$\frac{b_{ts}}{h_{ts}}, \frac{b_{tr}}{h_{tr}} \leq 7 \qquad 4.5.1$$

Where b_{ts}, b_{tr} are stator and rotor tooth width.

4.5.2 Mono-objective Optimization

As mentioned in Section 4.3, the system energy losses over the driving cycle are minimized in the mono-objective optimization. This optimization was carried out on a four-pole and six-pole IMs. The computation time on an Intel Xeon(R) CPU E5-2690 0 @ 2.9 GHZ using 4 core

was between 24 to 48 hours. The evolution of the fitness function is presented in Figure 4.5.1, which shows the convergence of the optimization.

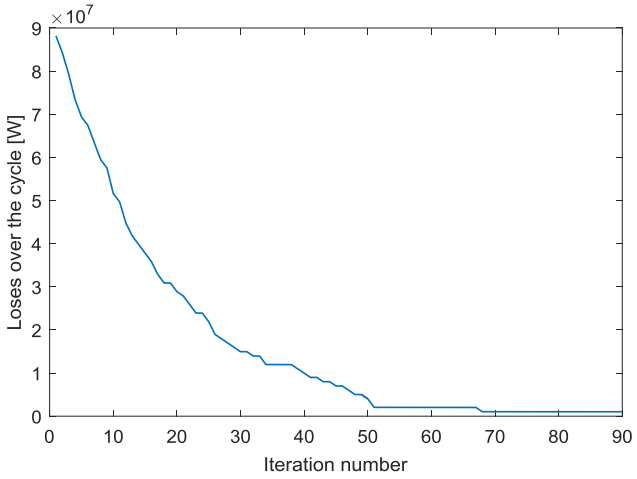

Figure 4.5.1 Evolution of the fitness function (system losses)

The optimal variables are detailed in Table 4.5.2, and the optimal motor geometry is presented in Figure 4.5.2. Since the initial point should satisfy the geometrical and dynamic constraint as presented in Section 4.3-4.4, it is chosen by the designer with a local direct optimization tool (Direct method ([EFIN03]).

Variable	***4-pole***	***6-pole***
L [mm]	190	200
g [mm]	0.5	0.5
n_s	24	24
n_r	30	43
h_{ts} [mm]	20.6	17
h_{tr} [mm]	32	29.4
h_{ys} [mm]	19.4	26.5
h_{yr} [mm]	37	40
τ_{ts}	0.6	0.54
τ_{tr}	0.52	0.51

Table 4.5.2 Value of the optimal variables for a 4-pole and a 6-pole IMs

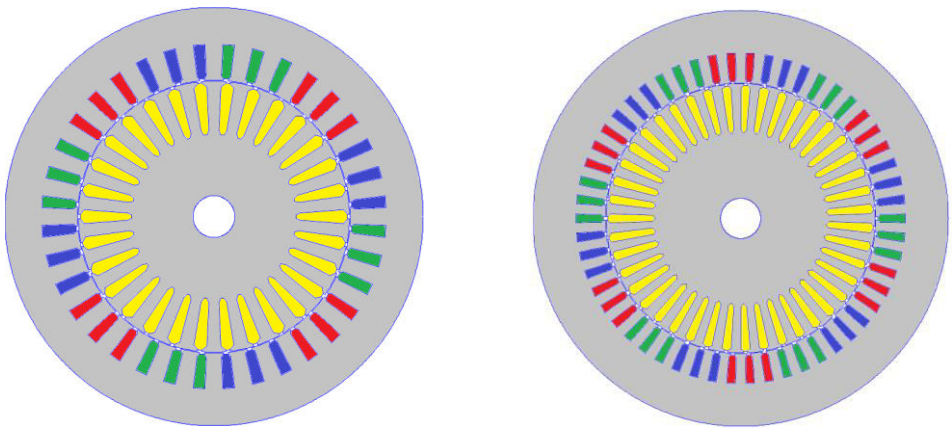

(a) (b)

Figure 4.5.2 Geometry of optimized 4-pole (a) and 6-pole (b) IMs with the same scale ratio

The two optimized IMs are compared from their volume, mass, cost and electromagnetic performances, and the results are illustrated in Table 4.5.3. The six-pole IM has a comparable volume with the four-pole IM. However, the four-pole IM weights less than the six-pole one as its iron volume is lower. As it could be supposed, the air-gap reaches its minimum dimension allowed by the constraints. The two motors use nearly the same copper, and the four-pole motor is a bit cheaper due to the higher stator coiling workforce cost in the six-pole IM. The two motors are compared from their mean energy efficiency and mean power factor over the driving cycle. Again from this point of view the four-pole IM is better than the six-pole one.

From the above comparisons, it is noted that the four-pole IM is more suitable for the traction application over the considered CADC cycle. The validation of the optimized motor by FEA tools could be found in Appendix 2.

Performance	***4-pole***	***6-pole***	***Ratio 6-pole/4-pole***
External diameter	250 mm	250 mm	1
Motor length	190 mm	200 mm	1.05
Volume	9.4 l	9.7 l	1.04
Mass	67 kg	75 kg	1.12
Motor Cost	1350 €	1552 €	1.15
Mean energy efficiency	0.937	0.928	0.99
Mean power factor	0.82	0.8	0.97

Table 4.5.3 Characteristic comparisons of optimized 4-pole and 6-pole IMs

4.5.3 Bi-objective Optimization

After the mono-objective optimization and the comparison, we focus on designing a four-pole IM. A bi-objective optimization is carried out, and the second objective is to minimize the cost. The optimal solution in mono-objective optimization is set as the initial point in this optimization. The final solutions are presented in the plan of Figure 4.5.3, with the normalized cost as the *x*-axis, and the normalized losses over the cycle as the *y*-axis. The red line indicates the Pareto Front. It is noted that when the energy losses are minimized, the motor cost is maximized. And when the cost is minimized, the energy losses are maximized.

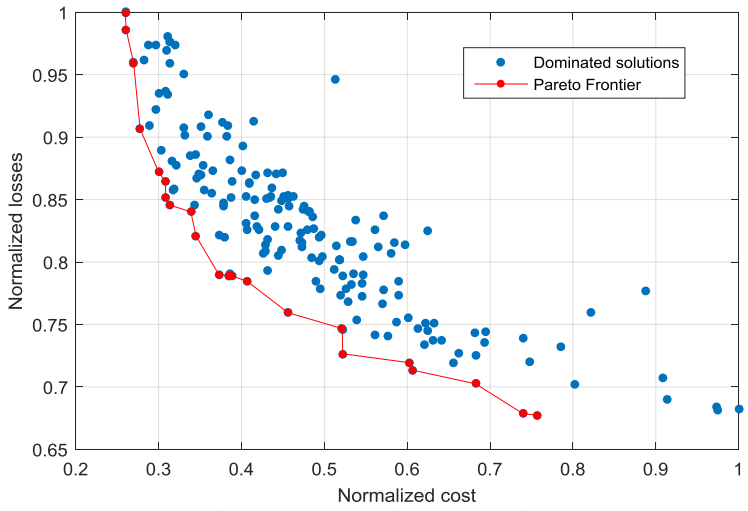

Figure 4.5.3 The dominated, non-dominated solutions and the Pareto Front of the bi-objective optimization

The influences of the optimization variable value on two objectives are investigated in Figure 4.5.4 (OBJ1) and in Figure 4.5.5 (OBJ2). The air-gap width is always on its minimum value since the motor air-gap flux density is higher with the smaller air-gap width. The winding turn number is always on its minimum value since the phase voltage at cycle limit points is largely constrained by the battery voltage volume. The motor with the minimum cost is with a smallest motor length, when the energy losses are maximized. When the stator slot height increases, the energy losses decreases and the motor cost increases, with the filling factor fixed. The rotor bar tends to be thin since a thinner bar contributes to a higher rotor resistance. With a higher rotor resistance, the motor generates a higher torque when the supply state keeps constant. The value of other variables oscillates in ranges that do not exceed the defined variable bounds. From the observations, it is noted that some variables such as the air-gap width g and the rotor tooth concentration ratio τ_{tr} can be removed from the optimization variables as the results show that they always tend to be on their boundary constraints.

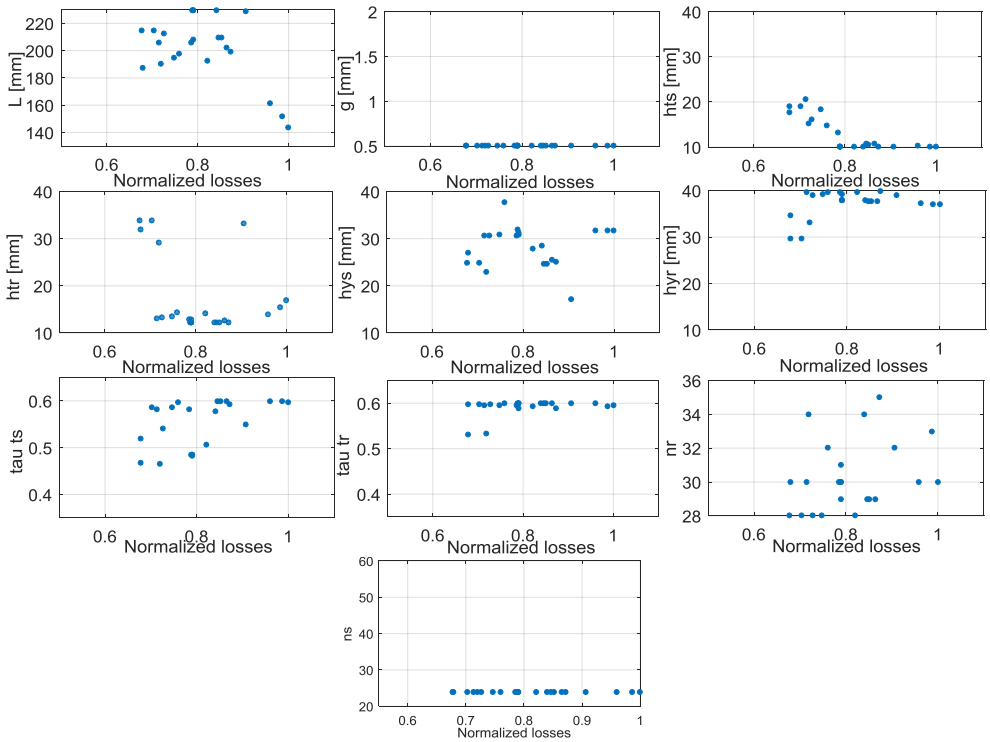

Figure 4.5.4 Geometrical variable value of the non-dominated solutions over the loss function

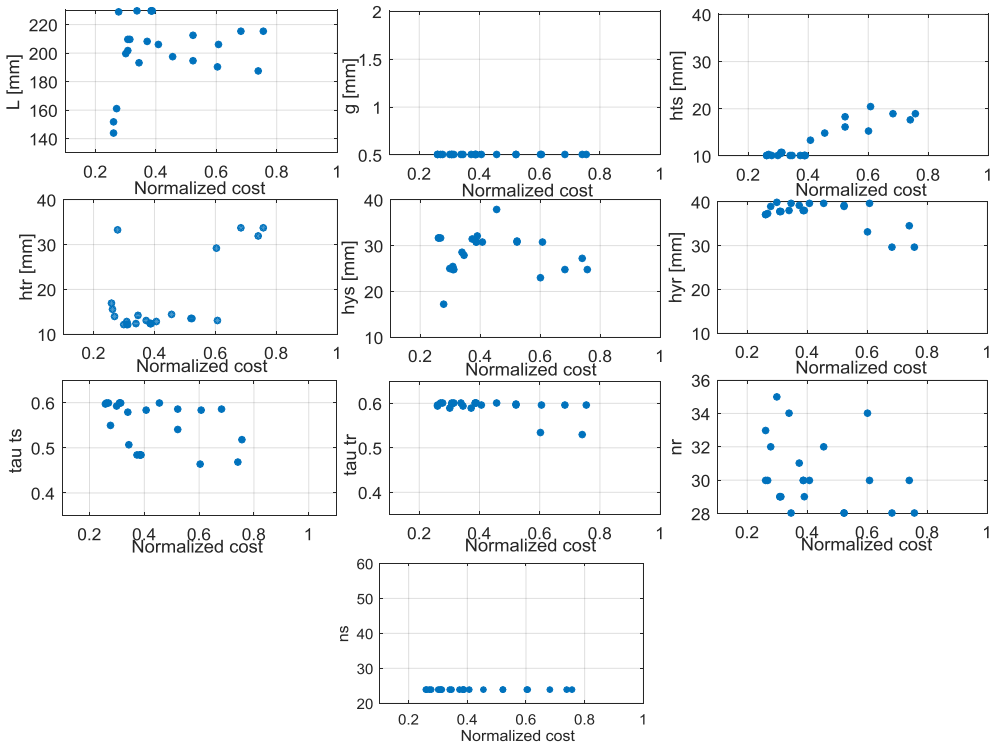

Figure 4.5.5 Geometrical variable value of the non-dominated solutions over the cost function

The optimization variables of the IM and the variable bounds have been defined firstly. With the mono-objective optimization, the optimized four-pole and six-pole IMs have been described and compared from the mass, the volume, the cost, the mean energy efficiency and the power factor. From these comparisons, the four-pole 50kW IM is more suitable for the chosen CADC cycle. Then the bi-objective optimization has been realized on the four-pole IM, the Pareto Front and the evolution of variable values over the objectives have been presented at last.

4.6 Synchronous Reluctant Motor Optimization

In this section we will present the methodology and the results of the Synchronous motor optimization.

4.6.1 Optimization Variables and Constraints

The variables concerning the stator geometry are the same as the ones of the IM. From the coparison of different rotor geometries in Subsection 3.3.2, the rotor geometry is taken as the ones in Figure 3.3.13. Therefore, the rotor is taken without the airgap opening and with radial bridges, and each barrier is a concentric arc. For the sake of the optimization time, the tooth concentration of the yoke between barriers is supposed to be the same as γ_{tr} (see Section 3.3), while the tangential bridge height is supposed as h_{tb}. The pole number is fixed to be four, and the barrier number per pole is determined as six. The optimization variables are chosen as shown in Table 4.6.1, which were discussed in literatures such as [STMW91] [MALI94] [BOLD96] [HAAT03]. Most variable boundaries values are taken from industrial experiences and system specifications.

Variable	*Bound*
Motor length *L* [mm]	[140 230]
Air-gap width *g* [mm]	[0.5 2]
Winding turn number per phase n_s	[24 60]
Stator tooth height h_{ts} [mm]	[10 40]
Stator yoke height h_{ys} [mm]	[10 40]
Stator tooth concentration ratio τ_{ts}	[0.4 0.6]
Rotor tooth concentration ratio τ_{tr}	[0.3 0.7]
Rotor tangential bridge width h_{tb} [mm]	[0.5 2]
Rotor external diameter D_r [mm]	[100 200]
Radius of the barrier nearest to the shaft D_{dr} [mm]	[22.5 42.5]

Table 4.6.1 Optimization variables and their boundaries for SynRM design

The above set of variables is not sufficient to determine the complete geometry of a SynRM: the span of each barrier is not determined, and the radial bridge width neither. The two geometrical dimensions are not chosen as variables, since their value is largely determined by the following constraints.

- ***Constraints of barrier positions***

The barrier span influences the torque ripple. From the discussion in Subsection 3.3.2, the barrier span of each barrier is suggested to be:

$$\beta_j = k\tau_s + \frac{\tau_s}{2} \quad \left(k = 1, 2, 3, \cdots, \frac{n_e}{2p}\right) \quad (j = 1, \cdots, N_{bar}) \tag{4.6.1}$$

Where:

- β_j: the mean barrier span of the j_{th} barrier;
- τ_s: the stator slot pitch.

Here, the barrier span is fixed to be: [85° 65° 55° 45° 35° 25°].

- ***Constraints of radial bridge width***

As introduced in Section 2.8, the bridge width determines the maximum stresses imposed on the radial and the tangential bridges, which should be avoided to surpass the tolerable range (security factor). Thus, the radial bridge width of each barrier is determined by the following equations:

$$\begin{gathered} S_E\left(e_{rb1\,j}, h_{tb_j}\right) = 1.6 \quad S_F\left(e_{rb2\,j}, h_{tb_j}\right) = 1.6 \\ e_{rb\,j} = \max(e_{rb1\,j}, e_{rb2\,j}) \end{gathered} \tag{4.6.2}$$

Where:

- S_E: the security factor of nominal stresses;
- S_F: the security factor of fatigue stresses;

- $e_{rb\,j}$: the radial bridge width on the j_{th} barrier;
- $h_{tb\,j}$: the tangential bridge height on the j_{th} barrier.

The detail expressions of the security factor were described in equation 2.8.4-9.

Besides, one should verify if the rotor is achievable with the above defined geometries before the calculation:

$$D_{oo'} > \frac{D_r}{2}$$
$$\frac{\tau_p}{2} < \beta'_{max} < \tau_p = 90° \qquad 4.6.3$$

Where:

- $D_{oo'}$: the distance between the motor center and the arc center (see Figure 4.6.1);
- D_r: the rotor outer diameter;
- β'_{max}: the maximum barrier opening angle with the reference of the arc center;
- τ_p: the pole pitch.

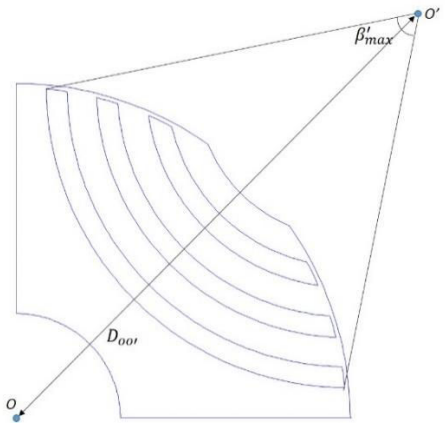

Figure 4.6.1 Some detail parameters of the SynRM rotor

In the SynRM design, the geometry information got from each individual shall be post-treated before calculating the function value in OPT 2. A simple flow chart in Figure 4.6.2 explains the step orders which couples OPT1 and OPT2.

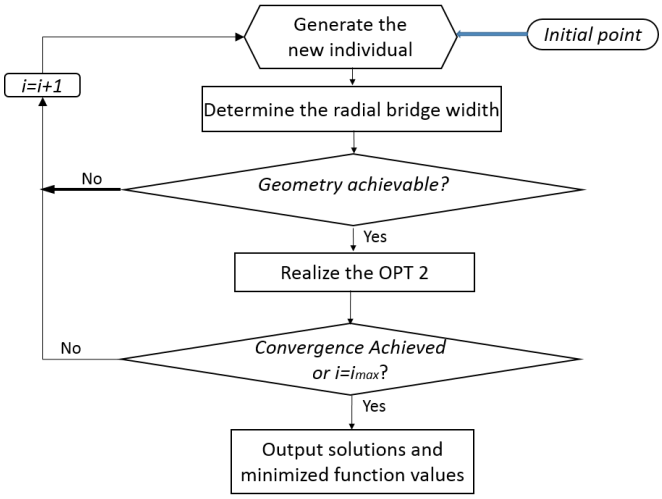

Figure 4.6.2 Flow chart of the SynRM design

4.6.2 Mono-objective Optimization

To compare with the optimized IMs, the objective is to minimize the system energy losses over the driving cycle as well. The variable values of the optimal solution are listed in Table 4.6.2, and the optimal four-pole SynRM geometry is described in Figure 4.6.3.

Variable	***4-pole***
L [mm]	198
g [mm]	0.5
n_s	36
h_{ts} [mm]	13.64
h_{ys} [mm]	31
h_{tb} [mm]	0.5
D_{dr} [mm]	50.5
D_r [mm]	164
τ_{ts}	0.6
τ_{tr}	0.6

Table 4.6.2 Value of optimal variables for the 4-pole SynRM

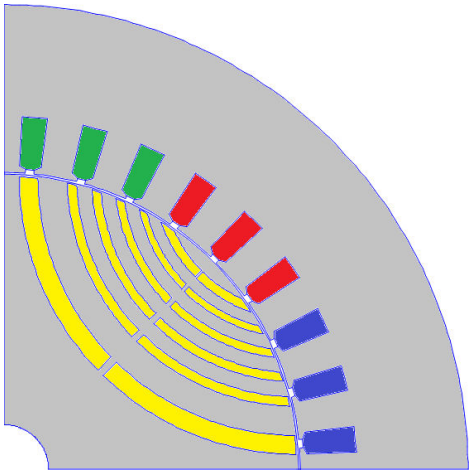

Figure 4.6.3 Geometry of optimized 4-pole SynRM: one pole

The optimized four-pole SynRM is investigated from its volume, mass, cost, the mean energy efficiency and power factor over the cycle, as shown in Table 4.6.3. The validation of the optimized motor by FEA could be found in Appendix 2.

Performance	***4-pole***
External diameter	255 mm
Motor length	198 mm
Volume	10 l
Mass	70 kg
Motor Cost	940 €
Mean energy efficiency	0.93
Mean power factor	0.75

Table 4.6.3 Characteristics of the optimized 4-pole SynRM

The torque pulsation of the optimized SynRM is investigated when it is fed by the maximum phase current (determined by the chosen converter), with a current angle of 45°. In Figure 4.6.4, the torque pulsation is presented with a ripple ratio about 32%. As mentioned in Section 1.7, the torque ripple could be reduced by skewing the rotor, by adjusting the barrier span, and by optimizing the stator winding structure and the stator slot opening.

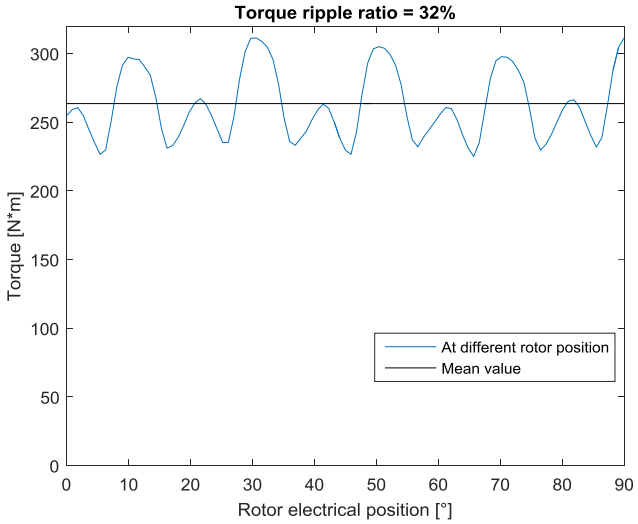

Figure 4.6.4 The torque evolution with the rotor position when $\hat{\imath}_s = i_{max}$, current angle = 45°

4.6.3 Bi-objective Optimization

The bi-objective optimization has been realized on the four-pole SynRM as well, with the same geometrical variables and the same constraints as in mono-objective optimization. With the same calculation processor, the bi-optimization of the SynRM takes nearly four weeks, three times longer than the optimization of the IM, because the analytical computation of the SynRM is more effort consuming. The Pareto Front is presented in Figure 4.6.5, with the cost function as the *x*-axis, and the loss function as the *y*-axis. The solution with the optimal cost is 45% cheaper than the solution with the optimal energy losses, while it consumes 25% more energy losses over the cycle than the other one.

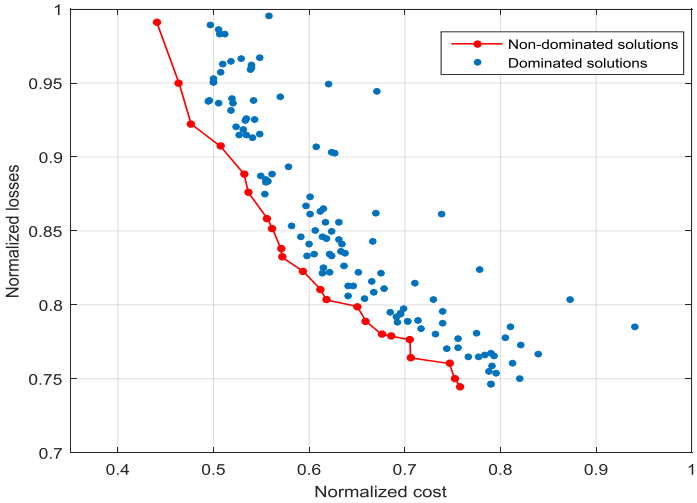

Figure 4.6.5 The dominated, non-dominated solutions and the Pareto Front of the bi-objective optimization

In Figure 4.6.6 and Figure 4.6.7, the evolution of the variables over the loss function and the cost function has been investigated respectively. Similarly to the IM optimization results, the air-gap width is optimized to be its minimum value, and the tangential bridge width is minimized as well to increase the *d*-axis magnetizing inductance. Besides, the motor cost increases with the increase of the motor length, the rotor diameter, and the stator tooth height, while the losses decreases. The winding turn number is constant with the objective function. From the above observations, variables such as the air-gap width and the tangential bridge width could be set as constant in the next optimizations.

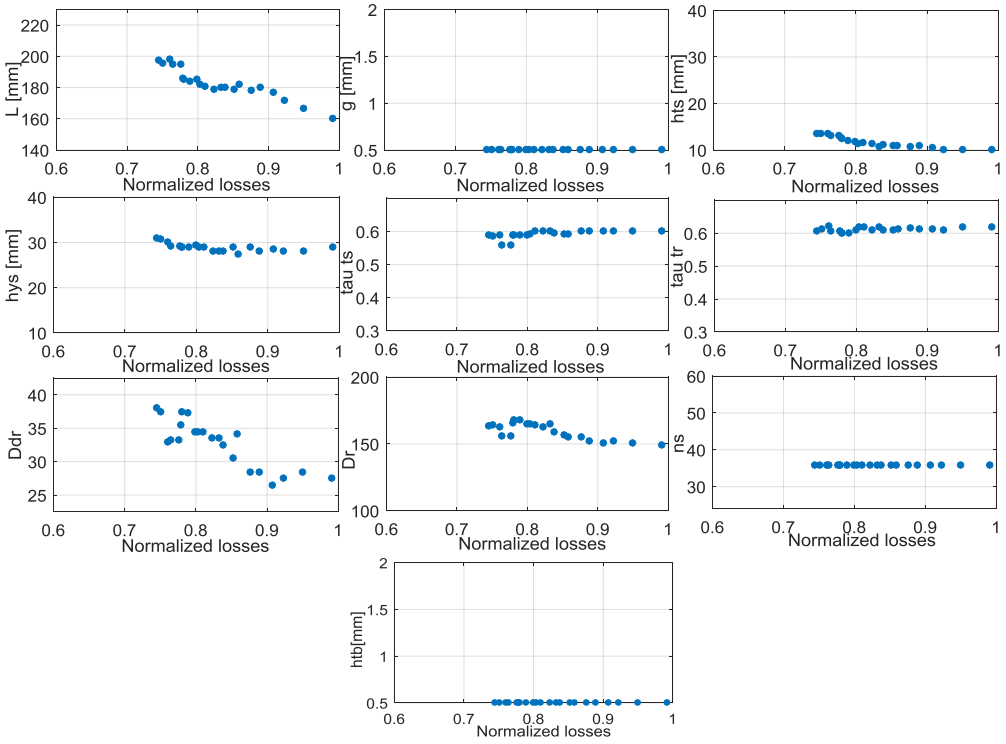

Figure 4.6.6 Geometrical variable value of the non-dominated solutions over the loss function

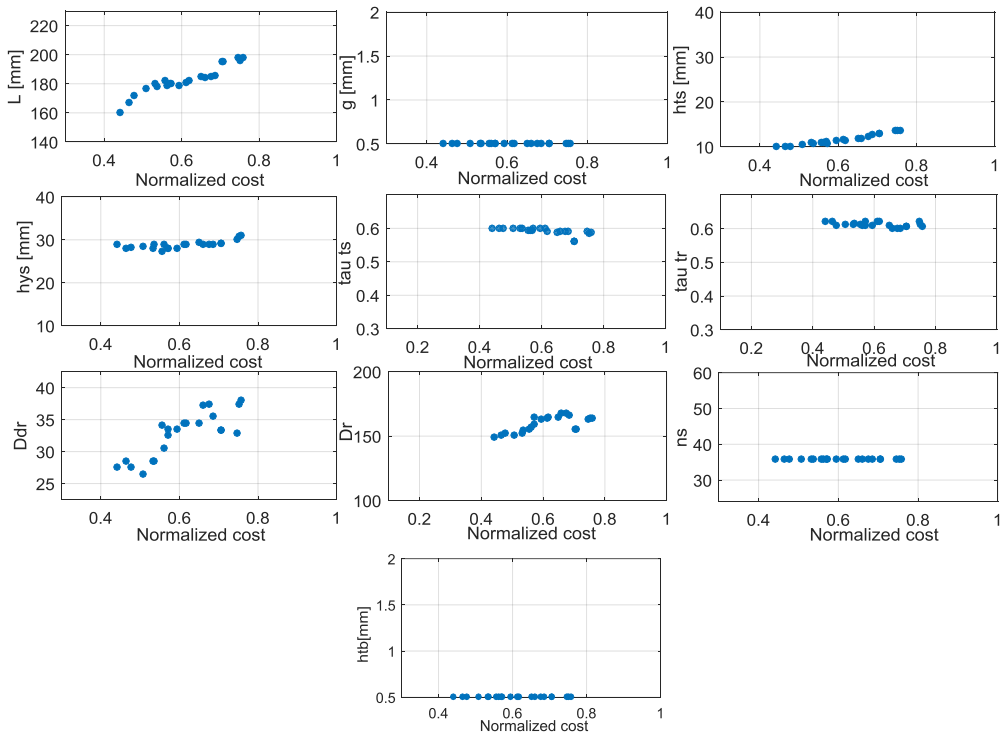

Figure 4.6.7 Geometrical variable value of the non-dominated solutions over the cost function

In this section, the optimization variable and constraints for the SynRM have been presented. The motor geometry should be complemented and verified before executing the calculation in OPT2. The four-pole SynRM has been defined to obtain the minimum energy losses over the cycle. The general characteristics of the optimized motor were illustrated, with its maximum torque ripple verified. Then the bi-objective optimization was realized, with the Pareto Front and the variable sensibility on two functions investigated.

4.7 Comparisons

Since mono-objective and bi-objective optimizations of the four-pole IM and SynRM have been realized respectively, the comparisons of the optimized motors will be carried out in this section.

4.7.1 Mono-objective Optimization

Firstly, the two optimized four-pole motors are compared from their volume, mass, cost, mean energy efficiency and power factor over the driving cycles, as shown in Table 4.7.1. It is noted that the two motors present nearly the same mass, volume, and energy efficiency. It is not surprising that the SynRM presents a mean power factor 10% lower than the IM. However, the SynRM costs 30% cheaper than the IM from the initial material cost and the total cost.

Performance	*IM*	*SynRM*
External diameter	1 *p.u.*	1.02 *p.u.*
Motor length	1 *p.u.*	1.04 *p.u.*
Volume	1 *p.u.*	1.03 *p.u.*
Mass	1 *p.u.*	1.06 *p.u.*
Motor Cost	1 *p.u.*	0.7 *p.u.*
Motor material Cost	1 *p.u.*	0.72 *p.u.*
Mean energy efficiency	1 *p.u.*	0.98 *p.u.*
Mean power factor	1 *p.u.*	0.91 *p.u.*

Table 4.7.1 Characteristic comparisons of the optimized 4-pole IM and SynRM

The histogram in Figure 4.7.1 shows that copper (with the end-winding material cost considered) costs the most in both the IM and the SynRM, since the copper costs much higher than aluminum and steel. The copper costs 50% more in the IM due to the longer stator slot (the filling factor constant). Besides, the IM rotor consumes aluminum, and the rotor workforce cost is higher than that of the SynRM since the rotor bars are wedged to the slots.

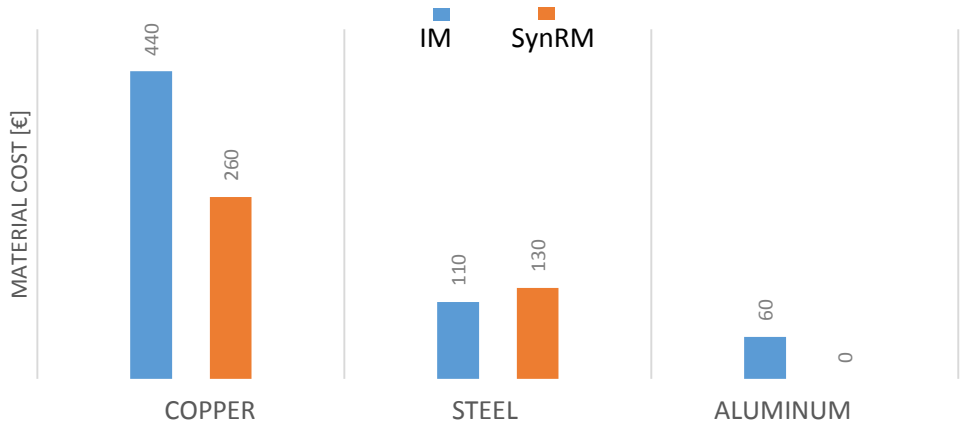

Figure 4.7.1 Composition of material cost in optimized motors

Over the whole speed and torque range, the control parameter optimization is carried out on both the optimized induction and synchronous reluctant machines. The cartography describing the energy efficiency difference between the IM and the SynRM is presented in Figure 4.7.2. As one could see, the induction machine is dominant over the whole range, especially in low rotation speed and high torque ranges. While in high speed and low torque range, the IM and the SynRM have a comparable efficiency. However, there is no obvious difference on the energy efficiency of the two machines over the whole cycle, since the energy efficiency difference is no higher than 0.1. In the considered working points, the energy efficiency difference is no higher than 0.05.

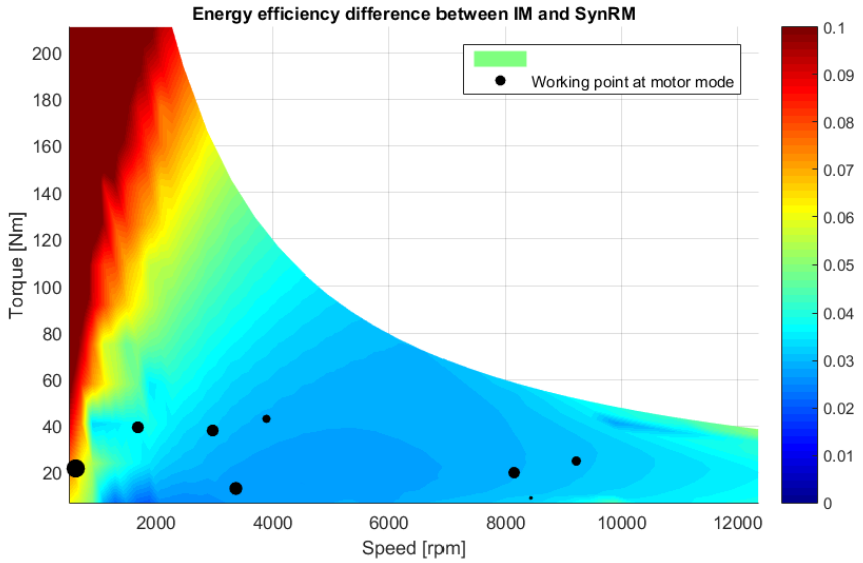

Figure 4.7.2 Cartography of the energy efficiency difference between the optimized IM and the optimized SynRM ($\eta_{IM} - \eta_{SynRM}$), with the working points marked

Similarly in Figure 4.7.2, the power factor difference between the optimized induction and synchronous reluctant machines over the whole range is investigated. Except some small regions (blue region), the power factor of the IM is nearly 10% higher than the SynRM. In the blue regions, the error may be generated because of the optimization settings (the initial value or the variable range).

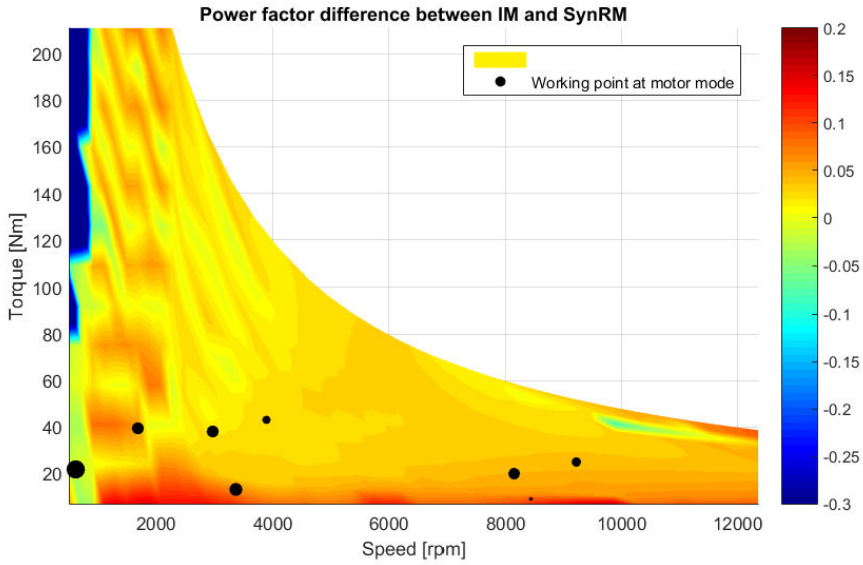

Figure 4.7.3 Cartography of the power factor difference between the optimized IM and the optimized SynRM (PF_{IM}- PF_{SynRM})

The energy loss distribution on different sources is presented in Figure 4.7.4. The energy losses were considered over the whole driving cycle. In the traction system with the IM, the winding losses occupy nearly a half, which includes the losses occurring in the stator and rotor. The core losses take for only 10%, and the mechanical losses could be even neglected (<1%). In the traction system with the SynRM, the core losses take for 24%, two times than the IM. And

the winding losses are less than those in the IM, since there are no winding losses in the rotor part. Besides, in both systems, the energy losses in the converter takes a large portion, because the motor phase current is kept high when the phase voltage is constrained by the battery volume.

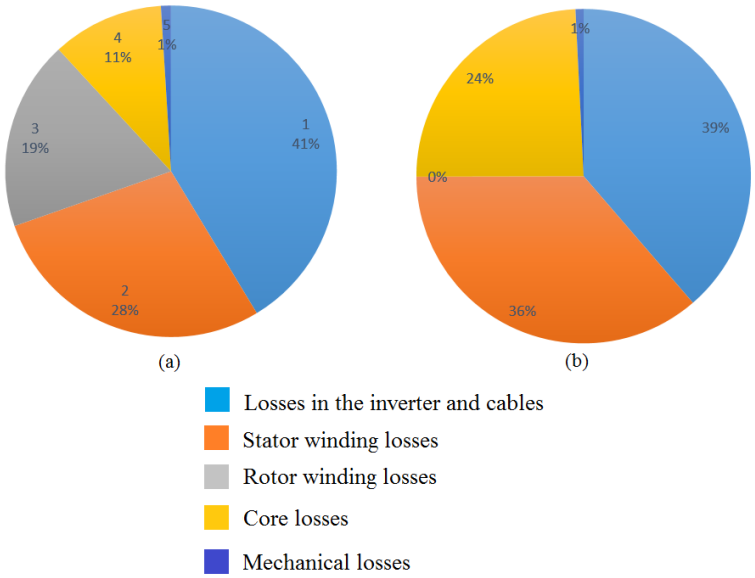

Figure 4.7.4 Composition of energy losses in the traction system: the IM (a) the SynRM (b)

4.7.2 Bi-objective Optimization

We compare the Pareto Front obtained from the bi-objective optimization of the IM and the SynRM in Figure 4.7.5. In the plan, *x*-axis indicates the normalized motor cost, and *y*-axis indicates the mean energy efficiency over the cycle. It is observed that in the solutions with the same cost, the SynRM solution is more energy efficient than the IM solution. However, the most energy efficient IM is 0.5% higher than the most efficient SynRM, while the IM costs nearly 50% higher than the SynRM. With some proper modifications applied on the geometrical constraints, the battery and converter specifications, the optimized SynRM may be more energy efficient.

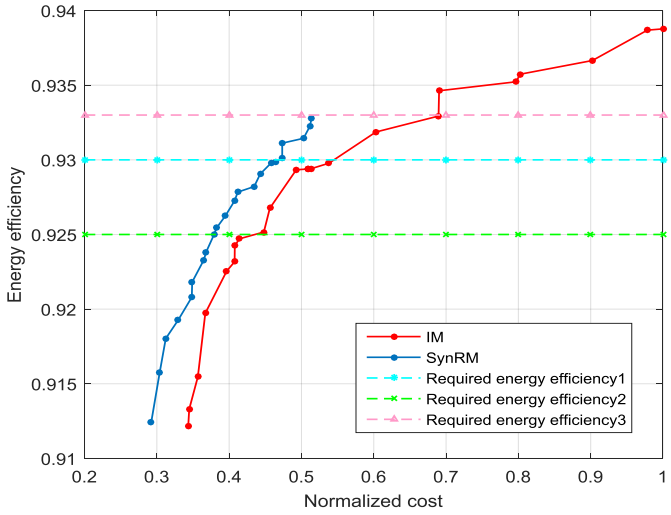

Figure 4.7.5 Pareto Front Comparison between the IM and the SynRM

We compare the cost of motors with the same energy efficiency in Table 4.7.2. It is concluded that the SynRMs cost from 10% to 25% less than the IMs with the same energy efficiency.

Required energy efficiency	*IM cost*	*SynRM cost*
0.93	1 *p.u.*	0.86 *p.u.*
0.925	1 *p.u.*	0.91 *p.u.*
0.933	1 *p.u.*	0.74 *p.u.*

Table 4.7.2 Cost comparisons of the optimized IMs and SynRMs with the same energy efficiency

In this section, we compared the optimized IM and SynRM with the highest energy efficiency. The two motors have a comparable mass and volume, but the SynRM is 30% cheaper than the IM since the IM uses more copper and aluminum. However, when the energy efficiency and the power factor of the two motors were investigated over the whole driving cycle, it is noted that the IM is more efficient than the SynRM over the whole range. However, the difference is less at high speed than low speeds. The IM power factor is nearly 10% higher than the SynRM one regardless of the working range. Then the loss composition of the traction system was studied. In the traction system with the IM, the winding losses take the largest portion, higher than the system with the SynRM. The core losses of the SynRM takes up a larger portion than that of the IM. However, the losses occurring in the converter are important in both two traction systems. The Pareto Front of the two motors were projected in the same plan and compared. Although the maximum energy efficiency of the IM is higher than that of the SynRM, the SynRM costs at least 10% less than the IM with the same energy efficiency.

4.8 Conclusions

Driving cycles, as one of the most important specifications for the EV traction design, have been presented firstly in this chapter. The Artemis driving cycles were considered as the driving database, which contain more than two thousand working points. Cluster and barycenter methods were applied to select several working points to represent the whole driving cycle, and the selected points are considered as the traction system specifications. Besides, two additional working points on the constant power speed range are taken as the cycle constraint on the electric motor.

Global optimization algorithms and multi-objective optimization methods have been reviewed. Differential evolution algorithm will be applied as the global optimization method, since they are efficient in treating large scale optimization problems with mixed variables and nonlinear constraints. Besides, it incorporates well with multi-objective optimization strategies. The general scheme of the mono-objective and the bi-objective optimization was presented, where both motor geometries and control parameters should be defined in the design. The optimization methodology is applicable in both induction machines and synchronous reluctant machines. The general specifications such as the electrical volume of the battery and the converter, and the motor geometrical constraints have been listed, which apply in both two kinds of machines.

In the control parameter optimization, the objective is to obtain high energy efficiency and power factor with proper control. The influences of different control state parameters on the energy efficiency and the power factor have been investigated at different rotation speeds, the control variable and the objective function were then determined based on that, for both two machines. Analytical model was embedded into this optimization, following the general principle to save optimization efforts.

The geometrical variables and their bounds in the induction machine optimization were described. The mono-optimization, to consider the energy losses during the whole cycle, was carried out on the four-pole and the six-pole induction motors. The four-pole motor weights and costs less than the six-pole motor, while it works with a higher energy efficiency and power factor. Thus, the bi-objective optimization was applied on the four-pole induction motor. The Pareto Front shows that the cost and the energy efficiency are two contradictory factors, the motor with the highest energy efficiency costs the most. The variable value of these non-dominated solutions on objective functions was investigated and analyzed. Similarly, the geometrical variables and bounds for the synchronous reluctant machine were described. The geometry should be complemented and verified with the defined set of variables. Then the mono-objective and bi-objective optimizations were realized on the four-pole synchronous reluctant machine. The optimized motor characteristics such as the cost, the volume, the power factor, and the maximum torque ripple ratio were presented. The Pareto Front and the variable sensibility on objective functions were investigated as well.

After the optimization step, the optimized induction and synchronous reluctant machines were compared. In the optimization to define the minimum energy losses over the driving cycle, the optimized four-pole IM has a comparable volume and mass with the four-pole SynRM, but

it costs 30% higher than the other one. When the energy efficiency and the power factor of the two motors were compared over the whole driving cycle, the IM was assumed to be dominant regardless of the range. The energy efficiency difference is slight, and the IM power factor is 10% higher than the SynRM. Then the Pareto Fronts of the IM and the SynRM was compared. The SynRMs cost from 10% to 25% less than the IMs with the same energy efficiency.

4.9 References

[ANDR04] M. André, "The ARTEMIS European driving cycles for measuring car pollutant emissions," *Science of The Total Environment*, vol. 334–335, pp. 73–84, Dec. 2004.

[BARR12] N. A. Barr, *The economics of the welfare state*, 5th ed. Oxford ; New York: Oxford University Press, 2012.

[BDGG09] L. Bianchi, M. Dorigo, L. M. Gambardella, and W. J. Gutjahr, "A survey on metaheuristics for stochastic combinatorial optimization," *Natural Computing*, vol. 8, no. 2, pp. 239–287, Jun. 2009.

[BLMB09] T. J. Barlow, S. Latham, I. S. Mccrae, and P. G. Boulter, "A reference book of driving cycles for use in the measurement of road vehicle emissions," *TRL Published Project Report*, 2009.

[BOLD96] I. Boldea, *Reluctance synchronous machines and drives*, Oxford: Clarendon Press, 1996.

[BONA10] I. Boldea and S. A. Nasar, *The induction machines design handbook*, 2nd ed. Boca Raton, FL: CRC Press/Taylor & Francis, 2010.

[BOTO00] P. T. Boggs and J. W. Tolle, "Sequential quadratic programming for large-scale nonlinear optimization," *Journal of Computational and Applied Mathematics*, vol. 124, no. 1–2, pp. 123–137, Dec. 2000.

[CHAK08] U. K. Chakraborty, *Advances in differential evolution*, Berlin: Springer Verlag, 2008.

[CRIN89] J. P. Crause, "Methodologie statistique pur l'étude des cinematiques et des consommations de vehicules legers," Institut national de recherche sur les transports et leur sécurité, 1989.

[DAGU13] B. Daguse, "Modélisation analytique pour le dimensionnement par optimisation d'une machine dédiée à une chaîne de traction hybride à dominante électrique," Thesis (CentraleSupélec), Jun-2013.

[DDVV12] B. Dagusé, P. Dessante, P. Vidal, J.-C. Vannier, J. Saint-Michel, and J.-L. Thomas, "Optimization and comparison of optimal saliency permanent magnet synchronous machines for electric vehicle application," *Przeglad Elektrotechniczny*, vol. R. 88, nr 7b, pp. 119–122, 2012.

[DHMO01] I. S. Dhillon and D. S. Modha, "Concept decompositions for large sparse text data using clustering," *Mach. Learn.*, vol. 42, no. 1–2, pp. 143–175, Jan. 2001.

[DPAM02] K. Deb, A. Pratap, S. Agarwal, and T. Meyarivan, "A fast and elitist multiobjective genetic algorithm: NSGA-II," *IEEE Transactions on Evolutionary Computation*, vol. 6, no. 2, pp. 182–197, Apr. 2002.

[EFIN03] D. E. Finkel, "Direct optimization algorithm user guide," Center for Research in Scientific Computation, North Carolina State University, Mar-2003.

[EISM03] A. E. Eiben and J. E. Smith, *Introduction to evolutionary computing*, New York: Springer, 2003.

[FLOU00] C. A. Floudas, *Deterministic Global Optimization Theory, Methods and Applications*, Boston, MA: Springer US, 2000.

[GEPO10] M. Gendreau and J.-Y. Potvin, Eds., *Handbook of metaheuristics*, 2nd ed. New York: Springer, 2010.

[GOLD89] D. E. Goldberg, *Genetic algorithms in search, optimization, and machine learning*, Reading, Mass: Addison-Wesley Pub. Co, 1989.

[HAAT03] J. Haataja, "A comparative performance study of four-pole induction motors and synchronous reluctance motors in variable speed drives," Thesis (Lappeenranta University of Technology), Jun-2003.

[HASS14] M. H. Hassan, "Méthodologies de conception optimale de systèmes de conversion électromécanique," Thesis (Paris-Sud), Apr-2014.

[HOPA95] R. Horst and P. M. Pardalos, Eds., *Handbook of global optimization*, Dordrecht ; Boston: Kluwer Academic Publishers, 1995.

[JVMG11] X. Jannot, J.-C. Vannier, C. Marchand, M. Gabsi, J. Saint-Michel, and D. Sadarnac, "Multiphysic Modeling of a High-Speed Interior Permanent-Magnet Synchronous Machine for a Multiobjective Optimal Design," *IEEE Transactions on Energy Conversion*, vol. 26, no. 2, pp. 457–467, Jun. 2011.

[KRCM12] G. Krebs, E. de Cecco, and C. Marchand, "Design approach of an axial flux motor for electrical powertrain vehicle," in *Electrical Machines (ICEM), 2012 XXth International Conference on*, 2012, pp. 2812–2817.

[MALI94] T. Matsuo and T. A. Lipo, "Rotor design optimization of synchronous reluctance machine," *IEEE Transactions on Energy Conversion*, vol. 9, no. 2, pp. 359–365, Jun. 1994.

[NEUM04] A. Neumaier, "Complete Search in Continuous Global Optimization and Constraint Satisfaction," Cambridge University Press, 2004.

[NOWR06] J. Nocedal and S. J. Wright, *Numerical optimization*, 2nd ed. New York: Springer, 2006.

[PRSL05] K. V. Price, R. M. Storn, and J. A. Lampinen, *Differential evolution: a practical approach to global optimization*, Berlin ; New York: Springer, 2005.

[PUGS09] G. Pugsley, "Modélisation paramétrique non linéaire des machines asynchrones et démarche d'optimisation associée. Application au dimensionnement dans les véhicules hybrides," Thesis (INP Grenoble), Jul-2009.

[QISU05] A. K. Qin and P. N. Suganthan, "Self-adaptive differential evolution algorithm for numerical optimization," 2005, vol. 2, pp. 1785–1791.

[SPAL03] J. C. Spall, *Introduction to stochastic search and optimization: estimation, simulation, and control*, Hoboken, N.J: Wiley-Interscience, 2003.

[STMW91] D. A. Staton, T. J. E. Miller, and S. E. Wood, "Optimisation of the synchronous reluctance motor geometry," in *Electrical Machines and Drives, 1991. Fifth International Conference on (Conf. Publ. No. 341)*, 1991, pp. 156–160.

[STPR97] R. Storn and K. Price, "Differential Evolution – a simple and efficient heuristic for global optimization over continuous spaces," pp. 341–359, Dec-1997.

General Conclusions

The objective of this thesis, which has been stated in the first chapter, is to study and to compare low cost electric machines for the electric vehicle traction applications. In the first chapter, we have discussed the research background. Some general knowledge about electric vehicles were presented, including the vehicle evolution history, the market state, the types of electric vehicles, and the traction system. Electric machines, especially their applications in the electric vehicles have been quickly reviewed. It has been stated that induction and synchronous reluctant machines, have moderate cost, similar power electronics and control strategies. From the view point of the cost, aluminum squirrel cage induction motors and transversally laminated synchronous motors are the candidate motors in our research. Many comparisons between the two kinds of electric machines had been conducted, therefore a general review of used comparisons was carried out. However, since the two kinds of machines were not designed under the same specifications and for the variable speed range, this work should be considered in our research. In order to realize it, the modeling and the design methodology for two motors were proposed respectively.

Under this context, we introduced the traction system modelling, especially the electric machine modelling in the second chapter. The multi-physical model includes the electromagnetic models of induction and synchronous reluctant machines, the energetic model to estimate the energy losses in the converter, in the cables and in the electric machines under steady state, the cost model to evaluate the system cost, and the mechanical model to evaluate the robustness of the synchronous reluctant machine rotor. All these models are analytical or semi-analytical for the sake of the computation time.

The analytical models of induction and synchronous reluctant machines are to deduce the motor electrical and magnetic performances with the awareness of the motor geometry and the control state parameters. In the analytical model of induction machines, the Lumped parameter circuit is applied. Firstly, all the equivalent parameters in the circuit, except the magnetizing inductance, the rotor resistance and leakage inductance are deduced with analytical equations. The rotor a.c. resistance and inductance are calculated with a numerical approach, by dividing a rotor bar with several layers tangentially. This method is considered to be applicable for an arbitrary bar shape. Then with the neglect of some flux leakages and with the help of Faraday's law, the relationship between the induction in the air-gap, in the yokes and in the teeth are established. With the proper magnetic circuit considered, the induction distribution in the air-gap is deduced with numerical methods. When the air-gap induction distribution was deduced, other performances such as the phase voltage and the power factor are then calculated. In the analytical model of synchronous reluctant machines, the *dq* space phasor is applied. Similarly, Ampere's and Faraday's laws are applied to find the air-gap induction distribution. For the air-gap position facing to the rotor tangential bridges, the magnetic circuit is treated differently with other regions, with particular assumptions taken. The analytical model of synchronous reluctant machines takes more time to converge because of more variables and the lack of knowledge of induction distribution in it.

In the loss model, the calculation of the steady-state losses occurring in the converter, in the cables and motor mechanical losses are the same in both kinds of motors. The calculation of the winding and core losses in the induction and synchronous reluctant motors were described respectively, with the skin effect and the influences of the iron saturation considered. The rotor winding losses of the induction motor, and the rotor core losses of the synchronous reluctant motor, should not be neglected. The phase voltage and current, and the air-gap induction are required during the motor loss calculations. In the economic model, the manufacturing cost of induction and synchronous reluctant machines is estimated with a coarse analytical model, requiring the geometrical parameters of electric machines. In the mechanical model of synchronous reluctant machines, the stresses imposed on the tangential and radial bridges under critical rotation speed are investigated. The security factor, as the ratio between the maximum stress and the material strength, should be assured to surpass the threshold in the rotor design.

After the establishment of traction system analytical models, especially the electric machine ones, these models were validated in the third chapter with finite element analysis. In the validation of the induction motor models, harmonic finite element methods were applied to validate the calculation of the rotor bar a.c. resistance and inductance over a wide frequency range. It is proved that the analytical model could be applied in motors with rectangular or non-rectangular bar shapes, by presenting a tolerable and steady error. For a given induction motor, the analytical model was then validated with transient finite element analysis at several slip ratios. The analytical error is considered tolerable in the design step. We proposed a method which combines the analytical model and the static finite element method, with which again the analytical model was validated from their performances including the electromagnetic torque, the phase voltage and the power factor. The analytical error is still acceptable. For different rotor geometries, the analytical model of the synchronous reluctant machine was validated with a static finite element method, which providing the average torque estimation within minimum experiments. With the same controls, these motors with different rotor geometries were validated and compared from the phase voltage, the torque, the power factor and the torque ripple. The analytical error was acceptable for tested rotor geometries. Besides, the rotor geometry applied in the design was determined from the comparisons. At last, the mechanical model was validated with two-dimensional finite element analysis for linear elasticity. The analytical stresses of the rotor bridges were compared with Von Mises stresses in the numerical model, with an error a bit high but still tolerable in the motor design.

The optimization methodology and optimization results were presented in the fourth chapter. The driving cycles were discussed, then several working points were selected from the whole cycle with cluster and barycenter methods. Differential Evolution algorithm was chosen to be applied in the global optimization, since it is efficient in treating complex mixed optimization problems. Besides, it works well in the bi-objective optimization, when NSGA-II method is applied to embed with the DE algorithm. The general optimization scheme was then proposed, where both motor geometrical and control variables are considered separately. Firstly, differential evolution method is applied to define the motor geometrical variables. For each individual of one population, the control parameter is optimized to find minimum energy losses and high power factor under several electrical and magnetic constraints. The influences of control parameters on the energy efficiency and the power factor were defined, for both induction and synchronous reluctant machines. Then the control parameter optimization variables and objectives

were presented. Besides, the flow chart to embed the analytical model with the control parameter optimization was described. Some general specifications of the traction system were defined for the global design.

Based on the introduced optimization methodology, the mono-objective and bi-objective optimizations were carried out on the induction and synchronous reluctant machines. In the mono-objective optimization with the objective to define minimum energy losses over the driving cycle, the four-pole and six-pole induction machines were optimized and compared from their mass, volume, cost, energy efficiency and power factor. The four-pole motor costs and weights less than the six-pole motor, and has a comparable energy efficiency and power factor. In the bi-objective optimization, we focused on design of the four-pole motor. The Pareto Front and the variable sensibility on the objective functions (losses and cost) were investigated. For synchronous reluctant machines, the motor geometry should be validated and verified with the defined set of optimization variables before the control parameter optimization. Similarly, the optimized motor geometry and the Pareto Front of the synchronous reluctant machine were presented.

At the last part of the fourth chapter, the comparisons based on the optimization results were realized. The induction motor with the highest energy efficiency has a comparable mass and volume than the synchronous reluctant motor with the highest energy efficiency. However, the induction motor costs 30% more than the synchronous reluctant motor, because it uses more copper and aluminum. The energy efficiency and the power factor of the optimized induction machine are dominant over the whole driving cycle. The induction machine power factor is nearly 10% higher than the synchronous reluctant machine. Compared to the power factor, the energy efficiency difference is slight. The phase current is high due to the voltage constraint of the d.c. battery, which brings important converter losses in the traction system. The winding losses in the induction machine are higher than those in the synchronous reluctant machines, while the core losses in the latter one are higher. The Pareto Fronts from the bi-objective optimization of the four-pole induction and synchronous reluctant machines were compared. The highest energy efficiency of the synchronous reluctant machine is 0.5% lower than that of the induction machine. However, the synchronous reluctant machine could be furtherly optimized with the geometrical and electrical constraints improved from the author's design experiences. When the two motors are with the same cost, the energy efficiency of the synchronous reluctant machine is higher than the induction machine. And when the machines with the same energy efficiency are compared, the synchronous reluctant machines cost from 10% to 25% less than the induction machines. That is to say, the synchronous reluctant machine is a better response to the lowest cost electric machine for the electric vehicle traction application, if there is no strict requirement (such as above 0.8) on the motor power factor.

To conclude briefly, the main contributions of this thesis consists of:

- Establishment and validation of the analytical models of squirrel cage induction motors and transversally laminated synchronous reluctant motors;

- Proposition and realization of the motor optimization for the electric vehicle traction application, based on the proposed analytical models;

- Comparisons between induction and synchronous reluctant machines based on the optimization results.

There are still some interesting works to enrich the diversity and the depth of this doctoral research:

- Add the thermal model to the analytical modelling, and realize the optimization and comparisons again, to look up the thermal influences on the optimization results;
- Develop the analytical model to estimate the torque ripple of the synchronous reluctant machine;
- Add the couplings between the electromagnetic and mechanical models;
- Resize the geometrical constraints, the battery and converter electrical volume, then realize again the similar optimization and comparison;
- Compare the optimized induction and synchronous reluctant machines with other electric machines, such as switched reluctant machines and wound-rotor synchronous machines.

Résumé en français

Introduction

L'utilisation excessive de combustibles fossiles a des conséquences négatives sur l'environnement, par exemple le réchauffement climatique, la pollution de l'air et de l'eau et l'atténuation des ressources naturelles. Le secteur du transport routier représente une part importante dans la consommation de ces combustibles. Dans ce contexte, le Véhicule Électrique (VE) redevient un axe de recherche essentiel depuis les années 90. Le véhicule électrique à batterie, attire l'attention de l'ingénierie, et sa part de marché augmente d'année en année. Toutefois, la part du véhicule électrique est encore mineure devant le véhicule thermique, en raison des limites de la technologie de recharge, de l'autonomie de conduite et du coût. Le composant le plus important d'un VE (Figure a) est le système de traction qui comprend, entre autres, la batterie, l'onduleur et le moteur électrique. Afin de démocratiser les véhicules électriques, il est nécessaire de parvenir à un coût du véhicule acceptable tout en garantissant un impact environnemental minimum. Le but recherché dans cette thèse est l'étude de moteurs électriques à bas coût appliqués aux VEs.

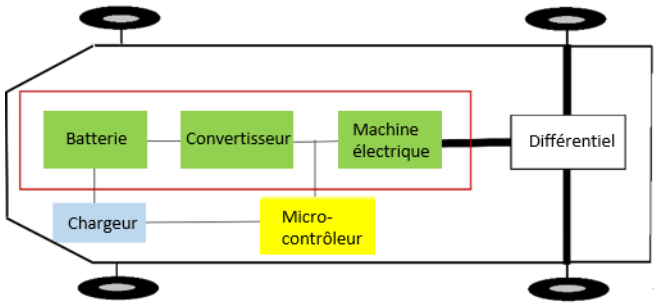

Figure a Composition d'un système de traction d'un VE à batterie

Après une revue des différents moteurs électriques selon plusieurs critères, les machines asynchrones et synchrones à réluctance variable apparaissent comme de bonnes candidates. Leurs principaux composants sont relativement propres et recyclables. De même, dans ces deux machines triphasées la structure et l'algorithme de contrôle de l'onduleur associé sont similaires. Considérant le facteur du coût, nous avons sélectionné les machines asynchrones à cage et synchrones à réluctance variable transversalement laminées, comme montré dans la Figure b.

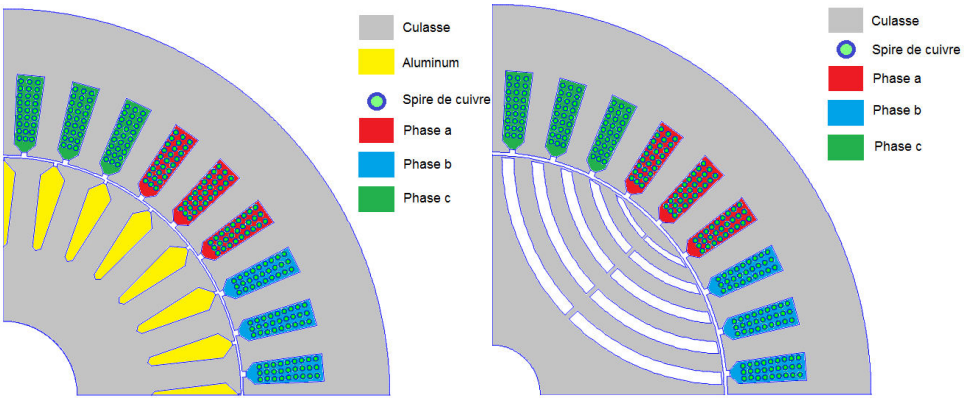

(a) (b)

Figure b Géométrie des machines étudiées : la machine asynchrone à cage (a) la machine synchrone à réluctance variable transversalement laminée (b)

Les comparaisons entre ces deux types de machines électriques ont déjà été traitées dans la littérature. Nous avons constaté que les comparaisons ont été effectuées lorsque les deux machines étaient dimensionnées mais selon des cahiers des charges différents. Afin de réaliser la comparaison de ces deux machines électriques, les travaux à mener dans cette thèse ont consisté à étudier tout d'abord les modèles électromagnétiques, énergétiques, et économiques de ces deux machines électriques. Ces modèles devant être rapides afin d'être couplés avec des logiciels d'optimisation tout en restant précis. Dans un second temps ces structures ont été optimisés en terme de coût et de pertes sur cycles automobiles.

Dans ce premier chapitre, quelques hypothèses ont été formulées pour nous aider à réaliser cette étyde : compte tenu de la complexité de la conception, les géométries des moteurs choisis sont assez simples, des détails tels que l'inclinaison du rotor et les matériaux d'isolation n'ont pas été pris en compte dans la conception. Les deux machines sont supposées d'avoir le même type d'enroulement et la même géométrie d'encoches statoriques.

Modèles Multiphysiques

Afin de réaliser les optimisations des chapitres suivants, il nous faut des modèles multiphysiques rapides et précis des deux machines étudier. C'est l'objet de ce chapitre.

Modèles électromagnétiques

Les modèles électromagnétiques estiment les comportements des machines asynchrones et synchrones à réluctance variables (couples, flux,…), sur la base de la géométrie du moteur et des paramètres de contrôle.

Machine asynchrone

Un circuit électrique équivalent est utilisé dans le cas du modèle analytique de la machine asynchrone. Tout d'abord, les paramètres équivalents du circuit, à l'exception de l'inductance magnétisante, la résistance et l'inductance du rotor sont déduits de formules analytiques. La résistance et l'inductance du rotor sont estimées par une méthode numérique, en divisant une barre du rotor

en plusieurs couches. Cette méthode est applicable pour une barre de forme arbitraire. Puis, en négligeant certains flux de fuite et à l'aide de la loi de Faraday, la relation entre l'induction dans l'entrefer, et celle dans les tôle et les dents sont établies. La distribution de l'induction dans l'entrefer est ensuite déduite avec une méthode numérique. Des caractéristiques comme la tension de phase et le couple électromagnétique sont alors calculés. Les étapes pour la construction du modèle analytique de la machine asynchrone sont illustrées dans la Figure c.

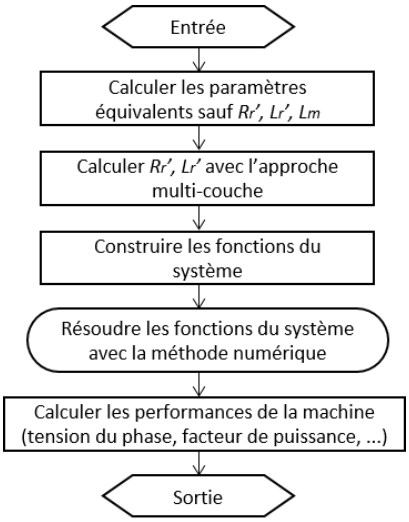

Figure c Ordre des étapes dans la construction de modèle analytique pour la machine asynchrone

Machine à reluctance variable

Pour le modèle analytique de la machine synchrone à reluctance variable, le repère *dq* est utilisé. De même que pour la machine asynchrone, le théorème d'Ampère et la loi de Faraday sont appliqués pour calculer la distribution de l'induction dans l'entrefer. Dans l'entrefer en face des ponts tangentiels (les régions en noir dans la Figure d), le circuit magnétique est traité particulièrement, en prenant en compte l'hypothèse que la culasse dans le stator se comporte linéairement.

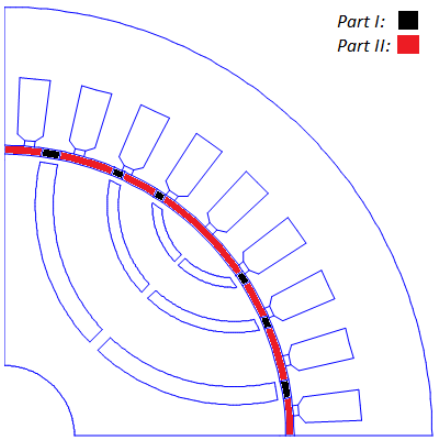

Figure d Division en régions de l'entrefer

Modèles des pertes, économiques et mécanique

Le modèle énergétique effectue le calcul des pertes dans le convertisseur, les câbles et les machines électriques. Les calculs des pertes par effet Joule, des pertes fer et des pertes mécaniques sont décrites dans ce mémoire. Dans le modèle économique, les coûts de fabrication de ces deux machines électriques sont estimés grossièrement : ils ne dépendent que des paramètres géométriques. Dans le modèle mécanique de la machine synchrone à réluctance variable, les contraintes imposées sur les ponts tangentiels et radiaux sont estimées. Un facteur de sécurité, rapport entre la contrainte maximale et la résistance nominale du matériau, est défini dans la conception.

Validation des modèles

Les modèles électromagnétiques et mécanique ont été validés à l'aide de simulations par éléments finis.

Pour la machine asynchrone, les calculs analytiques de la résistance et de l'inductance des barres pour différentes géométries ont été validés par une analyse éléments finis en régime harmonique sur une grande plage de fréquence. Les faibles différences ont montré que le modèle analytique est valable pour des barres rectangulaires ou non-rectangulaires.

Ensuite sur une machine asynchrone prédéfinie, le modèle analytique a été validé par une modélisation par éléments finis en régime transitoire et pour plusieurs valeurs de glissements. L'erreur analytique est considérée comme tolérable pour la conception.

Nous avons aussi proposé une méthode qui combine le modèle analytique et les éléments finis statiques : dans le cas éléments finis. Dans ce cas, le courant induit dans les conducteurs du rotor est imposée par l'estimation analytique dans la simulation éléments finis. Cela nous permet d'estimer la tension de phase et le facteur de puissance avec un calcul numérique.

Une méthode basée sur des analyses éléments finis en régime statique a été appliquée pour la validation du modèle analytique de la machine synchrone à réluctance variable. Elle fournit une estimation du couple moyen avec un nombre minimal de simulations. Le modèle analytique a été validé par cette méthode numérique pour différentes géométries de rotors. Avec les mêmes paramètres de commande, ces machines avec différents rotors ont été validées et comparées à partir de la tension de phase, le couple moyen, le facteur de puissance et l'ondulation de couple. L'erreur analytique est acceptable pour ces machines testées. En outre, la géométrie du rotor appliquée dans la conception (voir Figure (b)) a été déterminée à partir des comparaisons.

Enfin, le modèle mécanique de la machine synchrone à réluctance variable a été validé par des analyses éléments finis (problème mécanique en élasticité linéaire). Les contraintes analytiques sur les ponts rotoriques ont été comparées avec les contraintes numériques (critère de Von Mises), avec une erreur un peu élevée, mais encore tolérable pour la conception.

Méthodologie et résultats d'optimisations

Méthodologie

Afin de réaliser une optimisation sur conditions réelles, il est nécessaire d'utiliser un cycle de roulage. Après une discussion sur les différents cycles existants, il a été décidé d'utiliser le cycle de conduite Artemis. Ce cycle possède de nombreux points et il est irréalisable de faire une optimisation sur l'ensemble de ces points (~ 12000). Plusieurs points représentatifs (dans le plan couple-vitesse) sont donc sélectionnés sur l'ensemble du cycle à l'aide d'une méthode de partitionnement de données (*kmeans clustering*) afin de réduire les temps de calcul.

Une technique innovante d'optimisation a été proposée. Deux optimisations imbriquées sont réalisées à l'aide de la séparation des variables électriques et géométriques. Le schéma global de l'optimisation est montré sur la Figure e.

Un algorithme d'évolution différentielle est en charge de l'optimisation globale qui va définir les paramètres géométriques des machines à optimiser. Pour chaque individu de la population, une optimisation locale des paramètres géométriques est réalisée afin d'obtenir pour une géométrie donnée la meilleure *commande* réalisable. Pour chaque individu d'une population, les paramètres de contrôle sont optimisés pour avoir des pertes énergétiques minimales et un facteur de puissance élevé, le tout sous plusieurs contraintes électriques et magnétiques.

Cet algorithme d'évolution différentielle est couplé lors d'optimisation multi-objectifs à une technique NSGAII.

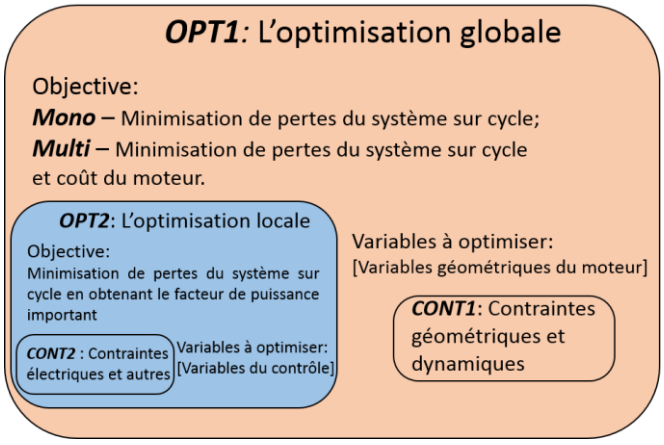

Figure e Optimisations globale et locale des machines électriques

Résultats d'optimisations

Optimisations mono-objectif

Pour l'optimisation mono-objective, le but est de parvenir à des pertes minimales sur cycle.

Des machines asynchrones à quatre et six pôles ont été dimensionnées et comparées à partir de leurs masses, volumes, coûts, rendements énergétiques et facteurs de puissance. La machine à quatre pôles est plus intéressante que celle à six pôles en termes de coût et facteur de puissance, lorsque leurs volumes et rendements énergétiques sont comparables.

D'après les résultats des optimisations mono-objectives, les deux machines optimisées possèdent un volume et une masse similaires. Toutefois, la machine asynchrone coûte 30% de plus que la machine synchrone à réluctance variable, car elle utilise plus de cuivre et d'aluminium. Le rendement et le facteur de puissance de la machine asynchrone sont plus intéressants au cours du cycle de conduite. Son facteur de puissance est près de 10% plus élevé que celui de la machine synchrone à réluctance variable. Par rapport au facteur de puissance, la différence du rendement est faible. Pour les deux machines électriques, le courant de phase est élevé en raison de la contrainte de tension de phase imposée par la batterie, qui apporte des pertes joules importantes dans l'onduleur. Les pertes joules de la machine asynchrone sont plus élevées, tandis que les pertes fer de la machine synchrone à réluctance variable sont plus élevées.

Optimisations bi-objectifs

Les Fronts de Pareto obtenus des optimisations bi-objectives ont été comparés, comme montré dans la Figure . Le rendement le plus élevé de la machine synchrone à réluctance variable est 0.5% moins élevé que celui de la machine asynchrone. Cependant, le rendement de la machine synchrone à réluctance variable pourrait être amélioré à partir de l'expérience du concepteur, et avec des contraintes géométriques et électriques redimensionnées. Sur la Figure f, le rendement de la machine synchrone à réluctance variable est supérieur à celui de la machine asynchrone pour un même coût. Et quand les machines optimisées en même rendement sont comparées, les machines synchrones à réluctance variable coûtent de 10% à 25% de moins que les machines asynchrones. Autrement dit, la machine synchrone à réluctance variable est une meilleure réponse à la machine électrique à bas coût pour véhicules électriques, s'il n'y pas d'exigences particulières sur le facteur de puissance.

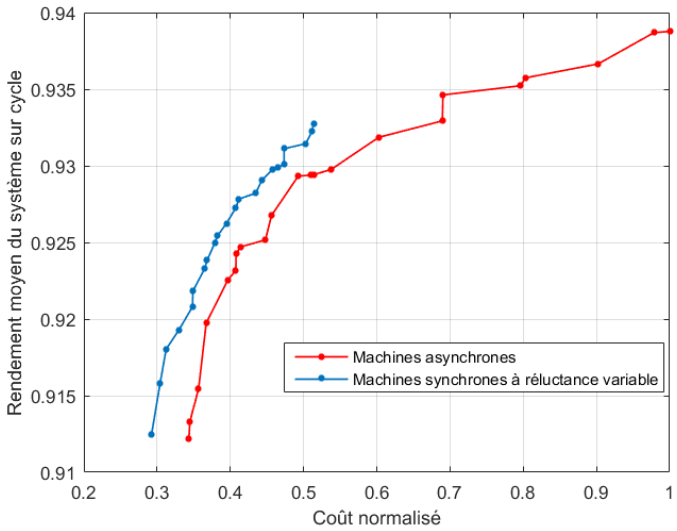

Figure f Comparaison des Fronts de Pareto des moteurs asynchrone et synchrone à réluctance variable

Conclusions

Les principales contributions de cette thèse reposent sur :

- la mise en place et la validation de modèles analytiques pour la machine asynchrone à cage et la machine synchrone laminée transversalement à réluctance variable;
- la proposition et réalisation de l'optimisation de ces deux machines pour la traction du véhicule électrique et sur la base des modèles analytiques proposées;
- les comparaisons de ces deux machines basées sur les résultats d'optimisation.

Les travaux pourraient être complétés par :

- l'ajout d'un modèle thermique à la modélisation analytique. Il s'agirait ensuite de réaliser l'optimisation et des comparaisons avec la même méthode, pour évaluer les influences thermiques sur des résultats d'optimisation ;
- le développement d'un modèle analytique pour estimer l'ondulation de couple de la machine synchrone à reluctance variable;
- un changement du cahier des charges concernant les contraintes géométriques, et la capacité de la batterie et l'onduleur, puis de réaliser des nouvelles optimisations et comparaisons;
- la comparaison des machines optimisées avec d'autres types de machines électriques, telles que les machines synchrones à rotor bobiné ou à réluctance variable à double saillance.

Appendix1 Calculations of leakage inductance and resistance

1.1 Induction motor

We classify the leakage inductances by component: leakage in the stator and leakage in the rotor. The following inductances are counted (see Figure A: 1.1):

- End-winding leakage inductance;
- Slot leakage inductance;
- Differential leakage inductance;
- Zigzag leakage inductance.

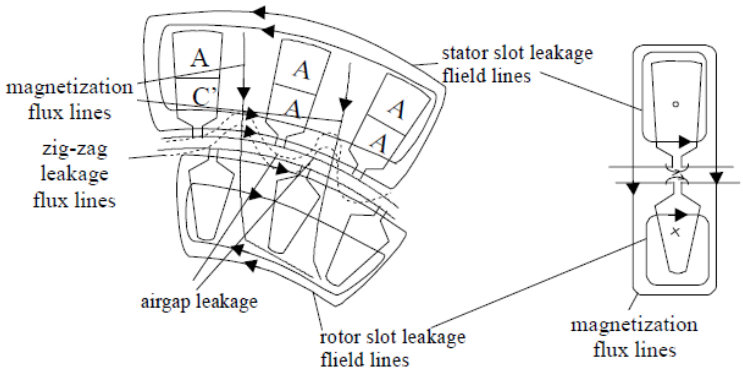

Figure A: 1.1 Flux distribution in IM ([BONA10])

Other issues such as skewing leakage are neglected.

- ***End-winding leakage inductance***

The exact calculation of the end-winding leakage is very difficult since the couplings between adjacent coils and adjacent phases on each other should be considered. Probably the most rigorous solution is from the help of 3D FE tools, which is far too complicated to be repeated here. The following formulas are taken from some classical books or articles ([ALGE65] [BONA10]).

To simplify the calculations, all the end-windings are treated as on the rounded shape with the same length (see Figure A: 1.2 (c)).

For a simple end-winding (with single bobbin), and from Biot-Savart Law, the linked flux passing through the bobbin is deduced by:

$$\phi_{endw} = \mu_0 \frac{l_{endw} i_a}{2\pi} \log\left(\frac{l_{endw}}{p_{endw}}\right) \qquad \text{A: 1.1}$$

Where i_a is the current passing through this end-winding, l_{endw} is the average length of the end-winding, and p_{endw} is the perimeter of its cross section. The average length of a rounded end-winding could be estimated in the following formula.

$$l_{endw} = \frac{2\pi\left(\frac{1}{2}D_s + h_{ts}\right)}{2p} + 2h_{ts} \qquad \text{A: 1.2}$$

Where D_s is the inner diameter of stator, h_{ts} is the stator slot height, and p the pole pair number.

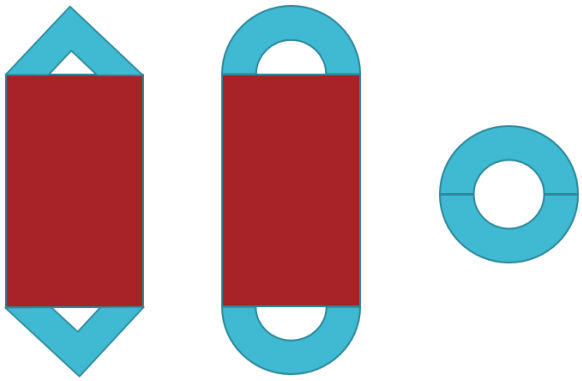

Figure A: 1.2 End-winding shapes

With n_s turns of coil in each phase and p pairs of poles, the leakage flux induced by three-phase winding is expressed in equation A: 1.3.

$$\phi_{endw} = \frac{4}{3}\frac{\mu_0 l_{endw} i_s}{2\pi} 2p \left(\frac{n_s}{2p}\right)^2 \log\left(\frac{l_{endw}}{p_{endw}}\right) \qquad \text{A: 1.3}$$

And the formula to quantify end winding inductance is applied as in equation A: 1.4.

$$L_{es} = \frac{\mu_0 l_{endw}}{3\pi}\frac{n_s^2}{p}\log\left(\frac{l_{endw}}{p_{endw}}\right) \qquad \text{A: 1.4}$$

For cage rotor with end rings attached to the rotor stack, an empirical formula is given ([WIMU90]):

$$L_{endr} = \frac{3\mu_0 D_{ir}}{n_r}\log\left(4.7\frac{D_{ir}}{a+2b}\right) \qquad \text{A: 1.5}$$

Where:

-l_{es}: the end connection length;
-D_{ir}: the average diameter of end-ring;
-a: the ring axial dimension;
-b: the ring radial dimension;
-n_r: the rotor bar number.

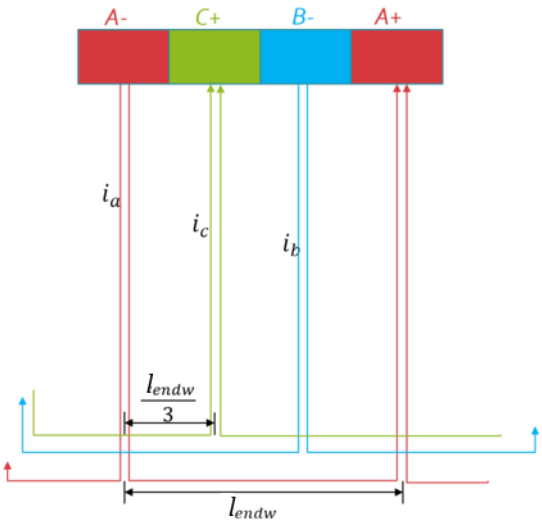

Figure A: 1.3 Phase end-winding distribution

- ***Slot leakage inductance***

For the stator slot leakage inductance, the inductance calculation depends mainly on its winding type and slot geometry. Here, we consider the case a rectangular stator slot and a distributed single layer winding. While in the case that both skin effect and back saturation neglected, with Ampere's Law applied in the contour as shown in Figure A: 1.4:

$$H(x)b_s = \frac{nIx}{h_s} \qquad (0 \le x \le h_s)$$
$$H(x)b_s = nI \qquad (h_s < x \le h_s + h_{os}) \qquad \text{A: 1.6}$$

The leakage inductance per slot is then deduced from magnetic energy:

$$\lambda_{sls} = \frac{2W_{em}}{I^2} = \frac{2}{I^2}\frac{1}{2}\int_0^{h_s+h_{os}} H^2(x)dx\, Lb_s = \mu_0 Ln^2\left(\frac{h_s}{3b_s} + \frac{h_{os}}{b_{os}}\right) \qquad \text{A: 1.7}$$

Where:

-b_s: the slot width;
-b_{os}: the slot opening width;
-h_s: the slot height;
-h_{os}: the slot opening height;
-L: the motor length.

For a three-phase full pitch winding, the phase equivalent slot leakage inductance is defined as:

$$L_{sls} = \frac{n_e}{m}\mu_0 L\left(\frac{n_s}{pq}\right)^2\left(\frac{h_s}{3b_s} + \frac{h_{os}}{b_{os}}\right) = \frac{2\mu_0 L{n_s}^2}{pq}\left(\frac{h_s}{3b_s} + \frac{h_{os}}{b_{os}}\right) \qquad \text{A: 1.8}$$

Where:

-q: the slot number per pole per phase;
-n_e: the stator slot number;

-*m*: the motor phase number.

The calculation of rotor slot leakage inductance with skin effect considered were discussed in Chapter 2.

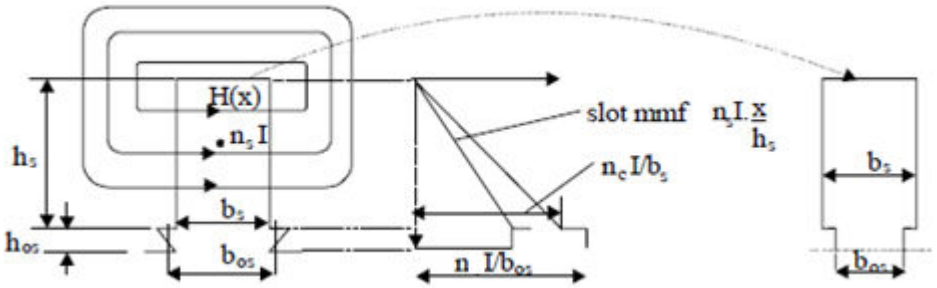

Figure A: 1.4 Rectangular slot leakage ([LIPO04])

- ***Differential leakage inductance***

Differential leakage comes from space flux density air-gap harmonics in the air-gap. It depends on the m.m.f. distribution form (winding type) and saturation ([LIPO04]). With only step m.m.f. harmonics considered, the phase stator differential leakage inductance could be expressed by the empirical formula in equation A: 1.9. It's valid only for full-pitch coil three-phase winding, with tooth saturation not considered.

$$L_{ds} = \frac{2\mu_0 L {n_s}^2}{qp}\left(\frac{5q^2+1}{12q^2}\frac{2\pi^2}{m^2 {k_w}^2} - 1\right) \qquad \text{A: 1.9}$$

Similarly, the rotor differential leakage inductance for a cage rotor (when rotor skew neglected) could be expressed by equation A: 1.10.

$$L_{dr} = \mu_0 L\left(\frac{1}{{\eta_r}^2} - 1\right) \qquad \text{A: 1.10}$$

$$\text{With} \quad \eta_r = \frac{\sin\left(\frac{\pi p}{n_r}\right)}{\frac{\pi p}{n_r}}$$

From equation A: 1.5-6, we conclude that increasing the stator slot number and rotor bar number could help to decrease differential leakage inductance.

- ***Zigzag leakage inductance***

Zigzag leakage flux refers to the air-gap flux which does not reach the other slotted structure, as it snakes out the teeth around slot openings. The empirical formulations of stator and rotor given in equation A: 1.11 ([BONA10]).

$$L_{zs} = \frac{2\mu_0 L {n_s}^2}{qp}\left(\frac{5gk_c}{4gk_c + 5b_{os}}\right)$$

$$L_{zr} = \mu_0 L\left(\frac{5gk_c}{4gk_c + 5b_{or}}\right)$$

A: 1.11

It should be noticed that the quantity of the zigzag leakage inductance is mainly dependent on the ratio between the air-gap width and the slot opening width.

Finally, the equivalent stator leakage inductance sums all these inductances.

$$L_s = L_{es} + L_{sls} + L_{ds} + L_{zs} \qquad \text{A: 1.12}$$

In a similar way, the equivalent rotor leakage inductance could be deduced.

The d.c. stator phase resistance could be plainly expressed by:

$$R_{sdc} = \rho_{Cu} l_c \frac{n_s}{nA_{cos}}$$

$$l_c = 2(L + l_{endw})$$

A: 1.13

Where:
- ρ_{Cu}: copper resistivity which depends on the winding temperature;
- l_c: one coil turn length;
- n_s: number of winding turns per phase
- L: motor length;
- l_{endw}: average length of the end-winding;
- n: number of conductors per coil turn;
- A_{cos}: conductor section area.

Slot filling factor K_{fill} represents the ratio between the coil cross section in each slot and slot section, and we assume it as a constant.

With penetration and proximity effects considered, the a.c. resistance could be expressed as in equation A: 1.14.

$$R_{sac} = \left(K_{se} + K_p\right)R_{sdc} \qquad \text{A: 1.14}$$

Where K_{se} indicates the skin effect coefficient, and K_p indicates the proximity effect coefficient. Skin effect coefficient for a coil containing n conductors per slot is expressed by the analytical formula in A: 1.15.

$$k_{se} = \lambda \frac{\sinh(2\lambda) + \sin(2\lambda)}{\cosh(2\lambda) - \cos(2\lambda)} + 2\lambda^2 \frac{n^2 - 1}{3} \frac{\sinh(2\lambda) - \sin(2\lambda)}{\cosh(2\lambda) + \cos(2\lambda)} \quad \text{A: 1.15}$$

Where λ is the reduced height of conductor ($\lambda = \frac{h}{\delta}$), in which h is the conductor height and δ is the skin depth:

$$\delta = \frac{1}{\sqrt{\sigma_{Cu}\mu_{Cu}\pi f}} \quad \text{A: 1.16}$$

Where σ_{Cu} and μ_{Cu} are the conductivity and permeability of copper, and f is the current frequency.

And the proximity effect coefficient K_p as a result of magnetic coupling between neigbouring currents is quantified by the following equation ([GREL89]):

$$k_p = \lambda' \frac{\sinh(2\lambda') + \sin(2\lambda')}{\cosh(2\lambda') - \cos(2\lambda')} - 1 \quad \text{A: 1.17}$$

Where $\lambda' = n\lambda$ is the total reduced height of conductors in one slot. The application of Litz wire or the reduction of conductor diameter could extenuate these two effects. The calculation of rotor resistance has been presented in Section 2.4.

1.2 Synchronous reluctance motor

As the stator winding types and slot forms of IM and of SynRM are the same, the calculations of stator leakage inductance and stator phase resistance are the same with the IM. One assumption that the stator leakage inductance is independent of the rotor position and to be identical along the direct and quadrature axis directions.

Appendix 2 Validations on the optimized motors

Working point database is listed in the following table:

Number	*Speed [tr/min]*	*Torque [Nm]*	*Power [kW]*	*Weight*
		Motor mode		
1	593	21.74	1.35	439
2	1666	39.55	6.9	193
3	2970	38.1	11.85	190
4	3355	12.95	4.55	223
5	3884	43.15	17.55	95
6	8134	20.16	17.17	180
7	8435	9.24	8.16	21
8	9216	24.93	24.06	120
		Brake mode		
9	681	-7.15	-0.51	202
10	1987	-12.5	-2.6	170
11	3062	-17.62	-5.65	113
12	6983	-11.66	-8.53	32

- ***Induction machine***

Under the same current supplies, the electromagnetic torque, the phase voltage, and the power factor calculated from analytical and numerical (harmonic and static finite element analysis) models of the IM are compared at the selected working points, as shown in the following tables.

Number	$\hat{i}_s$ *[A]*	*Slip ratio*	*Analytical torque [Nm]*	*Numerical torque [Nm]*	*Error [%]*
			Motor mode		
1	41.2	0.014	21.8	20.9	4.3
2	61.3	0.0077	39.6	38.3	3.4
3	58,2	0.0038	38.1	37	3
4	34.6	0.0037	13	12.4	4.8
5	63.6	0.0032	43.2	41.7	3.6
6	89	0.0036	20.16	19.2	4.7
7	61.5	0.0036	9.3	8.8	5
8	119	0.0046	25	24.3	2.9
			Brake mode		
9	23.3	-0.0084	-7.2	-6.9	-4.3
10	31.3	-0.0043	-12.5	-11.8	-5.9
11	37.2	-0.0028	-17.7	-17.1	-3.4
12	31.4	-0.0019	-11.7	-11.2	-4.5

Number	Analytical phase Voltage [V]	Numerical phase Voltage [V]	Error [%]
	Motor mode		
1	37	35	5.4
2	112	108	3.6
3	206	200	2.9
4	130	129	0.8
5	273	266	2.6
6	224	218	1.8
7	155	141	4.9
8	257	238	2.3
	Brake mode		
9	27	26	3.7
10	85	80	5.8
11	155	149	0.7
12	259	251	3.1

Number	Analytical power factor	Numerical power factor	Error [%]
	Motor mode		
1	0.76	0.77	-1.3
2	0.84	0.86	-2.4
3	0.81	0.83	-2.5
4	0.83	0.84	-1.2
5	0.83	0.84	-1.2
6	0.86	0.88	-2.3
7	0.86	0.88	-2.3
8	0.87	0.89	-2.3
	Brake mode		
9	0.67	0.69	-3
10	0.8	0.82	-2.5
11	0.8	0.83	-3.8
12	0.89	0.89	0

- ***Synchronous reluctance machine***

Similarly, the electromagnetic torque, the phase voltage, and the power factor calculated from analytical and numerical models (static finite element analysis) of the SynRM are compared at the selected working points, as shown in the following tables.

Number	*$\hat{i}_s$ [A]*	*Current Angle [°]*	*Analytical torque [Nm]*	*Numerical torque [Nm]*	*Error [%]*
			Motor mode		
1	44.8	55.9	21.7	21.4	1.4
2	64.7	60	39.5	39	1.3
3	64	62.2	38.1	37.1	2.7
4	35	59.3	13	12.7	2.4
5	70.4	64.6	43.1	41.7	3.4
6	53.7	72	20.2	19.3	4.7
7	32.7	66.7	9.2	9.1	1
8	60	72	24.9	23.7	5
			Brake mode		
9	24.7	-50	-7.1	-7.1	0
10	33.1	-53.2	-12.3	-12.4	0.8
11	40.6	-58	-17.3	-17.4	0.5
12	35.6	-64.8	-11.4	-11.5	0.9

Number	*Analytical phase Voltage [V]*	*Numerical phase Voltage [V]*	*Error [%]*
	Motor mode		
1	32	34	-5.9
2	110	113	-2.7
3	185	190	-2.6
4	136	142	-4.2
5	241	249	-3.2
6	303	315	-3.8
7	250	263	-4.9
8	382	391	-2.3
	Brake mode		
9	24	26	-7.7
10	86	92	-6.5
11	145	152	-4.6
12	241	250	-3.6

Number	*Analytical power factor*	*Numerical power factor*	*Error [%]*
		Motor mode	
1	0.75	0.72	4.2
2	0.77	0.76	1.3
3	0.78	0.78	0
4	0.75	0.74	1.4
5	0.8	0.79	1.3
6	0.82	0.8	2.5
7	0.78	0.76	2.6
8	0.82	0.8	2.5
		Brake mode	
9	0.67	0.64	4.6
10	0.7	0.69	1.4
11	0.74	0.73	1.4
12	0.78	0.76	2.6